NASA CONTRACTOR REPORT

NASA CR-737

NASA CR-737

AERODYNAMIC CHARACTERISTICS FOR CONE-CYLINDER-FRUSTUM-CYLINDER CONFIGURATIONS AT MACH NUMBERS FROM 0.7 TO 1.96

VOLUME I - LINEAR LOAD DISTRIBUTIONS

by J. F. Thompson

Prepared by
LOCKHEED MISSILES & SPACE COMPANY
Huntsville, Ala.
for George C. Marshall Space Flight Center

NATIONAL AERONAUTICS AND SPACE ADMINISTRATION • WASHINGTON, D. C. • APRIL 1967

NASA CR-737

AERODYNAMIC CHARACTERISTICS FOR CONE-CYLINDER-FRUSTUM-CYLINDER CONFIGURATIONS AT MACH NUMBERS FROM 0.7 TO 1.96

VOLUME I. LINEAR LOAD DISTRIBUTIONS

By J. F. Thompson

Prepared under Contract No. NAS 8-20121 by
LOCKHEED MISSILES & SPACE COMPANY
Huntsville, Ala.

for George C. Marshall Space Flight Center

NATIONAL AERONAUTICS AND SPACE ADMINISTRATION

For sale by the Clearinghouse for Federal Scientific and Technical Information
Springfield, Virginia 22151 – CFSTI price $3.00

FOREWORD

This report presents the results of work performed by Lockheed Missiles & Space Company, Huntsville Research & Engineering Center, under Contract NAS8-20121, "Determination and Presentation of Experimentally Derived Load Distributions."

This work was done for the Marshall Space Flight Center Aero-Astrodynamics Laboratory by the Aerodynamics & Propulsion Section of the HREC Aero-Mechanics Department.

ACKNOWLEDGEMENT

Acknowledgement is made for the contributions to this report by Louis F. Conner, Michael F. Doktor, C. Ray Turner and Charles D. Cope. Initial planning and direction of the study was accomplished by R. L. Hamner. The wind tunnel test program was conducted by A. D. Leff.

SUMMARY

The data from an extensive wind tunnel pressure distribution test program were analyzed to provide linear aerodynamic load distributions in the high subsonic, transonic and low supersonic Mach number regimes for cone-cylinder-frustum-cylinder configurations.

The configurations were of such geometry as to be compatible with the previous cone-cylinder work which together provide a knowledge of the loads on selected cone-cylinder-frustum-cylinder configurations.

The geometrical parameters varied in this study were (1) the cone semivertex angles (from 15° to 40°); (2) the conical frustum angles (from 7.5° to 20°); (3) cylinder diameter ratios (D_2/D_4 = 0.4, 0.6, 0.8); and (4) the forward cylinder lengths (from 0.5 to 4.0 calibers). The aft cylinder lengths were constant at 3.5 calibers.

A comprehensive set of design curves is presented which will enable the designer to determine aerodynamic loads in a Mach number range where adequate information has not been available. Local normal force slope distributions for the segments of a cone-cylinder-frustum-cylinder were developed on a parametric basis for the area of interest. The local normal force slope distributions for the nose cone have been determined in the previous cone-cylinder study and are not presented here. The loads presented here are the distributed loads on the other three sections of the cone-cylinder-frustum-cylinder configuration: forward cylinder, frustum and aft cylinder.

The pressure data obtained from the wind tunnel test was analyzed, using computer programs formulated by Lockheed. The pressure distribution data was integrated to obtain local normal force and then slopes of local normal force versus angle-of-attack curves were obtained and integrated to obtain total normal force slopes. Correlations of the pressure data and loads data were made for the parametric ranges of geometries to produce well-defined variations of loads as functions of the various aerodynamic and geometric parameters. The cone-cylinder loads data which was obtained from the previous study was combined with the distributions for the first cylinder, frustum, and second cylinder to produce the complete body local normal force slope distributions for all the configurations. Comparisons of C_{N_α} and C_{M_α} from force test and pressure data showed very favorable correlation (within 10%). The distributions were then separated into body sections and carpet plots were prepared for the parameters for each section. These carpet plots are published in this report.

Many flowfield and load characteristics were noted from the carpet plots and are discussed in more detail in the discussion sections. Some of the more general characteristics that were observed from the plots are summarized. The large normal force gradients aft of the nose cone previously noted in the cone-cylinder study are not significantly affected by the flare for the front cylinders longer than two calibers. For the short forward cylinder case, the load distribution values on the forward cylinder are reduced because of the large influence of the flare upstream. Boundary layer separation occurs after the cone and before and after the flare for some combinations of cone and flare angles. The approximate conditions in which separation occurs can be noted from the location of the discontinuity in the local normal force carpet plots. Mach number has a pronounced effect on the cylinder load distributions. A near normal shock occurring on the cylinder in transonic flow is accompanied by a sudden surface pressure rise. Negative spikes of local normal force, corresponding to these shocks, occur due to angle of attack.

The local normal force slope carpet plots, presented for all the parameters in 120 plots, provide the most complete study results available to the designer to determine aerodynamic loads on cone-cylinder-flare-cylinder configurations.

CONTENTS

SYMBOLS

C_M	pitching moment coefficient, $M/q_\infty SD$
C_{M_α}	pitching moment coefficient slope, $\partial C_m/\partial\alpha$, per radian
C_N	normal force coefficient, $F_N/q_\infty S$
C_{N_α}	normal force coefficient slope, $\partial C_N/\partial\alpha$, per radian
C_N'	local normal force coefficient, $\partial C_N/\partial(X/D)$, per caliber
C_{N_α}'	local normal force coefficient slope, $\partial C_N'/\partial\alpha$, per radian caliber
D	base (reference) diameter, D_4 = 2.0 inches - pressure model 1.5 inches - force model
F_N	normal force
L	segment length
M	pitching moment about mrp
M_c	critical Mach number
M_∞	freestream Mach number
mrp	moment reference point (see Figure 1)
q	dynamic pressure, $\rho V^2/2$
R_N	Reynolds number, $\rho V/\mu$, per foot
S	reference area, $\pi D_4^2/4$
V	velocity
X	distance downstream of segment leading edge
α	angle of attack, degrees
θ_N	cone or flare semivertex angle, degrees (N denotes segment number)

μ	coefficient of absolute viscosity
ρ	density
ϕ	radial angle, degrees
D_N	segment maximum diameters (N denotes segment number)

Subscripts

∞	freestream
1	cone segment
2	forward cylinder segment
3	flare segment
4	aft cylinder segment
N	body segment number

Wind Tunnel Model Configuration Symbols

A complete typical cone-cylinder-flare-cylinder configuration is identified by the following symbols - $6N_{15}\ C_4\ F_{7.5}\ B_{3.5}$

1. 6 the diameter ratio of forward and aft cylinders (D_2/D_4) (in tenths, i.e., $D_2/D_4 = 0.6$)
2. N_{15} the nose cone; subscript denotes cone half angle (15°)
3. C_4 the forward cylinder; subscript denotes cylinder length $(L_2/D_2 = 4.0)$
4. $F_{7.5}$ the flare; subscript denotes flare half angle (7.5°)
5. $B_{3.5}$ the aft cylinder with a 3.5 caliber length

LIST OF FIGURES

Section 1
INTRODUCTION

The aerodynamic characteristics for cone-cylinder-frustum-cylinder configurations are often required for design studies of launch vehicles. One of the requirements is to establish the local normal force distributions over the vehicle. The purpose of the present study, referred to as "the trisonic frustum aerodynamic loads study" because of the 3-velocity ranges covered, is to establish a set of aerodynamic loads design curves for cone-cylinder-frustum-cylinder configurations on a parametric basis. The Mach number range of interest is from 0.7 to 2.0. The requirement to extend the study of the aerodynamic loads on cone-cylinder configurations to cone-cylinder-flare-cylinders was established so that accurate preliminary design loads can be predicted for a wide variety of launch vehicle configurations.

An extensive wind tunnel test program (Reference 1) was conducted in the MSFC 14x14-inch wind tunnel in order to obtain sufficient data to adequately define the linear aerodynamic loads design curves. The geometry of these configurations is frequently cone-cylinder-flare-cylinder. (During the course of this report the geometrical body section which is defined as a conical frustum will also be referred to as a flare.) A fairly successful study (Reference 2) was conducted at LMSC/HREC to determine loads on flares but a complete parametric definition could not be obtained because of lack of data. The source of all data in the present study was the wind tunnel test program. It is not a collection of data from various sources. This permitted very compatible results to be obtained, and the quality of the results obtained indicates this.

The study of cone-cylinder configurations (Reference 3) established the loads on the cone, and these are not presented in this study. Carry-over loads on the forward cylinder from the cone, presented in Reference 3, were used in this study to help evaluate the carryover loads

obtained on the forward cylinder. To retain the compatibility and usefulness of the data from previous and present studies, data for identical Mach numbers were used. The established set of design curves will predict the linear gradient loads on cone-cylinder-flare-cylinder configurations, and will do it quite accurately for preliminary design requirements. Other aspects of the problem of predicting aerodynamic phenomena such as non-linear loads, hysteresis effects, Reynolds number effects, and unsteady (oscillation) flow are not investigated here. A set of shadowgraph pictures was taken to clarify the flow characteristics of some of the configurations. These pictures were published in Reference 4. The previous cone cylinder study was quite useful in predicting aerodynamic loads for cone cylinder configurations and the present study supplements this work with design curves for more complicated configurations.

Section 2
OBJECTIVES

The purpose of the study for which results are presented here was to establish a set of aerodynamic loads design curves for cone-cylinder-flare-cylinder configurations on a parametric basis. The Mach number range of interest is from 0.7 to 2.0. The loads presented in this report are local normal force slopes, total normal force slopes and total pitching moment slopes; all presented in coefficient form. Configuration geometries which were varied were nose cone angle, θ_1; first cylinder length, L_2/D_2; and frustum angle, θ_3. Inherent in these is the variable of body station for each segment. The variation of parameters is briefly discussed below (configuration geometries are shown in Figure 1):

1. Cone Angle: The semivertex angle, θ_1, was varied between 15° and 40° similar to the manner in which cone cylinder data was obtained in the previous cone cylinder study.
2. Frustum and First Cylinder Station: The local normal force distributions are dependent on axial distance, X, from the front of the segment. For convenience, the flare and first-cylinder are non-dimensionalized by the segment length L_N. The values of X/L_N then vary between 0 and 1.0.
3. Frustum Angle, θ_3: This is the semivertex angle of the conical frustum (flare) as shown in Figure 1. This angle is varied as the diameter ratio (D_2/D_3) is held constant. The different diameter ratios used were: 0.4, 0.6 and 0.8. This angle affects the loads on the flare and on the aft cylinder and in some cases affects the load on the forward cylinder.
4. Cylinder Length: The length of the aft cylinder is non-dimensionalized by the diameter. The distance x/D_4 is used in describing axial variations to a maximum value of 3.5.
5. Angle of Attack: The angle of attack was varied from 0 to 8° in the wind tunnel test. Angle-of-attack effects are included by the presentation of slopes of the variation of loads and forces with angle of attack. The angles tested did not show significant nonlinear effects in the total loads.

6. Mach Number: To be compatible with the previous cone-cylinder data, the identical Mach numbers were used. These Mach numbers are from 0.7 to 2.0.

7. Reynolds Number: The cone-cylinder-flare-cylinder configurations were tested at a nominal Reynolds number (5.3 to 6.7 million per foot) for the various Mach numbers and at the highest Reynolds number conditions available (6.9 to 12 million per foot). Some runs were made both with and without boundary layer trips. The basic objective was to obtain data at a high enough Reynolds number (turbulent boundary layer) that no appreciable effect would be expected for increasing Reynolds number.

Boundary layer trips, both grit and steel balls, were used to try to establish positively a turbulent boundary layer over the model. In the range of Reynolds numbers that was used in the test, the boundary layer was turbulent over the flare even though transition on the cone downstream of the trip was not apparent. Also for the Reynolds numbers tested, it was established from the pressure data that there was little effect. Additional characteristics are discussed further in Section 4: Discussion of Results.

Section 3
METHOD OF APPROACH

The data utilized in this study were obtained from wind tunnel tests and previously published cone-cylinder data. The tests performed at the MSFC 14 x 14-inch wind tunnel were both pressure and force test programs. The results from the force test were used to check the results of integration of the pressure data. Cone-cylinder data were used because it was unnecessary to repeat the testing of the cone cylinder and also to check compatability between the data obtained from the cone cylinder and the present study. The pressures obtained from the tests were integrated to obtain distributed loads. These distributed loads for the cone-cylinder-flare-cylinder configurations were obtained from the extensively instrumented pressure model. The pretest report (Reference 1) gives the details of test conditions and the configurations tested. The pressure model was instrumented with a row of pressure orifices on the top and bottom of the model (ϕ=0 and 180°). To obtain pressures at various radial positions at each station, the model was rotated to roll angles of 0, 15, 30 and 60 degrees and tested at each angle of attack and Mach number. When the model was rolled, the top row (ϕ=0) of orifices would measure the pressures at each roll angle for ϕ=0, 15°, 30° and 60°. The bottom row (ϕ=180°) of orifices would measure the pressures at ϕ=180°, 175°, 150° and 120°. These measurements were collated and, assuming symetrical pressure distributions to exist about the vertical plane, the complete radial pressure distributions were defined.

All pressure model configurations were tested at angles of attack of 0, 2°, 4° and 8° so that normal force gradients could be obtained. Pressures were read at every orifice for each roll angle at the 4 angles of attack and punched on IBM data cards. After the pressure testing was completed, the pressures were reduced to coefficient form. From these data, the loads analysis was performed. A detailed description of the data analysis is presented in the following discussion.

Data were analyzed in the following manner. The pressure coefficient data were punched on cards. The original test C_p output was punched as one C_p per card. The one-C_p-per-card data was rearranged to eight-pressure-coefficients-per-card (a radial distribution at one station). The resulting groups of eight-C_p-per-card decks were used in computing local normal force at each angle of attack for all configurations tested.

The computer program used to obtain the loads is the pressure integration program (Reference 5). This program formulated by LMSC, computes local normal force from radial pressures at each body station along with a complete development of the pressure forces and moments in the normal and axial planes. To further facilitate the data reduction required, the program was modified to perform curve fits of local normal force versus angle of attack and calculate local normal force slopes using the curve fits. First, second and third order polynomials were used to establish curves through the data points. After curves were established, tangent slopes from the three orders of curve fits and the average slopes between 0 and 3^o from the second and third order curve fits were calculated. In addition, to check the machine-computed slopes, slopes were read manually. The local normal force distributions were integrated and each was compared with the corresponding force data for that configuration. By comparing force and integrated pressure data it was established that the third order and third order average between 0 and 3^o curve fit slopes gave the best agreement. The average slope between 0 and 3^o angle of attack from the third order curve fit was computed by establishing a linear slope between zero and the C_N value at 3-degrees angle of attack established by the curve fit. (In other words, no data was actually at the 3^o point, but the value was established by the curve fitted by the polynomial through the actual data points.) This linear slope from 0 to 3^o angle of attack establishes a reasonable value of local normal force slope for locations on the body where separation occurs and/or the local normal force curve was nonlinear.

All the local normal force values for the body stations versus angle of attack and the local normal slopes obtained from the curve fits were plotted

by the SCR-4020 machine. This was done to obtain working plots as the data were processed. Since it was established that the third order curve fit tangent and the third order average slopes gave the best estimates of slopes, both sets of these data points were plotted by the computer for each body station for use in making fairings.

The data from the cone-cylinder study was used to complete the distributions for cone-cylinder-flare-cylinder configurations. Data from the previous test (cone-cylinder local normal force slopes) were converted to a new reference based on the diameter of the aft cylinder. These data were combined with the cylinder-flare-cylinder local normal force slopes from the present study to obtain complete distributions along the body. They were then integrated to obtain the normal force and pitching moment buildups.

For the final local normal force distributions plotted by the SCR-4020 machine, the cone-cylinder data, the third order curve fit and the third order average between 0 and 3^{o} slopes were used. By using two estimates of slopes, an indication was obtained of the difference in slopes attributable to the analytical procedure.

Fairings were made on the combined distributions of cone-cylinder and cone-cylinder-frustum-cylinder data through the data points that correspond to the third order average curve fit slopes and the cone cylinder data. The combined sets of data overlap each other on the forward cylinder. By inspection, it was determined if the two sets of data agreed; and, if not, the most reasonable data points were used and faired. Errors in the local normal force were observed and related to pressure orifices which malfunctioned during the test. These data points were not used when the distributions were faired, but are included as data points in the carpet plots. After the machine plots were faired to establish the final distributions to be used to construct local normal force carpet plots, they were integrated to determine the C_{N_α} and C_{M_α} buildups.

The faired distributions (from the third order average values and the cone-cylinder data) were used in a computer program to integrate the local normal force distributions to obtain C_{N_α} and C_{M_α} buildups, using a trapezoidal integration scheme. Inputs to this integration routine were taken close enough together to yield an essentially exact value of the area under the curve. These integrated buildups were then directly compared with normal force and pitching moment slopes obtained from the force tests. A 10% error band was used as the criterion to determine whether the pressure data agrees with the force test data. It was felt the accuracy of the data and the methods used would warrent using this 10% error criterion. After the forces and moments were compared, the loads distributions were refaired where necessary from force and pressure data so that the integrated results would agree within 10% of the force data. These fairings were used to establish the final curves to be used in the report presentation. The same carpet plots as those used in the cone cylinder report are used to present the local normal force slopes obtained from the test data (pressures). This method of presentation has proven to be quite desirable since curves for constant values of two variables may be presented on one plot, thereby permitting more accurate correlation and interpolation.

Carpet plots were prepared, presenting the loads distributions for individual components (segments) of the configurations. From Reference 3 and the carpet plots presented here, the complete configuration loads distribution can be prepared for cone-cylinder-flare-cylinder configurations.

Section 4
DISCUSSION OF RESULTS

4.1 GENERAL DISCUSSION

The design curves, constructed to represent the loads distributed over each individual body section, are presented in Figures 2 through 10. Each section of the body has its respective loads presented to isolate effects on the individual section. Carryover loads are included for the body sections on which they occur. The isolation of the effects of each section is useful in obtaining distributed loads for selected composite body geometry. The geometrical parameters which varied for each body section (forward cylinder, flare and aft cylinder) are: diameter ratio (D_2/D_4); flare angle (θ_3); front cylinder length (L_2); and nose cone angle (θ_1). The effects of these geometrical variables on the flow field are discussed in the following paragraphs so that how the loads occur on the body sections can be better understood.

Flow separation is one of the most significant flow phenomena that affects the distributed loads. It affects the vehicle loads by significantly changing the pressure distributions on a body in comparison to those obtained from attached flow. Angle of attack has affect upon separation by tending to retard separation on the windward side with the opposite effect on the leeward side. Large changes in normal force occur due to the radical pressure changes caused by the unsymmetrical separated flow pattern. The attached flow case does not create such significant asymmetric patterns. It is desirable to know the combinations of body parameters and flow conditions where flow separation occurs. Boundary layer separation occurs for some combination of Mach numbers, Reynolds number, and body geometry. Their effects on local normal force are apparent from examination of the results of this study. More detailed discussions of how separation affects the loads on each body section are presented under their appropriate titles.

Reynolds number affects the critical Mach number where separation occurs. All the configurations tested carried nose-transition strips to trip the boundary layer. In the range of Reynolds numbers tested, there were no significant effects found on the measured loads. The boundary layer was tripped in most cases. Shadowgraph pictures of the flow field of the cone-cylinder-flare-cylinder are presented in Reference 4.

Shadowgraphs were taken at various Mach numbers to help evaluate if the boundary layer was turbulent or laminar after the trip. It could not be definitely established from the shadowgraphs that the boundary layer was turbulent after the trips because of the extremely thin boundary layer. The trips were located quite near the nose tip and the combined effects of the natural turbulence and the induced turbulence did not appear to induce transition of the boundary layer on the cone. Shock-induced transition on the forward cylinder was noted in examining the shadowgraphs. It was not determined if the boundary layer conditions on the cone had any effect on the distributed loads. Since shock-induced transition was found on the first cylinder and no influence on pressure distributions was noted in the Reynolds number study, it was concluded that the loads which had been obtained and presented correspond to turbulent boundary layer conditions.

4.2 COMPONENT LOADS AND FLOW CHARACTERISTICS

The flow characteristics of each geometrical section of the configuration are discussed separately in the following paragraphs. All the loads which occur will be related to the flow field characteristics and discussed. These sections are forward cylinder, flare, and aft cylinder.

A discussion of the loads on the nose cone was published previously in Reference 3.

4.2.1 Forward Cylinder

The local normal force distributions for the forward cylinder are presented in Figures 2 through 4 for the parameters tested. These loads are plotted by using X/L_2 as the length parameter because of the variation of this length with configurations. The X/L_2 parameter varies from 0 to 1.0 for all the configurations. The other parameters which were varied are nose cone angle, forward cylinder, length (L_2), diameter ratio (D_2/D_4), and flare angle (θ_3).

The first set of curves, presented in Figures 2a, b and c, show how the loads vary by changing frustum angle for various diameter ratios. For diameter ratios of 0.4, 0.6 and 0.8, the front cone angle and cylinder length were held constant. This forward cylinder length ($L_2/D_2 = 4.0$) is sufficient to isolate the effects of the cone from the flare on the forward cylinder. The distribution of load on the forward cylinder, which is 90% carryover from the cone, has the same variation for all the diameter ratios tested. However, the magnitude of the loads change due to the change in diameter of the forward cylinder and the flare carryover changes with increasing flare angles (θ_3). Therefore, the carryover loads for a constant diameter ratio from the nose cone were equal in magnitude, but only the carryover (loads induced on the forward cylinder) from the flare increased with increasing flare angle. The flare angles used were 7.5°, 10°, 15° and 20° for each of the three diameter ratios. The length of the forward cylinder increased for increasing diameter ratio (D_2/D_4). This variable is eliminated by using X/L_2 as the variable on the carpet plots.

The next condition to be discussed is the effect of nose cone angle on the forward cylinder loads. This is presented in Figure 3. The configuration consists of the variables: nose cone, forward cylinder ($L_2/D_2 = 2.0$ calibers), diameter ratio ($D_2/D_4 = 0.6$), and 15° flare angle (θ_3). Loading characteristics at $M = 0.7$ and 0.8 indicate that separation occurs between a $\theta_1 = 15^\circ$ to 25°

and the separated flow occurs over a greater length of the forward cylinder as θ_1 is increased.

The carryover loads on the cylinder at $\theta_1 = 40^o$ do not drop to essentially zero before the loads are affected by the flare carryover, because separation occurs between the nose-cone-cylinder juncture and the aft cylinder. The flow also tended to be unsteady as indicated by the shadowgraphs.

At M = 0.9, separation occurs between $\theta_1 = 15^o$ and 25^o. Using the results from the cone-cylinder study, separation was assumed to occur at 23^o. Again, at this Mach number, the leeward side is completely separated at angle of attack. Separation is assumed to occur at $\theta_1 = 31^o$ at M = 0.95, using the same criteria. At M = 1.0, the cylinder loads increase for larger nose cone angles, but the load increases negatively at the front of the cylinder while the frustum carryover loads increase. At the supersonic Mach numbers, the movement of the lee frustum shock forward at angle of attack causes a negative spike load on the cylinder. At M = 1.96, a strong nose shock is present, but the flare shock tends to be weak with only a small amount of separation. The supersonic flow field also causes an increase in carryover load on the cylinder from the cone.

The next variable to be analyzed is the effect of varying the length of the forward cylinder, while the remaining geometry is kept constant (33^o nose cone angle, diameter ratio $D_2/D_4 = 0.6$, and $\theta_3 = 15^o$). For this configuration, flare separation occurred at all subsonic Mach numbers. The magnitude of the cone carryover on the cylinder was observed to increase with decreasing cylinder length. Also observed was that at M = 0.7 and 0.8 the loads on the front cylinder are affected considerably by the length increase from 0.5 to 4.0 calibers. For the short cylinders, the carryover effect begins at approximately a X/L_2 of 0.3, while for the long front cylinders, the carryover loads from the cone and the flare are distinct. This trend is evident throughout the supersonic and transonic Mach range. At M = 1.0 for $L_2/D_2 = 2.0$, the load does not peak and drop off before the flare carryover affects it as it does on the $L_2/D_2 = 4.0$ cylinder. A shock standing on

the $L_2/D_2 = 2.0$ cylinder causes a negative load that occurs over 1/4 of the length. At supersonic Mach numbers, the shock shift again creates the negative spike loads, which increase with increasing cylinder length. At the supersonic Mach numbers, the loads for the highest frustum angle increase with angle of attack because of the separation of the flow before the cylinder-flare juncture.

4.2.2 Flare

The variation of loads on the flare created by changing geometrical parameters is shown in Figures 5, 6 and 7. The identical parameters that were varied for the front cylinder are therefore used to obtain their effects on the flare distributed loads. Because the length of the flare varies when the angle is changed for a constant D_2/D_4, the X parameter is nondimensionized by the length of the flare (L_3). The X/L_3 parameter then varies from 0 to 1.0 for all configurations. The effect of changing flare geometry on the distributed loads on the frustum for constant diameter ratios is presented in Figures 5a, b and c. One of the most significant effects noted was that for a body diameter ratio of 0.6, the loads increase in magnitude linearly with flare angle for all Mach numbers except 1.45 and 1.96. The shape of the constant X/L_3 lines indicate that the loads are nonlinear at the supersonic Mach numbers because the flow will not turn through the larger frustum angles; whereas they will turn through the smaller frustum angle. This phenomenon is substantiated by Reference 6. As the flow will not turn through the higher angles, it separates on the leeward side of the flare after the shock and creates a greater pressure differential than would normally occur if the flow did not separate; therefore, the higher loading exists on the 15^o and 20^o flare.

Separation also occurs on the flare with a diameter ratio of 0.4 which creates nonlinear load variation for constant X/L_3 lines between 0 and 0.3. Fairly linear variation of loads occurs on the aft end of the flare, as noted in Figure 5a. No separation occurs on the flare at any angle for a D_2/D_4

ratio of 0.8. This is indicated by the linear X/L_3 lines and the magnitude of the loads is smaller than the loads on either the flares with $D_2/D_4 = 0.4$ and 0.6.

The characteristics of the local normal forces on the flare with a diameter ratio of 0.8 are depicted in Figure 5c. When the distributions on the flare for the three-diameter ratios are compared, a definite difference in loading is observed.

Another parameter varied to determine its effects on the flare local normal forces is the length of the front cylinder. L_2/D_2 was varied from 0.5 to 4.0 calibers, and it was noted that the effect of the short front cylinder was considerable A short front cylinder increases the local normal force on the forward portion of the flare because of the influence of the cone carry-over flow field on the forward portion of the flare. At the supersonic Mach numbers, the length of the forward cylinder had no effect on the frustum loads (as shown by the load values for constant X/L_3 lines in Figure 7).

The final flare parameter effects investigated were the variation of nose cone angle, as well as how those loads on the flare reacted to the nose cone angle. At the subsonic Mach numbers, the loads were practically unchanged when the nose cone angles were varied from 15^o to 40^o and then only on the front of the flare, but the loads decreased rapidly at $X/L_3 = 0.5$ to 0.9.

Just the reverse is true at transonic Mach numbers with the loads changing considerably with nose cone angle. The load lines for constant X/L_3 are definitely nonlinear and have considerable variation from X/L_3 of 0 to 1.0. As the Mach number further increased, the effect of the nose cone angle diminished, and a constant variation again existed. All these effects are shown for all the Mach numbers in Figure 6.

4.2.3 Aft Cylinder

The final set of carpet plots which are presented are the local normal force slope distributions on the aft cylinder. In these plots, identical parameters are used that were varied for the front cylinder and the flare to obtain these affects on the distributed loads.

The effect of changing flare angle for a constant diameter ratio is presented in Figures 8, 9 and 10. They show the result of separation and other flow characteristics on the distributed loads. The most obvious feature of these plots is the discontinuity of constant X/D_4 curves caused by boundary layer separation at the flare-cylinder juncture. The characteristic shapes of the normal force distribution curves for the separated and attached flows are different. This discontinuity occurs somewhere between 15^o and 20^o for M = 0.7 and 0.8 and the exact location was determined by Reference 3.

Using the curve from Reference 3, separation is assumed to occur at a 16^o flare angle at M = 0.7 and 20^o at M = 0.8. The effect of diameter ratio cannot be determined from the data available, but it would seem that the separation angle where separation occurs would be different. At M = 0.9, 0.95 and 1.0, separation will not occur because the angle where separation occurs is larger than the maximum flare angle tested. Figure 8a and b show the approximate location where separation occurs for diameter ratios of 0.4 and 0.6.

An additional effect noted is that the carryover load increases with increasing flare angle for all the Mach numbers used.

The characteristics of the loads of the aft cylinder for a diameter ratio of 0.8 and the same flare angles are changed significantly from the characteristics established for the other diameter ratios. It seems that no significant separation occurs after the flare cylinder juncture for M = 0.7 and 0.8 nor at the higher Mach numbers.

One of the least significant effects on the aft cylinder loads is created by variation of the nose cone angle. The carpet plots for both subsonic and supersonic Mach conditions indicate very little change when this parameter is varied even with a forward cylinder length of two calibers. Note that the negative loads just aft of the flare at transonic Mach numbers do increase. These effects are apparent in Figure 9.

The variation of front cylinder length has a small effect on the aft cylinder loads similar to the effect of nose cone angle. Figure 10 does indicate a slight effect at the transonic Mach numbers. The most significant effect noted for all of the aft cylinder loads is the influence of the base on the loads near the base. This is discussed further in the comparison of the force and pressure data in the next section.

Mach number has a definite effect on the pressures on the aft end of the second cylinder. As is noted in the aft cylinder local normal force distributions, the loads tended to increase at the 3.0 caliber location at subsonic and transonic Mach numbers and to drop to zero for the supersonic Mach numbers. This difference in base effect occurs because the pressure cannot be transmitted forward of the base in supersonic flow. The base effect had a significant impact on the correlation of force and pressure data results. The percentage increase in load required to allow the integrated loads distributions to agree with force test data varied with Mach number, and each distribution had to be modified independently of each other to account for the difference in aft cylinder length for the force and pressure models. The distributions, as presented in the carpet plots, were not modified, because the base effect is included in the aft cylinder section. This effect is indicated by the rapid increase in load from 3.0 to 3.5 calibers.

4.2.4 Comparison of Force and Pressure Data Results

All the distributions that were plotted were checked to determine if, when integrated, the total loads would agree with what was obtained from the

force test. Figures 11a, b and c show the comparison of the total normal force and pitching moment obtained from the force and pressure tests. There were problems which existed when the pressure and force loads were being compared. In the majority of cases where pressure data did not agree with the force data, the pressure data had loads which were lower and moments which were higher. Base effects were found to be causing this disagreement between the force and pressure data. The 2-caliber aft cylinder on the force test model was compared with the 2-caliber position on the 3.5-caliber pressure model, and the increase in load due to the base was essentially eliminated in the region comparable to the force model length. The base effects did exist on the force model. When this base effect was shifted on the pressure data to the 2-caliber position, the loading agreed with the force test data. The comparisons presented in Figure 11 include the base pressure corrections.

Section 5
CONCLUSION

A comprehensive set of aerodynamic loads design curves for forward-cylinders, flares and aft-cylinder were constructed from integrated pressure data and were documented. These curves will enable the designer to ascertain the aerodynamic load distributions of cone-cylinder-flare-cylinder configurations for a broad range of geometric parameters in a Mach number range where adequate methods were previously unavailable.

These curves, when supplemented by the design curves for cones and cylinders in Reference 3, provide a complete set of design curves for evaluating the distributed loads for any combination of a wide range of vehicle geometric parameters.

Section 6

REFERENCES

1. Leff, Alan D., "Pretest Report for the Trisonic Cone-Cylinder-Frustum-Cylinder Test Series," TM 54/20-31, Lockheed Missiles & Space Company, Huntsville Research & Engineering Center, Huntsville, Alabama, April 1965.

2. Benefield, J. W., R. L. Hamner, R. J. Hauser and A. D. Leff, "A Correlation of Transonic and Supersonic Aerodynamic Characteristics for Cones, Cylinders and Flares," TM 54/01-42, Lockheed Missiles & Space Company, Huntsville Research & Engineering Center, Huntsville, Alabama, 30 January 1964, Confidential.

3. Hamner, R. L., and A. D. Leff, "Linear Aerodynamic Loads on Cone-Cylinders at Mach Numbers from 0.7 to 2.0," LMSC/HREC A710463, Lockheed Missiles & Space Company, Huntsville Research & Engineering Center, Huntsville, Alabama, 10 March 1965.

4. Leff, Alan D., "Shadowgraph Study of Cone-Cylinder and Cone-Cylinder-Frustum-Cylinder Configurations," TM 54/20-66, Lockheed Missiles & Space Company, Huntsville Research & Engineering Center, Huntsville, Alabama, 15 December 1965.

5. Benefield John W., "A Revised Program for the Integration of Pressure Distribution Data for Bodies of Revolution," TM 54/40-133, Lockheed Missiles & Space Company, Sunnyvale, California, February 1963.

6. Ames Research Staff, Equations,"Tables and Charts for Compressible Flow," Report 1135, National Advisary Committee for Aeronautics, Moffett Field, California, 1953.

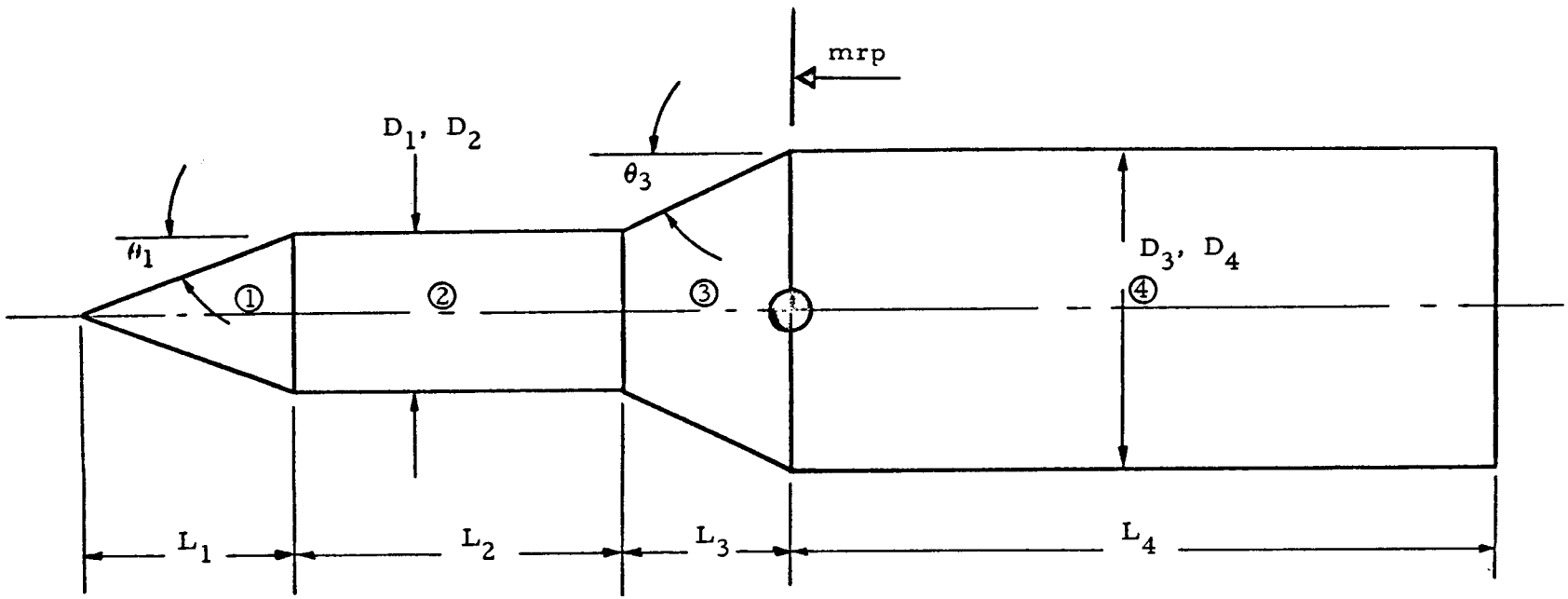

θ_1	L_2/D_2	D_2/D_3	θ_3	L_4/D_4
15°	0.5	0.4	7.5°	3.5
25°	1.0	0.6	10°	
33°	2.0	0.8	15°	
40°	4.0		20°	

Figure 1 - Configuration Sketch

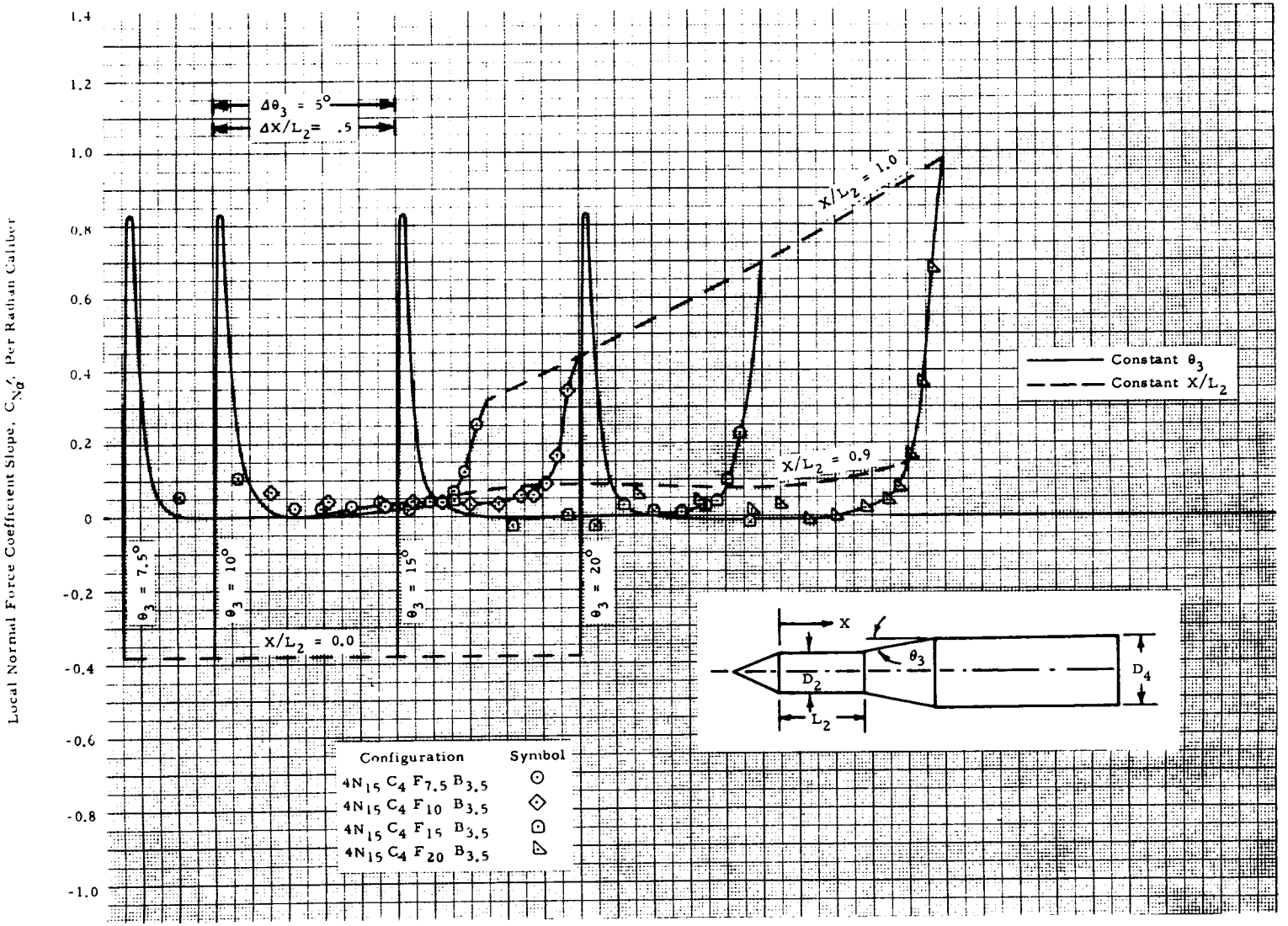

(1) M = 0.70

Figure 2a - The Effect of Frustum Angle on Forward Cylinder Local Normal Force Slope Distributions for Cone-Cylinder-Flare-Cylinders, $D_2/D_4 = 0.4$

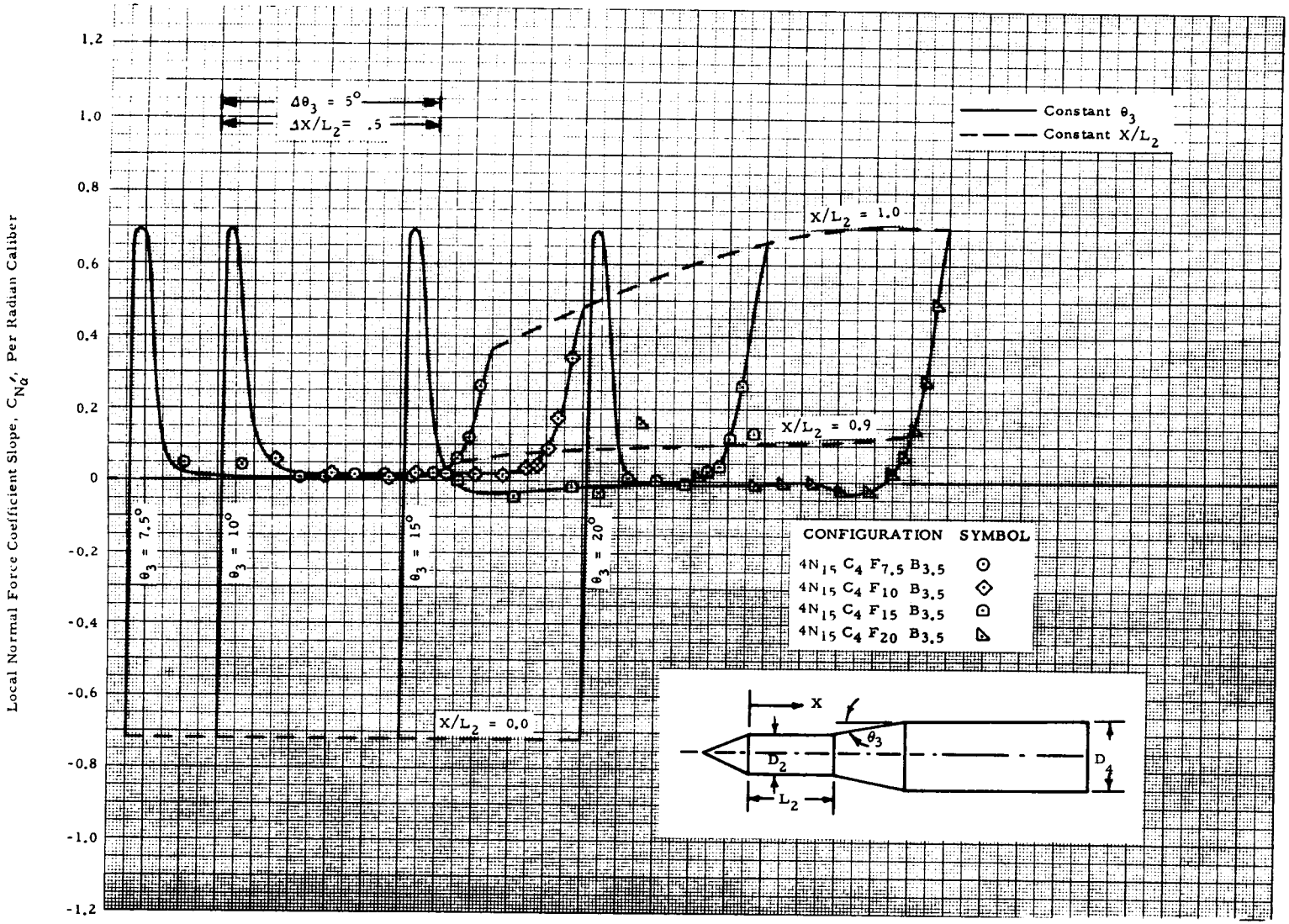

(2) M = 0.80

Figure 2a - The Effect of Frustum Angle on Forward Cylinder Local Normal Force Slope Distributions for Cone-Cylinder-Flare-Cylinders, $D_2/D_4 = 0.4$ (Cont'd)

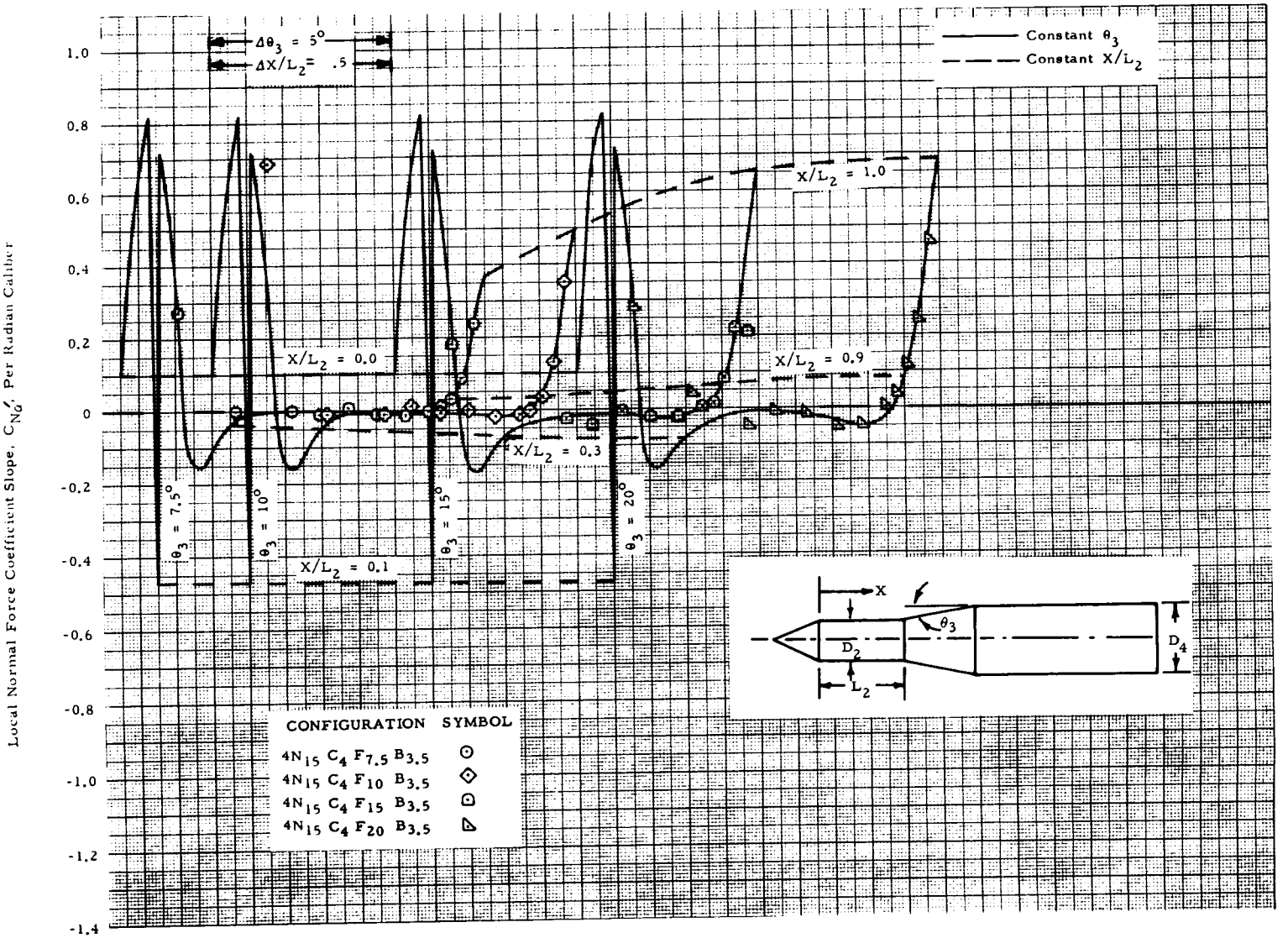

(3) M = 0.90

Figure 2a - The Effect of Frustum Angle on Forward Cylinder Local Normal Force Slope Distributions for Cone-Cylinder-Flare-Cylinders, $D_2/D_4 = 0.4$ (Cont'd)

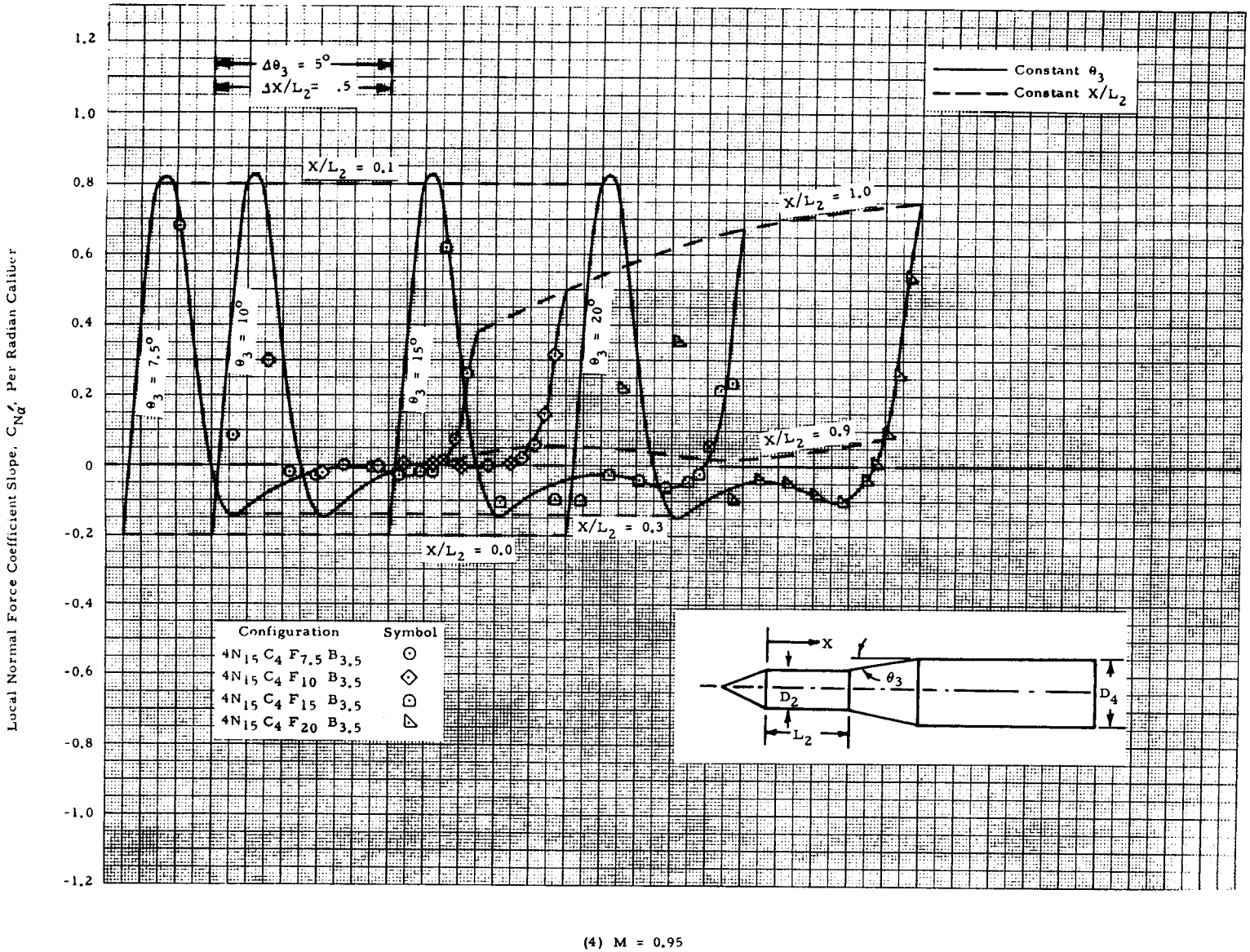

(4) M = 0.95

Figure 28 - The Effect of Frustum Angle on Forward Cylinder Local Normal Force Slope Distributions for Cone-Cylinder-Flare-Cylinders, $D_2/D_4 = 0.4$ (Concluded)

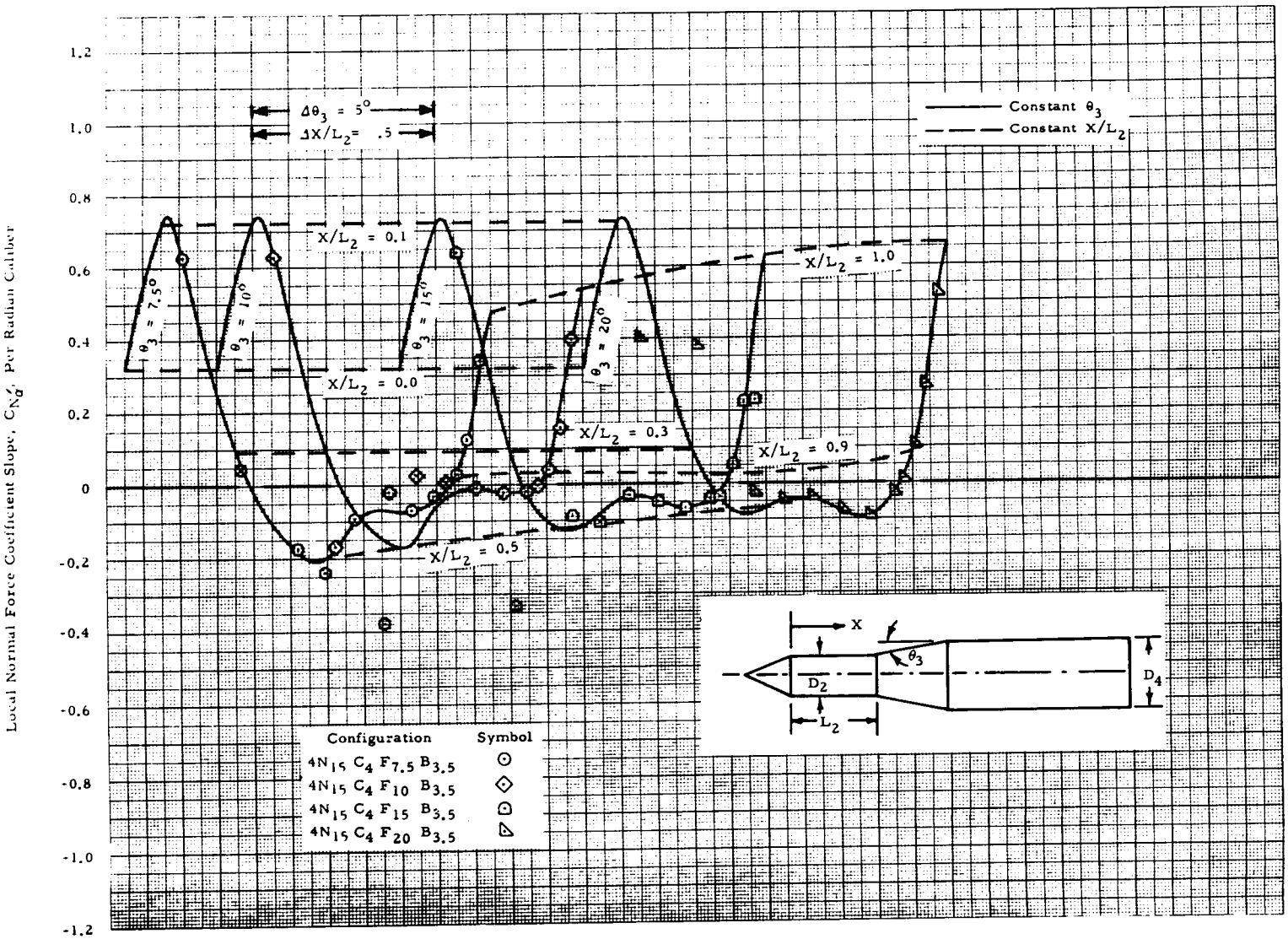

(5) M = 1.00

Figure 2a - The Effect of Frustum Angle on Forward Cylinder Local Normal Force Slope Distributions for Cone-Cylinder-Flare-Cylinders, $D_2/D_4 = 0.4$ (Cont'd)

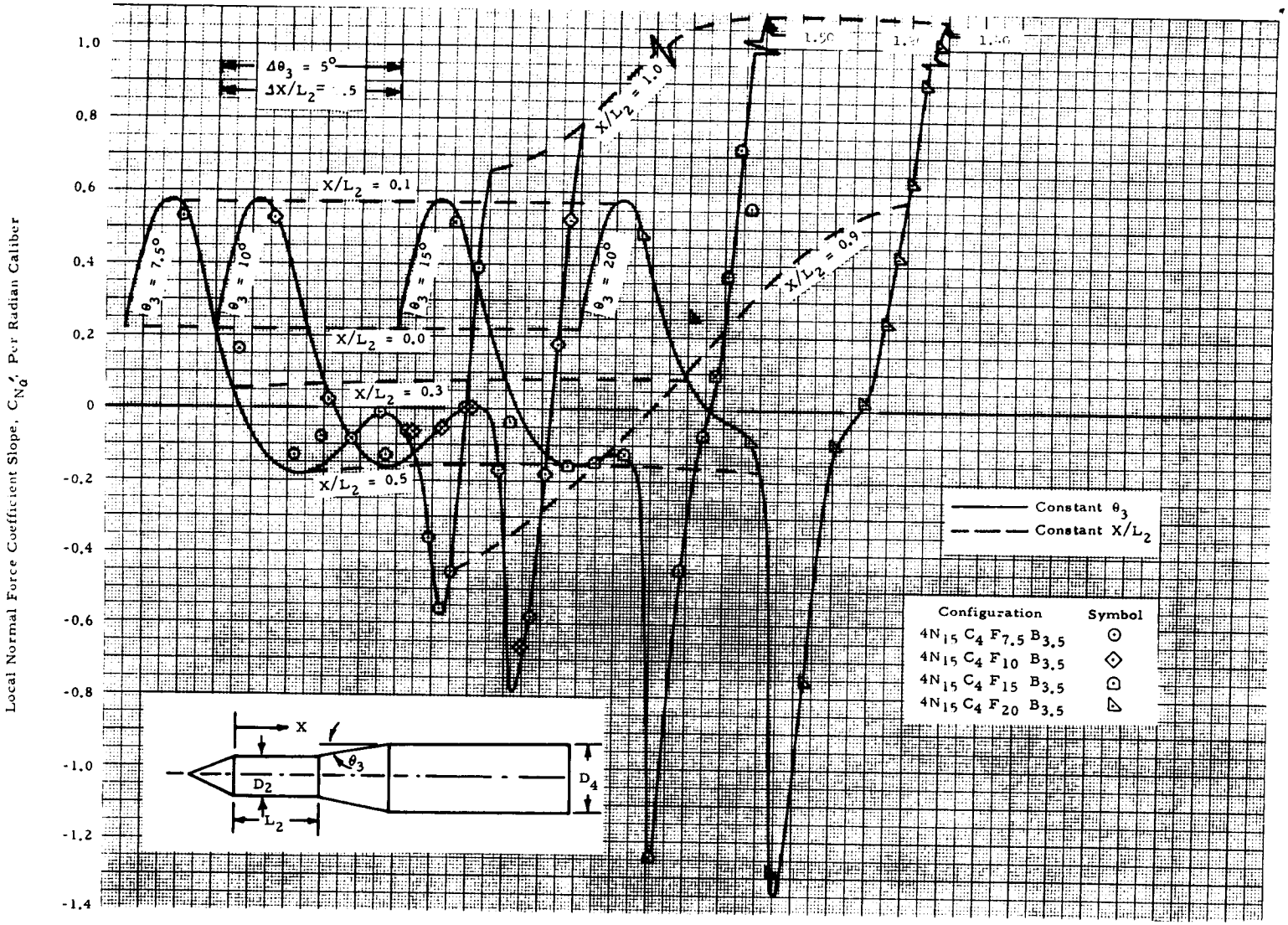

(6) M = 1.1

Figure 2a - The Effect of Frustum Angle on Forward Cylinder Local Normal Force Slope Distributions for Cone-Cylinder-Flare-Cylinders, $D_2/D_4 = 0.4$ (Cont'd)

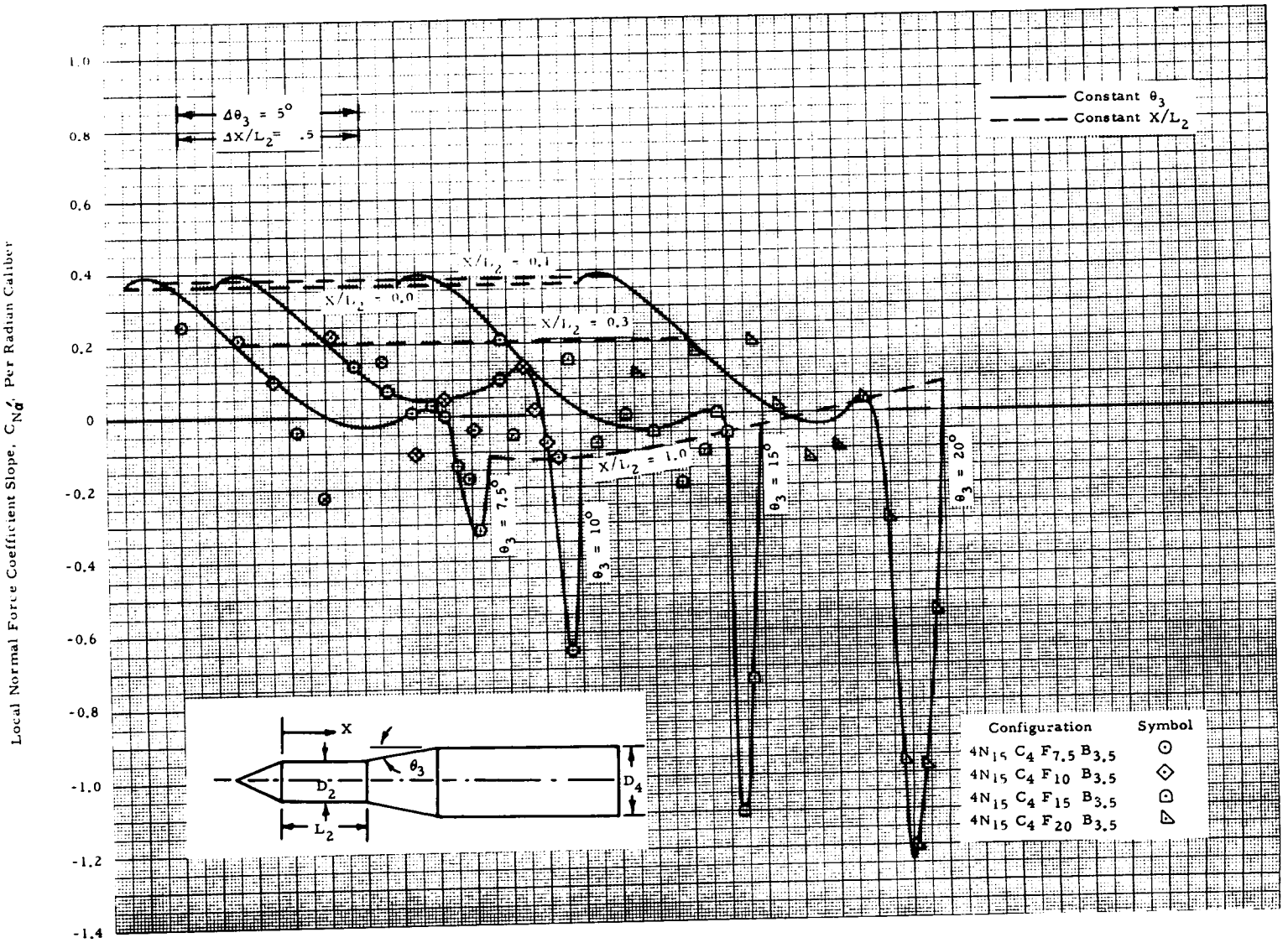

(7) M = 1.46

Figure 2a - The Effect of Frustum Angle on Forward Cylinder Local Normal Force Slope Distributions for Cone-Cylinder-Flare-Cylinders. D_2/D_4 = 0.4 (Cont'd)

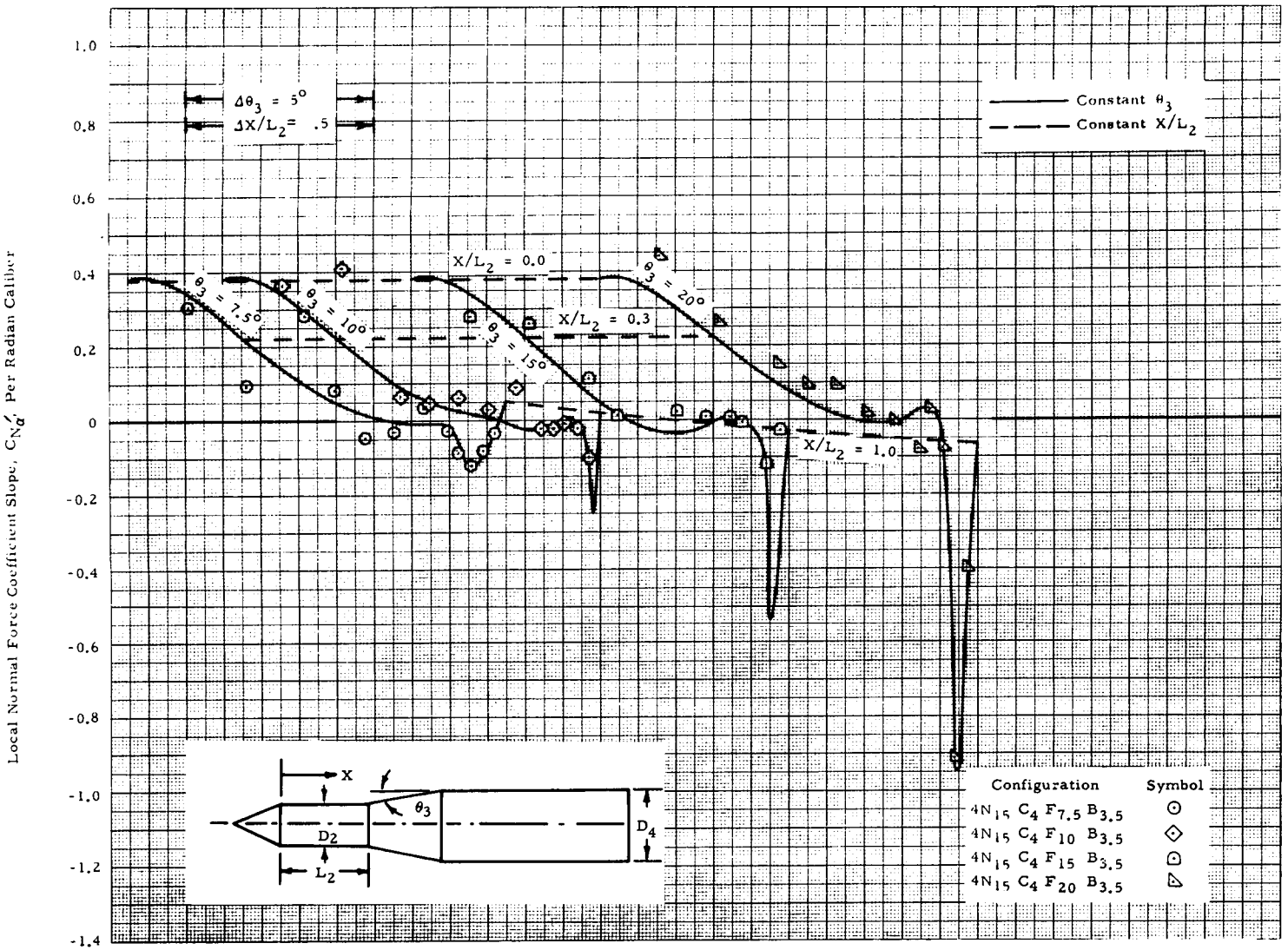

(8) M = 1.96

Figure 2a - The Effect of Frustum Angle on Forward Cylinder Local Normal Force Slope Distributions for Cone-Cylinder-Flare-Cylinders, $D_2/D_4 = 0.4$ (Concluded)

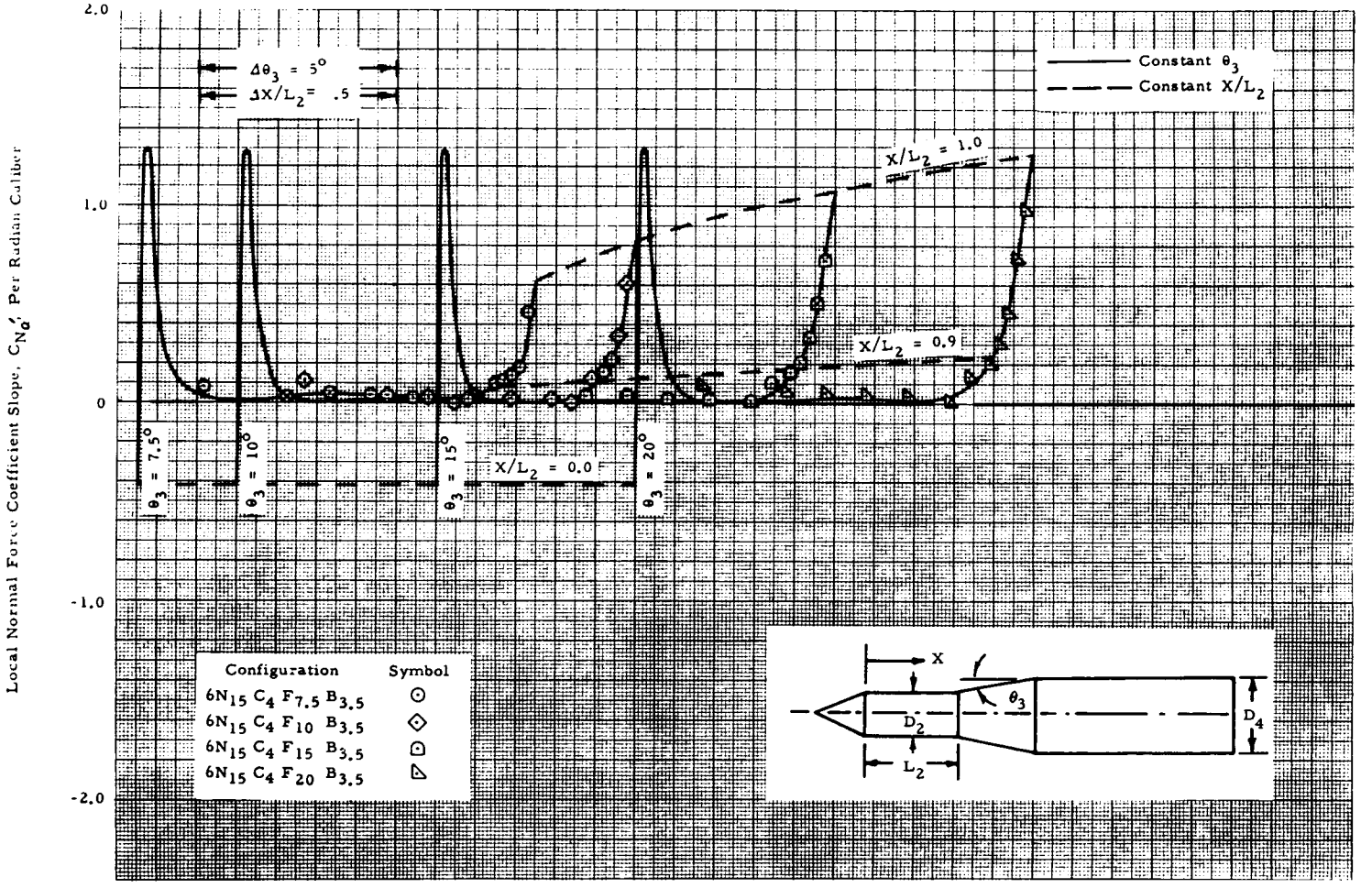

(1) M = 0.7

Figure 2b - The Effect of Frustum Angle on Forward Cylinder Local Normal Force Slope Distributions for Cone-Cylinder-Flare-Cylinders, $D_2/D_4 = 0.6$

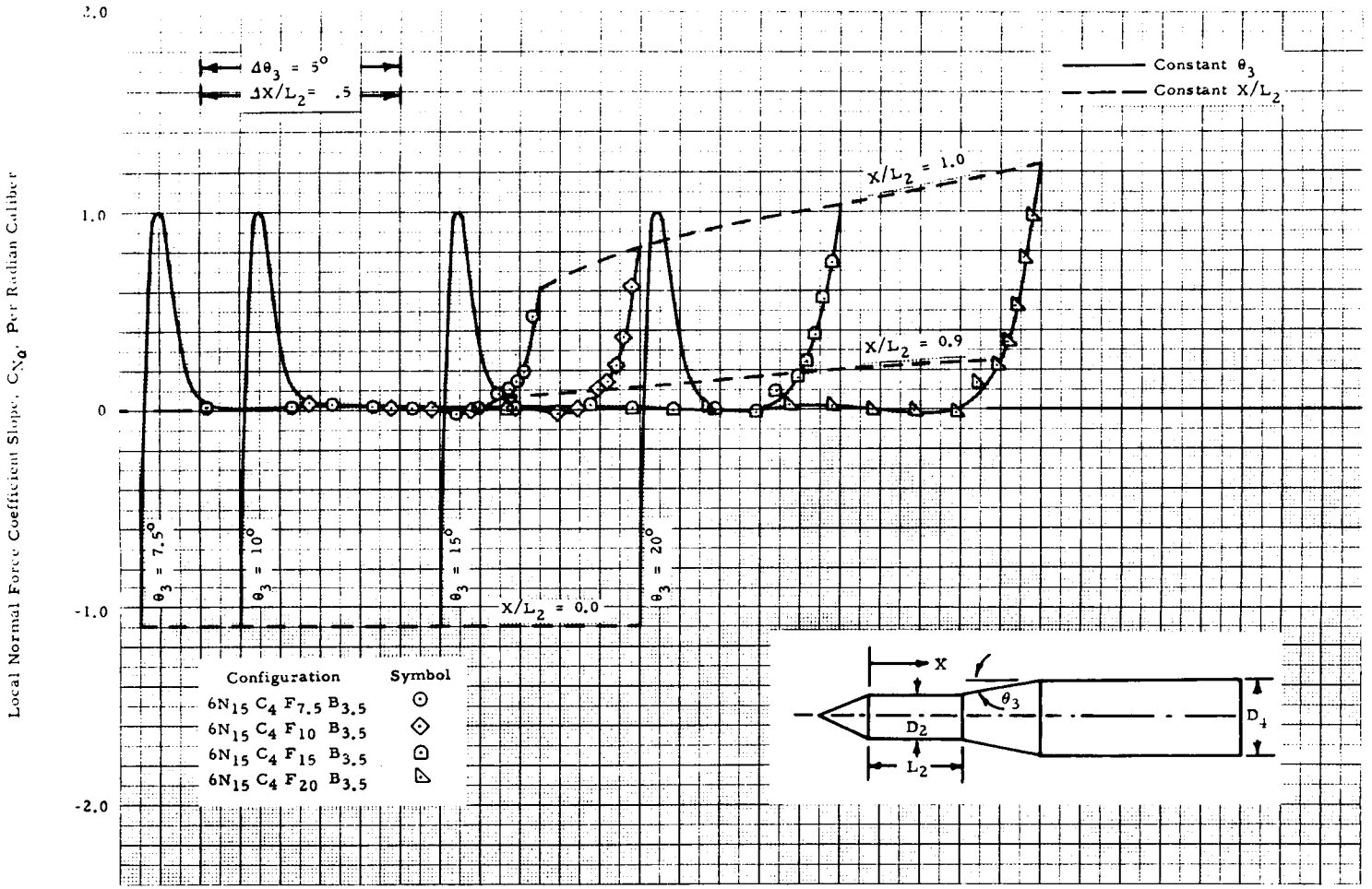

(2) M = 0.80

Figure 2b - The Effect of Frustum Angle on Forward Cylinder Local Normal Force Slope Distributions for Cone-Cylinder-Flare-Cylinders, $D_2/D_4 = 0.6$ (Cont'd)

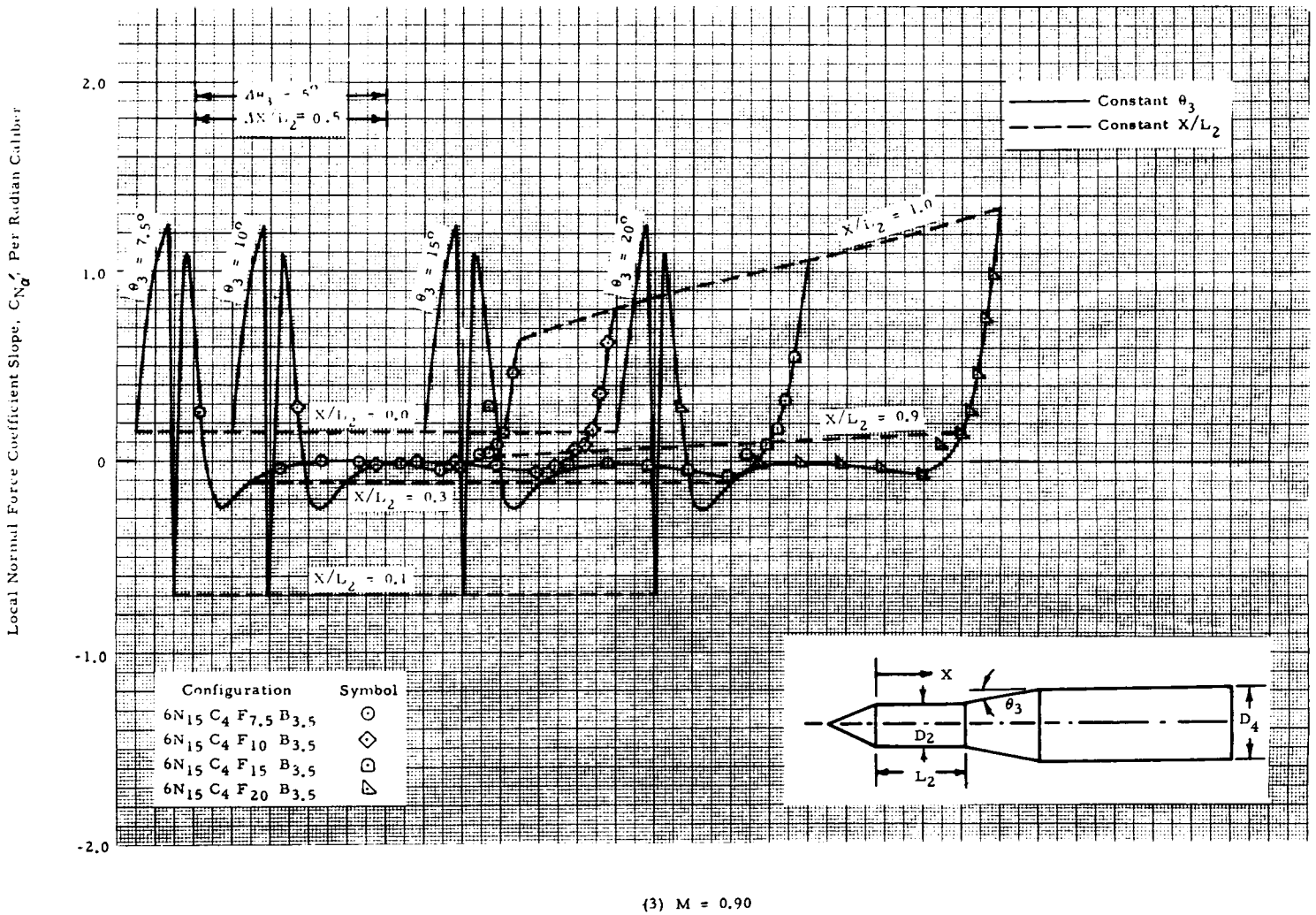

(3) M = 0.90

Figure 2b - The Effect of Frustum Angle on Forward Cylinder Local Normal Force Slope Distributions for Cone-Cylinder-Flare-Cylinders, D_2/D_4 = 0.6 (Cont'd)

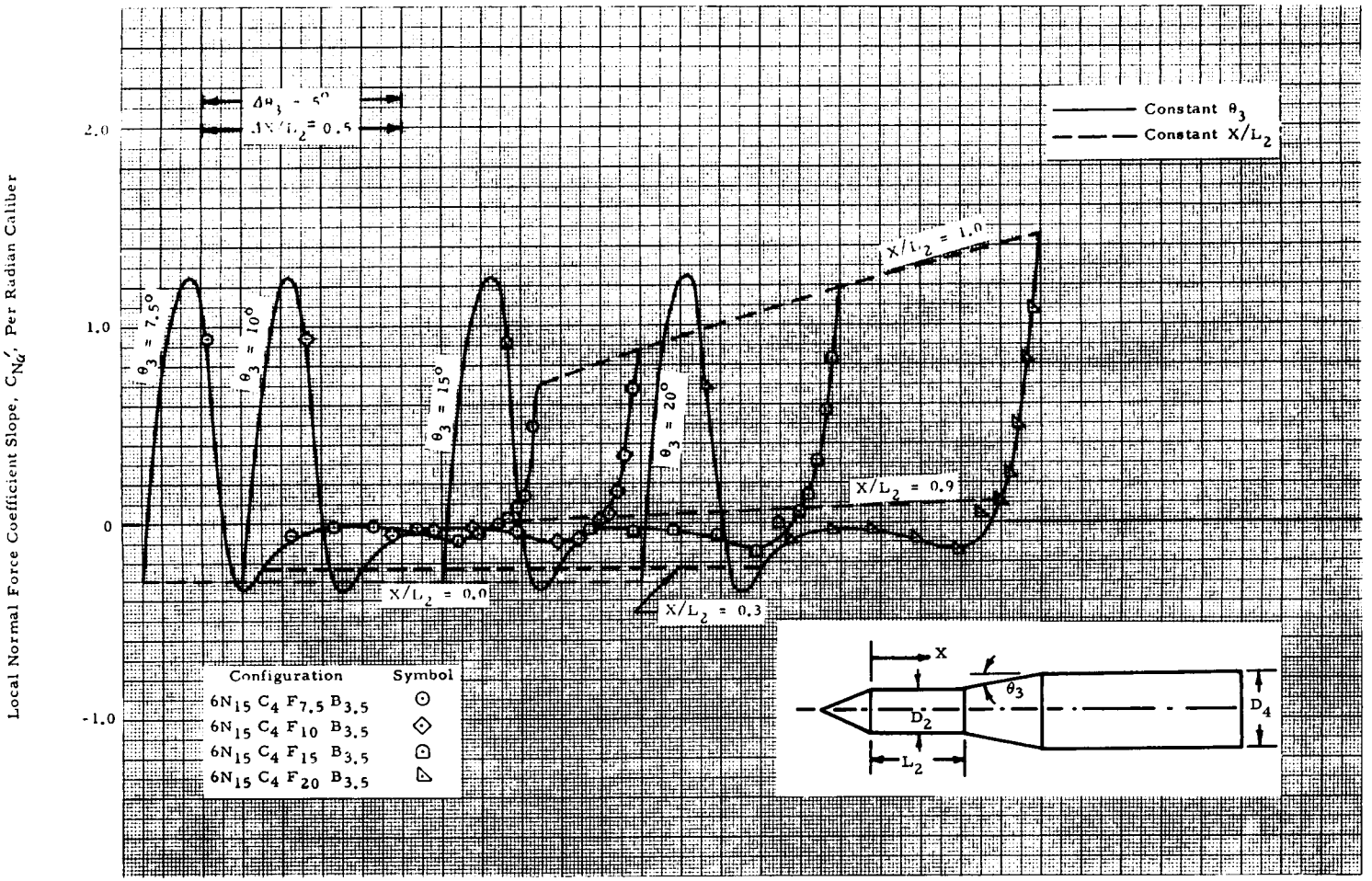

(4) M = 0.95

Figure 2b - The Effect of Frustum Angle on Forward Cylinder Local Normal Force Slope Distributions for Cone-Cylinder-Flare-Cylinders, D_2/D_4 = 0.6 (Cont'd)

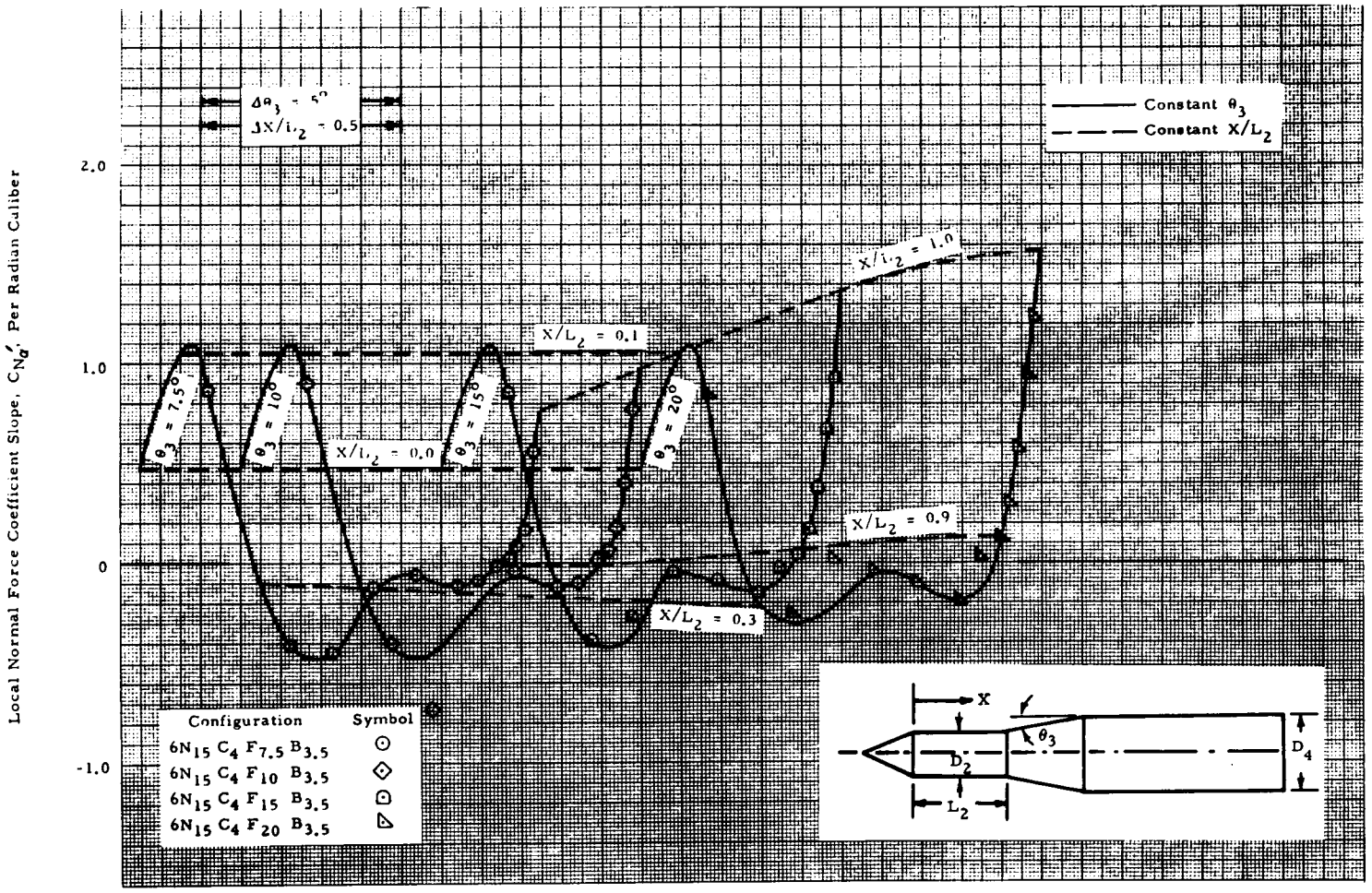

(5) M = 1.00

Figure 2b - The Effect of Frustum Angle on Forward Cylinder Local Normal Force Slope Distributions for Cone-Cylinder-Flare-Cylinders, D_2/D_4 = 0.6 (Cont'd)

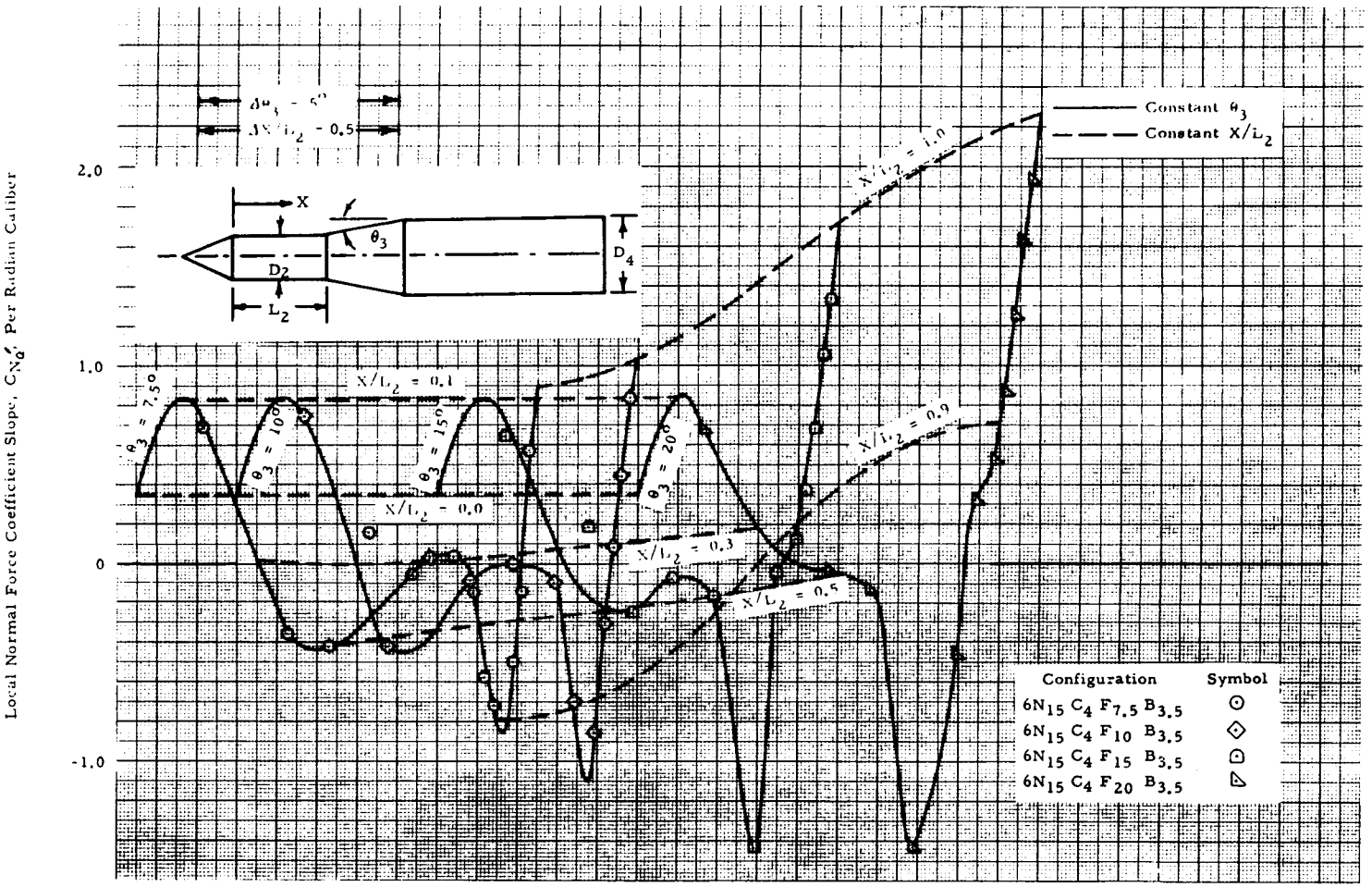

(6) M = 1.10

Figure 2b - The Effect of Frustum Angle on Forward Cylinder Local Normal Force Slope Distributions for Cone-Cylinder-Flare-Cylinders, $D_2/D_4 = 0.6$ (Cont'd)

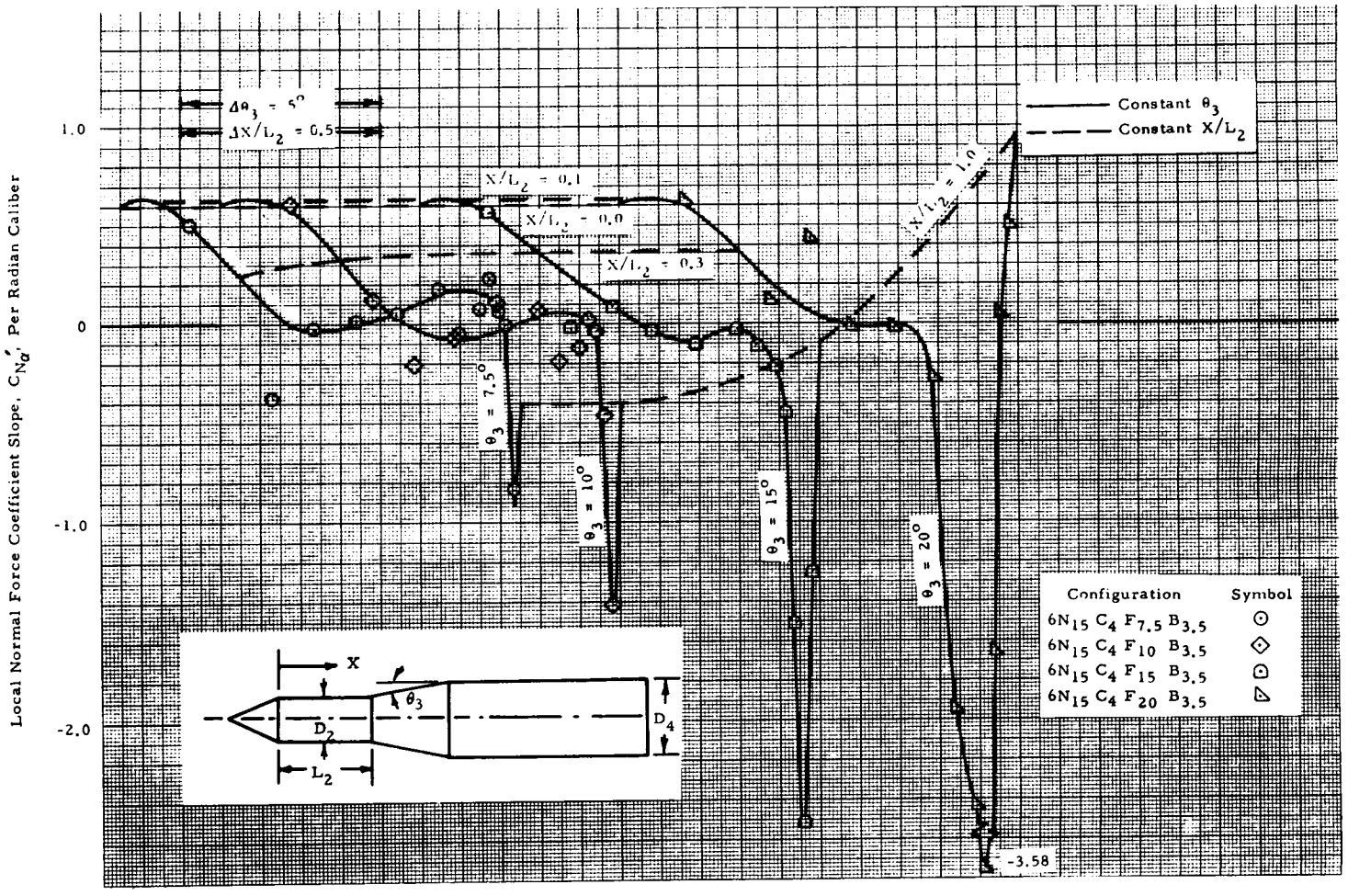

(7) M = 1.46

Figure 2b - The Effect of Frustum Angle on Forward Cylinder Local Normal Force Slope Distributions for Cone-Cylinder-Flare-Cylinders, D_2/D_4 = 0.6 (Cont'd)

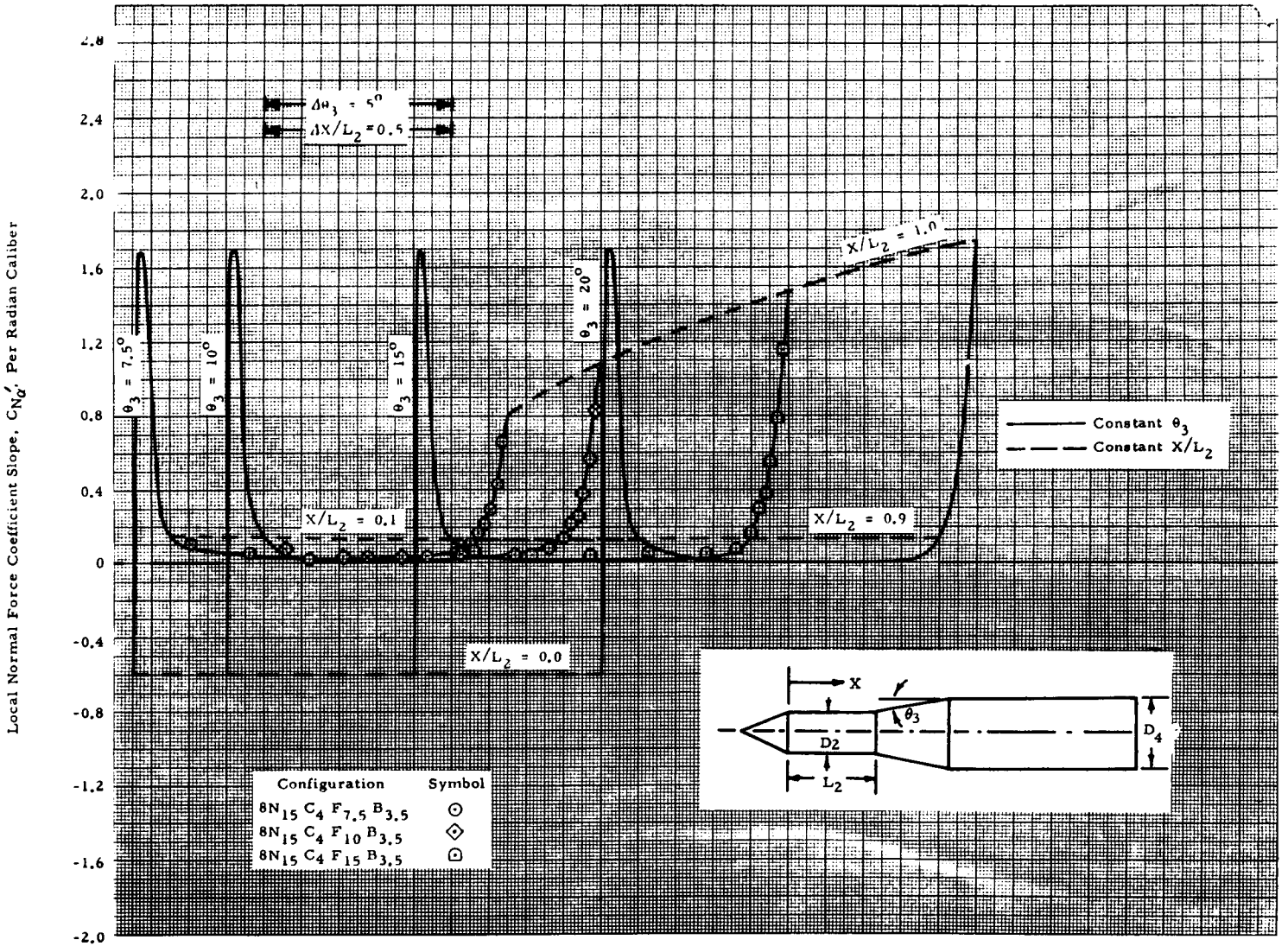

(1) M = 0.7

Figure 2c - The Effect of Frustum Angle on Forward Cylinder Local Normal Force Slope Distributions for Cone-Cylinder-Flare-Cylinders, $D_2/D_4 = 0.8$

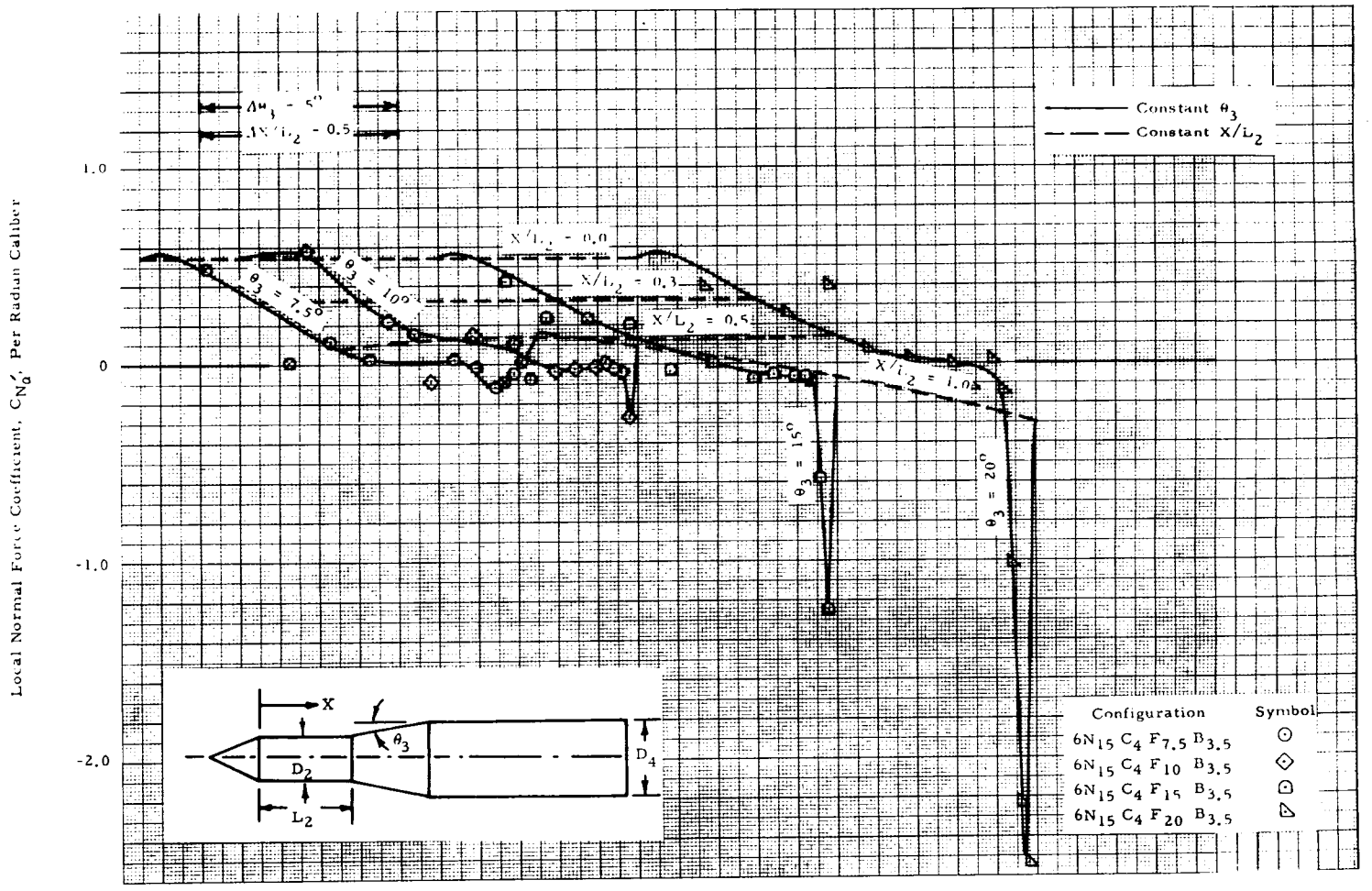

(8) M = 1.96

Figure 2b - The Effect of Frustum Angle on Forward Cylinder Local Normal Force Slope Distributions for Cone-Cylinder-Flare-Cylinders, D_2/D_4 0.6 (Concluded)

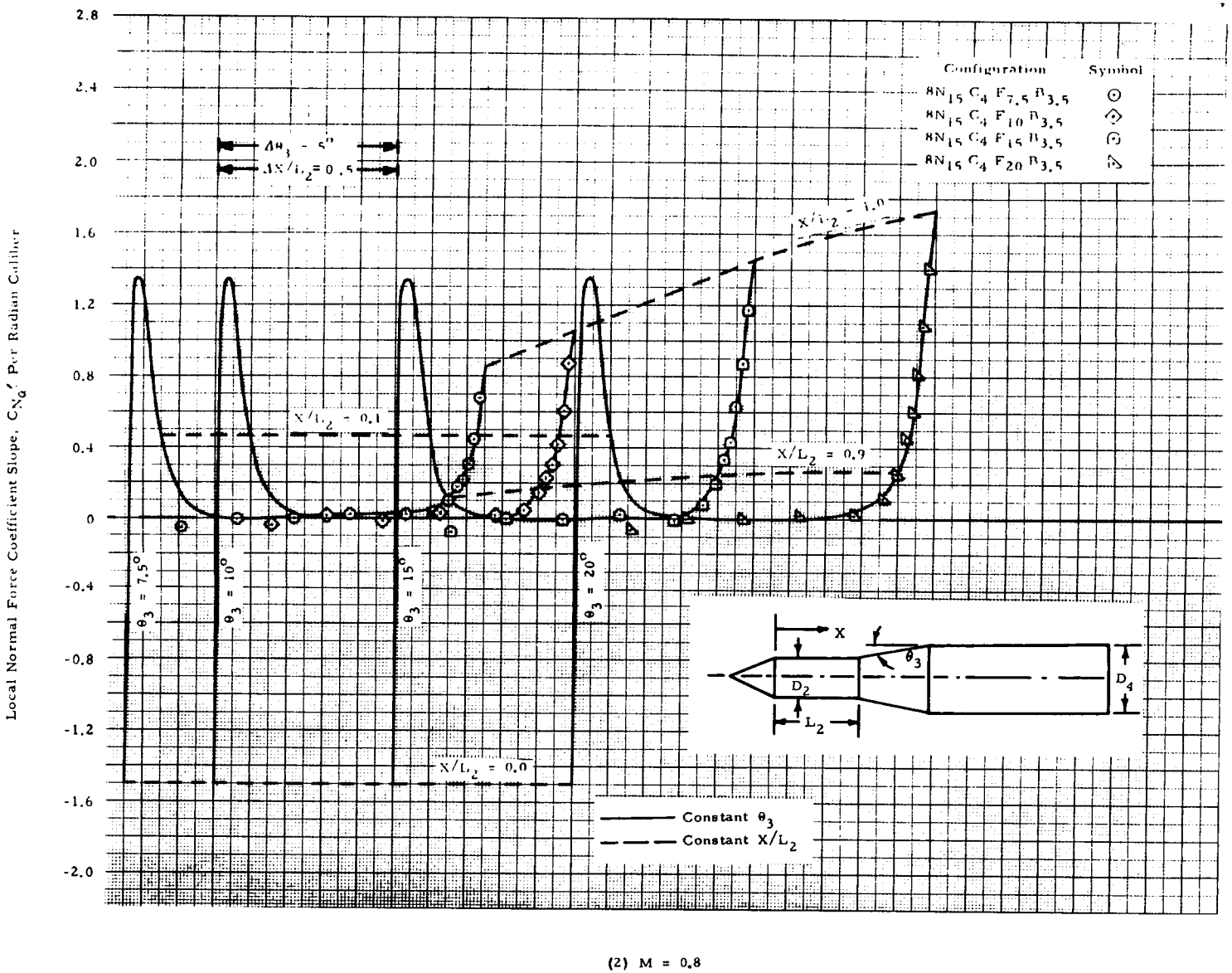

(2) M = 0.8

Figure 2c - The Effect of Frustum Angle on Forward Cylinder Local Normal Force Slope Distributions for Cone-Cylinder-Flare-Cylinders, D_2/D_4 = 0.8 (Cont'd)

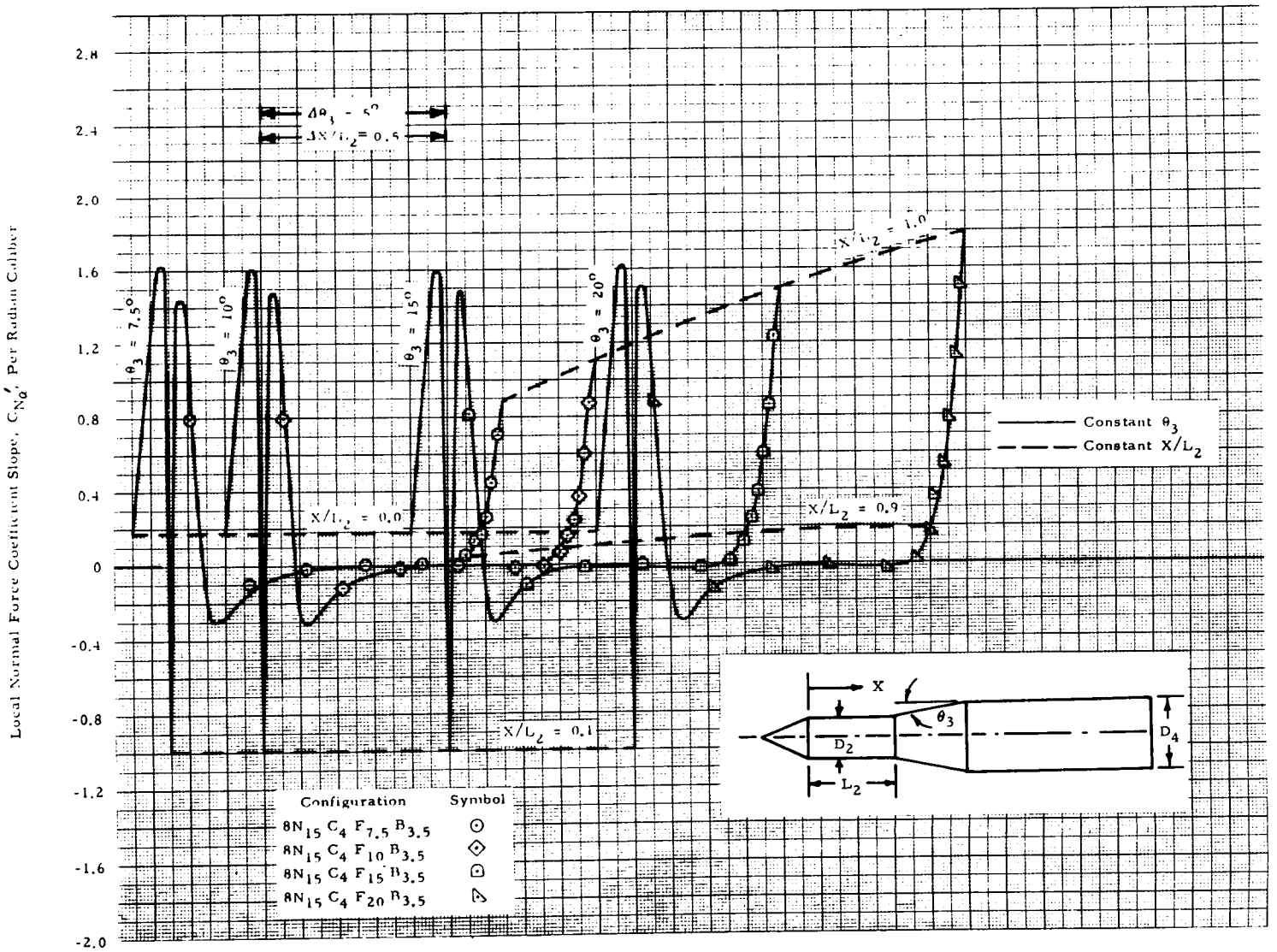

(3) M = 0.9

Figure 2c - The Effect of Frustum Angle on Forward Cylinder Local Normal Force Slope Distributions of Cone-Cylinder-Flare-Cylinders, D_2/D_4 = 0.8 (Cont'd)

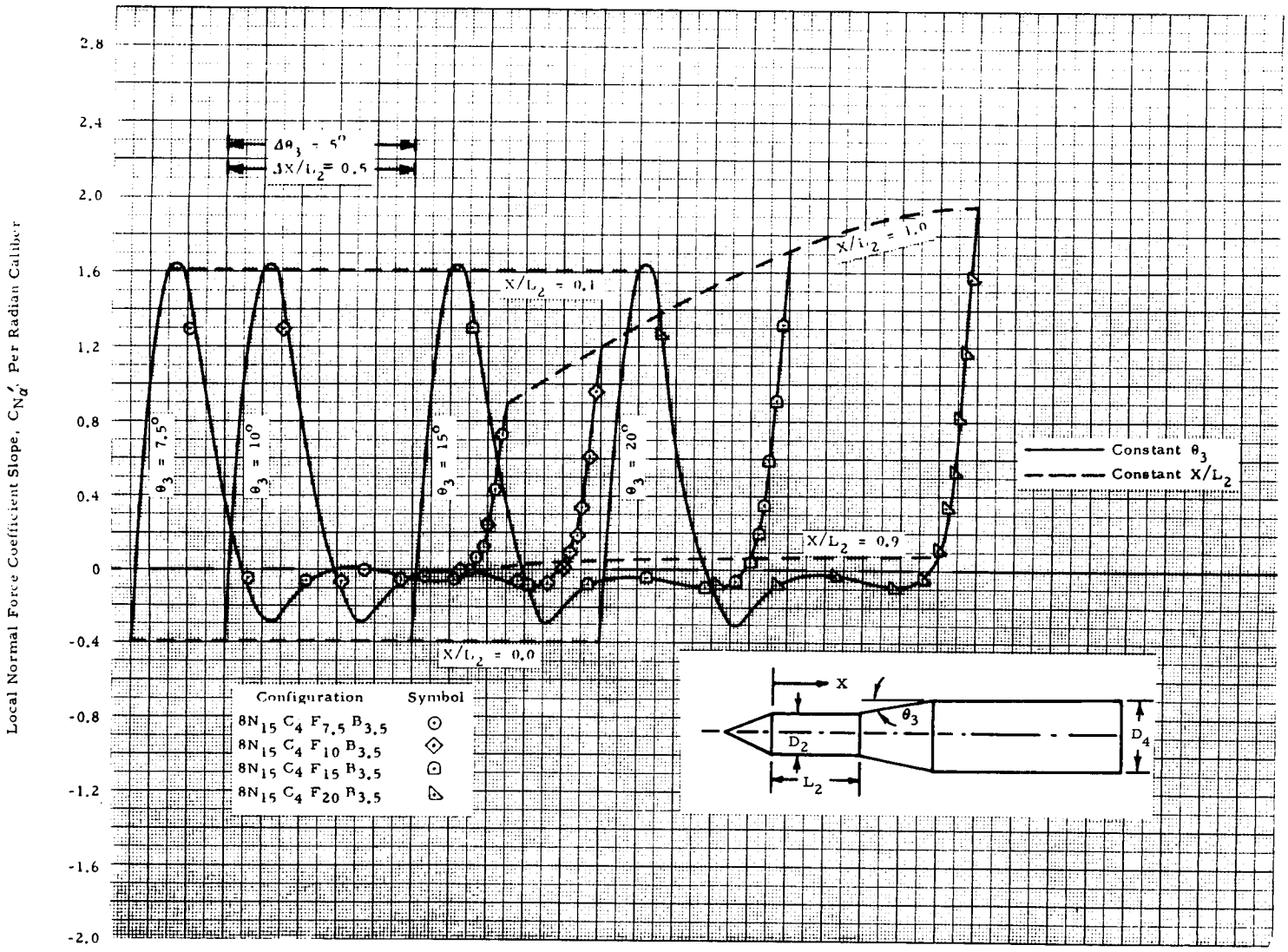

(4) M = 0.95

Figure 2c - The Effect of Frustum Angle on Forward Cylinder Local Normal Force Slope Distributions of Cone-Cylinder-Flare-Cylinders, D_2/D_4 = 0.8 (Cont'd)

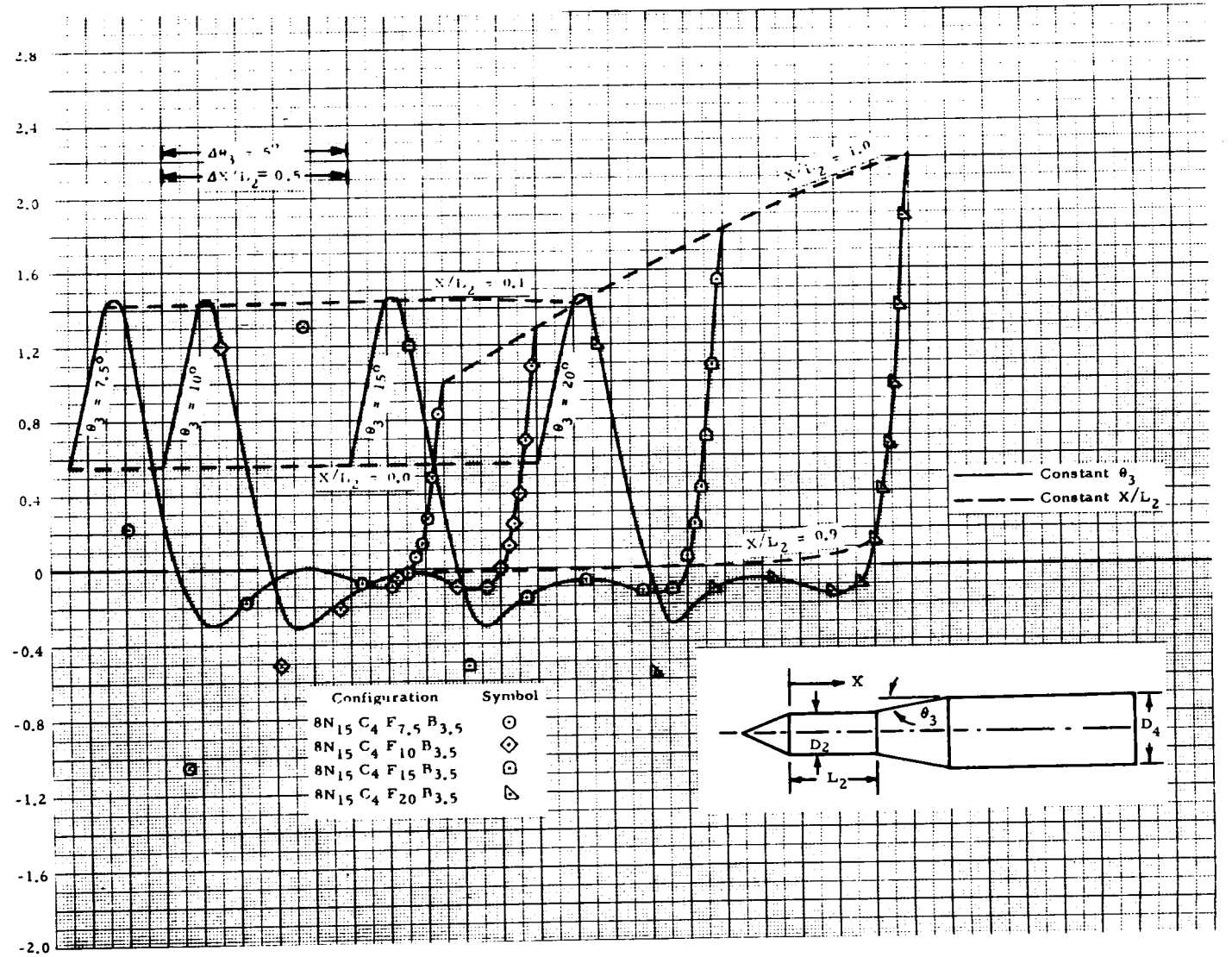

(5) M = 1.0

Figure 2c - The Effect of Frustum Angle on Forward Cylinder Local Normal Force Slope Distributions for Cone-Cylinder-Flare-Cylinders, D_2/D_4 = 0.8 (Cont'd)

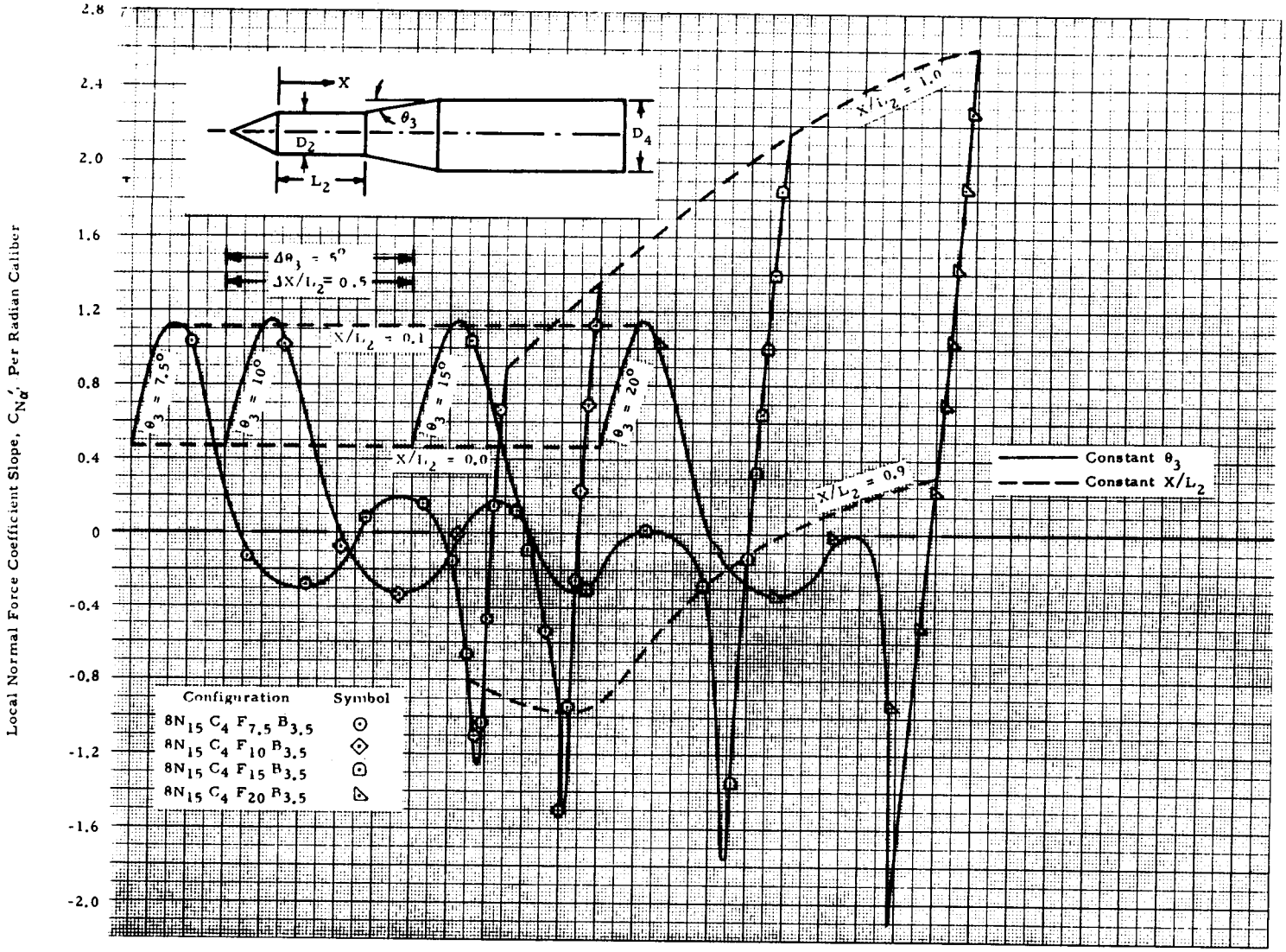

(6) M = 1.1

Figure 2c - The Effect of Frustum Angle on Forward Cylinder Local Normal Force Slope Distributions for Cone-Cylinder-Flare-Cylinders, $D_2/D_4 = 0.8$ (Cont'd)

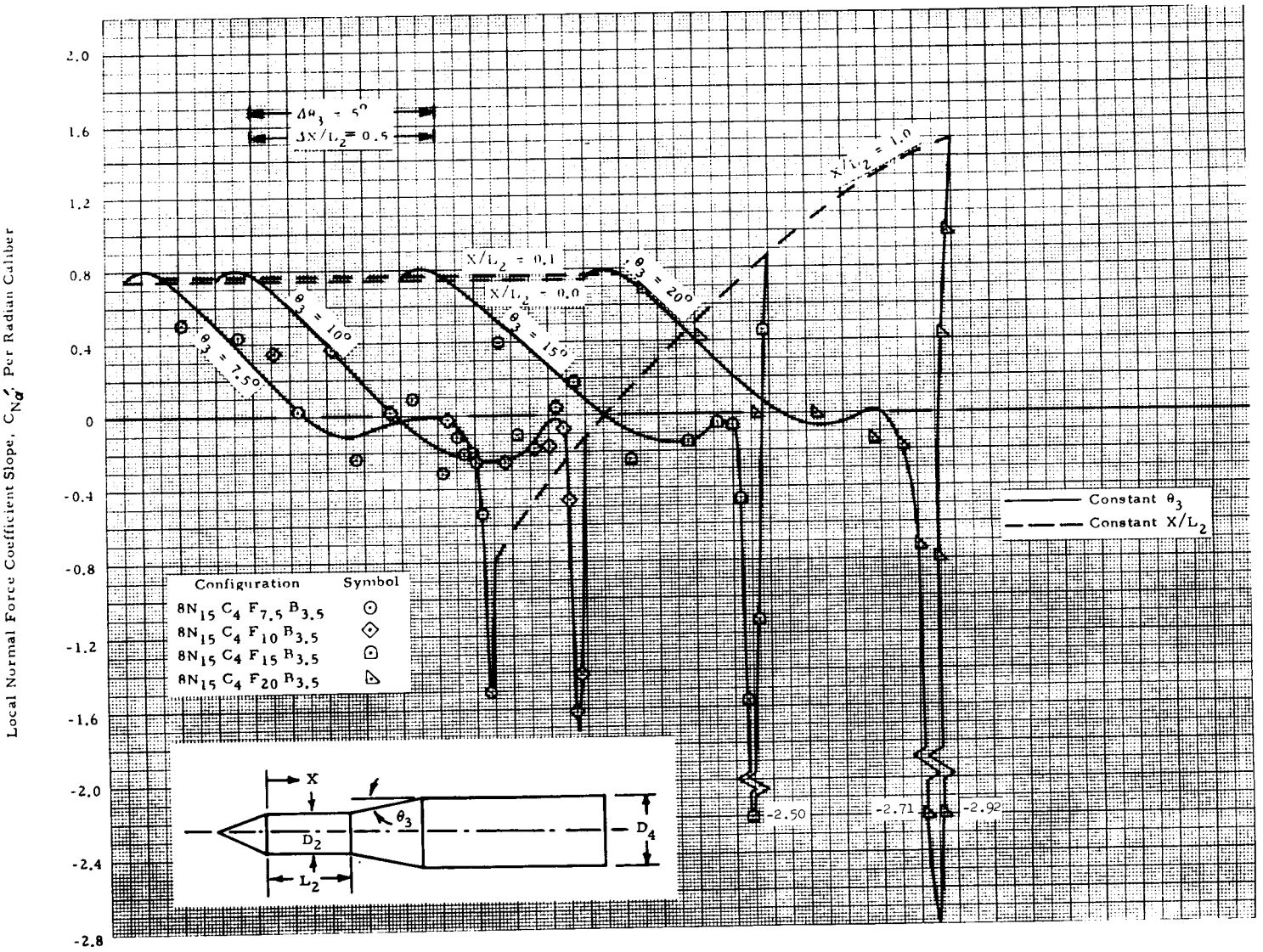

(7) M = 1.46

Figure 2c - The Effect of Frustum Angle on Forward Cylinder Local Normal Force Slope Distributions for Cone-Cylinder-Flare-Cylinders, $D_2/D_4 = 0.8$ (Cont'd)

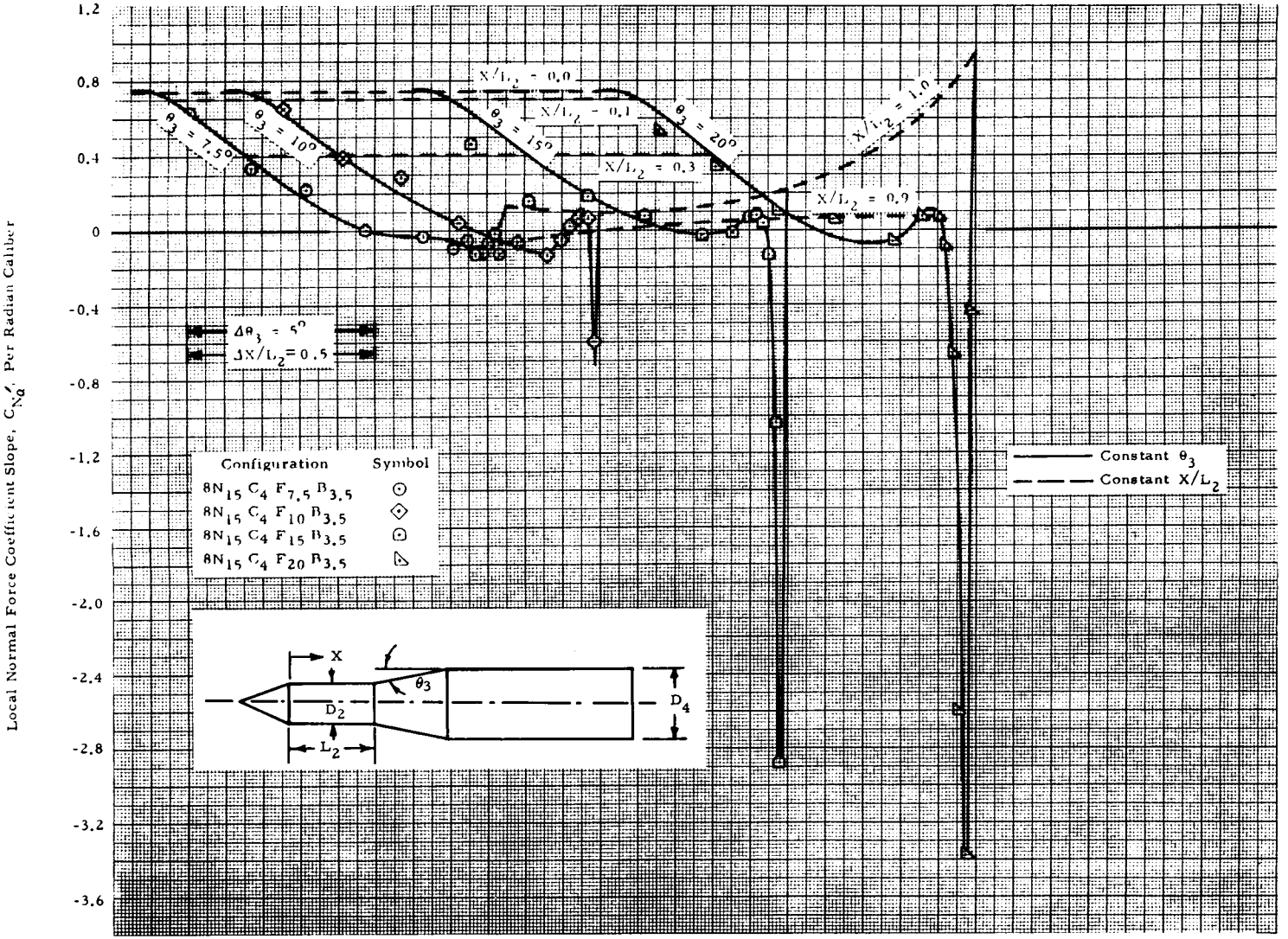

(8) M = 1.96

Figure 2c - The Effect of Frustum Angle on Forward Cylinder Local Normal Force Slope Distributions for Cone-Cylinder-Flare-Cylinders, $D_2/D_4 = 0.8$ (Concluded)

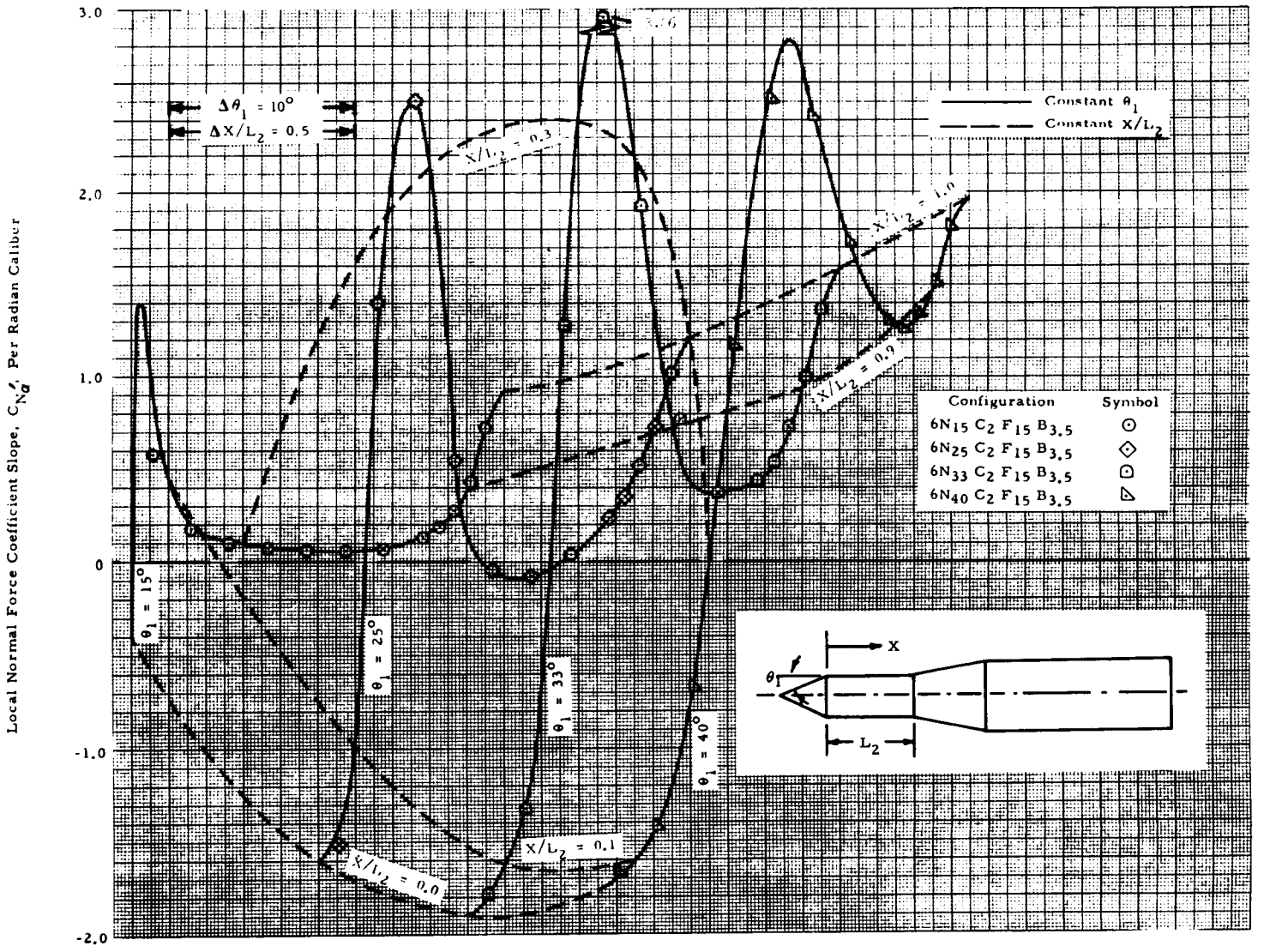

(a) M = 0.70

Figure 3 - The Effect of Cone Angle on Forward Cylinder Local Normal Force Slope Distributions for Cone-Cylinder-Flare-Cylinders

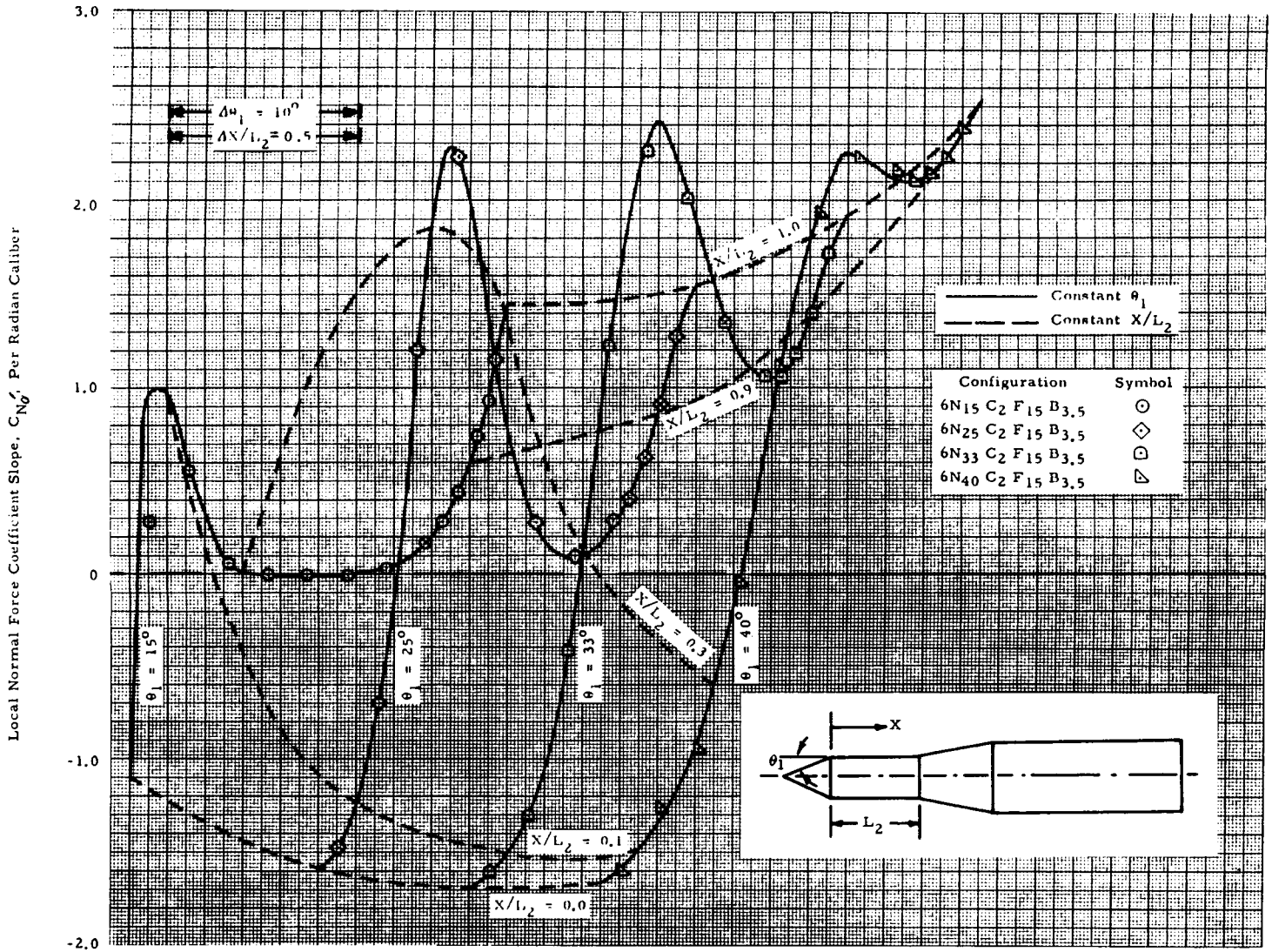

(b) M = 0.80

Figure 3 - The Effect of Cone Angle on Forward Cylinder Local Normal Force Slope Distributions for Cone-Cylinder-Flare-Cylinders (Cont'd)

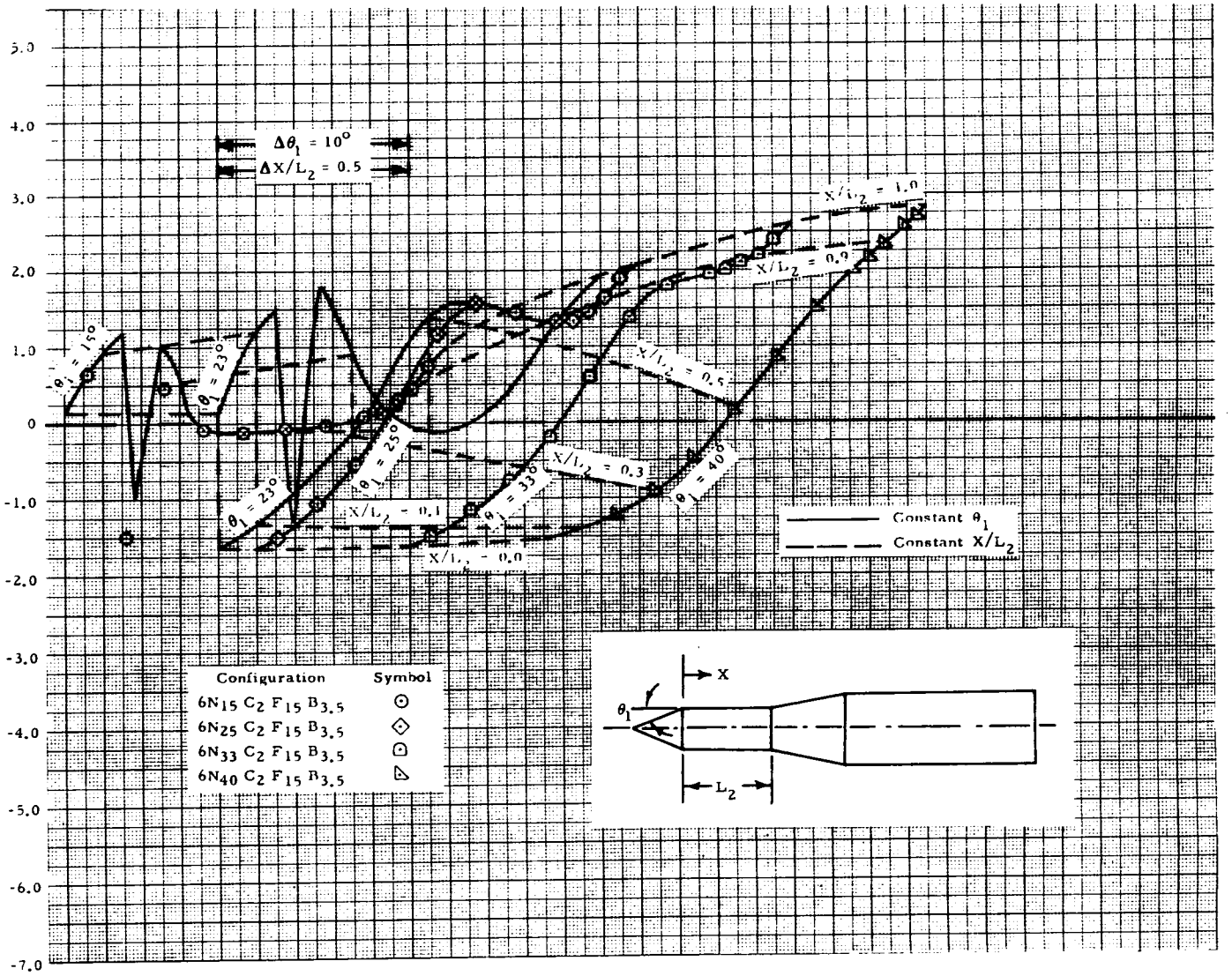

(c) M = 0.90

Figure 3 - The Effect of Cone Angle on Forward Cylinder Local Normal Force Slope Distributions for Cone-Cylinder-Flare-Cylinders (Cont'd)

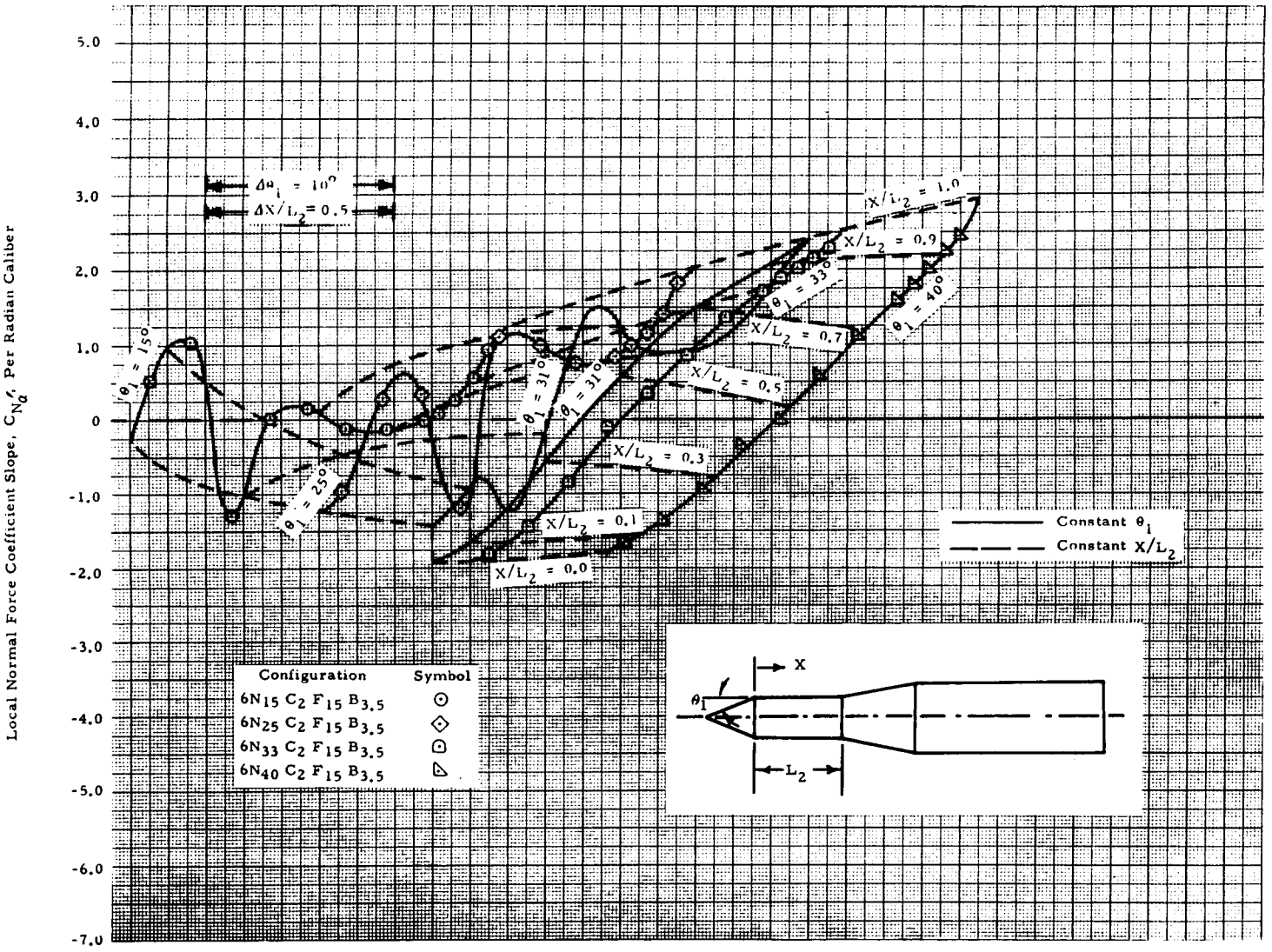

(d) M = 0.95

Figure 3 - The Effect of Cone Angle on Forward Cylinder Local Normal Force Slope Distributions for Cone-Cylinder-Flare-Cylinders (Cont'd)

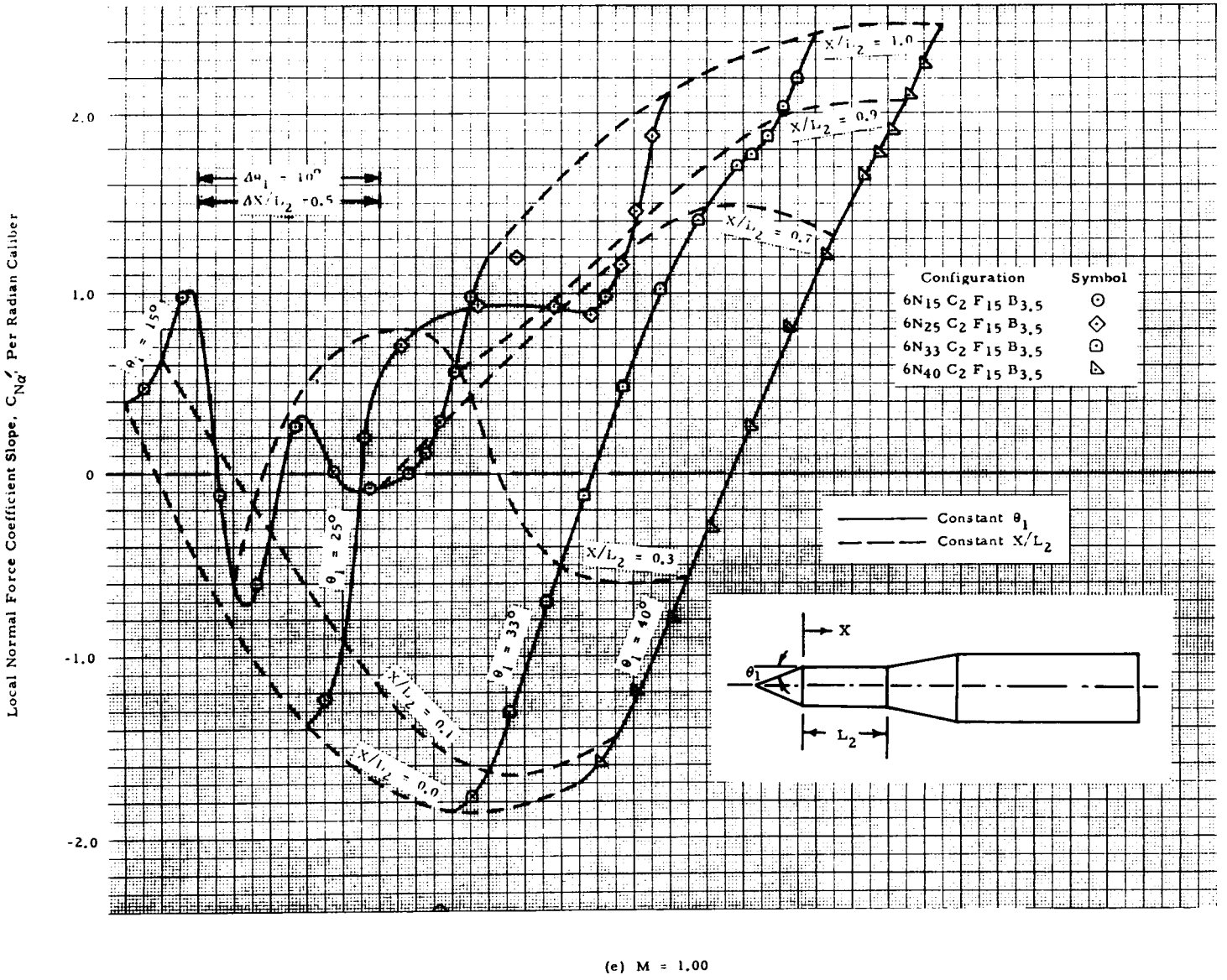

(e) M = 1.00

Figure 3 - The Effect of Cone Angle on Forward Cylinder Local Normal Force Slope Distributions for Cone-Cylinder-Flare-Cylinders (Cont'd)

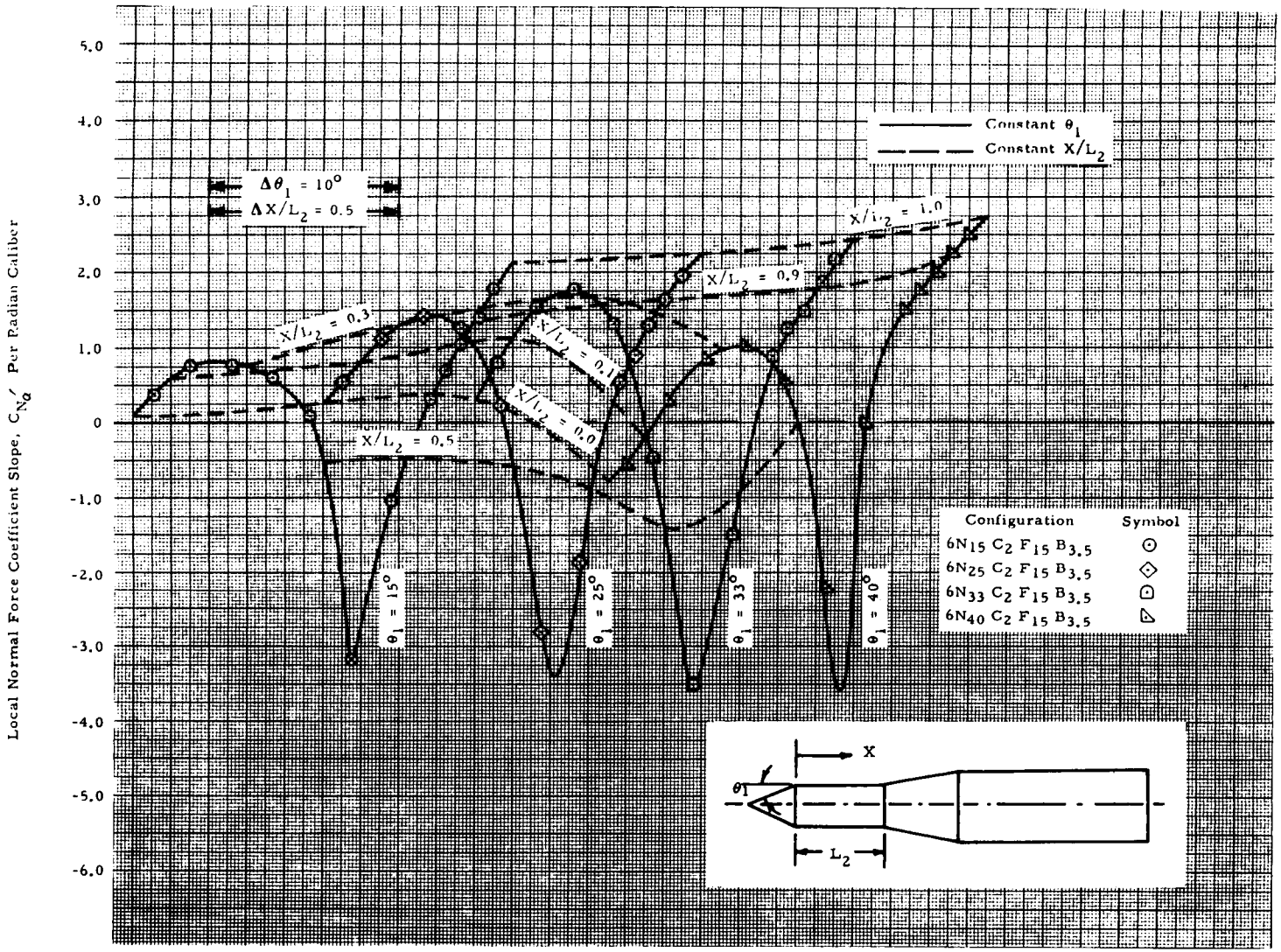

(f) M = 1.10

Figure 3 - The Effect of Cone Angle on Forward Cylinder Local Normal Force Slope Distributions for Cone-Cylinder-Flare-Cylinders (Cont'd)

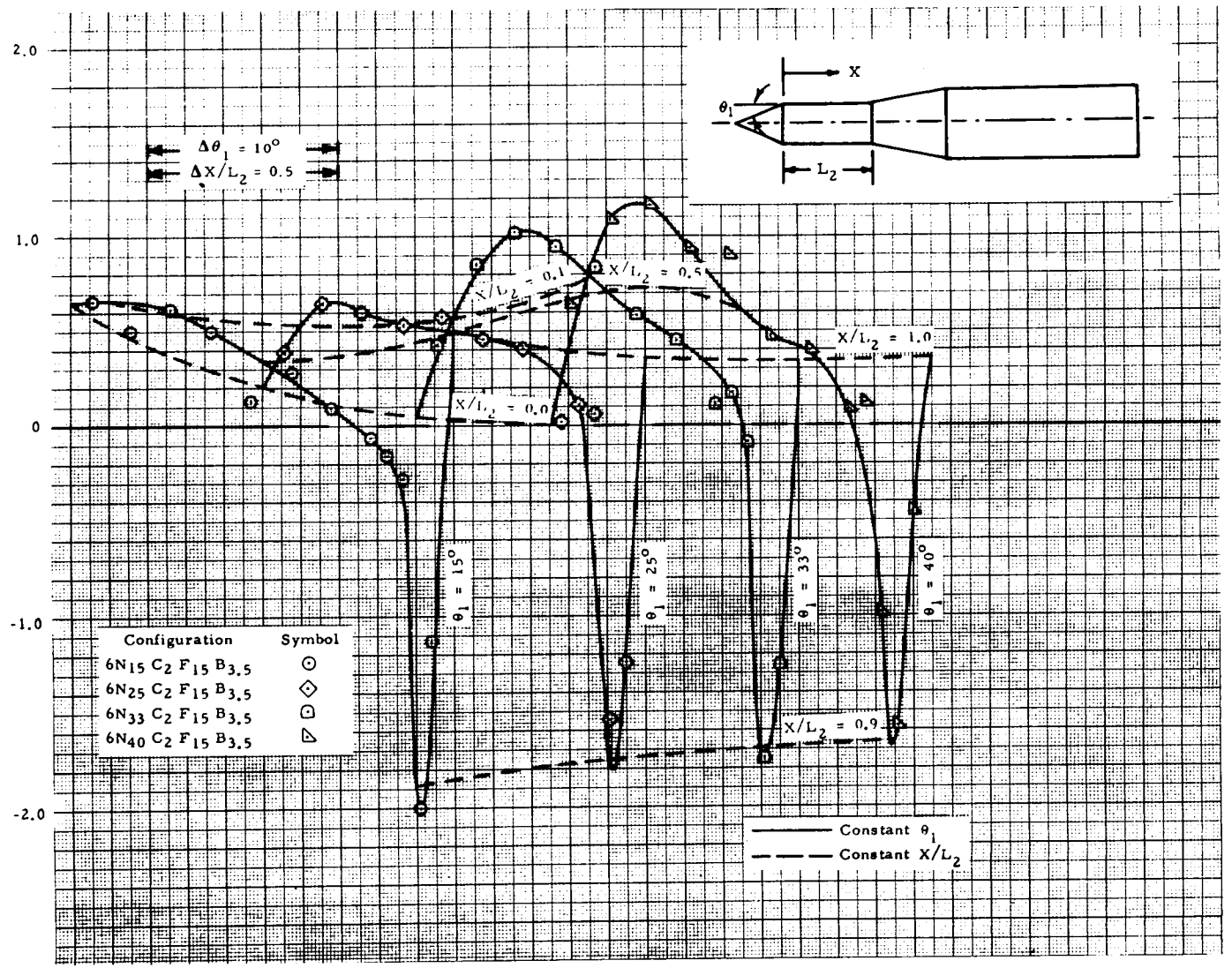

(g) M = 1.46

Figure 3 - The Effect of Cone Angle on Forward Cylinder Local Normal Force Slope Distributions for Cone-Cylinder-Flare-Cylinders (Cont'd)

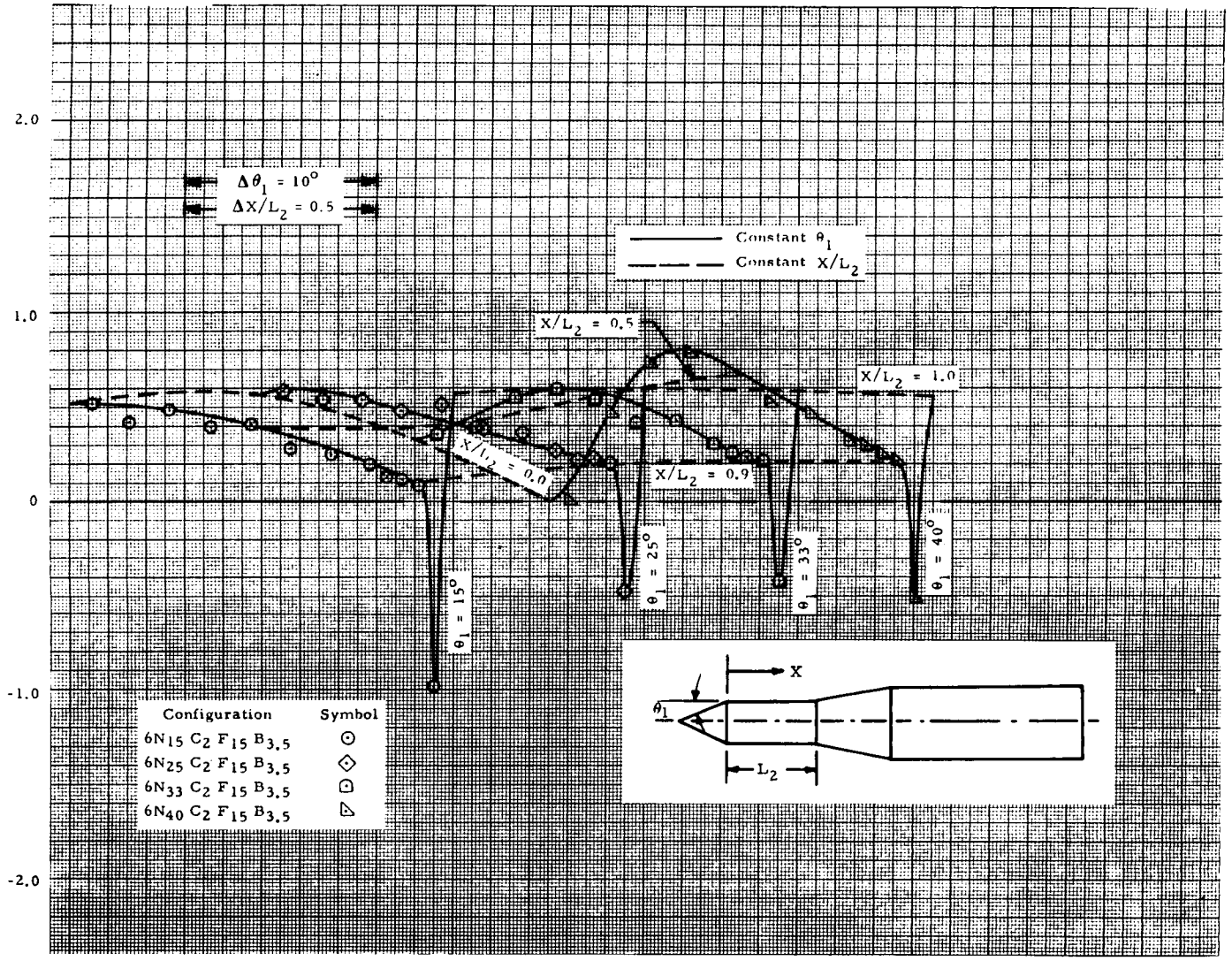

(h) M = 1.96

Figure 3 - The Effect of Cone Angle on Forward Cylinder Local Normal Force Slope Distributions for Cone-Cylinder-Flare-Cylinders (Concluded)

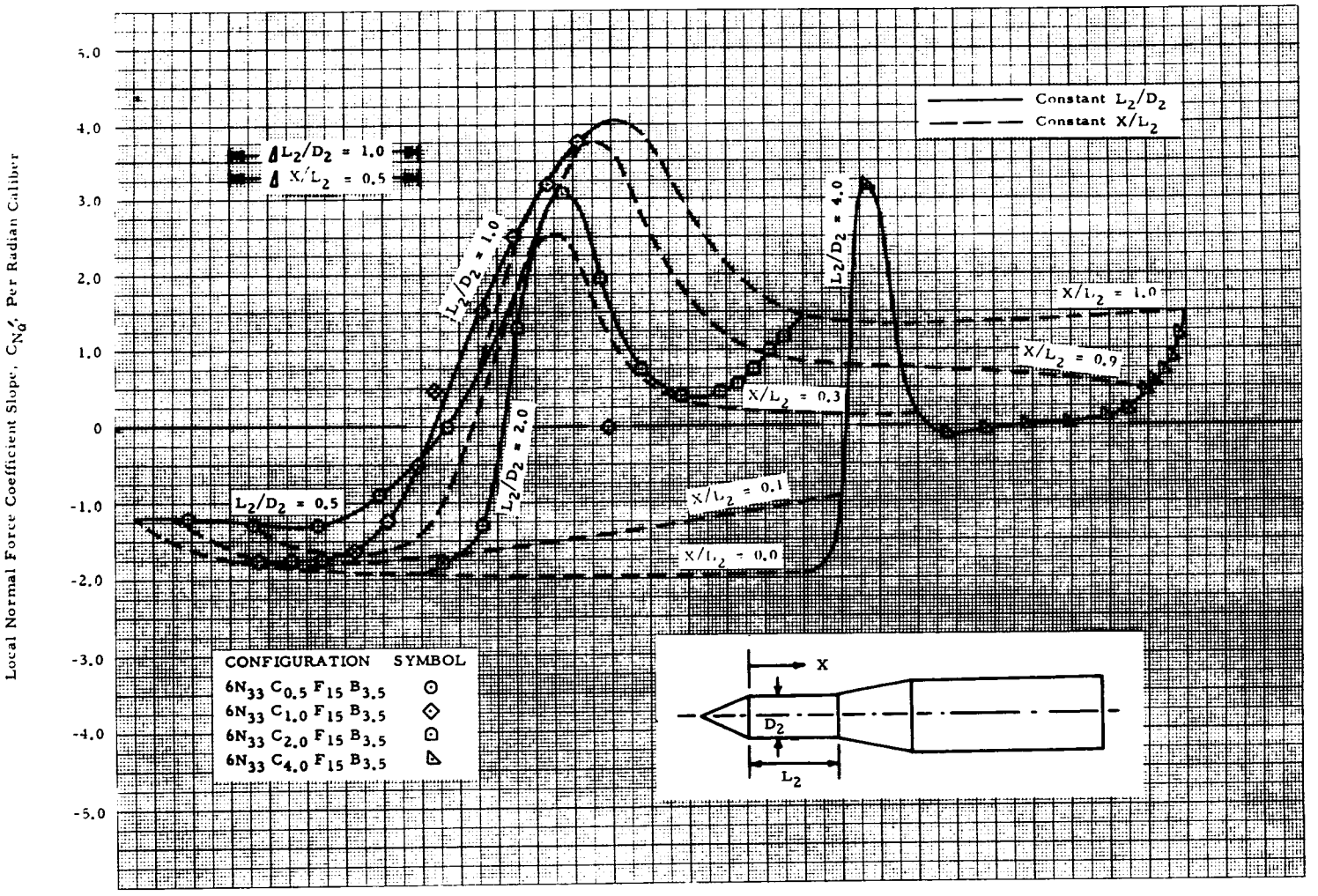

(a) M = 0.7

Figure 4 - The Effect of Length on Forward Cylinder Local Normal Force Slope Distributions for Cone-Cylinder-Flare-Cylinders

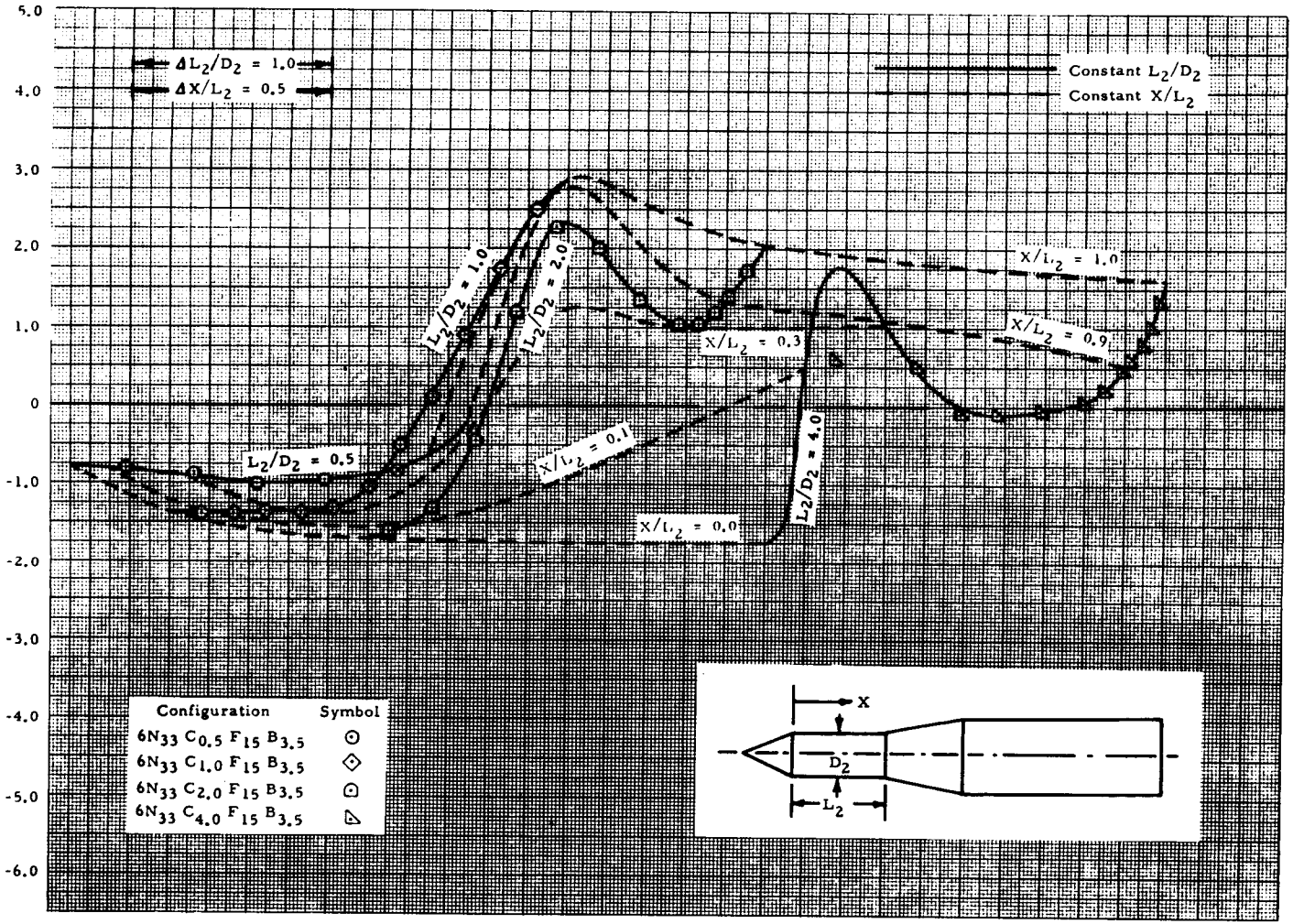

(b) M = 0.8

Figure 4 - The Effect of Length on Forward Cylinder Local Normal Force Slope Distributions for Cone-Cylinder-Flare-Cylinders (Cont'd)

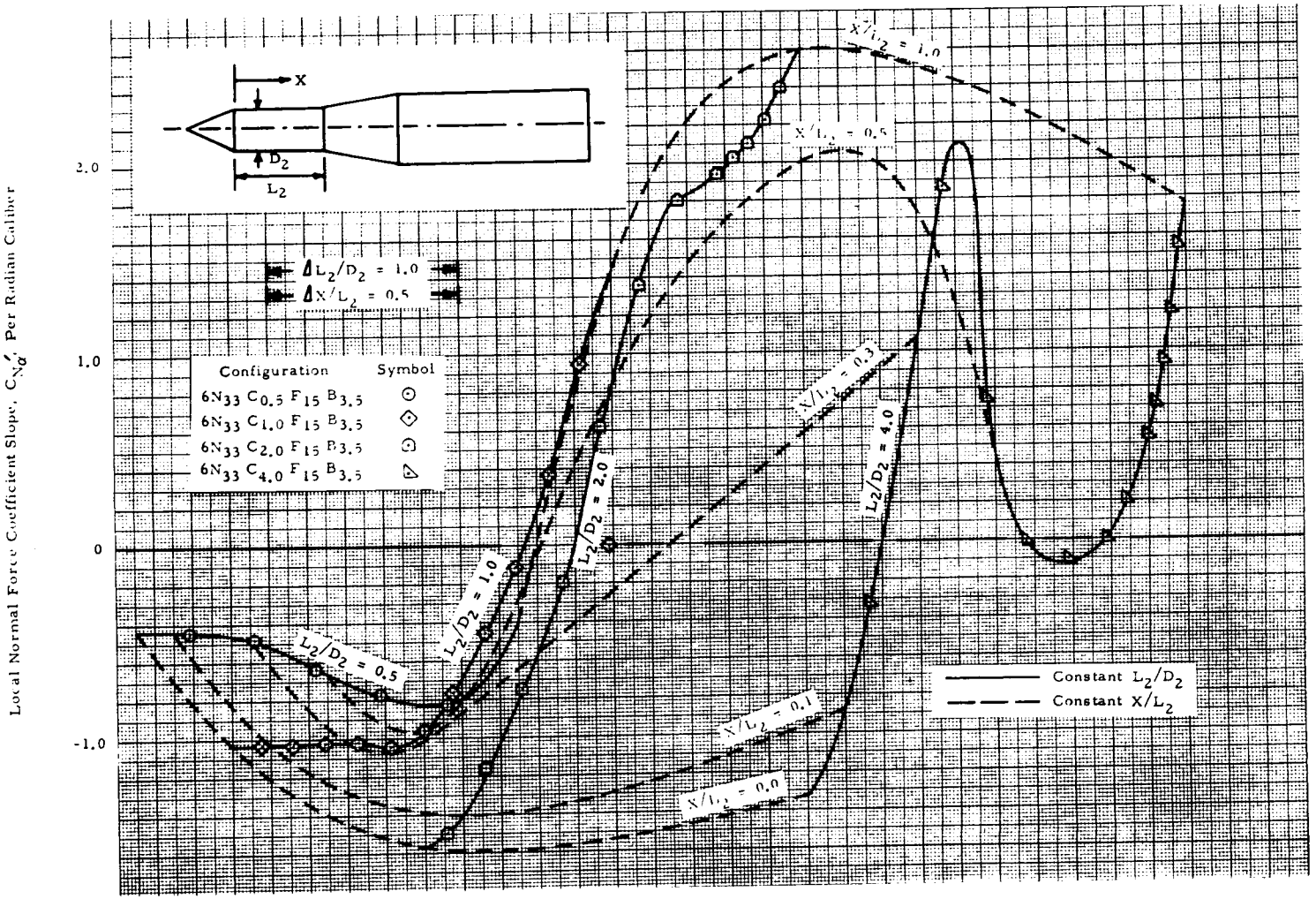

(c) M = 0.9

Figure 4 - The Effect of Length on Forward Cylinder Local Normal Force Slope Distributions for Cone-Cylinder-Flare-Cylinders (Cont'd)

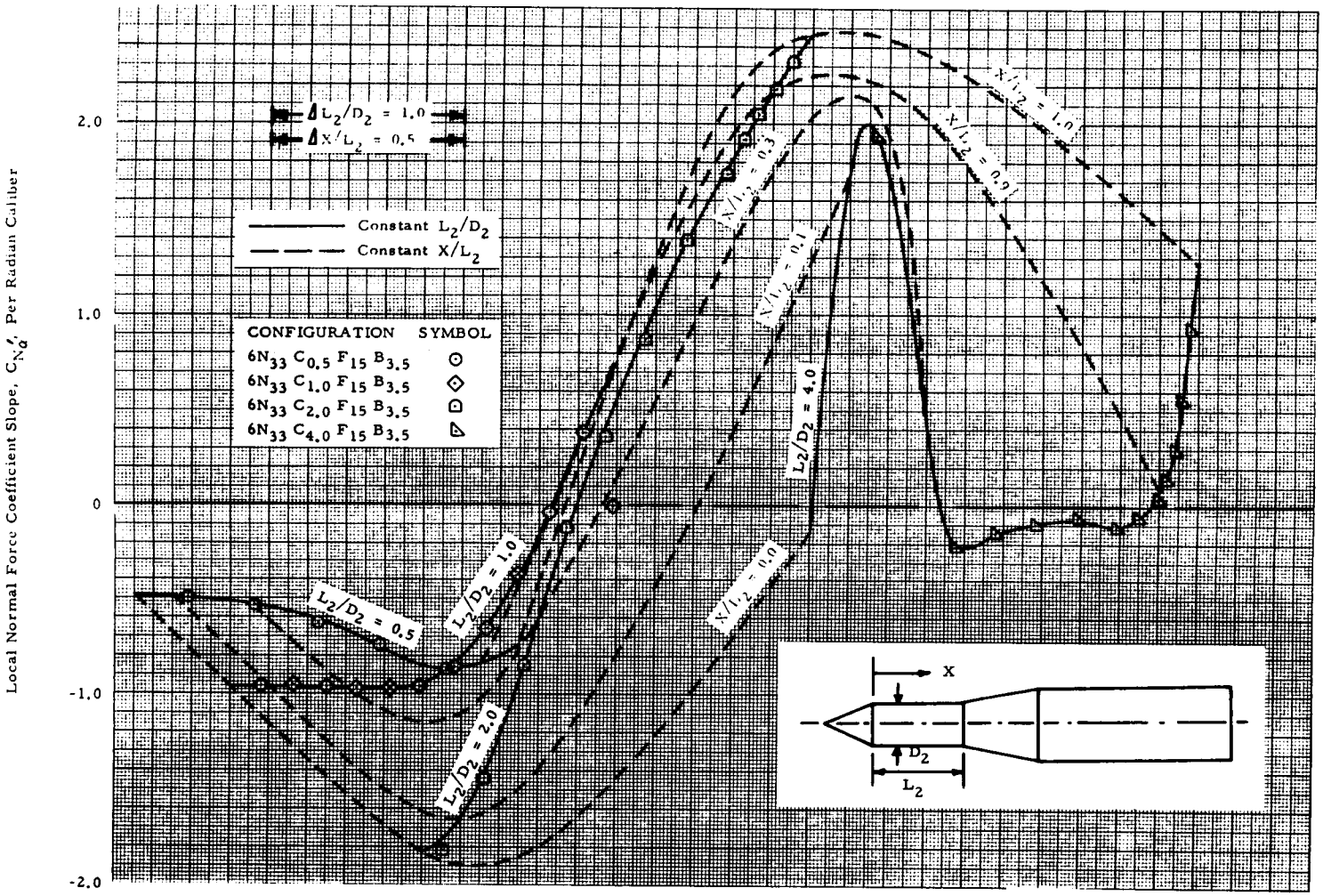

(d) M = 0.95

Figure 4 - The Effect of Length on Forward Cylinder Local Normal Force Slope Distributions for Cone-Cylinder-Flare-Cylinders (Cont'd)

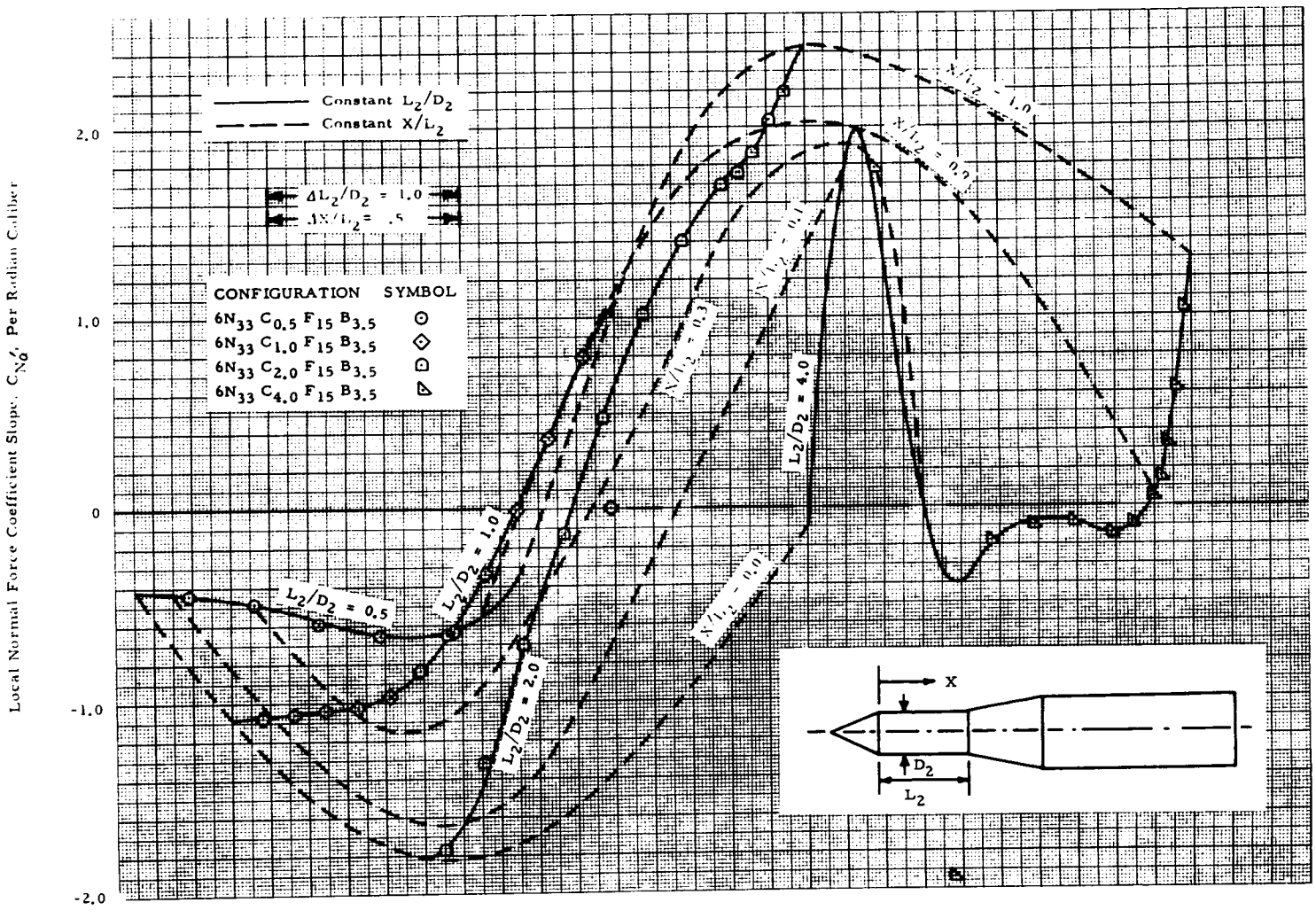

(e) M = 1.0

Figure 4 - The Effect of Length on Forward Cylinder Local Normal Force Slope Distributions for Cone-Cylinder-Flare-Cylinder (Cont'd)

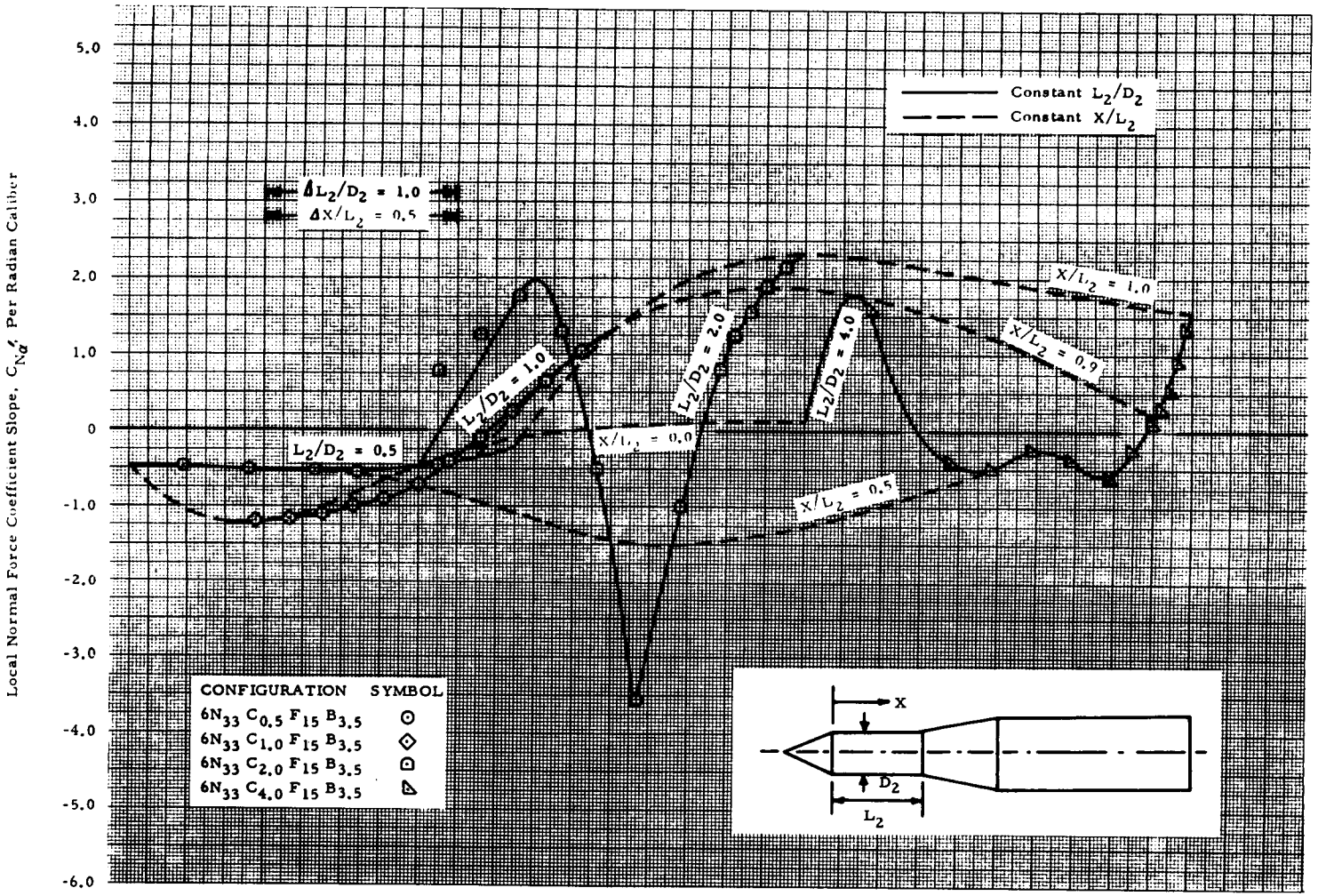

(f) M = 1.1

Figure 4 - The Effect of Length on Forward Cylinder Local Normal Force Slope Distributions for Cone-Cylinder-Flare-Cylinders (Cont'd)

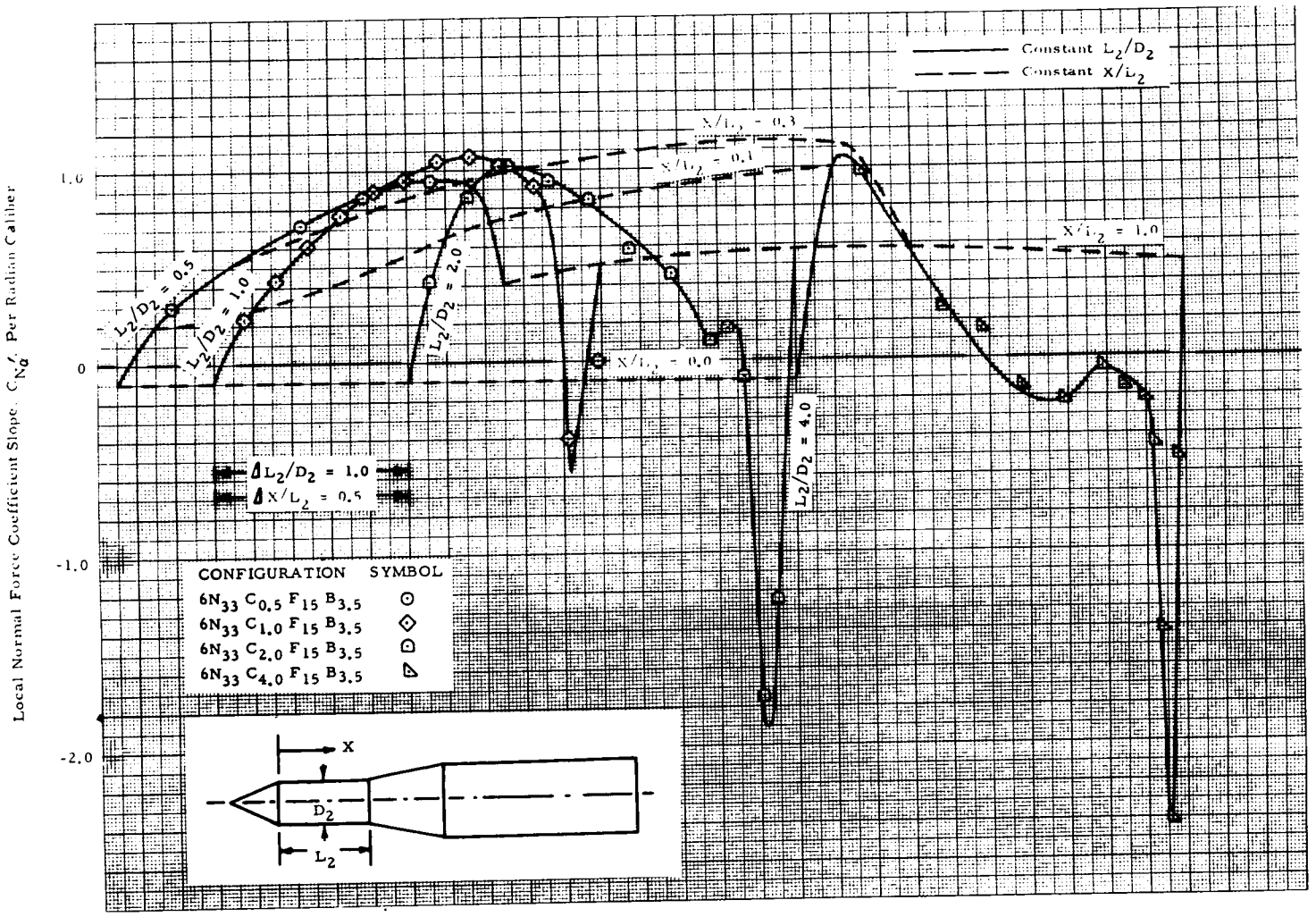

(g) M = 1.46

Figure 4 - The Effect of Length on Forward Cylinder Local Normal Force Slope Distributions for Cone-Cylinder-Flare-Cylinders (Cont'd)

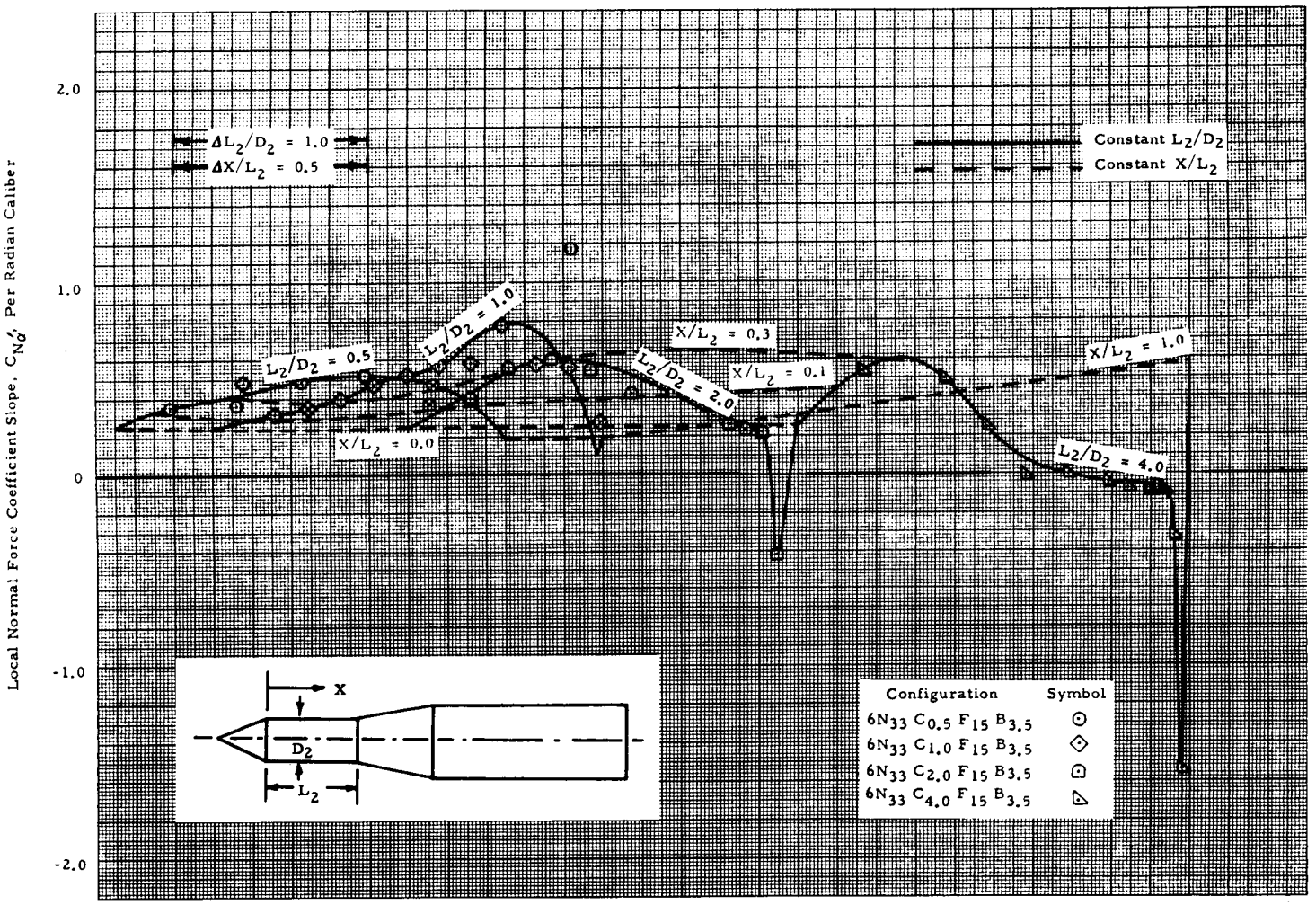

(h) M = 1.96

Figure 4 - The Effect of Length on Forward Cylinder Local Normal Force Slope Distributions for Cone-Cylinder-Flare-Cylinders (Concluded)

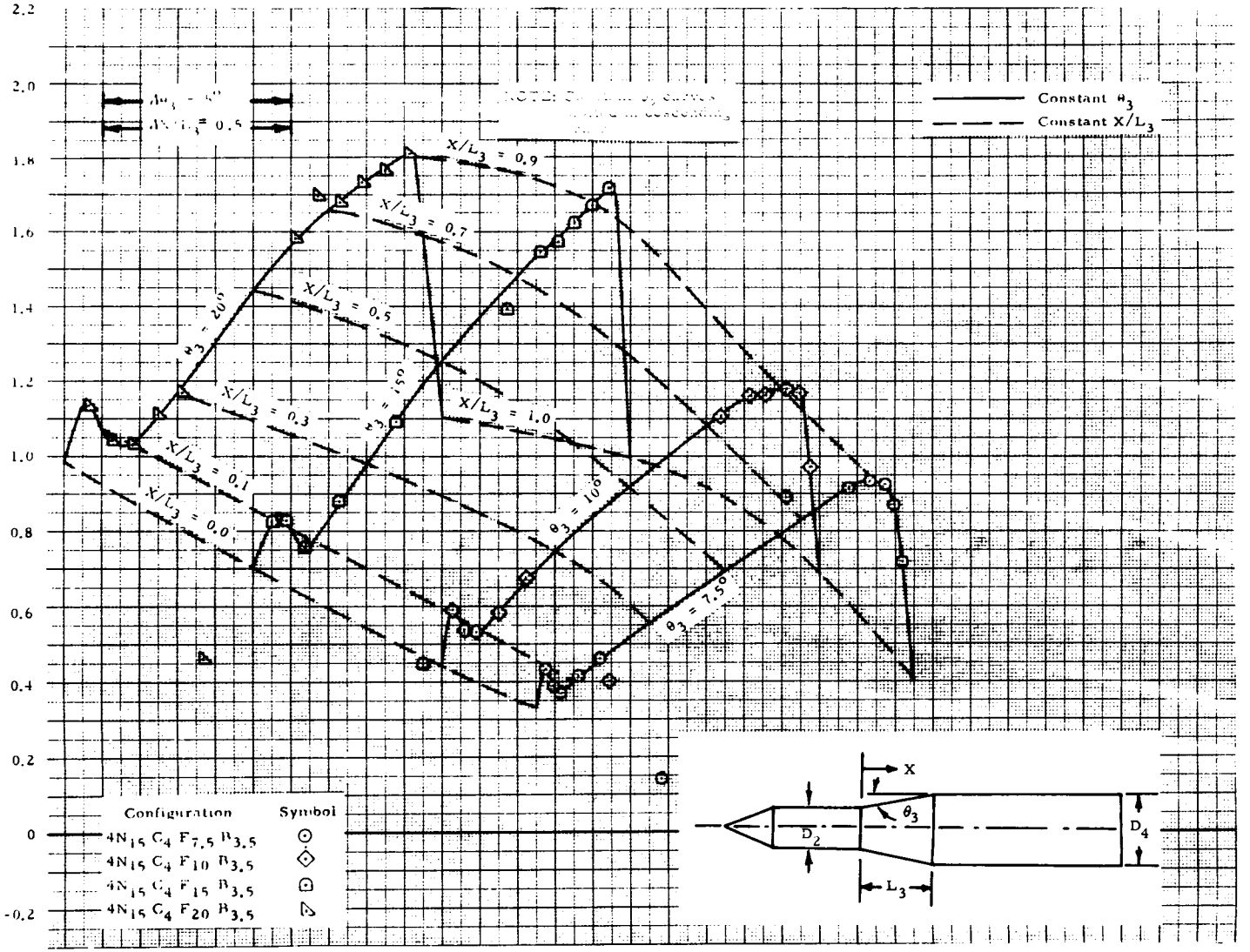

(1) M = 0.70

Figure 5a - The Effect of Frustum Angle on Local Normal Force Slope Distributions for Flares. $D_2/D_4 = 0.4$

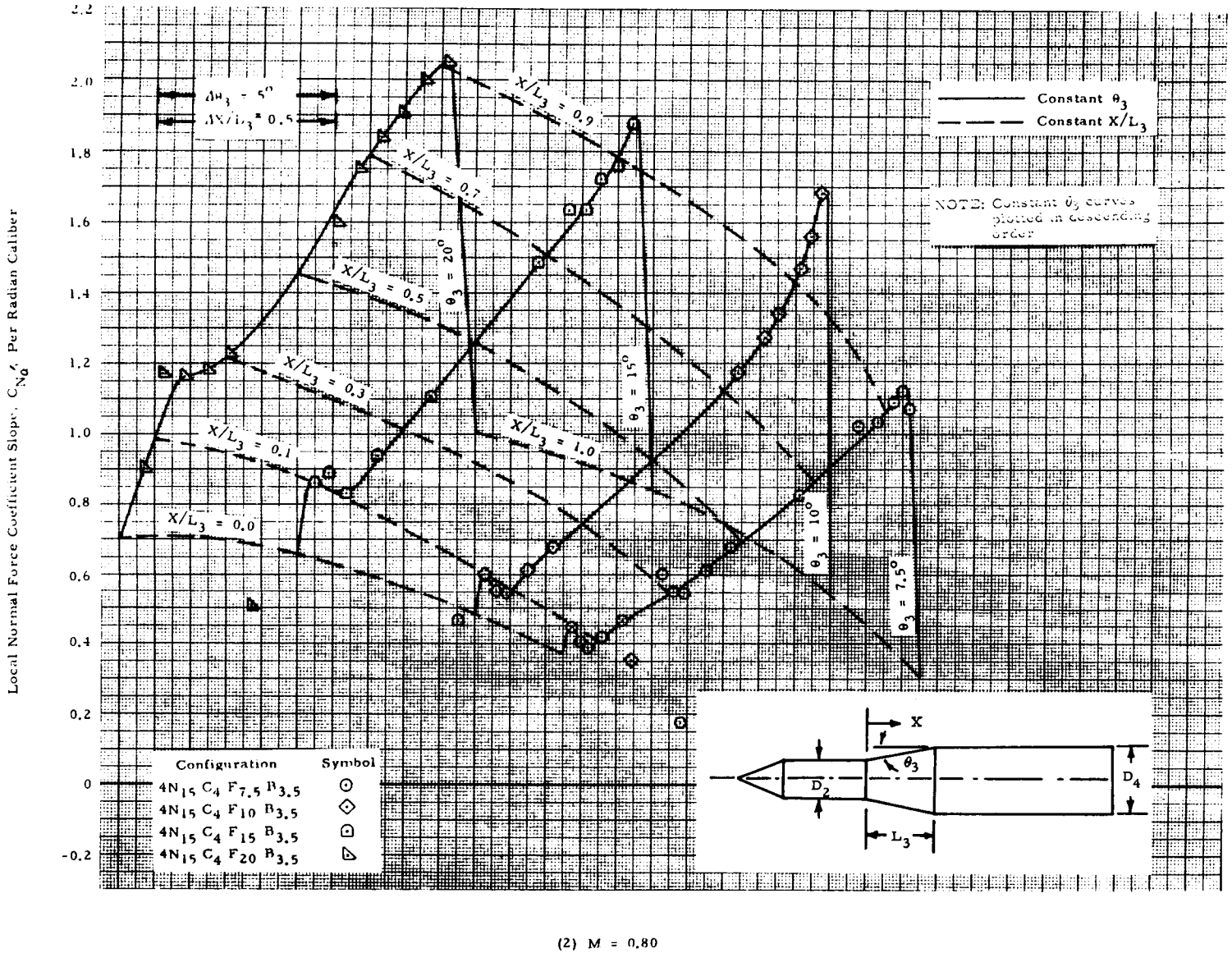

(2) M = 0.80

Figure 5a - The Effect of Frustum Angle on Local Normal Force Slope Distributions for Flares, D_2/D_4 = 0.4 (Cont'd)

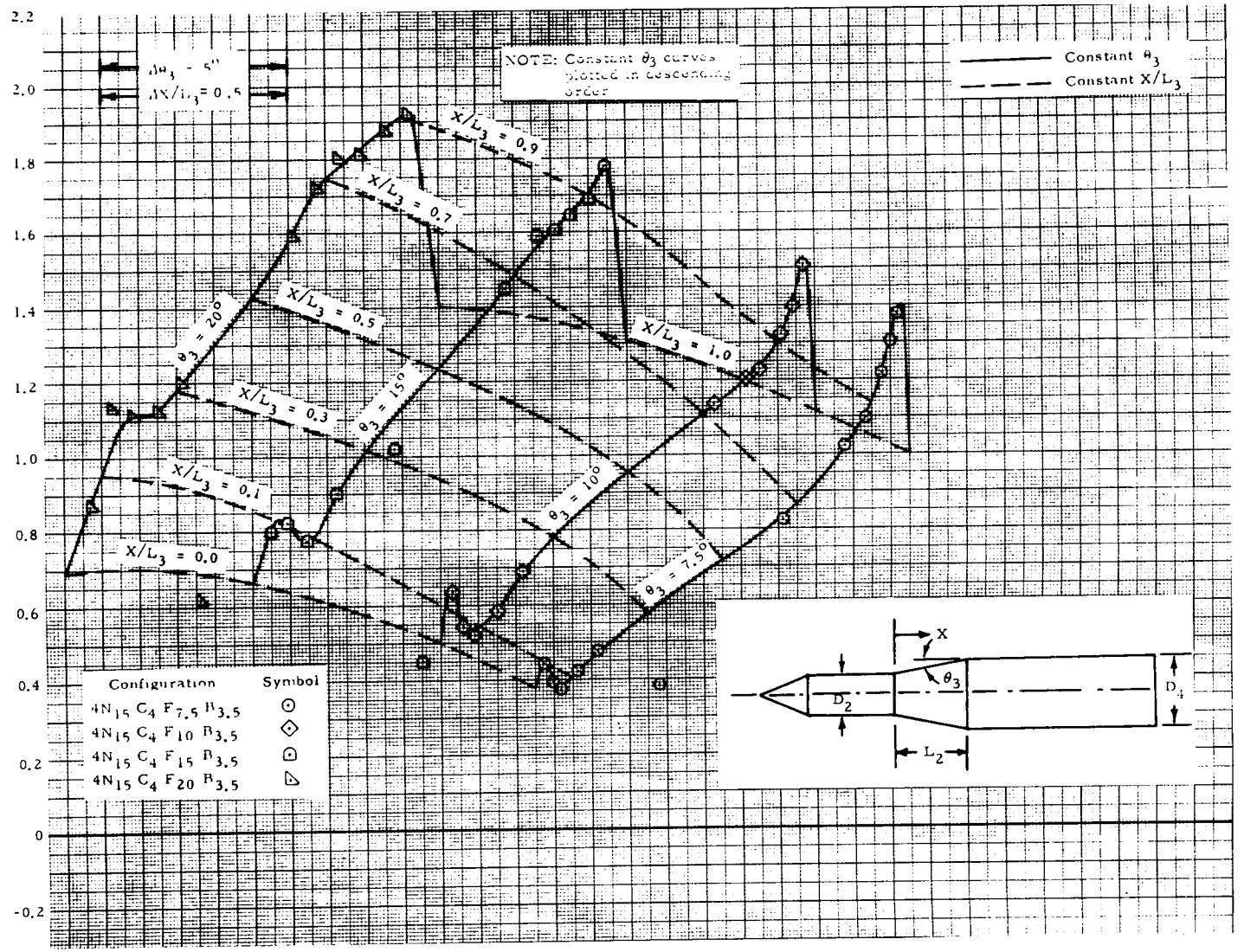

(3) M = 0.90

Figure 5a - The Effect of Frustum Angle on Local Normal Force Slope Distributions for Flares. $D_2/D_4 = 0.4$ (Cont'd)

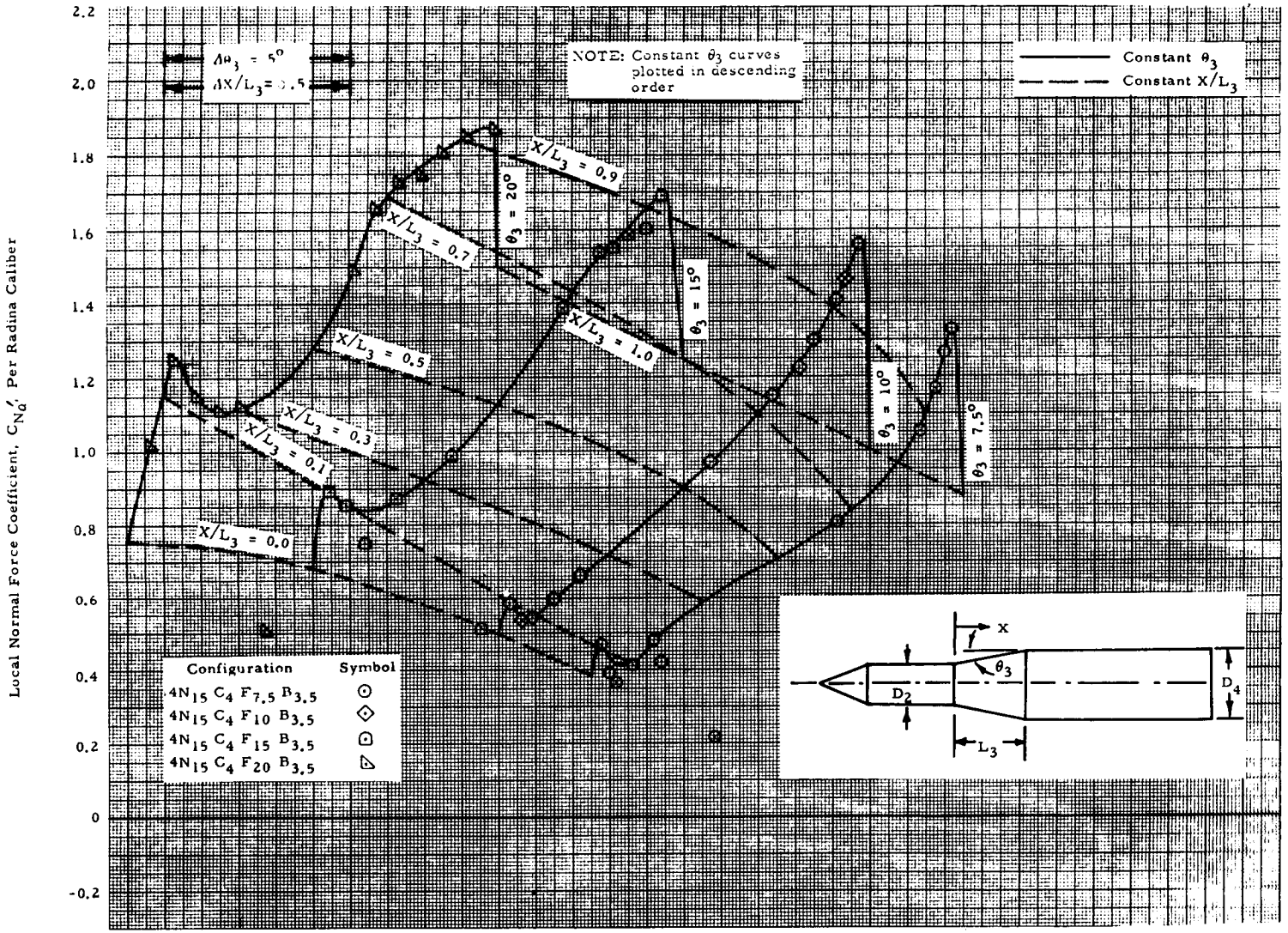

(4) M = 0.95

Figure 5a - The Effect of Frustum Angle on Local Normal Force Slope Distributions for Flares, D_2/D_4 = 0.4 (Cont'd)

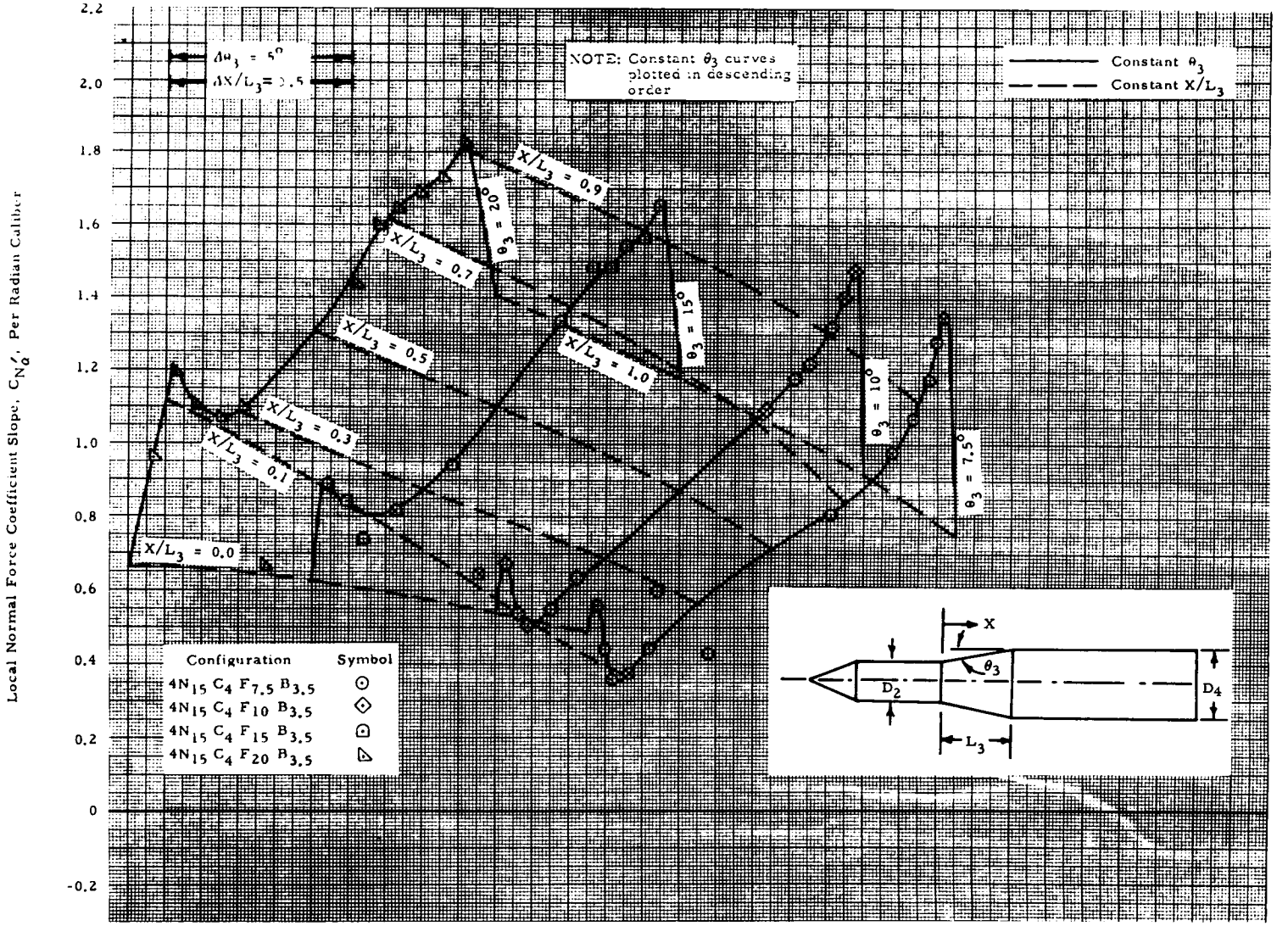

(5) M = 1.00

Figure 5a - The Effect of Frustum Angle on Local Normal Force Slope Distributions for Flares, D_2/D_4 = 0.4 (Cont'd)

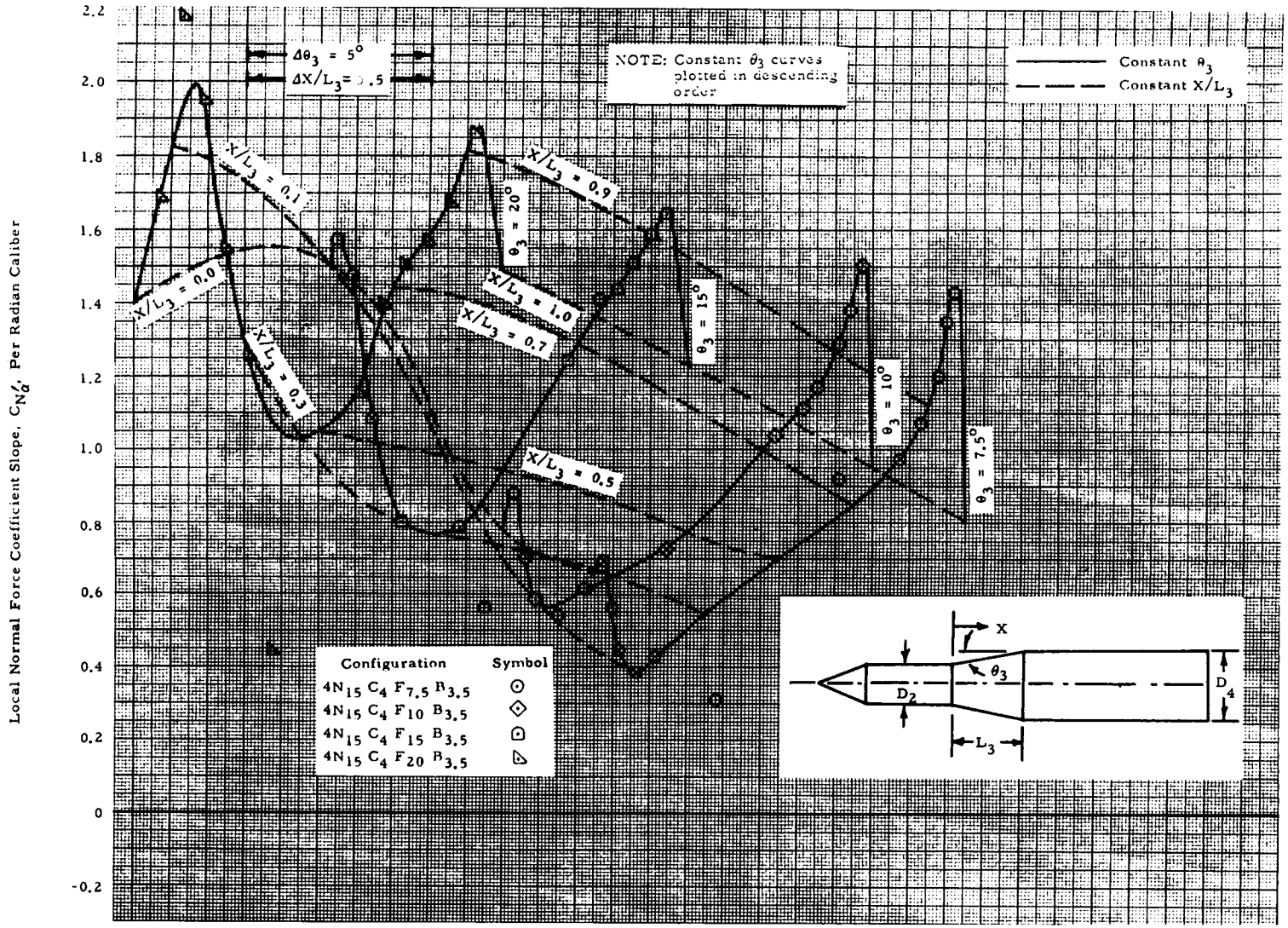

(6) M = 1.10

Figure 5a - The Effect of Frustum Angle on Local Normal Force Slope Distributions for Flares, $D_2/D_4 = 0.4$ (Cont'd)

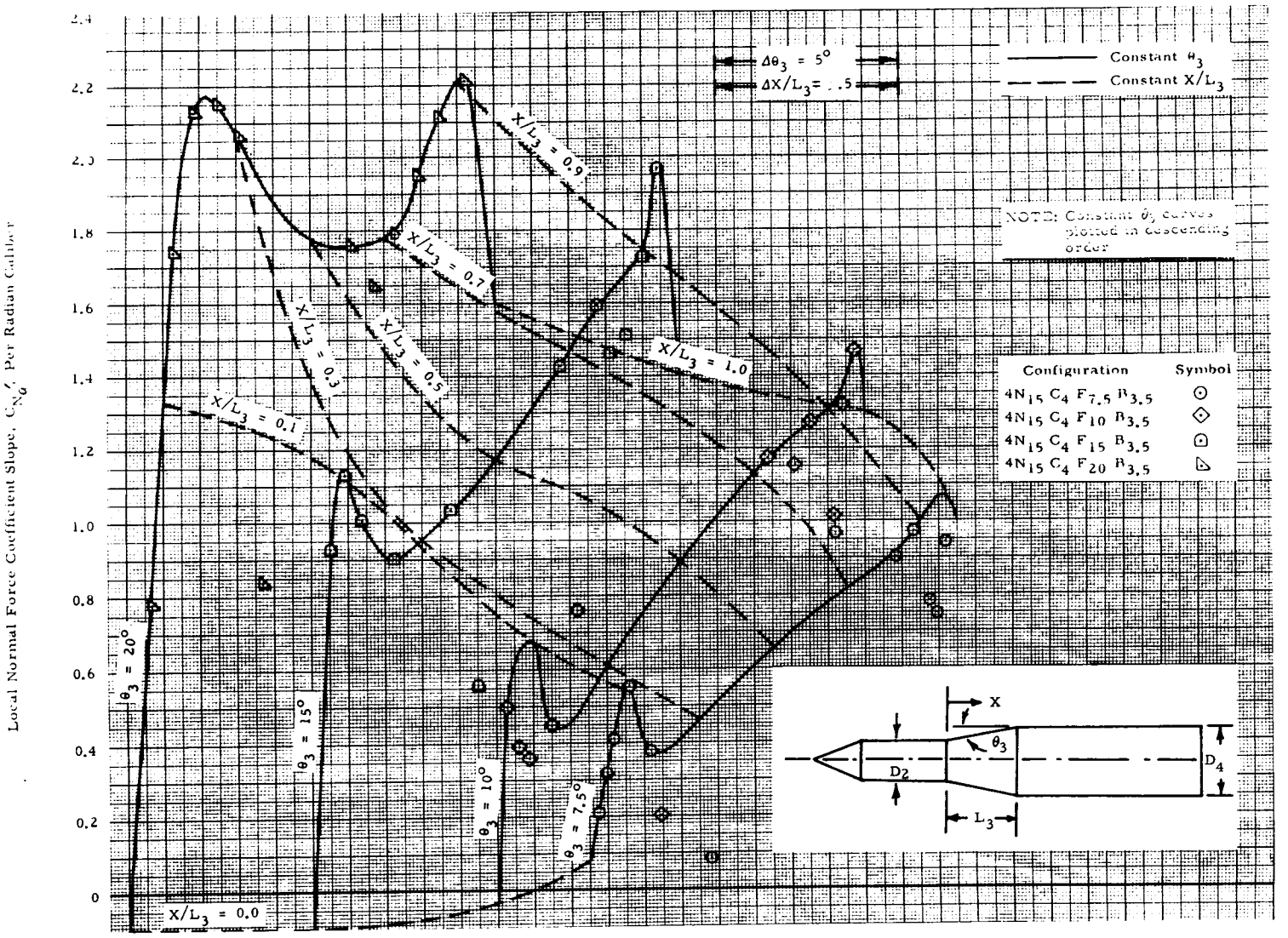

(7) M = 1.46

Figure 5a - The Effect of Frustum Angle on Local Normal Force Slope Distributions for Flares, $D_2/D_4 = 0.4$ (Cont'd)

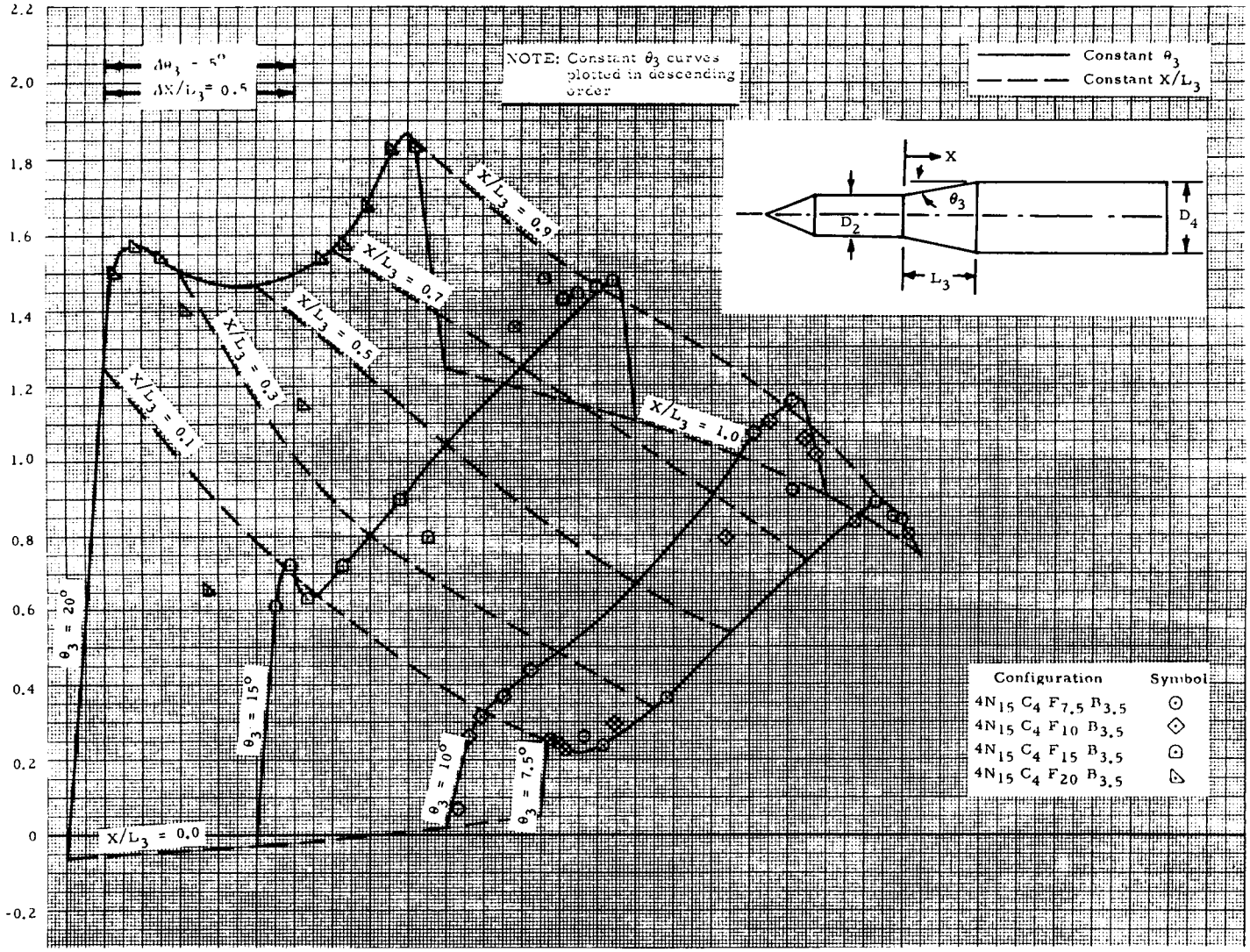

(8) M = 1.96

Figure 5a - The Effect of Frustum Angle on Local Normal Force Slope Distributions for Flares, D_2/D_4 = 0.4 (Concluded)

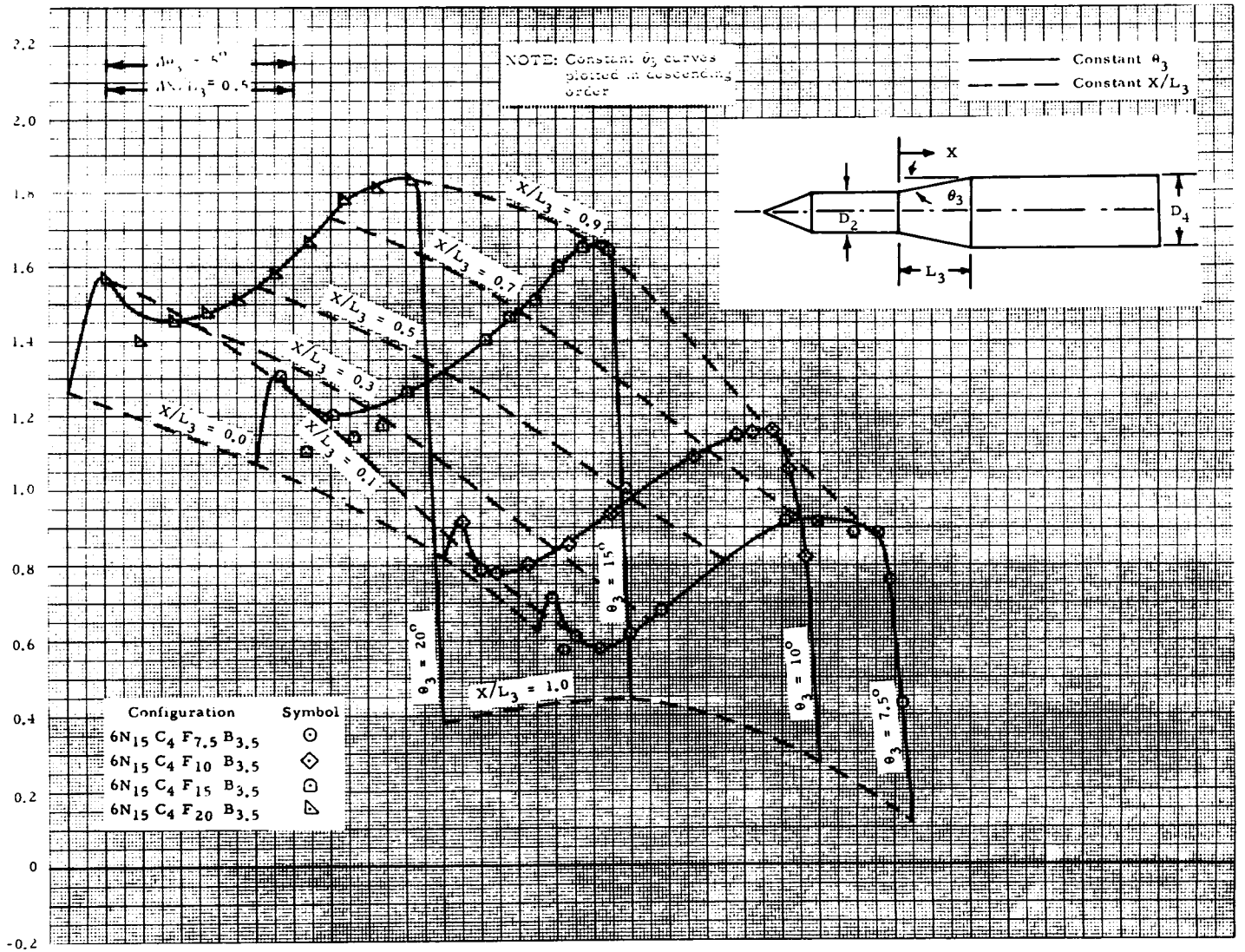

(1) M = 0.70

Figure 5b - The Effect of Frustum Angle on Local Normal Force Slope Distributions for Flares, $D_2/D_4 = 0.6$

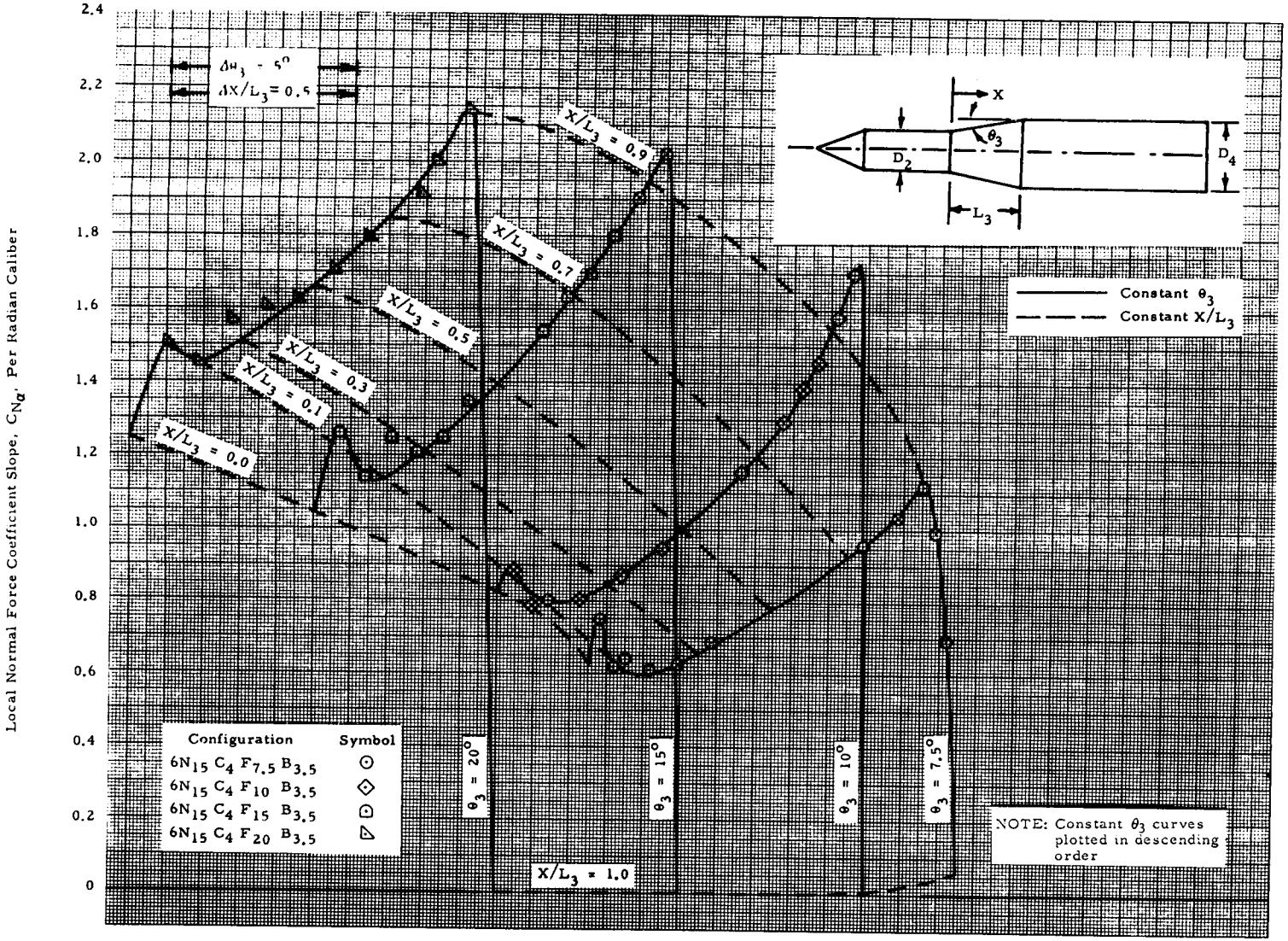

(2) M = 0.80

Figure 5b - The Effect of Frustum Angle on Local Normal Force Slope Distributions for Flares, D_2/D_4 = 0.6 (Cont'd)

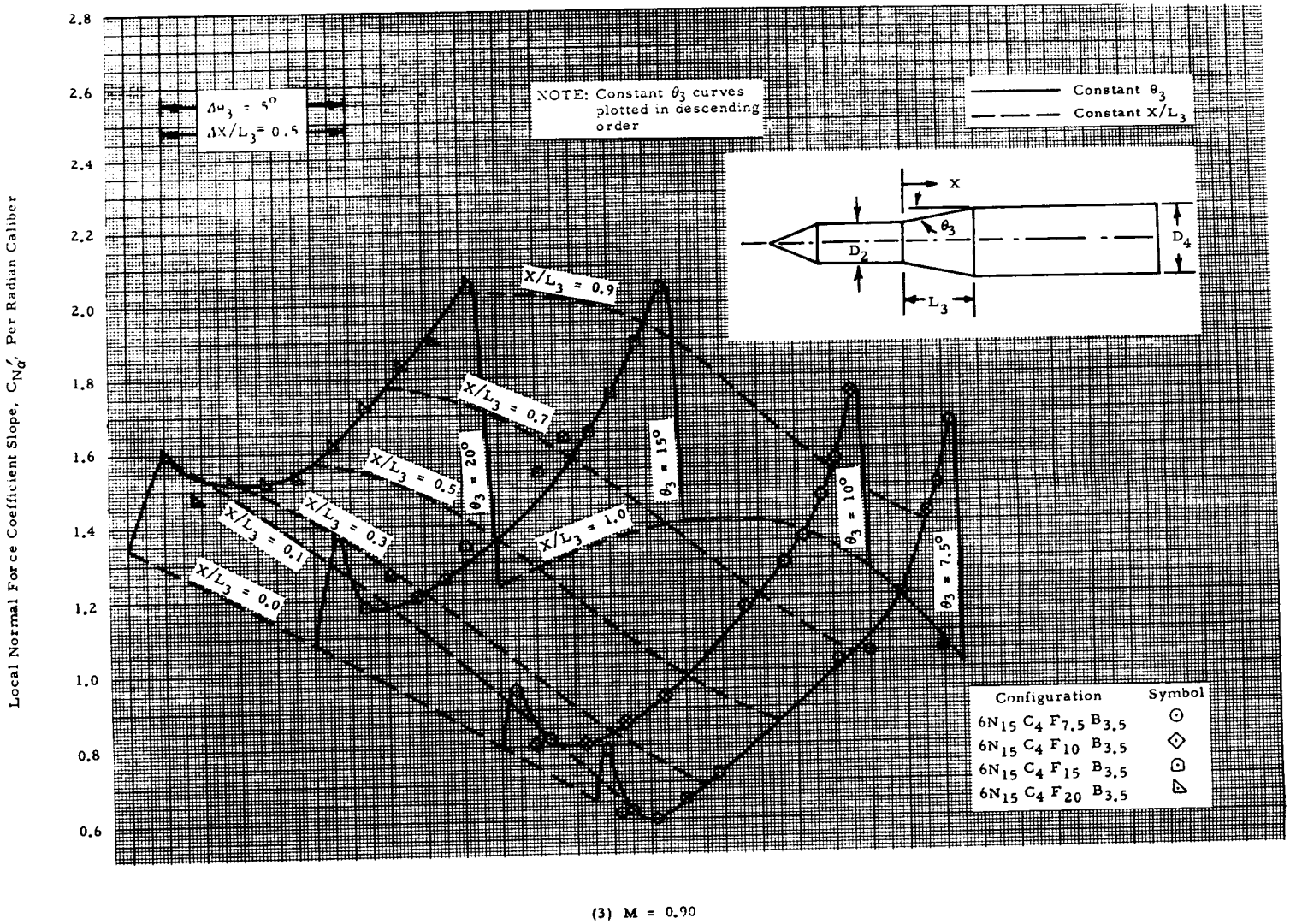

(3) M = 0.90

Figure 5b - The Effect of Frustum Angle on Local Normal Force Slope Distributions for Flares, $D_2/D_4 = 0.6$ (Cont'd)

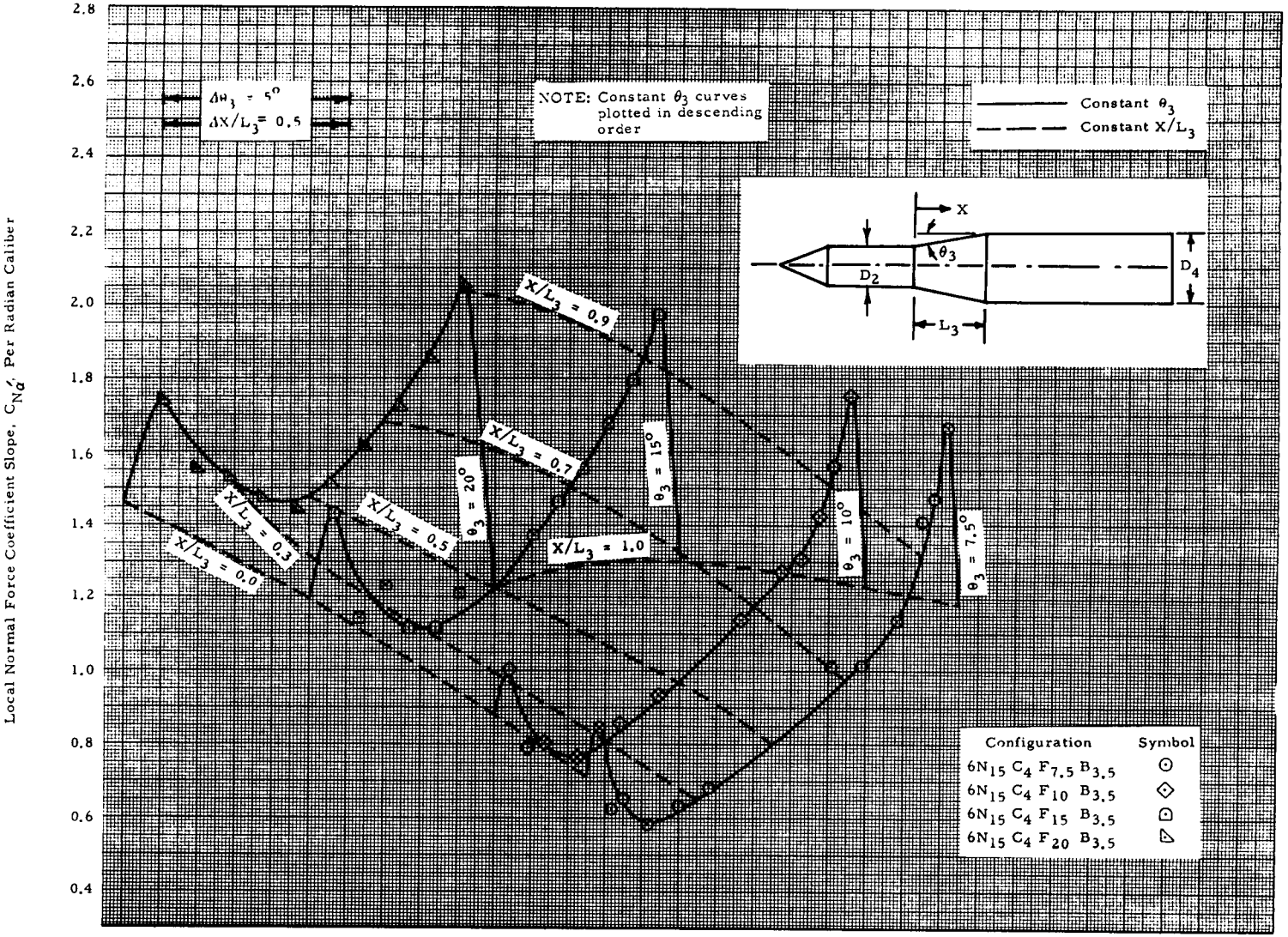

(4) M = 0.95

Figure 5b - The Effect of Frustum Angle on Local Normal Force Slope Distributions, $D_2/D_4 = 0.6$ (Cont'd)

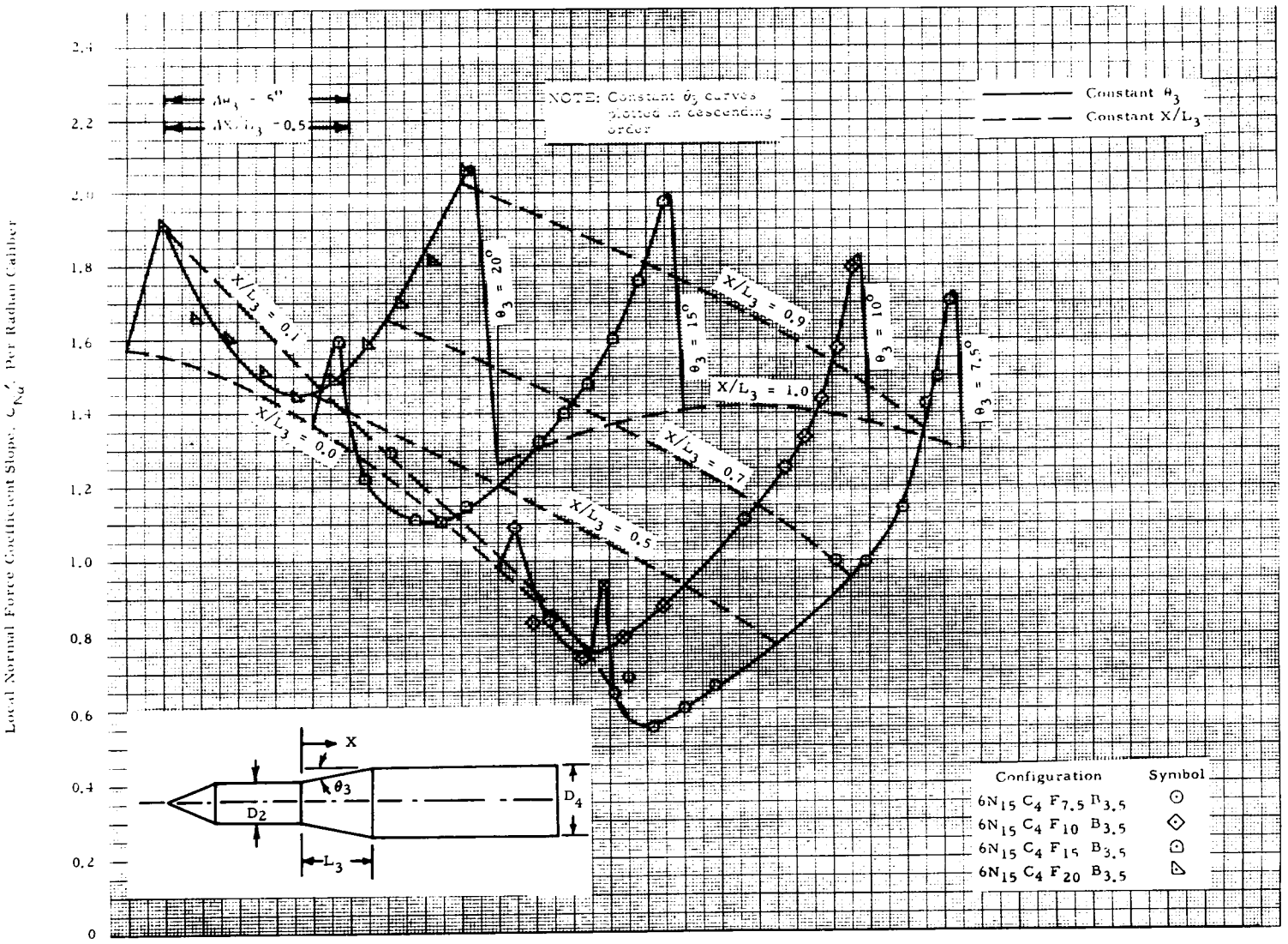

(5) M = 1.00

Figure 5b - The Effect of Frustum Angle on Local Normal Force Slope Distributions for Flares, D_2/D_4 = 0.6 (Cont'd)

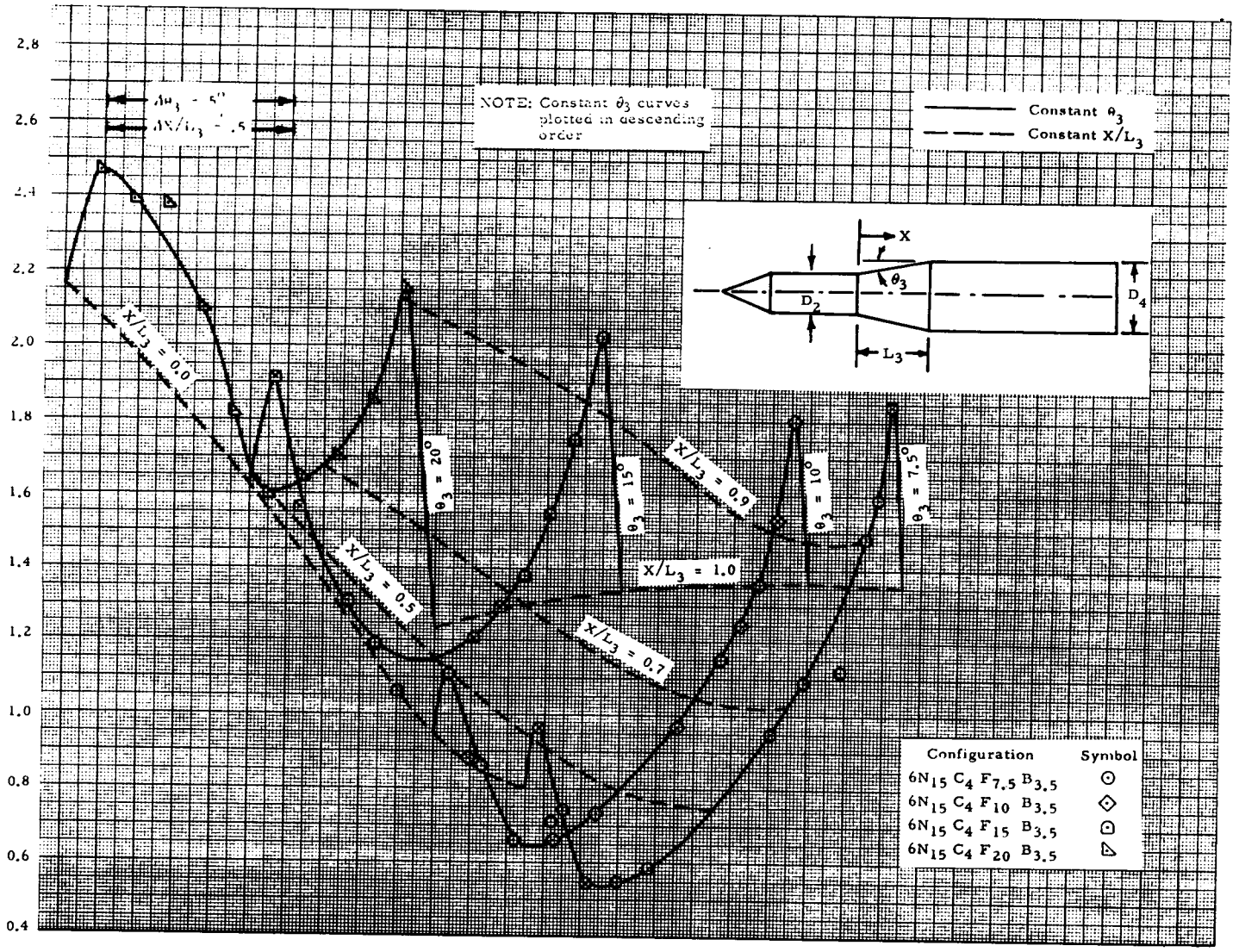

(6) M = 1.10

Figure 5b - The Effect of Frustum Angle on Local Normal Force Slope Distributions for Flares, D_2/D_4 = 0.6 (Cont'd)

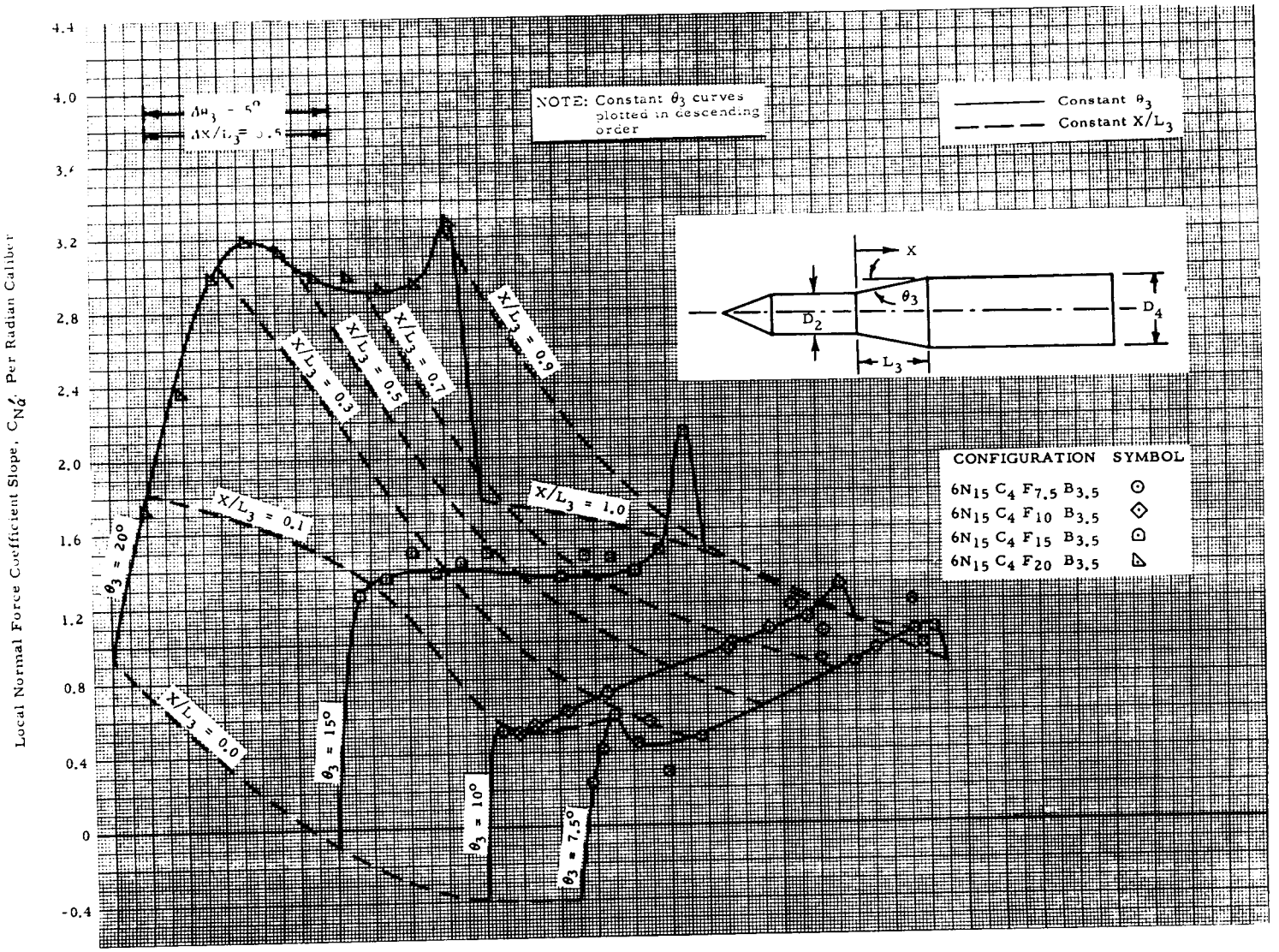

(7) M = 1.46

Figure 5b - The Effect of Frustum Angle on Local Normal Force Slope Distributions for Flares, $D_2/D_4 = 0.6$ (Cont'd)

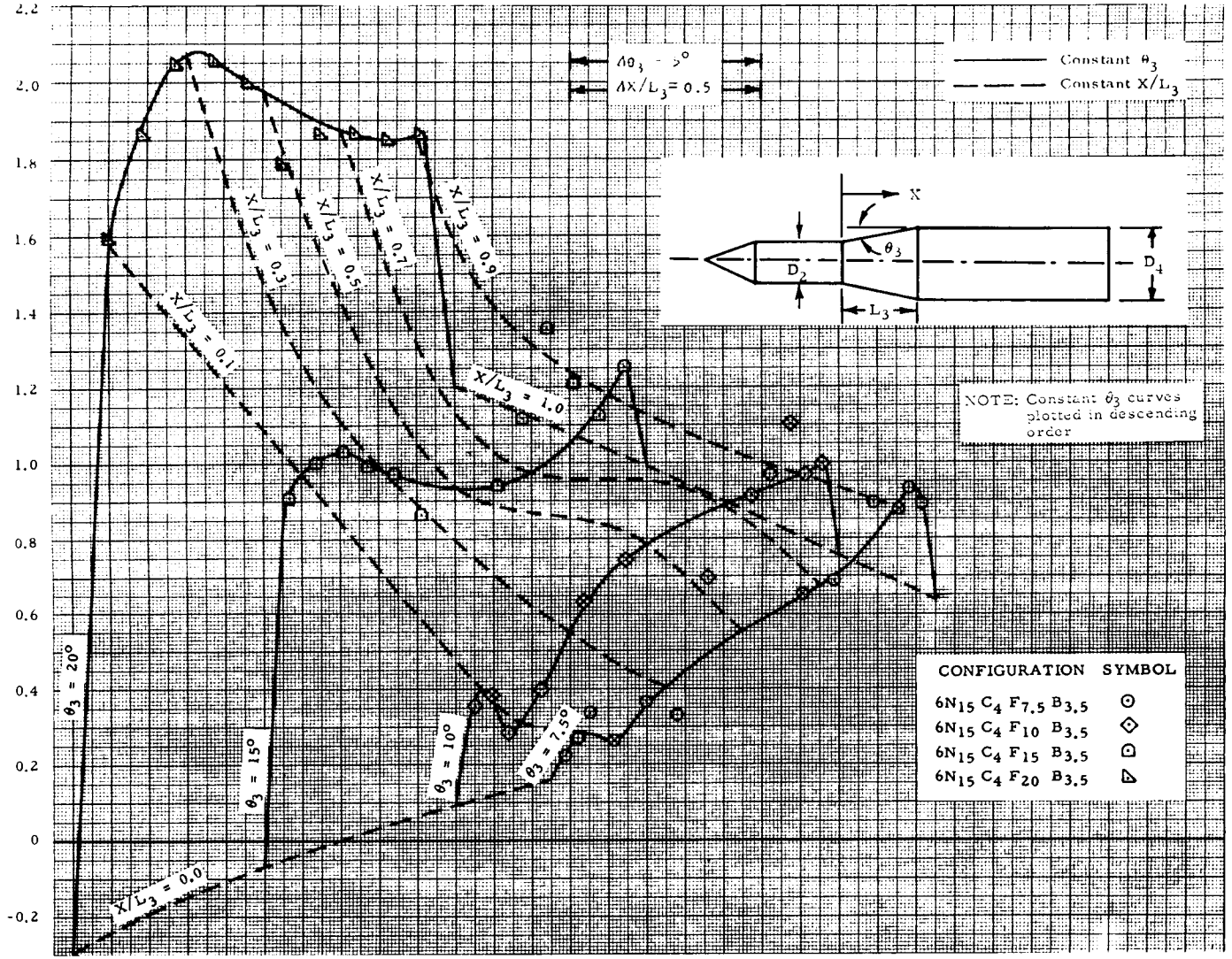

(3) M = 1.96

Figure 5b - The Effect of Frustum Angle on Local Normal Force Slope Distributions for Flares, D_2/D_4 = 0.6 (Concluded)

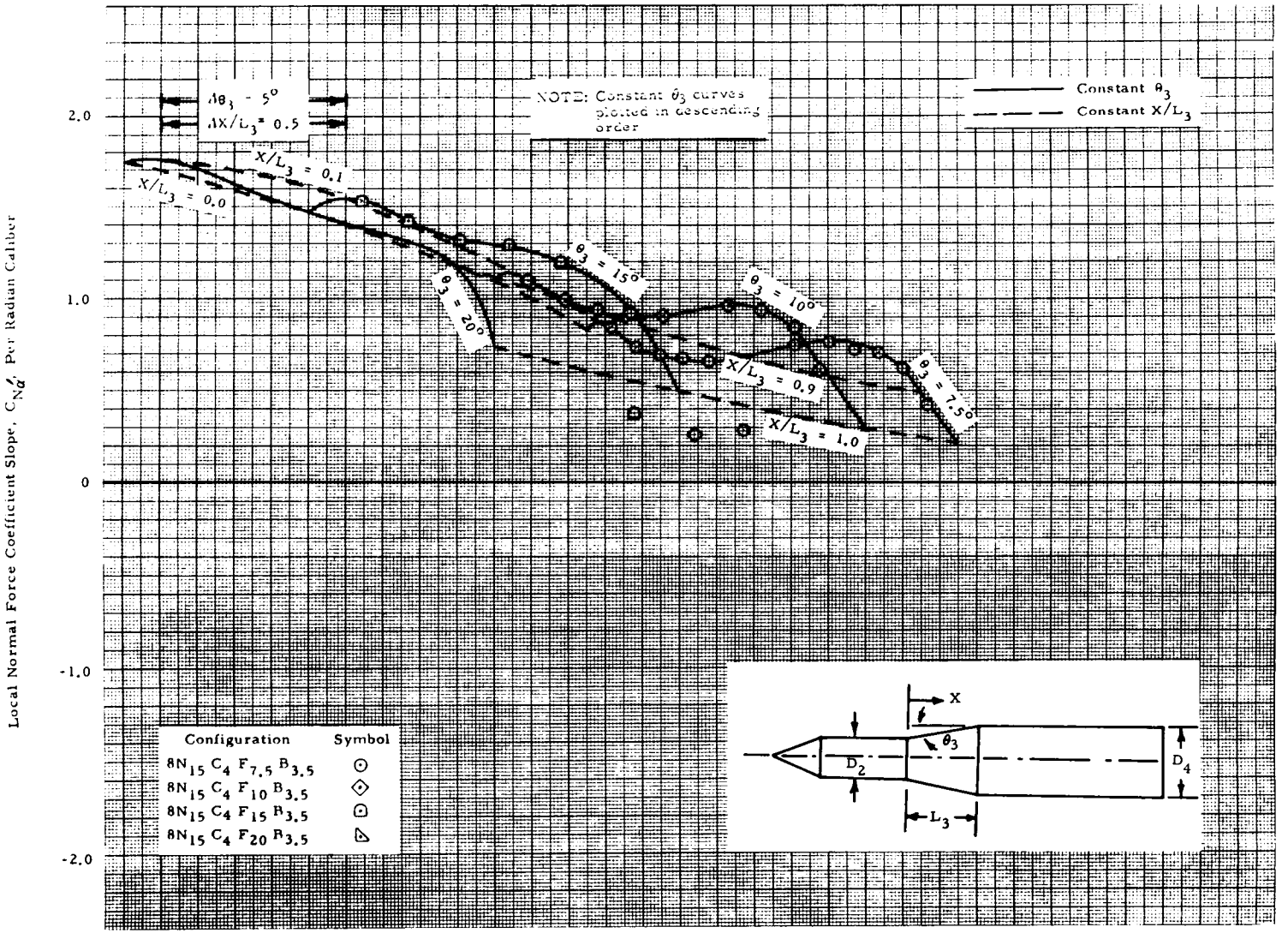

(1) M = 0.70

Figure 5c - The Effect of Frustum Angle on Local Normal Force Slope Distributions for Flares. D_2/D_4 = 0.8

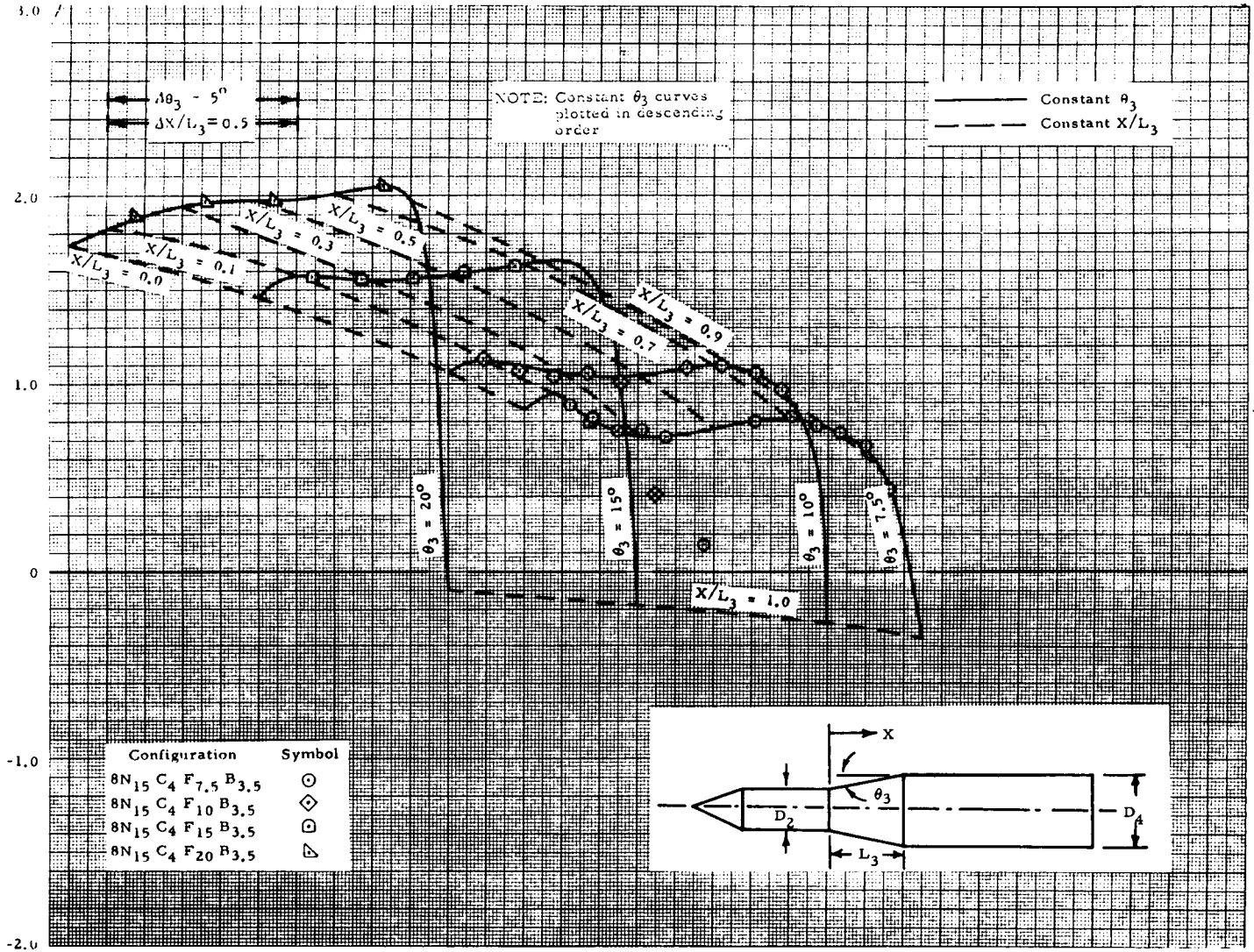

(2) M = 0.80

Figure 5c - The Effect of Frustum Angle on Local Normal Force Slope Distributions for Flares, D_2/D_4 = 0.8 (Cont'd)

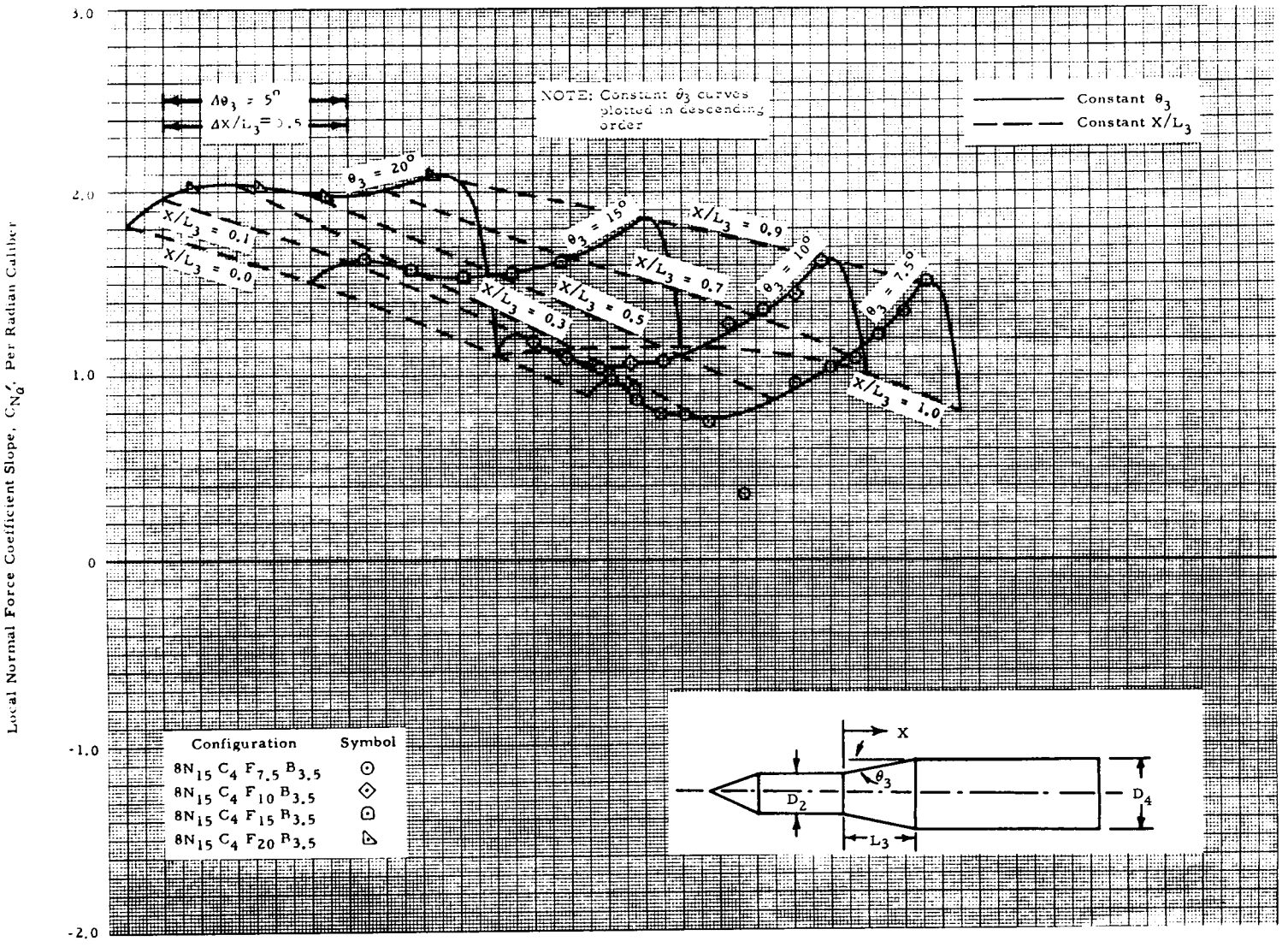

(3) M = 0.90

Figure 5c - The Effect of Frustum Angle on Local Normal Force Slope Distributions for Flares, $D_2/D_4 = 0.8$ (Cont'd)

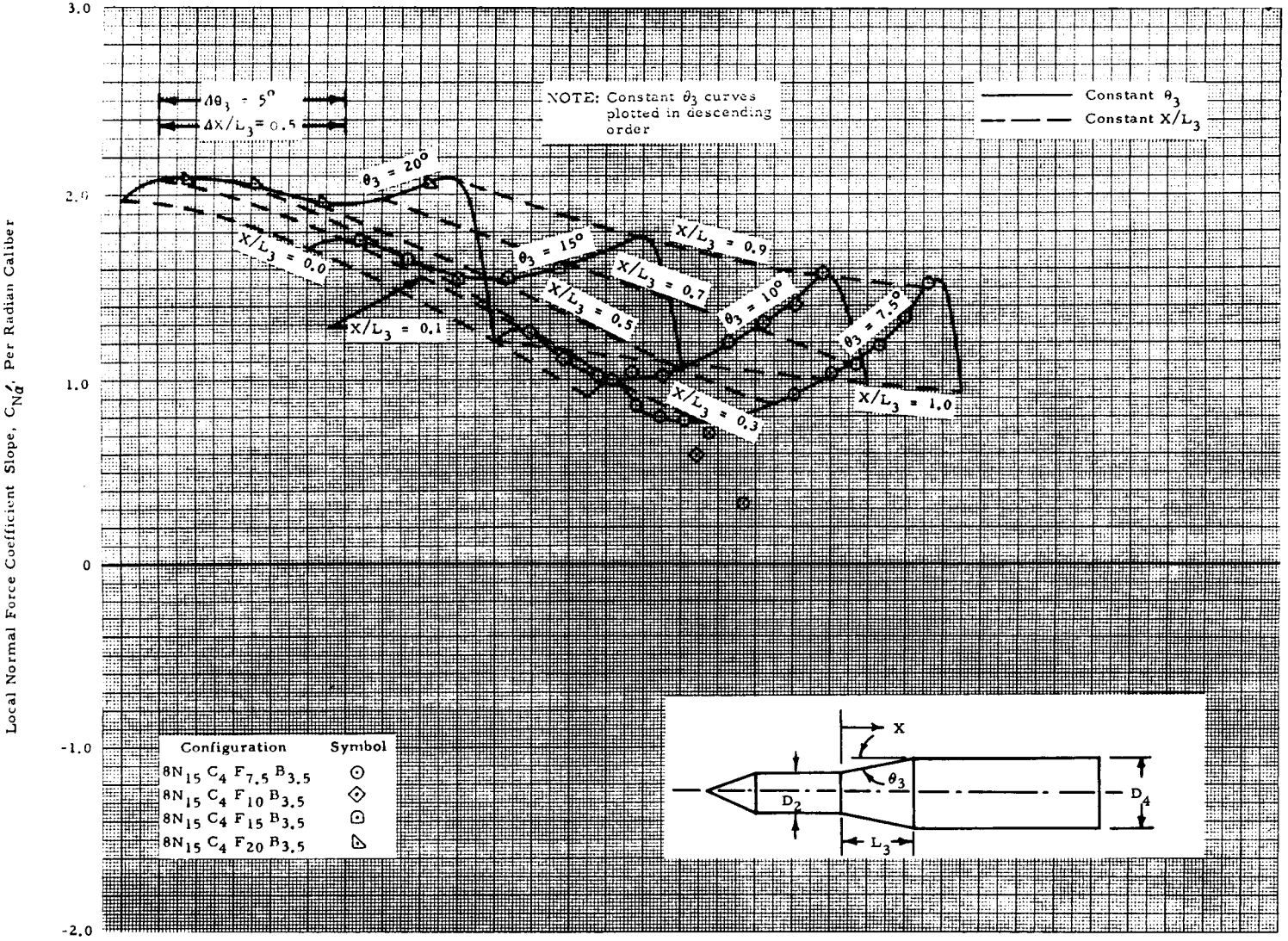

(4) M = 0.95

Figure 5c - The Effect of Frustum Angle on Local Normal Force Slope Distributions for Flares, D_2/D_4 = 0.8 (Cont'd).

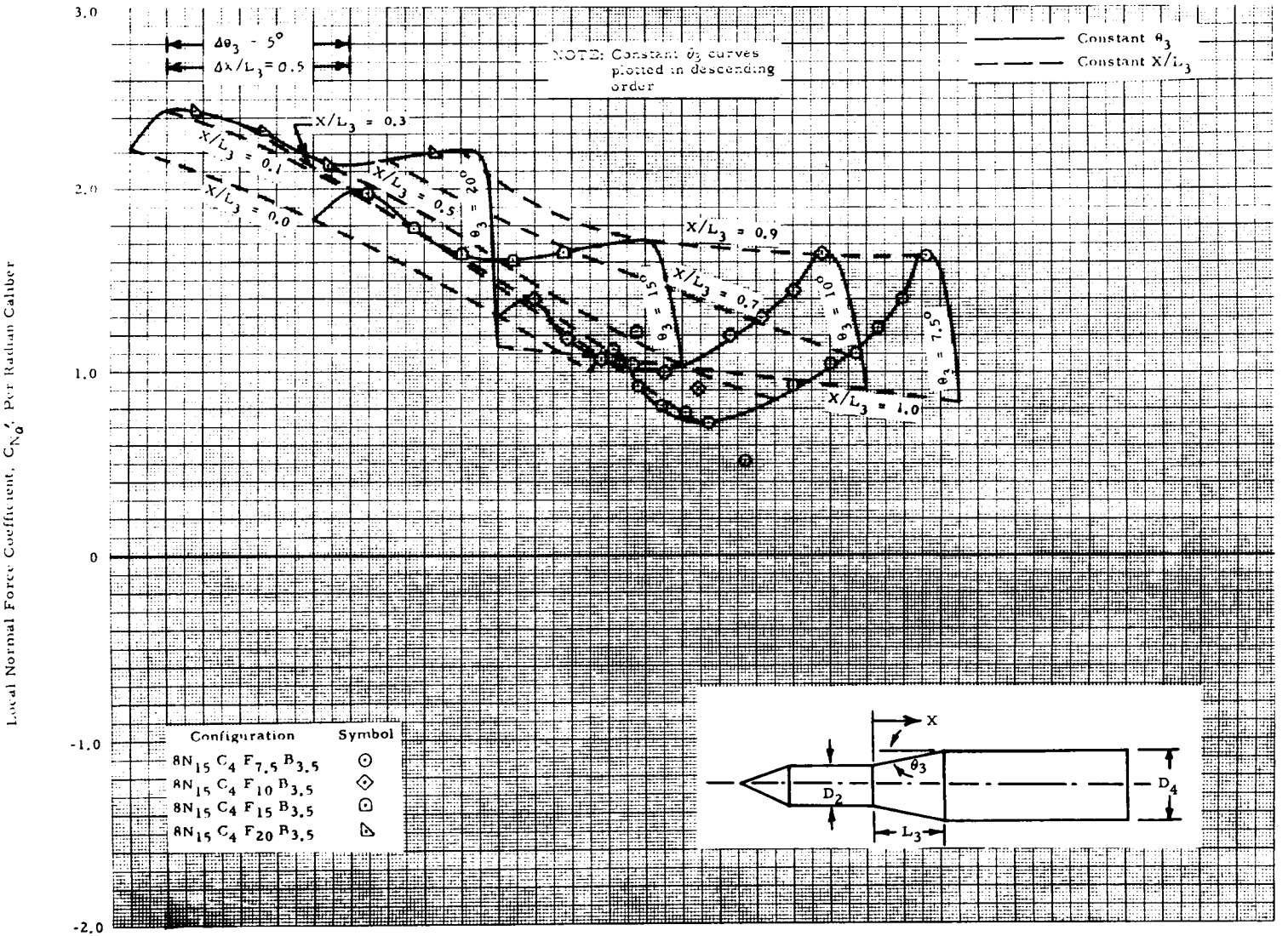

(5) M = 1.00

Figure 5c - The Effect of Frustum Angle on Local Normal Force Slope Distributions for Flares, D_2/D_4 = 0.8 (Cont'd)

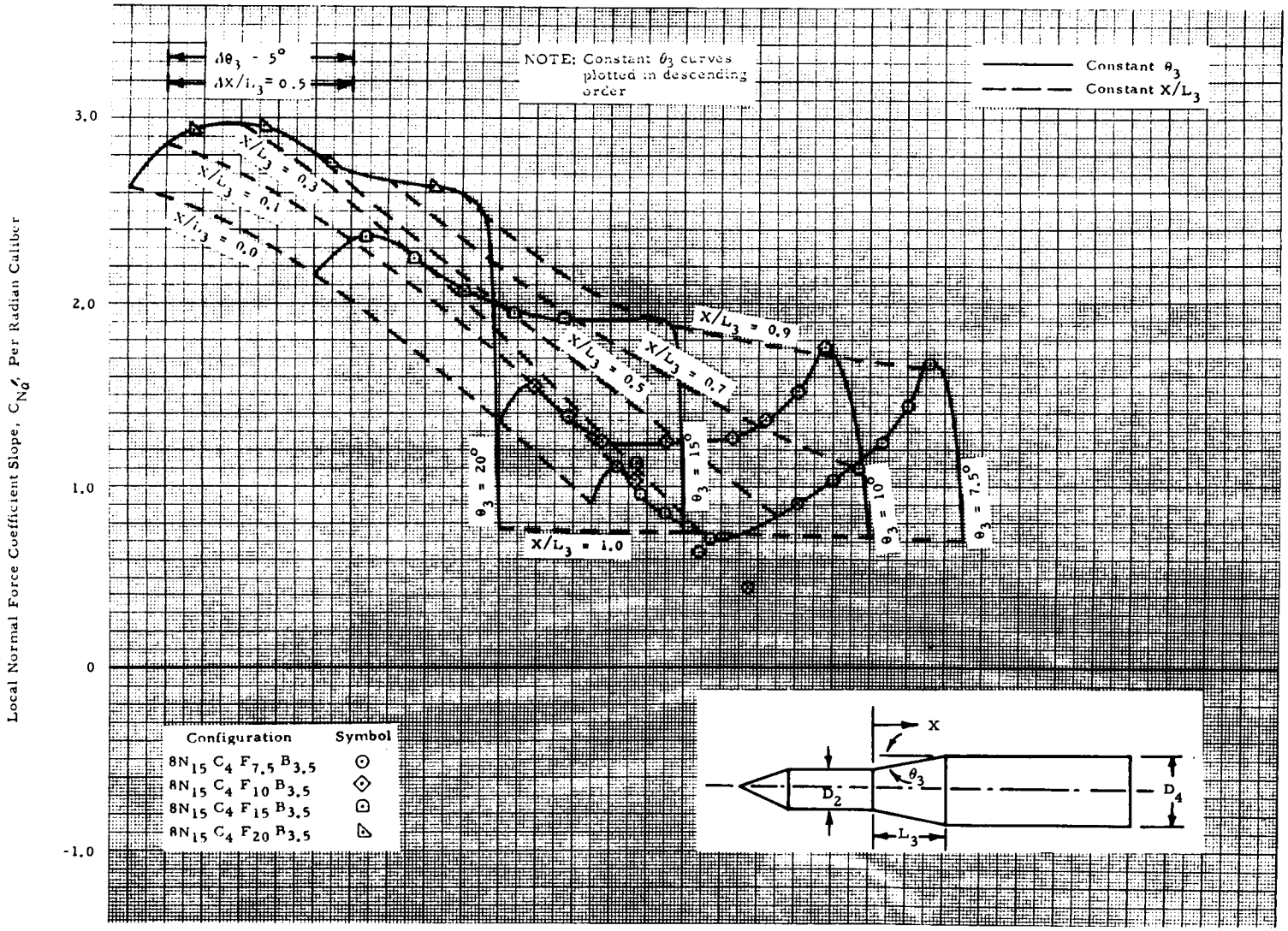

(6) M = 1.10

Figure 5c - The Effect of Frustum Angle on Local Normal Force Slope Distributions for Flares, D_2/D_4 = 0.8 (Cont'd)

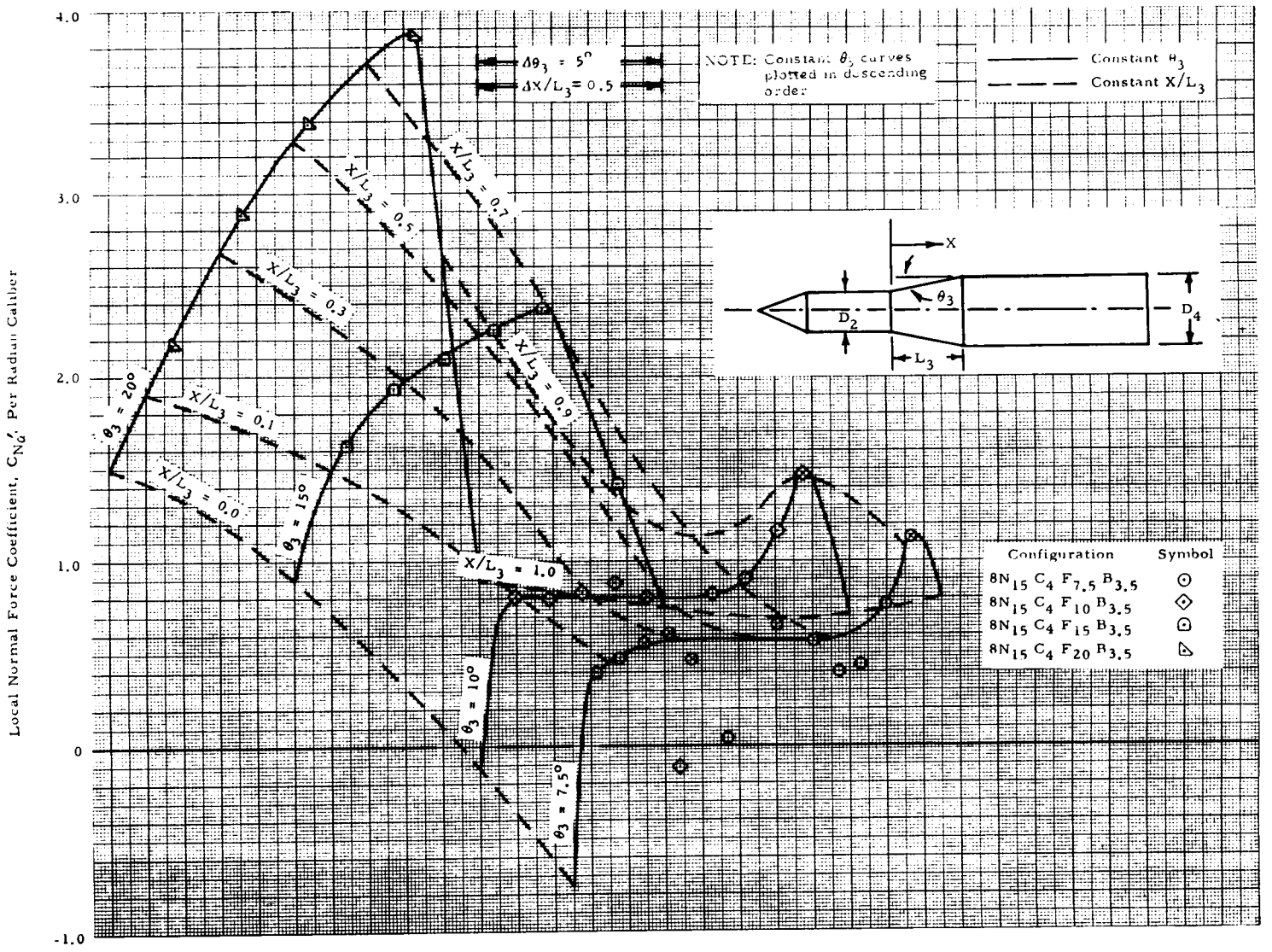

(7) M = 1.46

Figure 5c - The Effect of Frustum Angle on Local Normal Force Slope Distributions for Flares, $D_2/D_4 = 0.8$ (Cont'd)

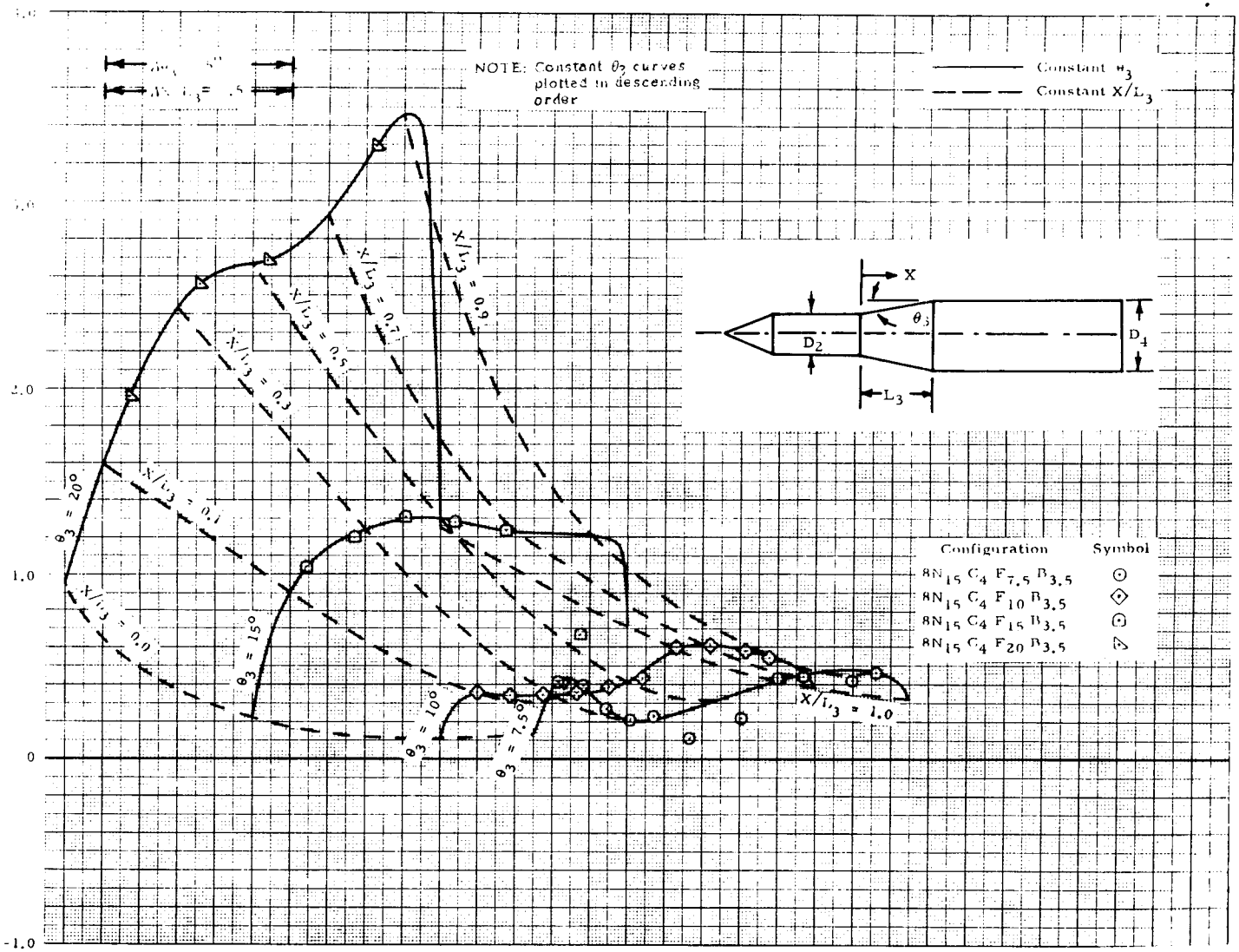

Local Normal Force Coefficient Slope, C_{N_α}' Per Radian, Cylinder

(8) M = 1.96

Figure 5c - The Effect of Frustum Angle on Local Normal Force Slope Slope Distributions for Flares, $D_2/D_4 = 0.8$ (Concluded)

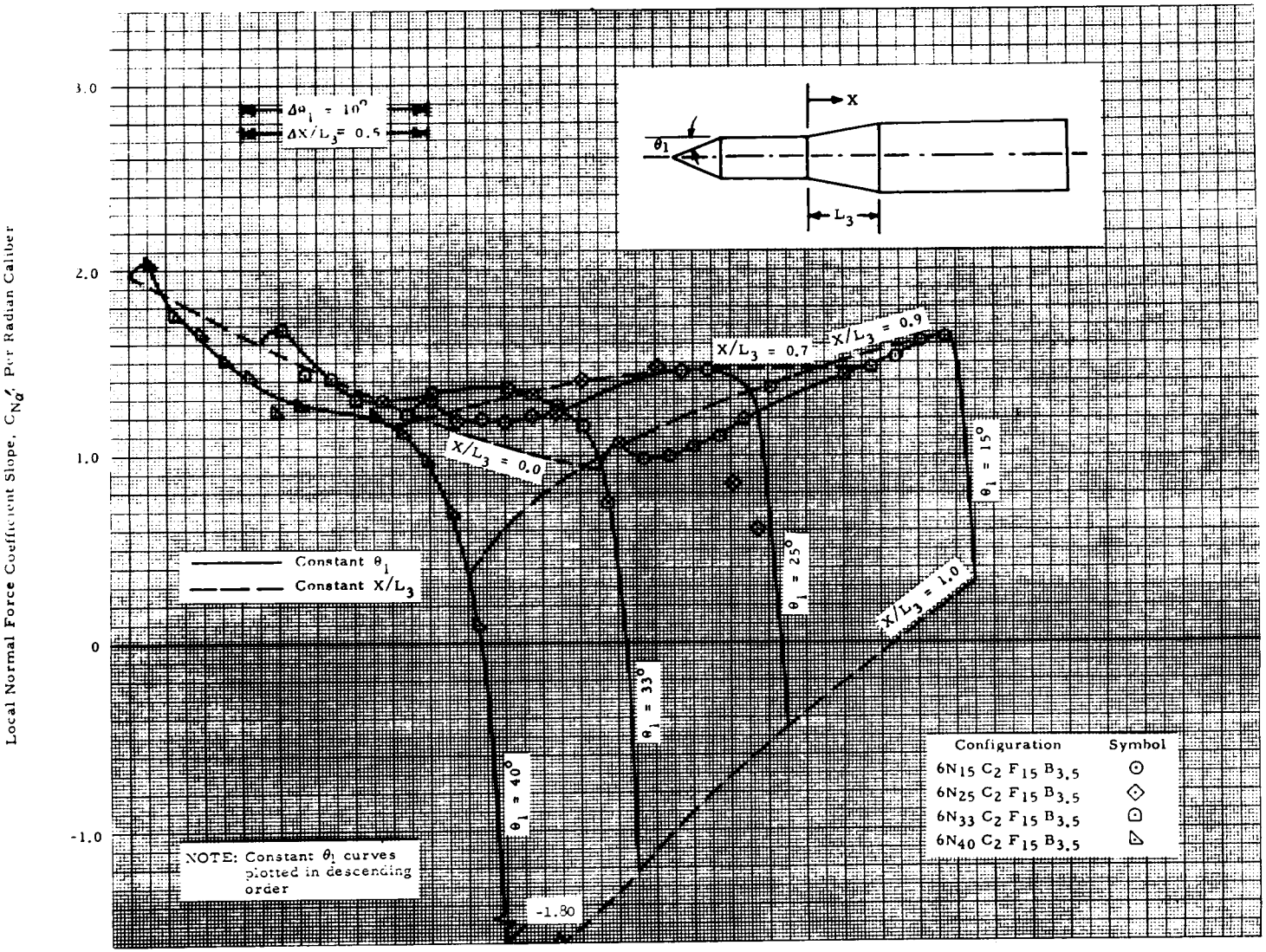

(a) M = 0.70

Figure 6 - The Effect of Cone Angle on Flare Local Normal Force Slope Distributions for Cone-Cylinder-Flare-Cylinders

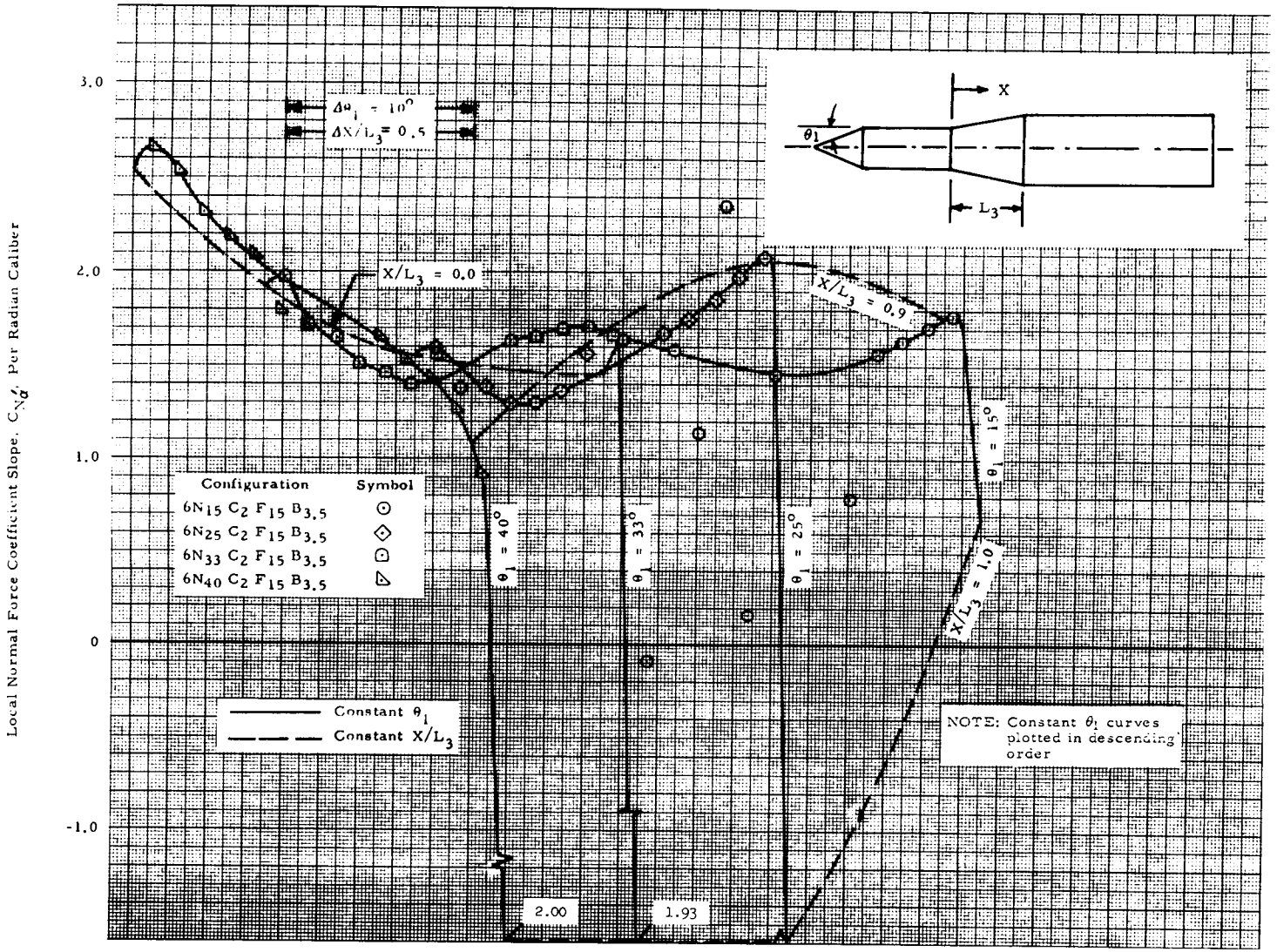

(b) M = 0.8

Figure 6 - The Effect of Cone Angle on Flare Local Normal Force Slope Distributions for Cone-Cylinder-Flare-Cylinders (Cont'd)

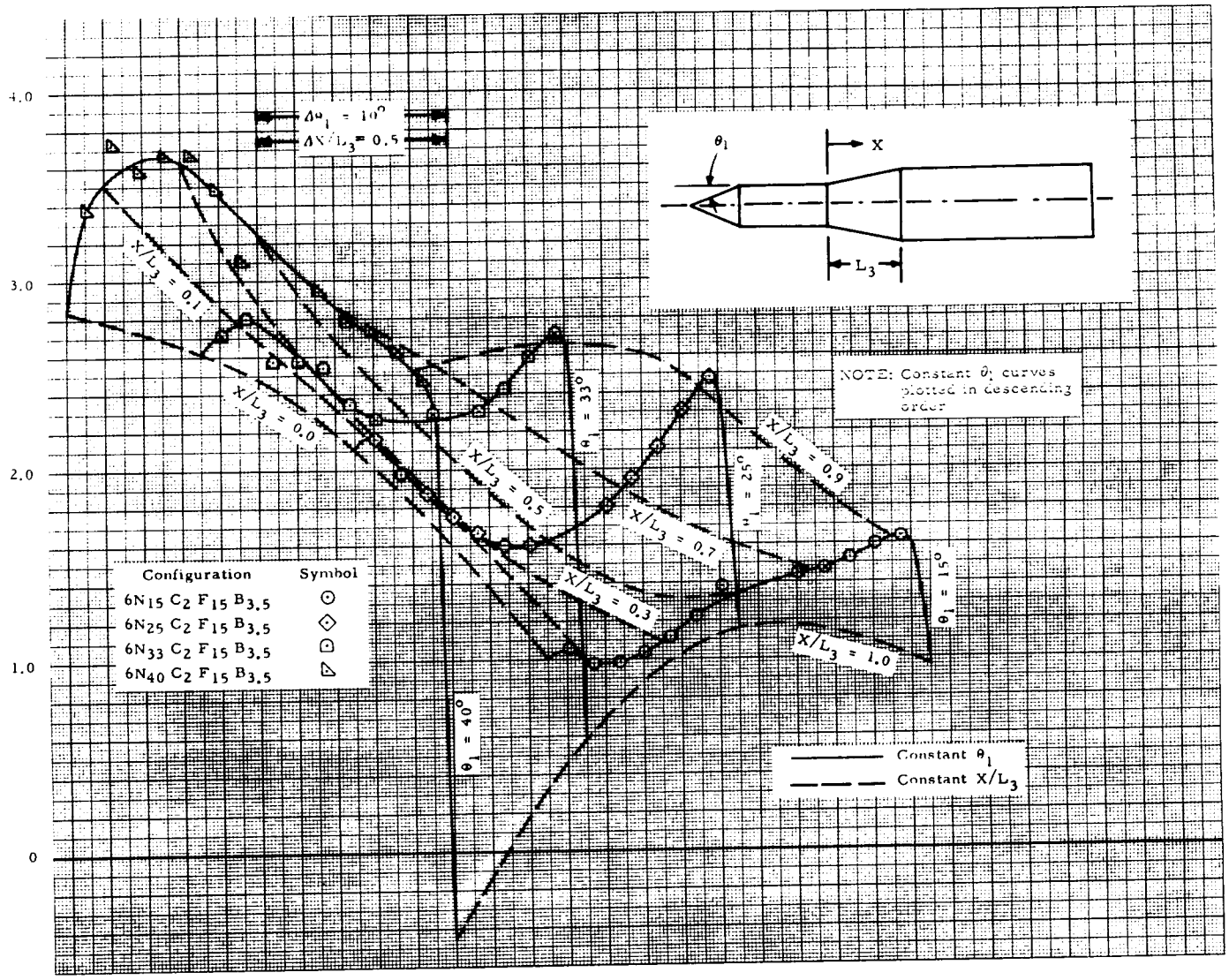

(c) M = 0.9

Figure 6 - The Effect of Cone Angle on Flare Local Normal Force Slope Distributions for Cone-Cylinder-Flare-Cylinders (Cont'd)

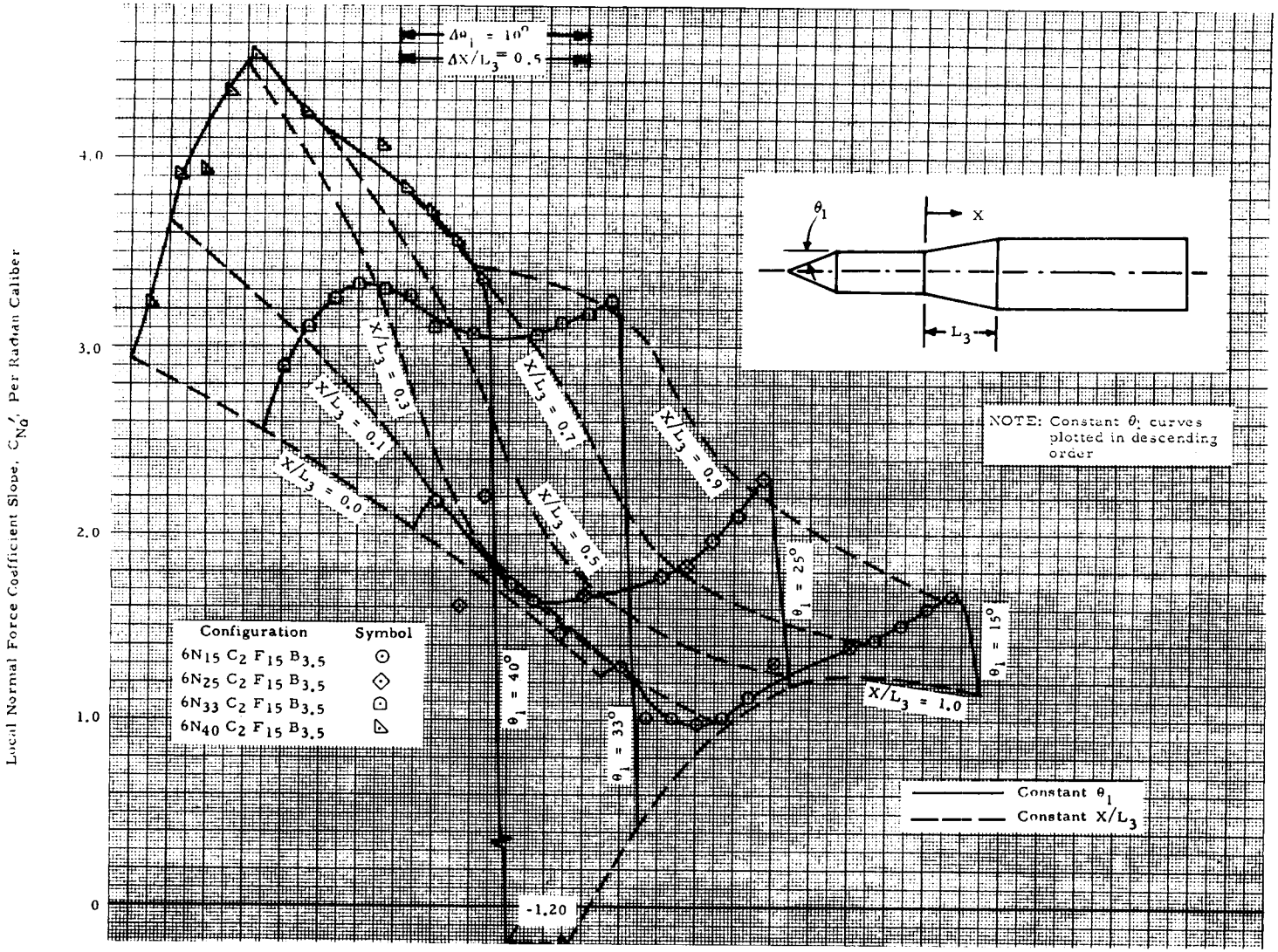

(d) M = 0.95

Figure 6 - The Effect of Cone Angle on Flare Local Normal Force Slope Distributions for Cone-Cylinder-Flare-Cylinders (Cont'd)

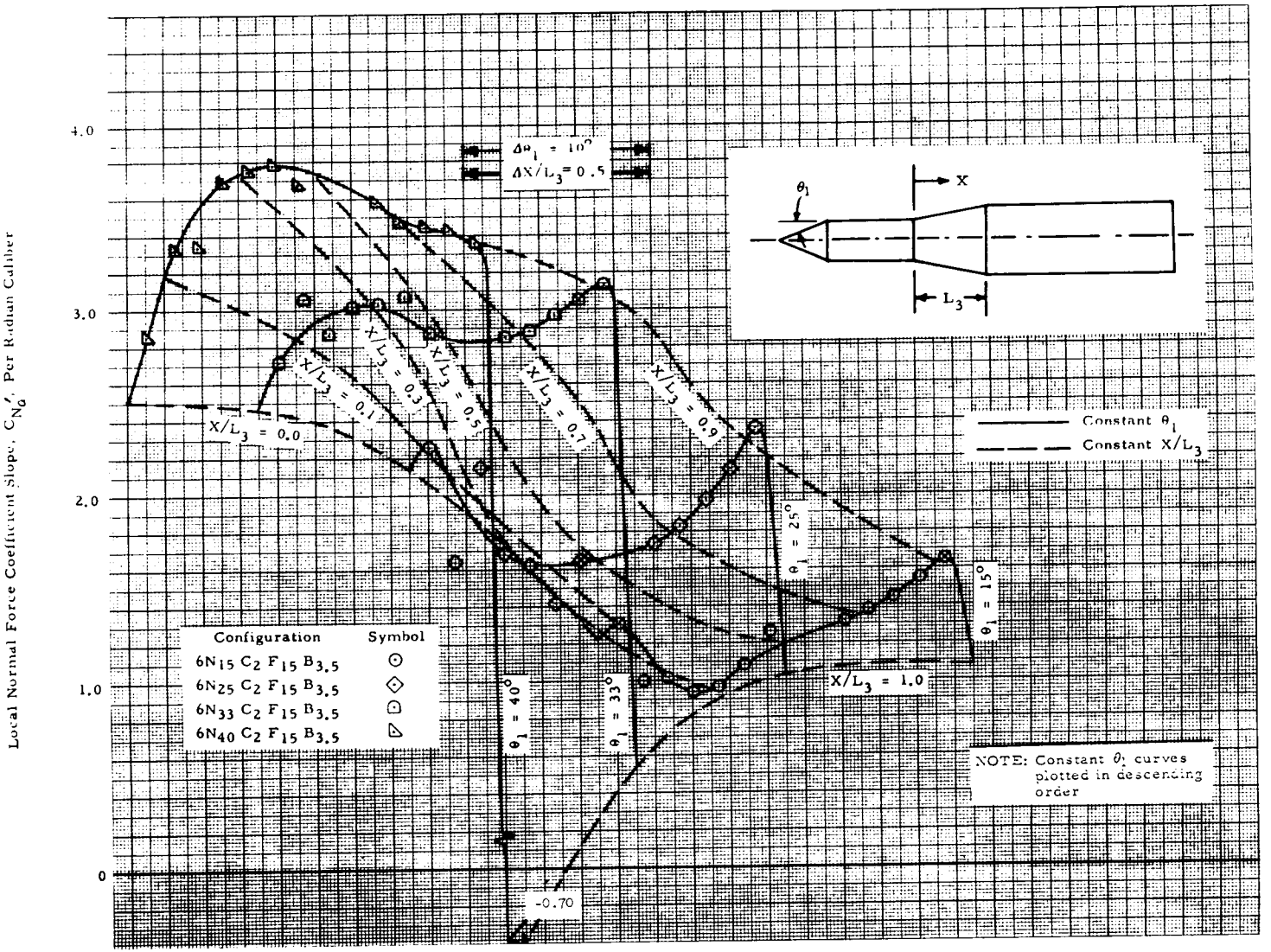

(e) M = 1.00

Figure 6 - The Effect of Cone Angle on Flare Local Normal Force Slope Distributions for Cone-Cylinder-Flare-Cylinders (Cont'd)

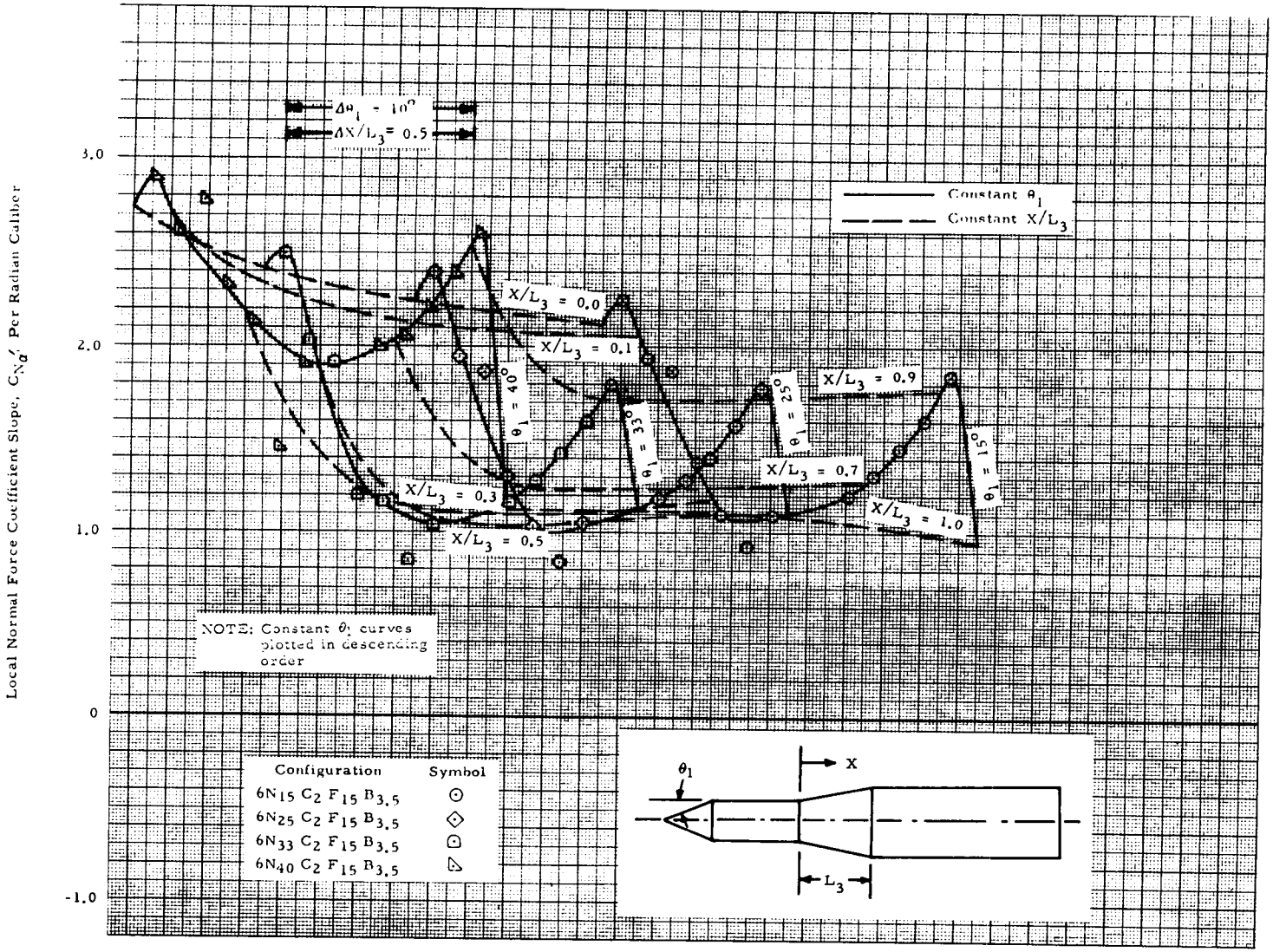

(f) M = 1.10

Figure 6 - The Effect of Cone Angle on Flare Local Normal Force Slope Distributions for Cone-Cylinder-Flare-Cylinders (Cont'd)

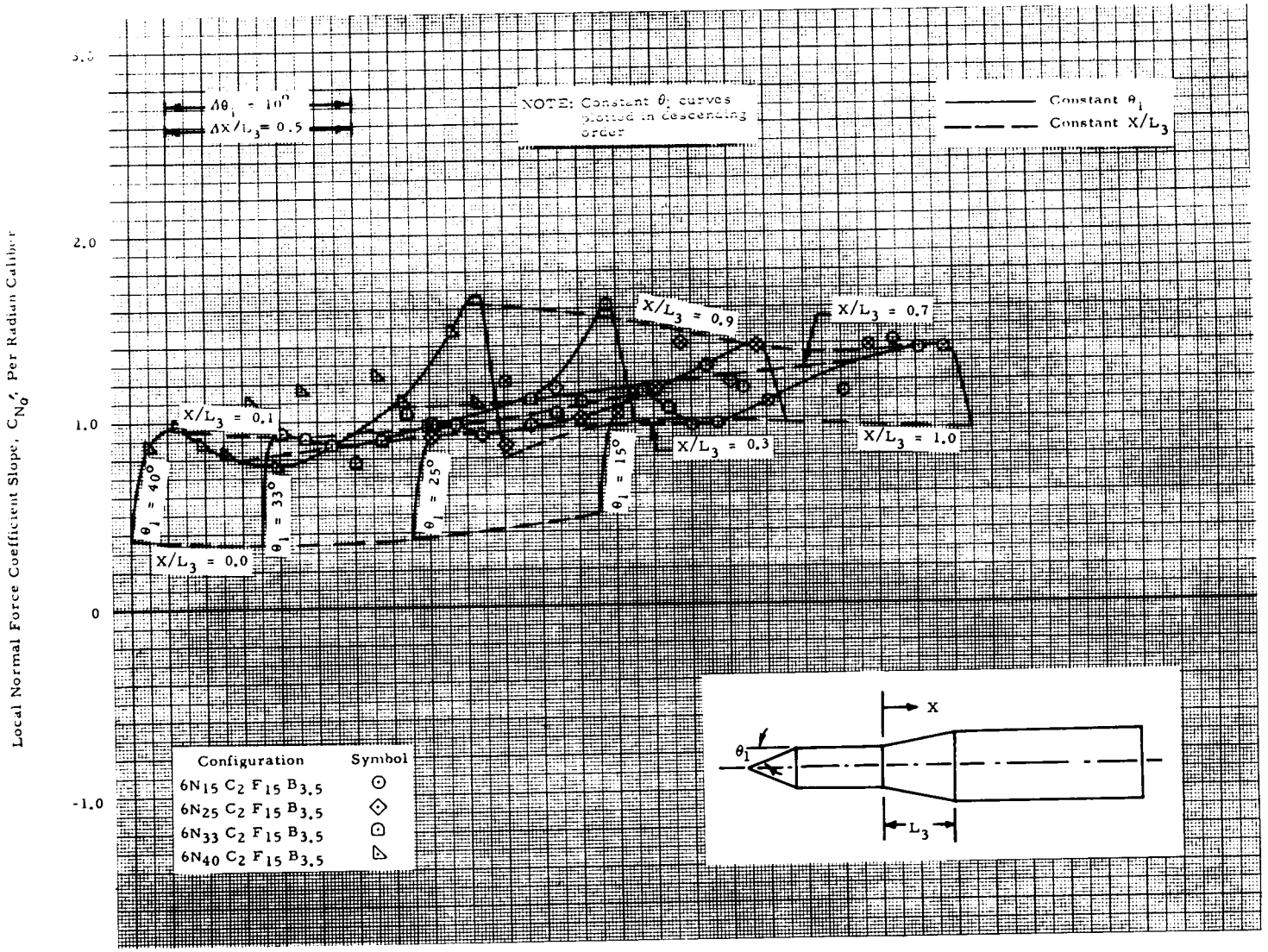

(g) M = 1.46

Figure 6 - The Effect of Cone Angle on Flare Local Normal Force Slope Distributions for Cone-Cylinder-Flare-Cylinders (Cont'd)

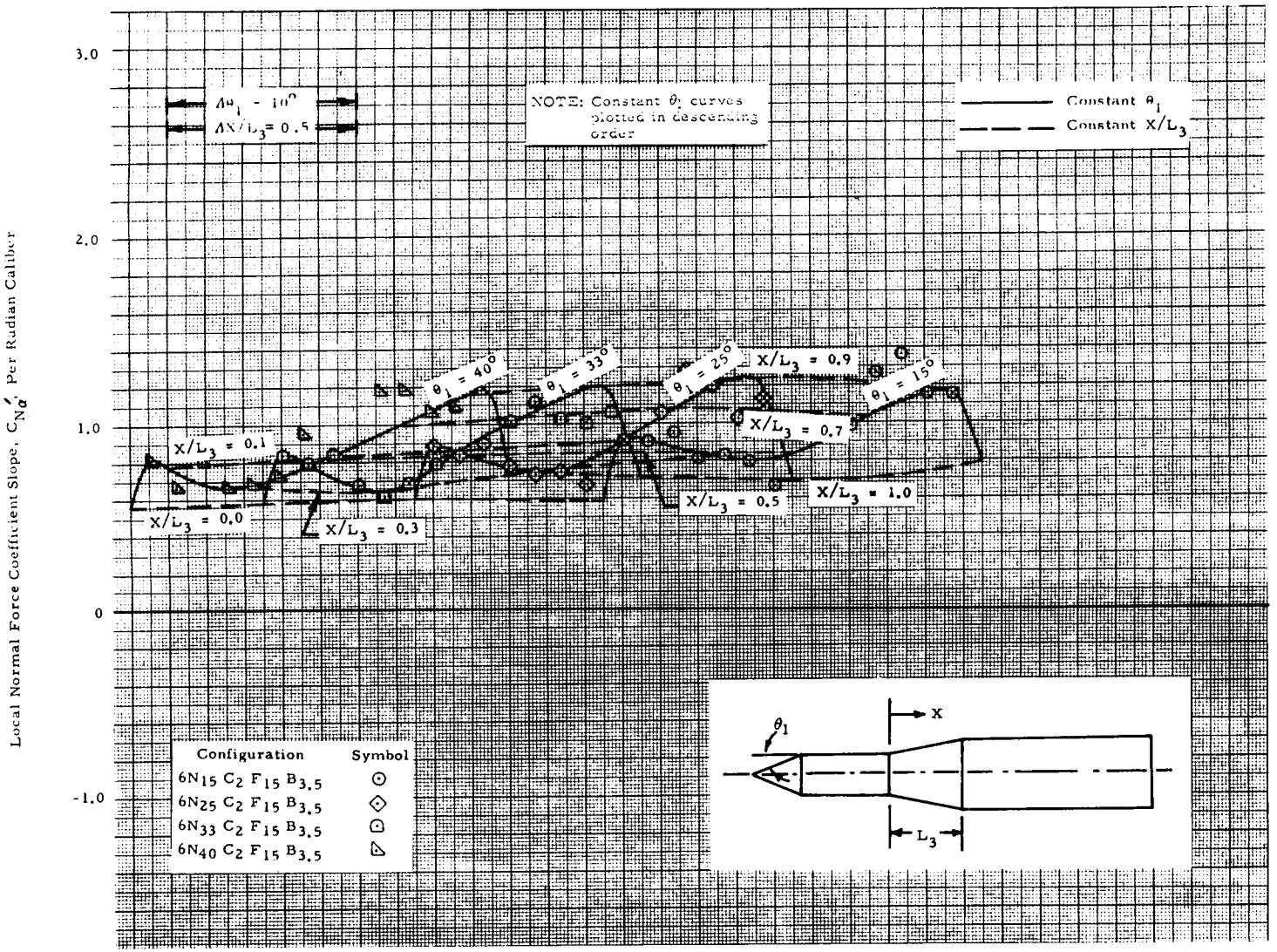

(h) M = 1.96

Figure 6 - The Effect of Cone Angle on Flare Local Normal Force Slope Distributions for Cone-Cylinder-Flare-Cylinders (Concluded)

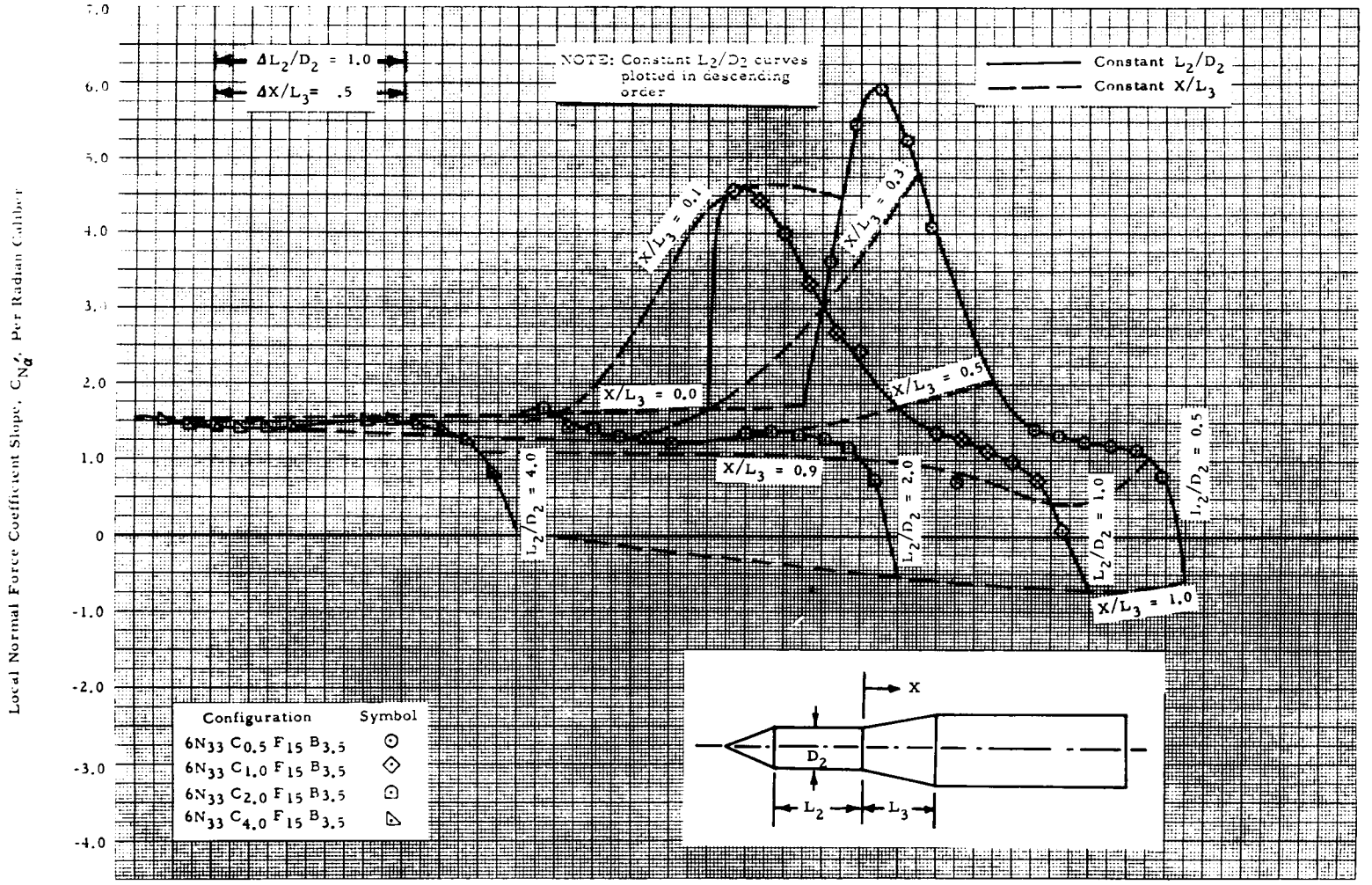

(a) M = 0.70

Figure 7 - The Effect of Forward Cylinder Length on Flare Local Normal Force Slope Distributions for Cone-Cylinder-Flare-Cylinders

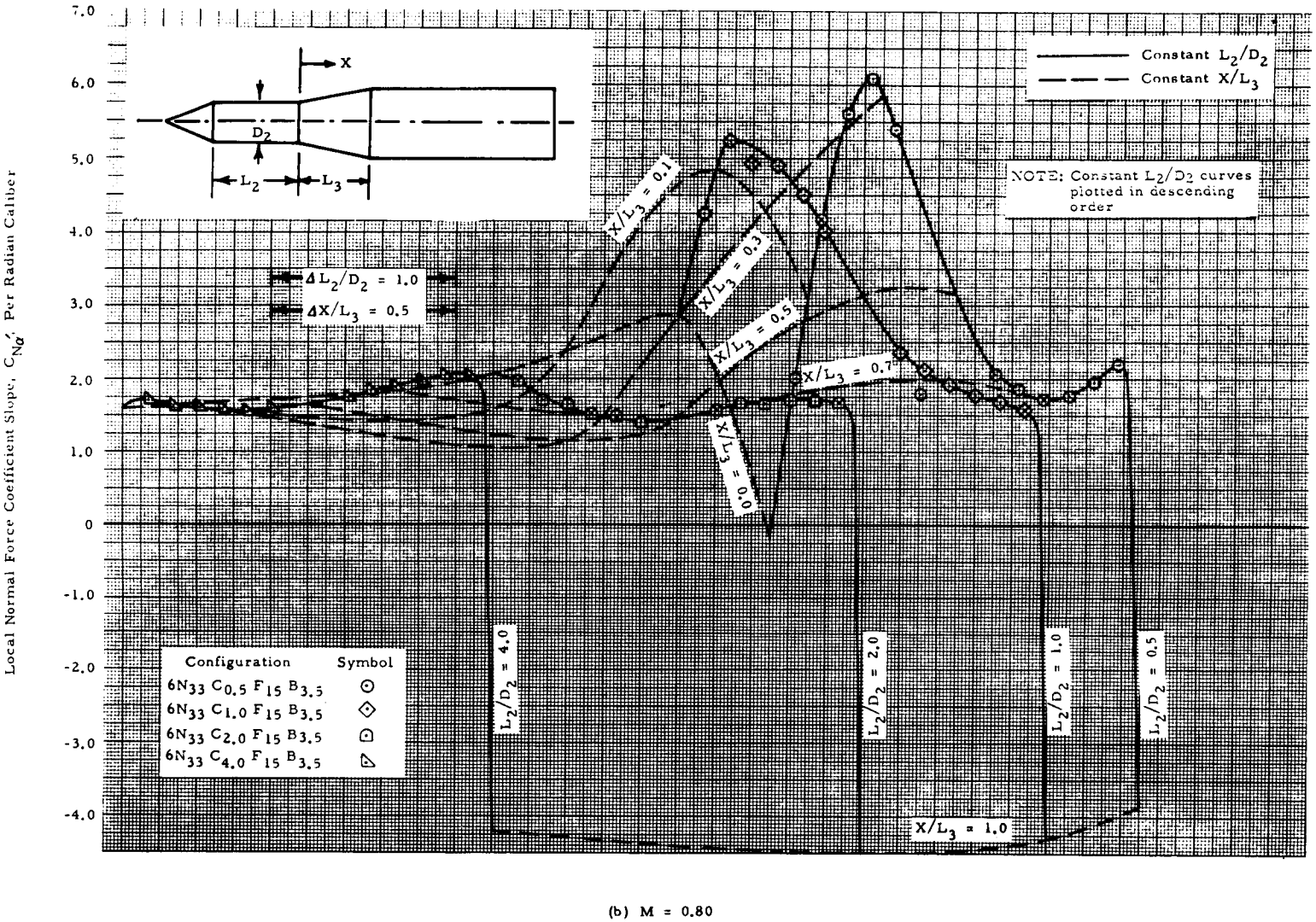

(b) M = 0.80

Figure 7 - The Effect of Forward Cylinder Length on Flare Local Normal Force Slope Distributions for Cone-Cylinder-Flare-Cylinders (Cont'd)

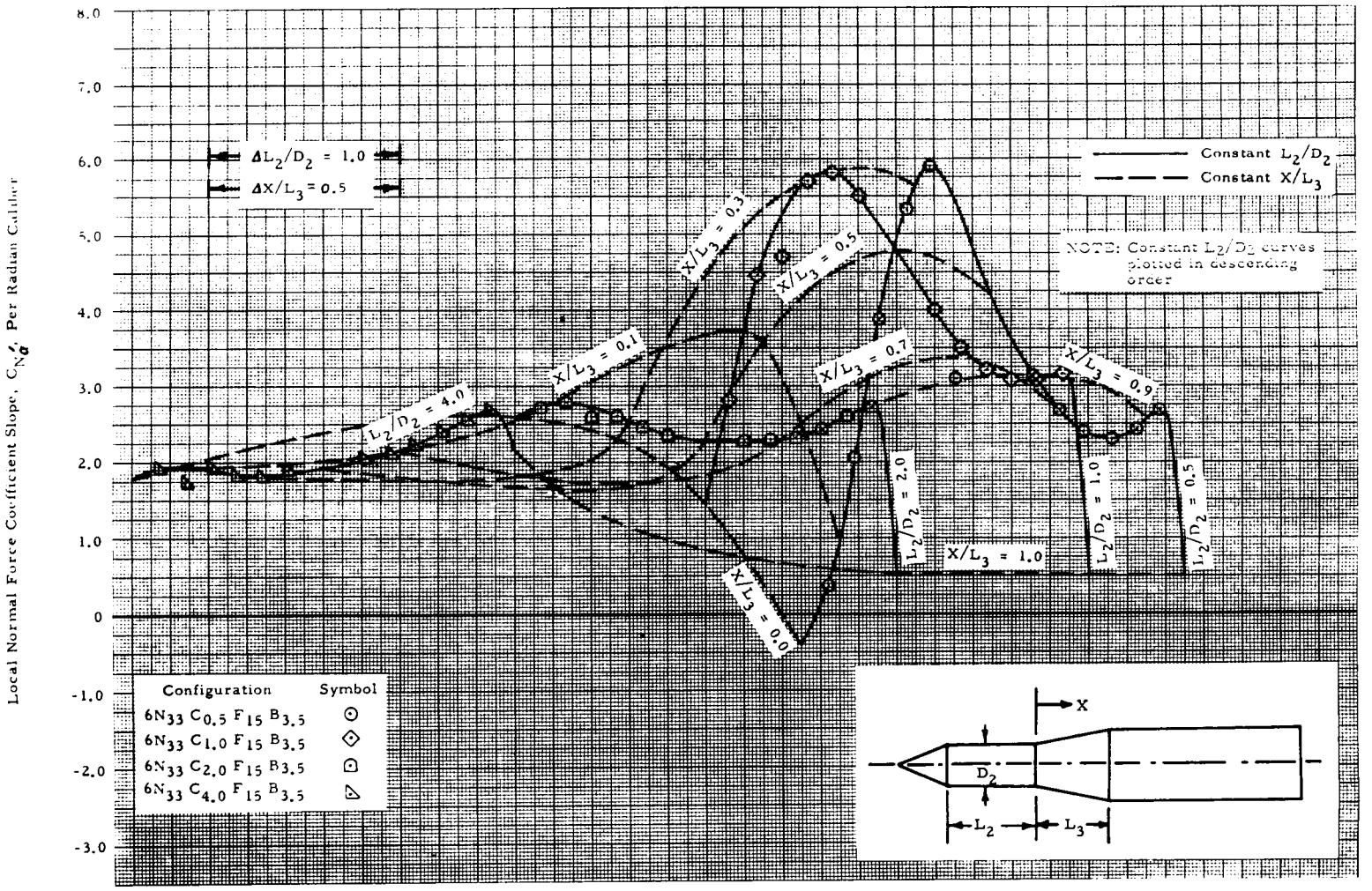

(c) M = 0.90

Figure 7 - The Effect of Forward Cylinder Length on Flare Local Normal Force Slope Distributions for Cone-Cylinder-Flare-Cylinders (Cont'd)

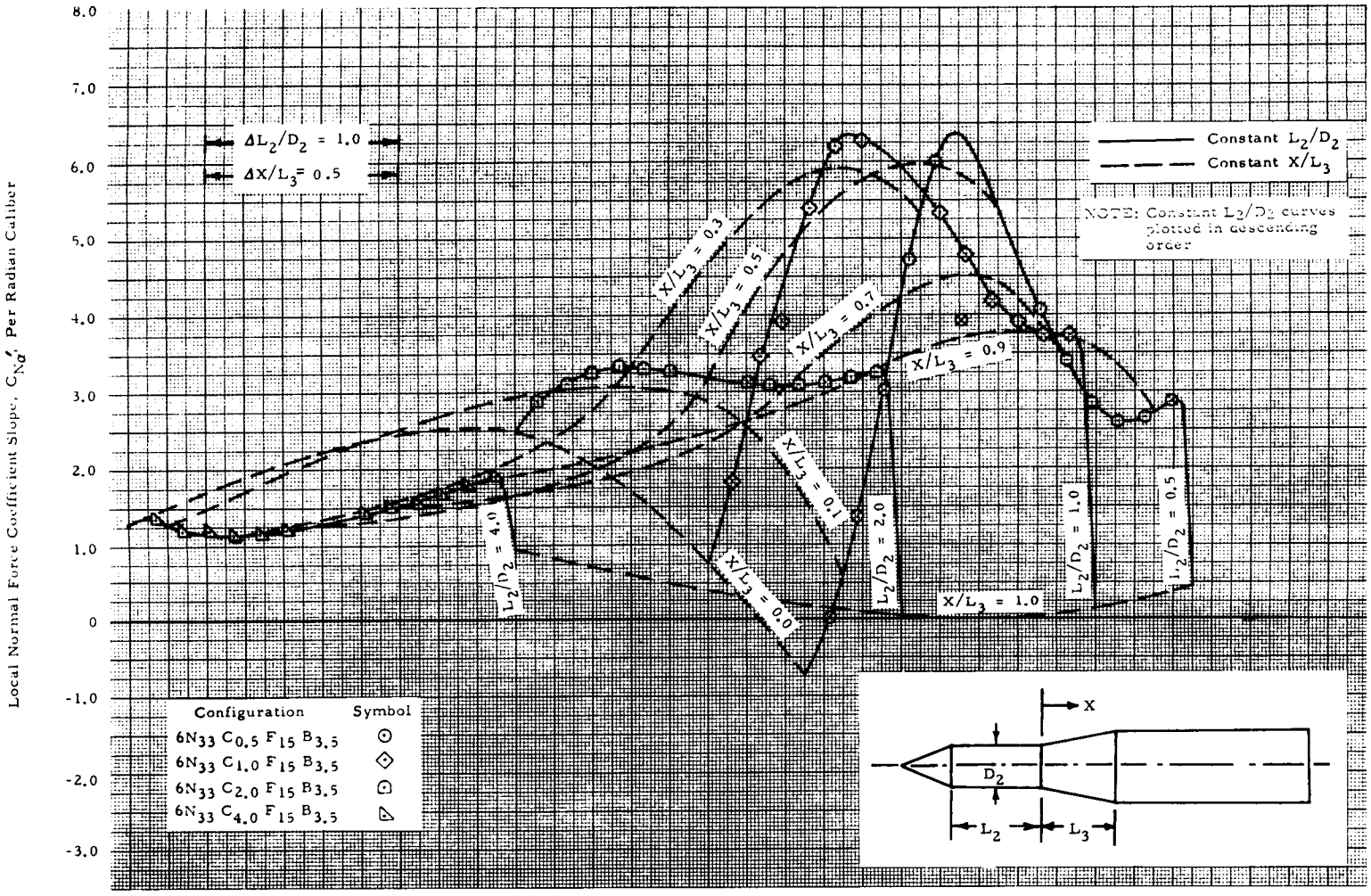

(d) M = 0.95

Figure 7 - The Effect of Forward Cylinder Length on Flare Local Normal Force Slope Distributions for Cone-Cylinder-Flare-Cylinder (Cont'd)

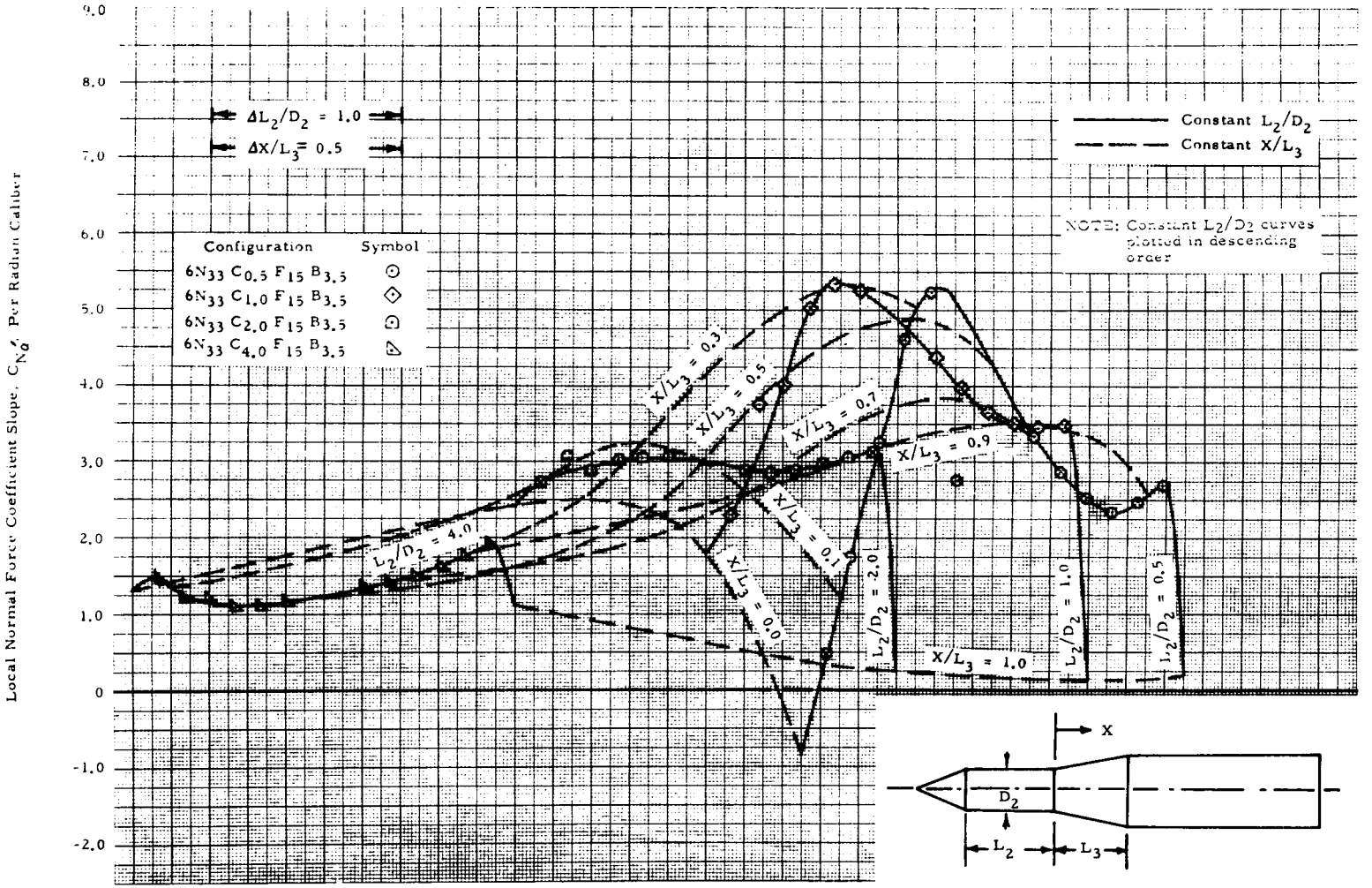

(e) M = 1.00

Figure 7 - The Effect of Forward Cylinder Length on Flare Local Normal Force Slope Distributions for Cone-Cylinder-Flare-Cylinders (Cont'd)

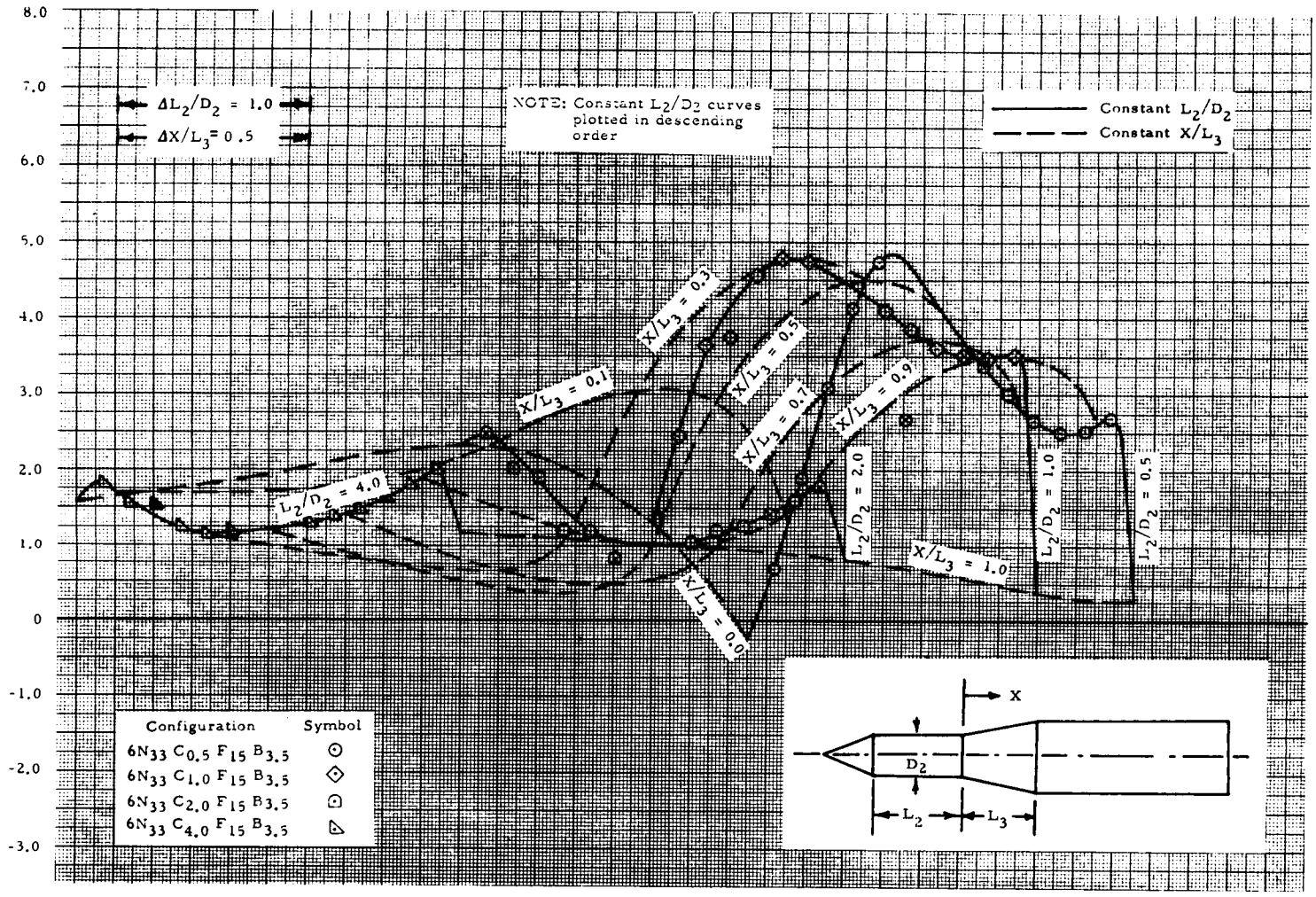

(f) M = 1.10

Figure 7 - The Effect of Forward Cylinder Length on Flare Local Normal Force Slope Distributions for Cone-Cylinder-Flare-Cylinders (Cont'd)

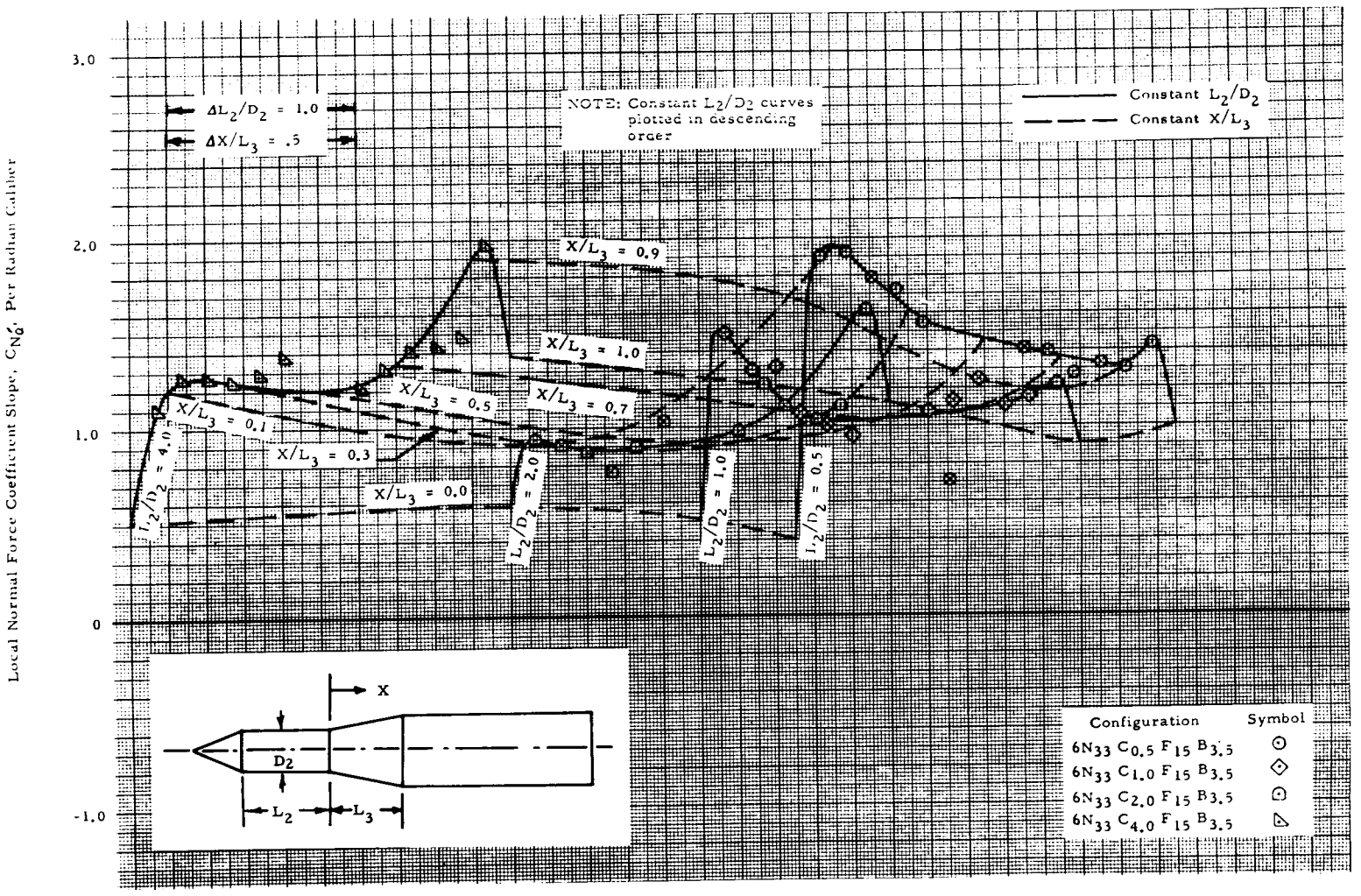

(g) M = 1.46

Figure 7 - The Effect of Forward Cylinder Length on Flare Local Normal Force Slope Distributions for Cone-Cylinder-Flare-Cylinders (Cont'd)

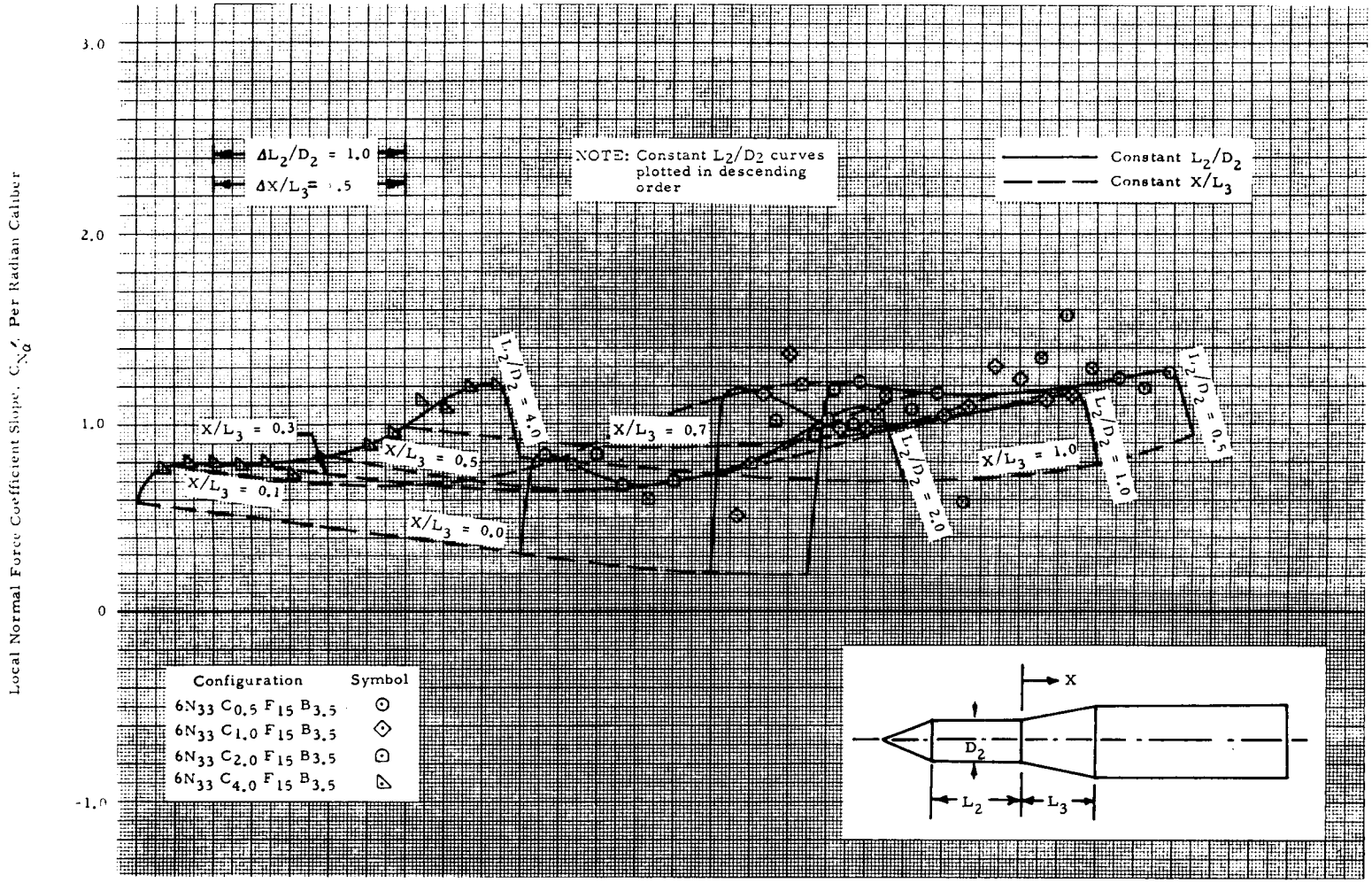

(h) M = 1.96

Figure 7 - The Effect of Forward Cylinder Length on Flare Local Normal Force Slope Distributions for Cone-Cylinder-Flare-Cylinders (Concluded)

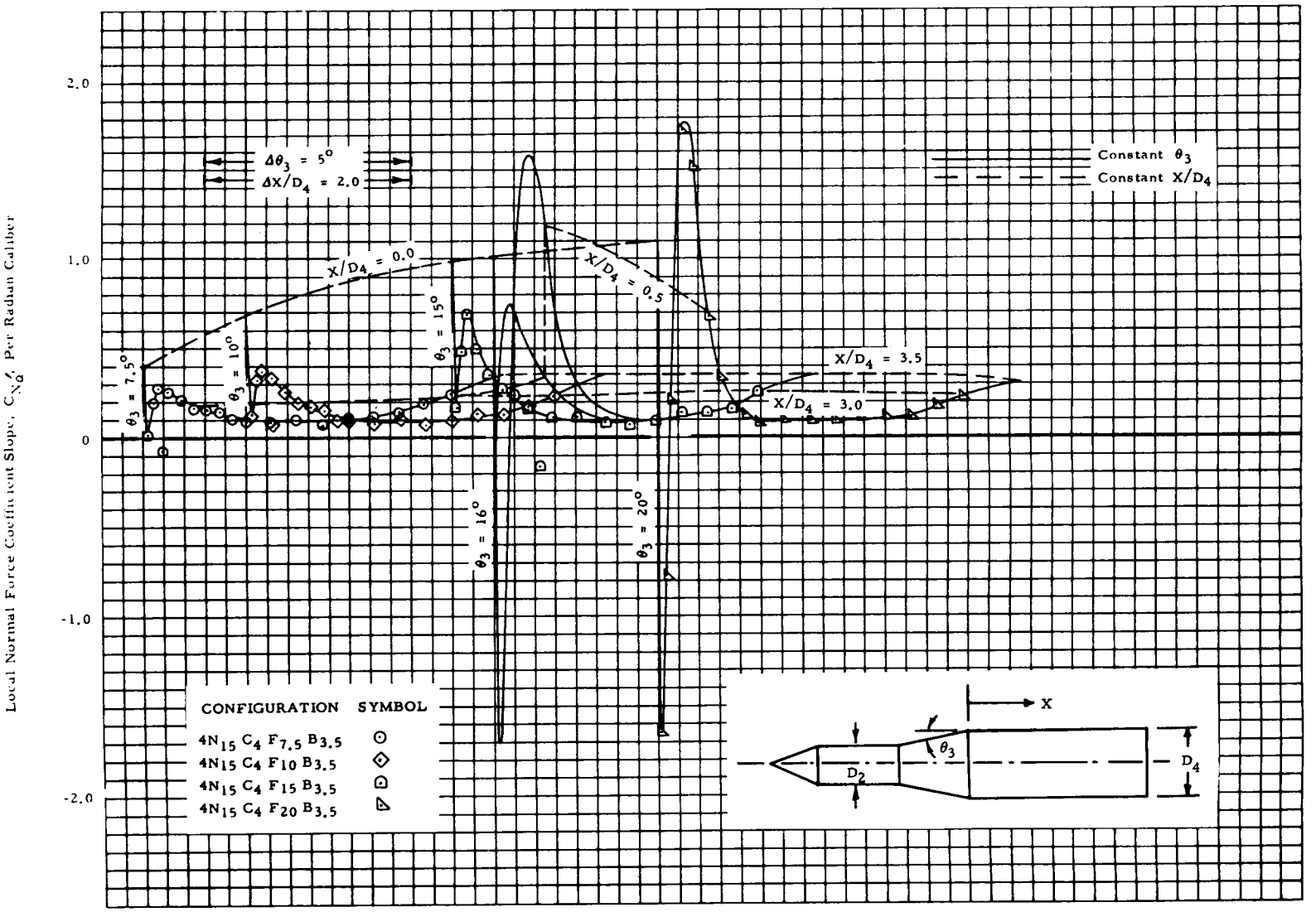

(1) M = 0.7

Figure 8a - The Effect of Flare Angle on Aft Cylinder Local Normal Force Slope Distributions for Cone-Cylinder-Flare-Cylinders, $D_2/D_4 = 0.4$

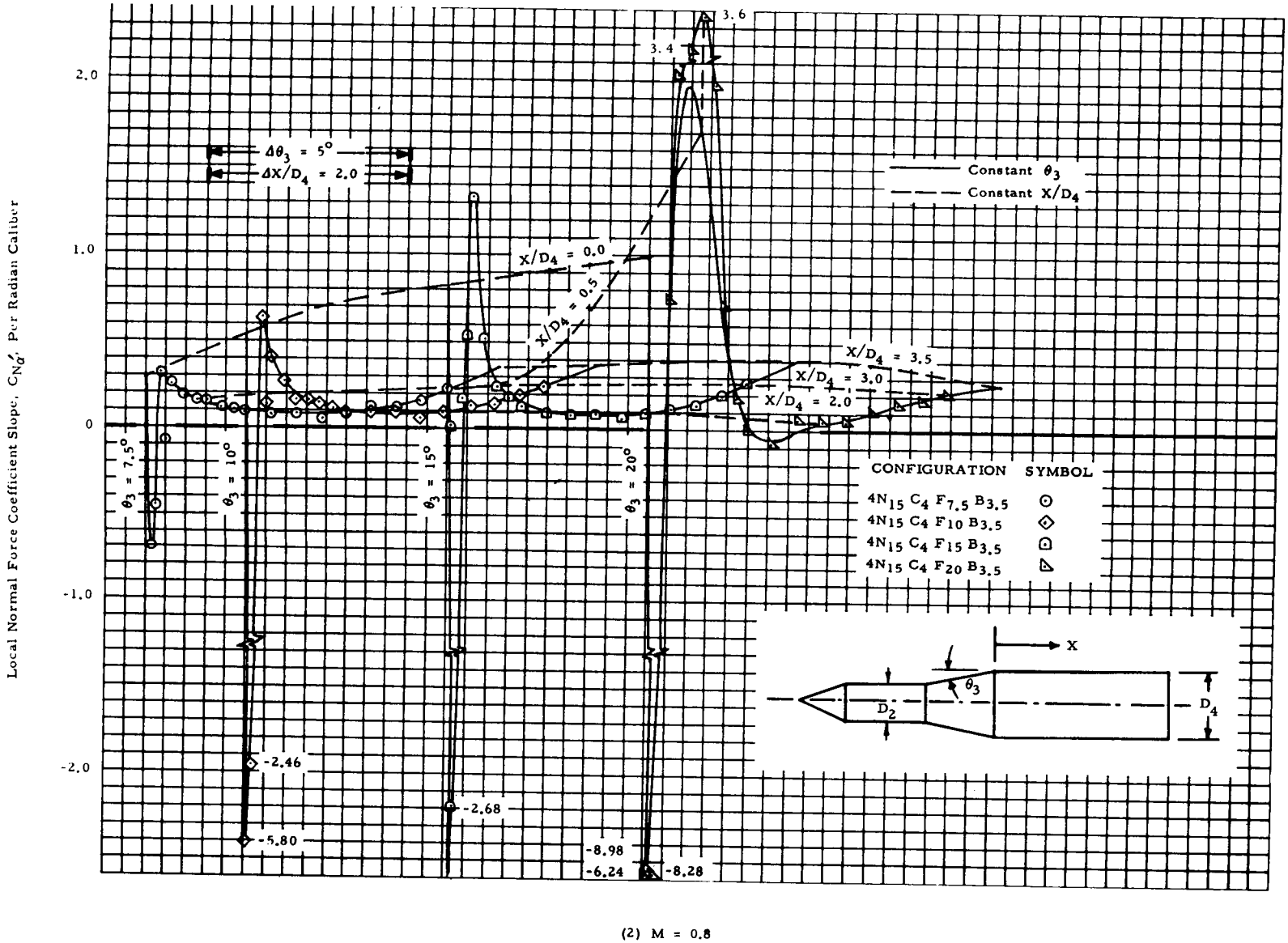

(2) M = 0.8

Figure 8a - The Effect of Flare Angle on Aft Cylinder Local Normal Force Slope Distributions for Cone-Cylinder-Flare-Cylinders, D_2/D_4 = 0.4 (Cont'd)

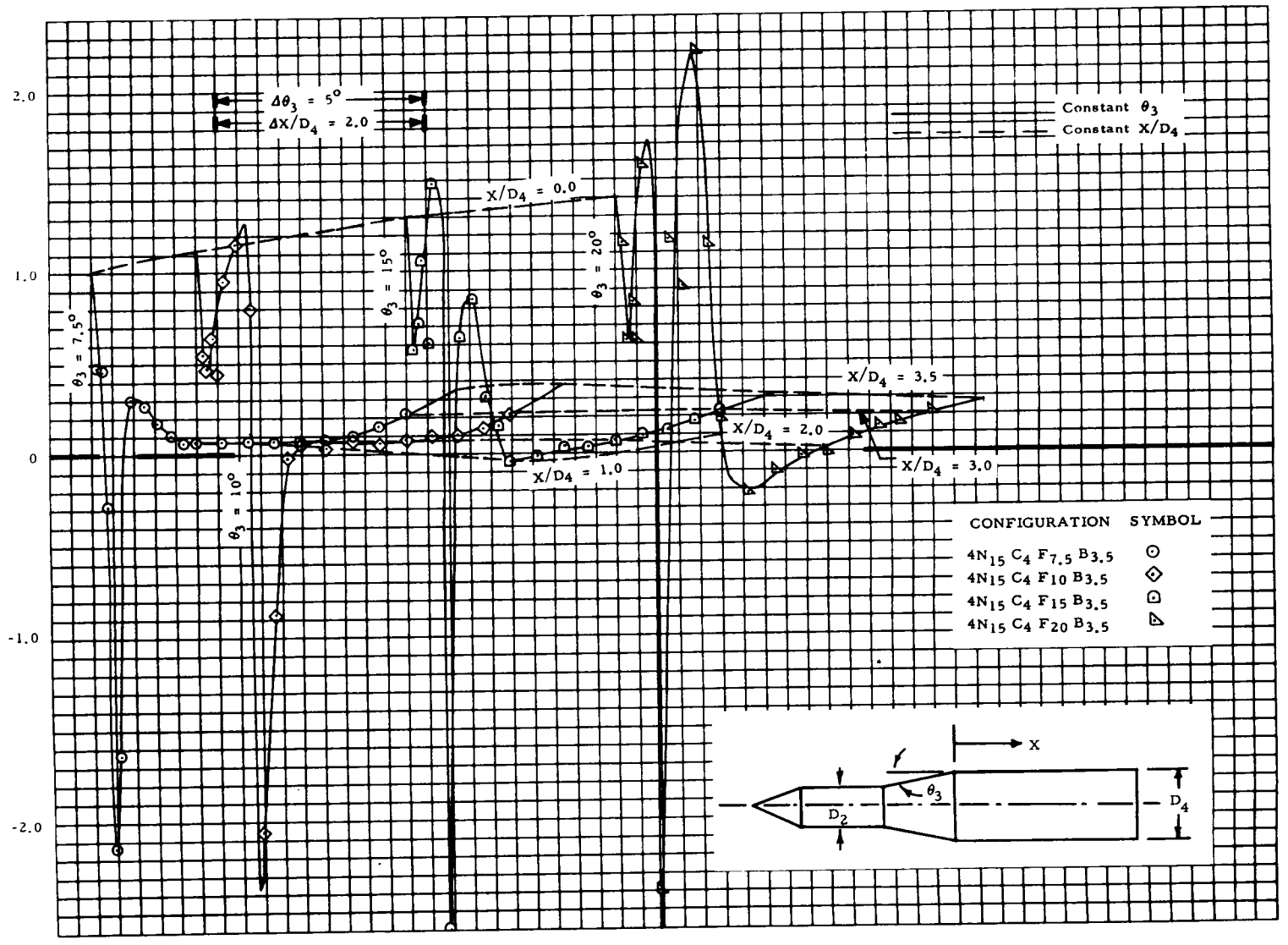

(3) M = 0.9

Figure 8a - The Effect of Flare Angle on Aft Cylinder Local Normal Force Slope Distributions for Cone-Cylinder-Flare-Cylinders, $D_2/D_4 = 0.4$ (Cont'd)

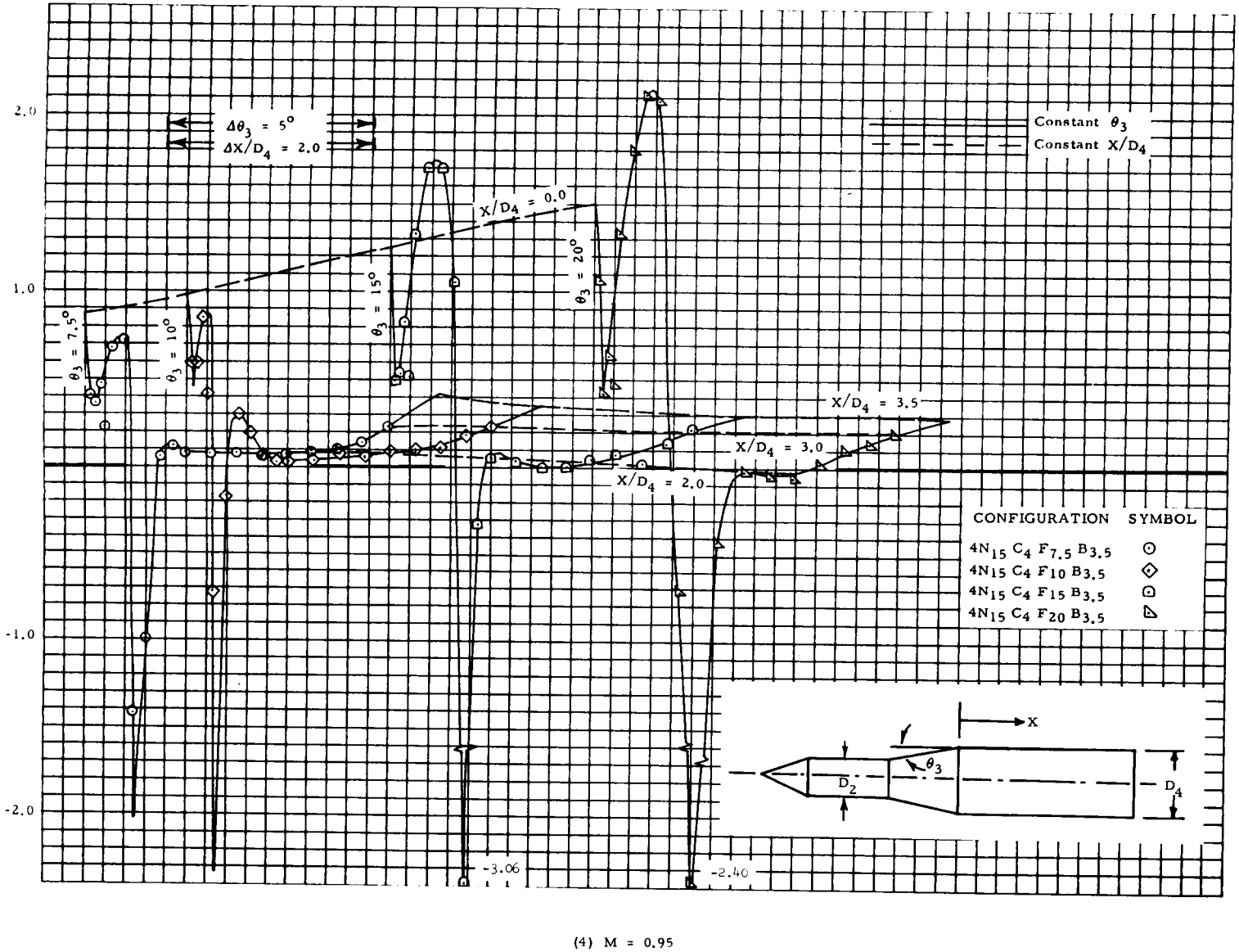

(4) M = 0.95

Figure 8a - The Effect of Flare Angle on Aft Cylinder Local Normal Force Slope Distributions for Cone-Cylinder-Flare-Cylinders, $D_2/D_4 = 0.4$ (Cont'd)

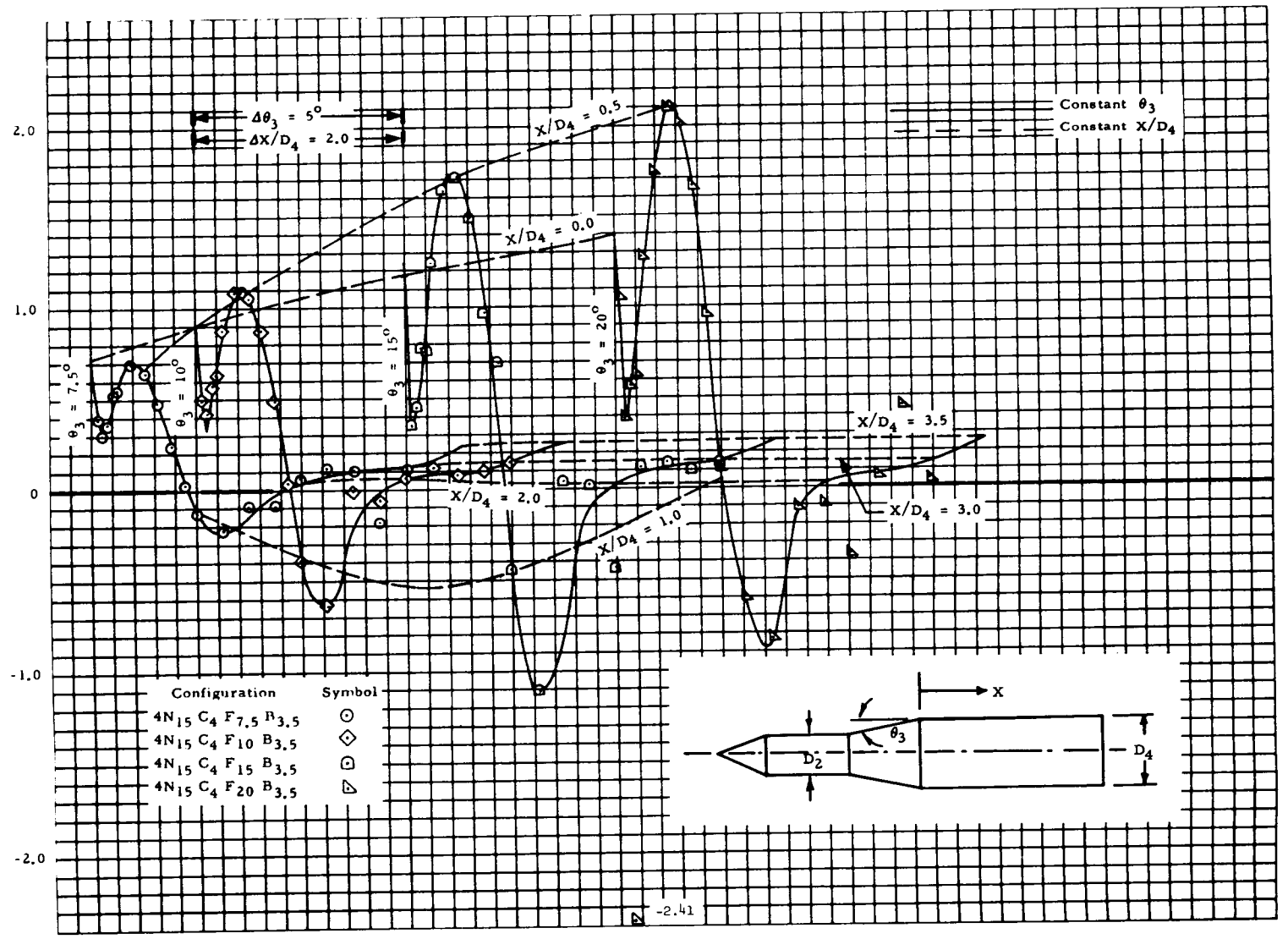

(5) M = 1.0

Figure 8a - The Effect of Flare Angle on Aft Cylinder Local Normal Force Slope Distributions for Cone-Cylinder-Flare-Cylinders, $D_2/D_4 = 0.4$ (Cont'd)

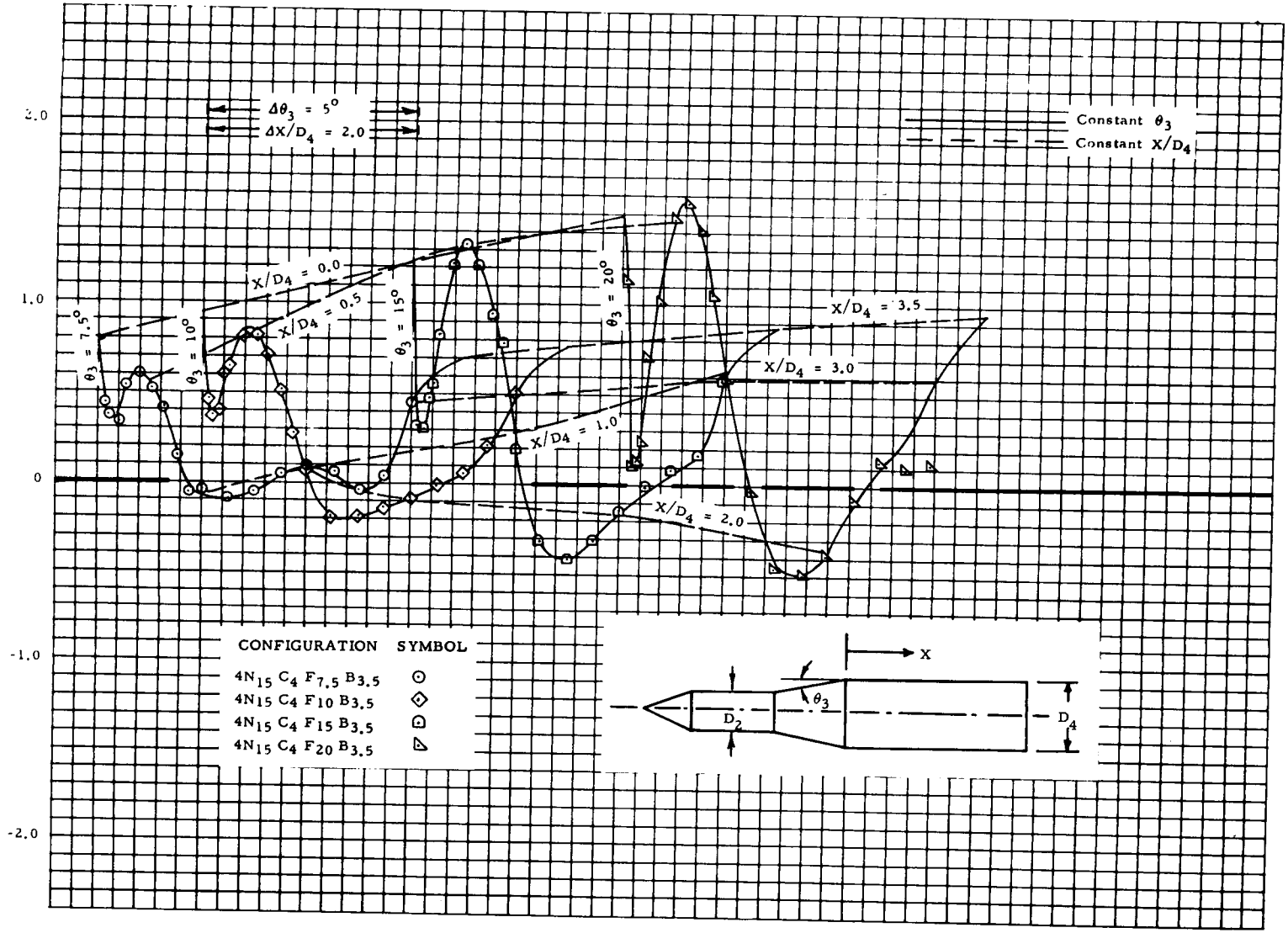

(6) M = 1.1

Figure 8a - The Effect of Flare Angle on Aft Cylinder Local Normal Force Slope Distributions for Cone-Cylinder-Flare-Cylinders, $D_2/D_4 = 0.4$ (Cont'd)

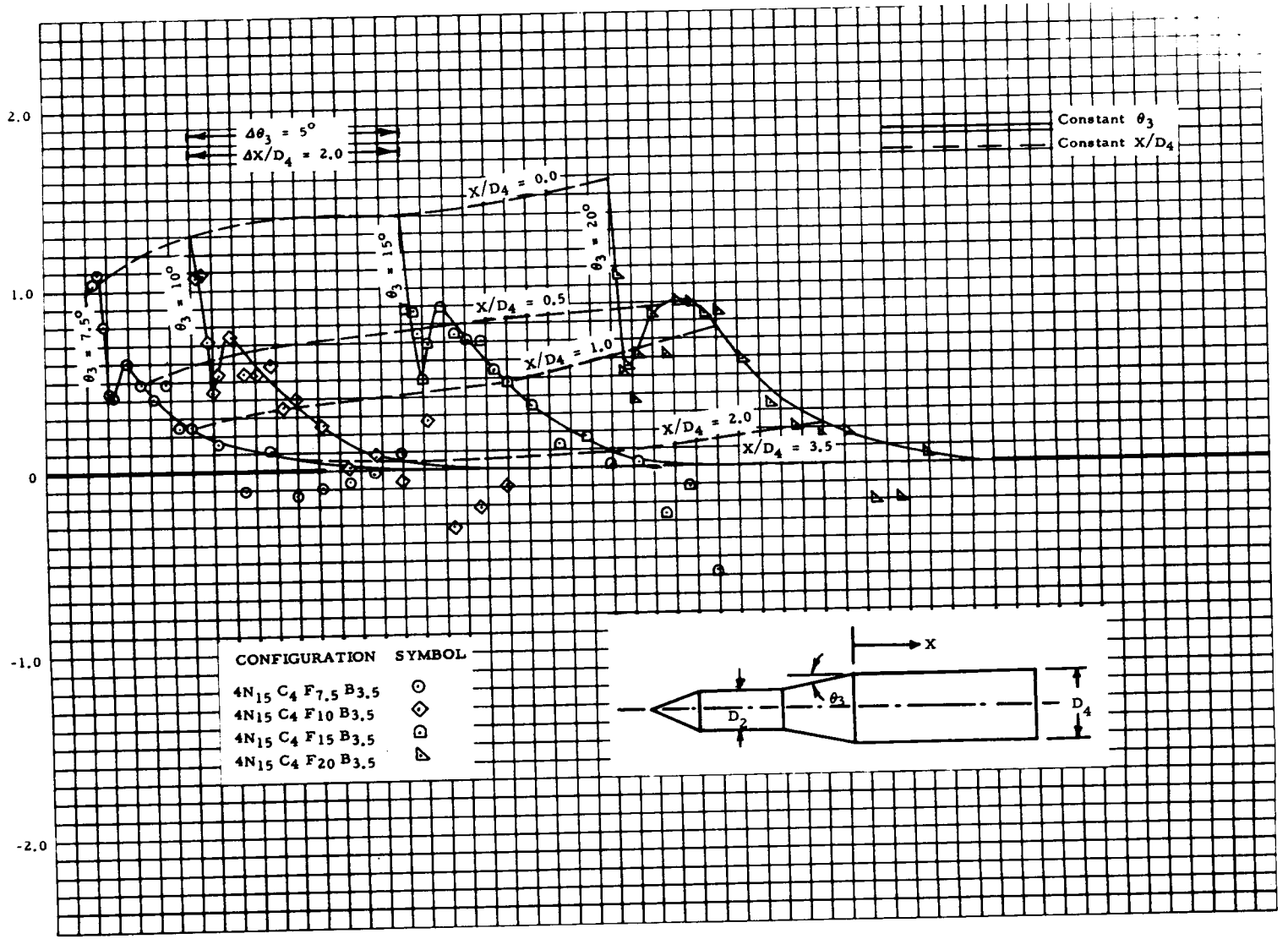

(7) M = 1.46

Figure 8a - The Effect of Flare Angle on Aft Cylinder Local Normal Force Slope Distributions for Cone-Cylinder-Flare-Cylinders, $D_2/D_4 = 0.4$ (Cont'd)

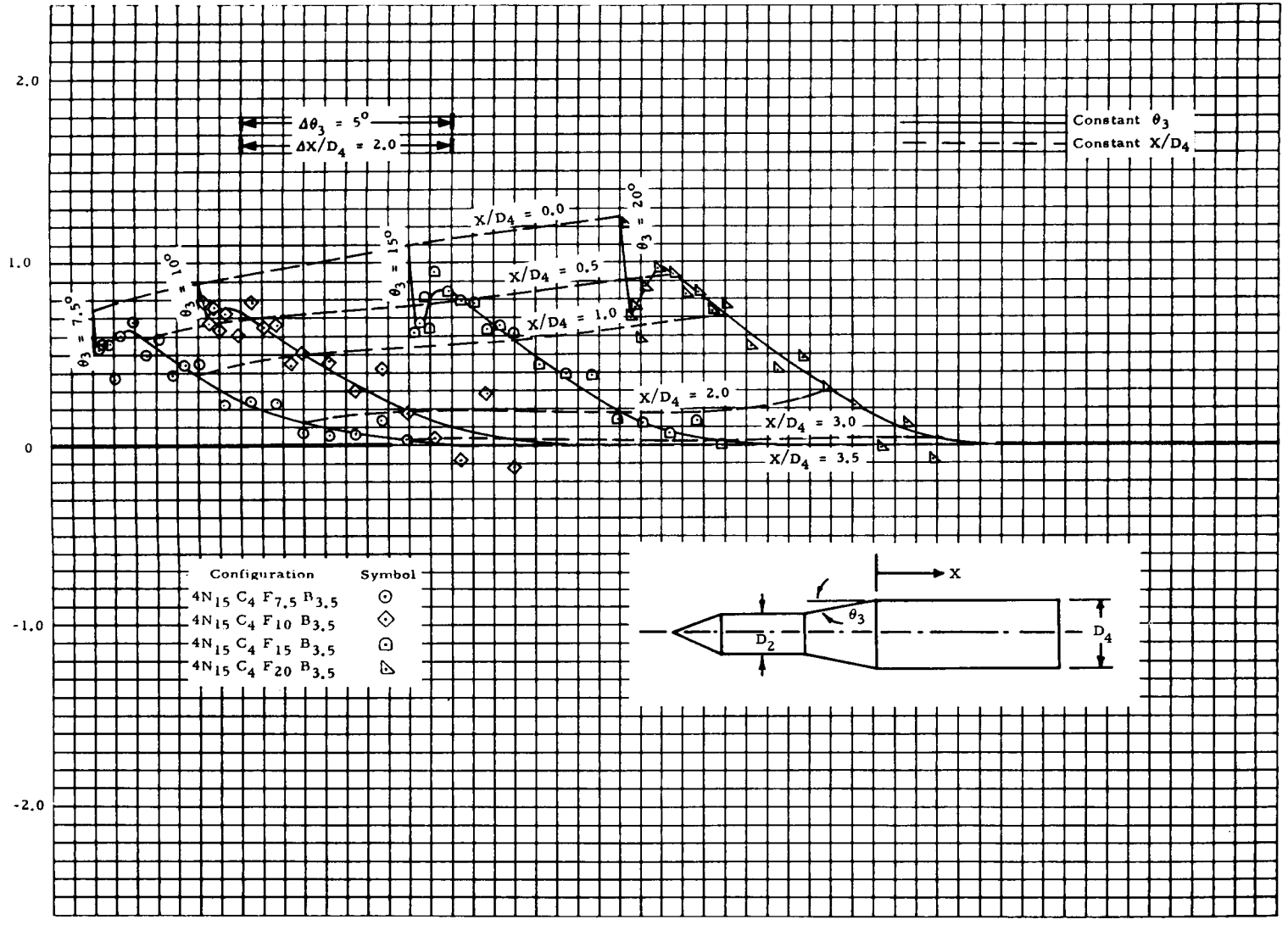

(8) M = 1.96

Figure 8a - The Effect of Flare Angle on Aft Cylinder Local Normal Force Slope Distributions for Cone-Cylinder-Flare-Cylinders, $D_2/D_4 = 0.4$ (Concluded)

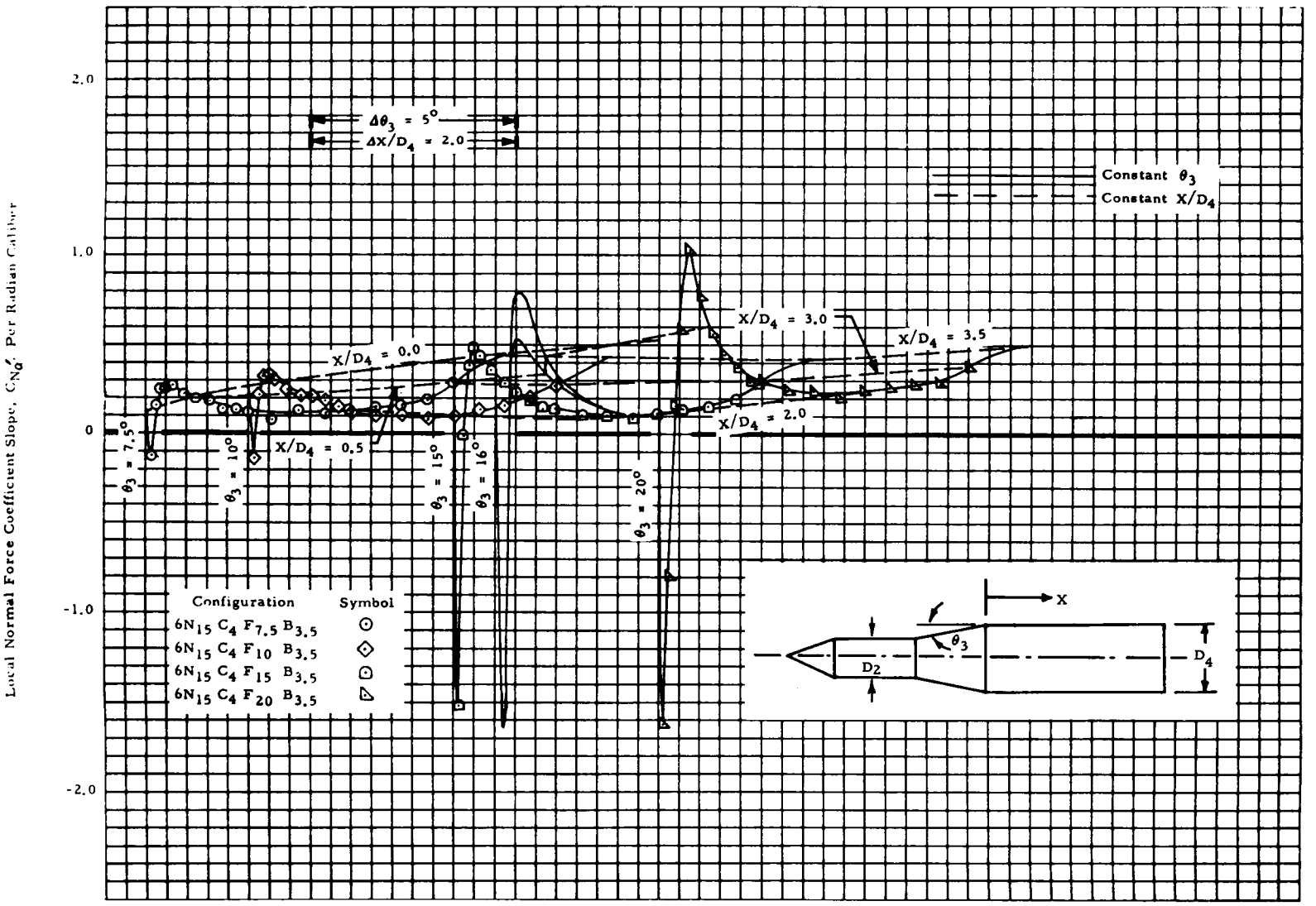

(1) M = 0.7

Figure 8b - The Effect of Flare Angle on Aft Cylinder Local Normal Force Slope Distributions for Cone-Cylinder-Flare-Cylinders, $D_2/D_4 = 0.6$

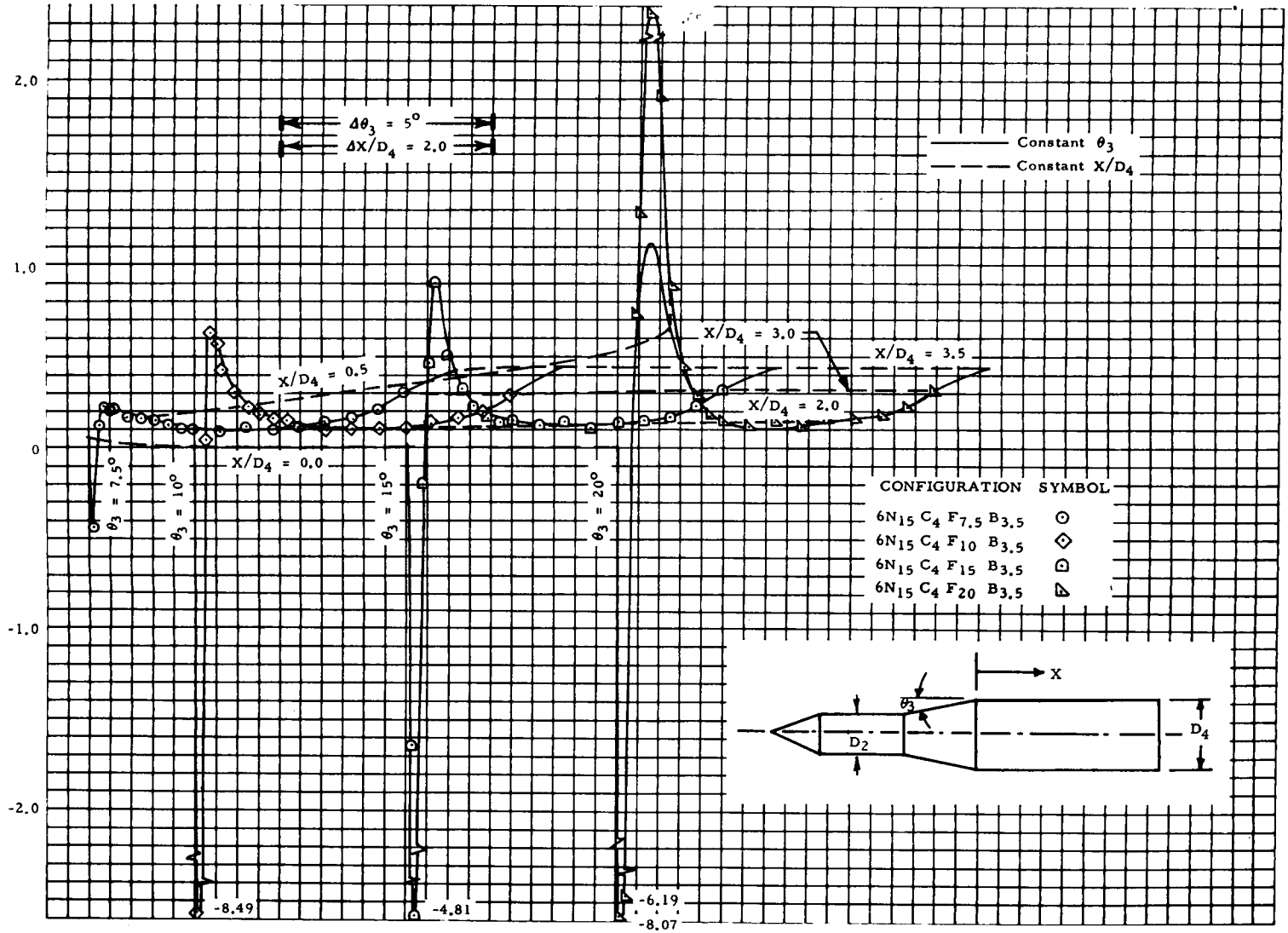

(2) M = 0.8

Figure 8b - The Effect of Flare Angle on Aft Cylinder Local Normal Force Slope Distributions for Cone-Cylinder-Flare-Cylinders, D_2/D_4 = 0.6 (Cont'd)

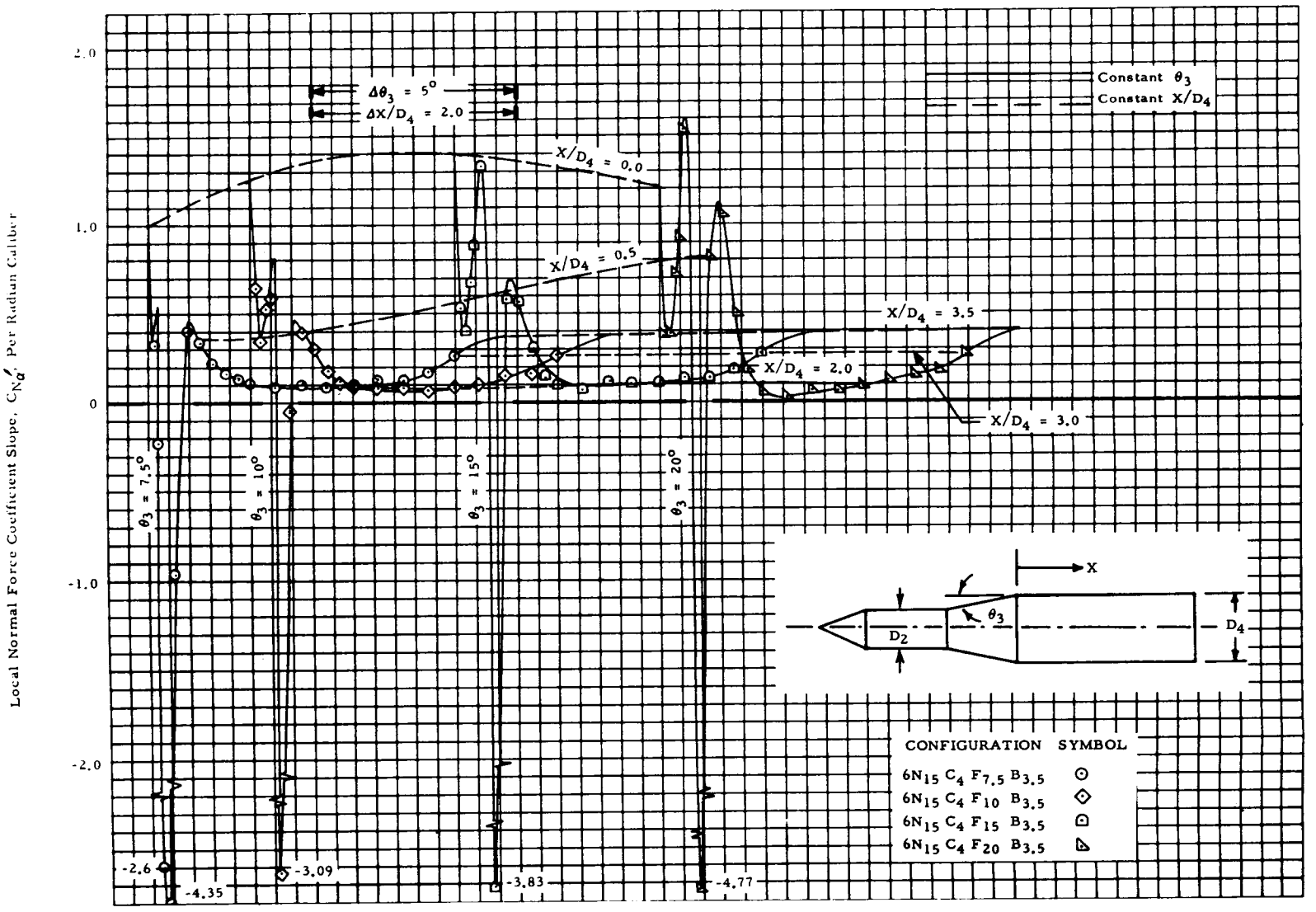

(3) M = 0.9

Figure 8b - The Effect of Flare Angle on Aft Cylinder Local Normal Force Slope Distributions for Cone-Cylinder-Flare-Cylinders, $D_2/D_4 = 0.6$ (Cont'd)

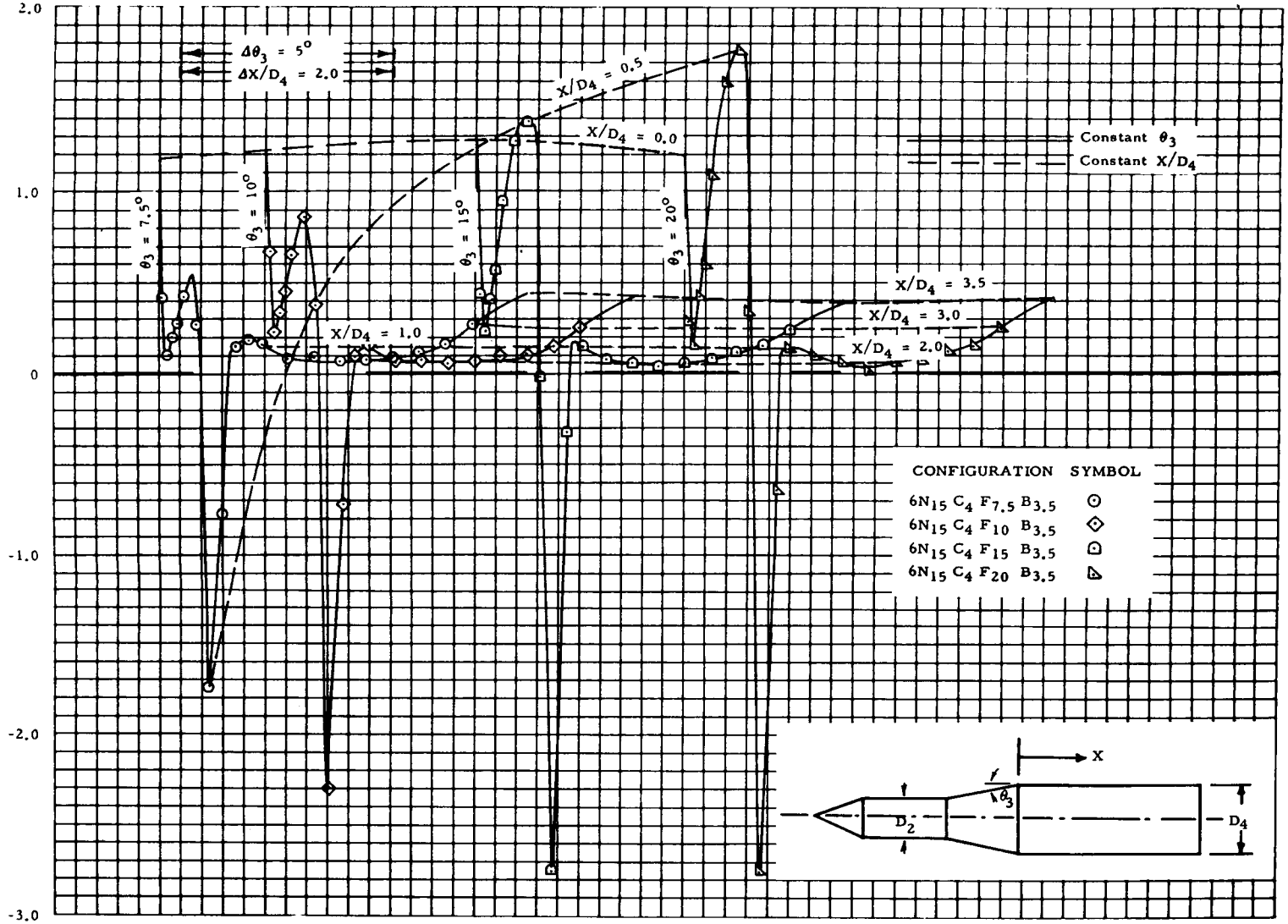

(4) M = 0.95

Figure 8b - The Effect of Flare Angle on Aft Cylinder Local Normal Force Slope Distributions for Cone-Cylinder-Flare-Cylinders, $D_2/D_4 = 0.6$ (Cont'd)

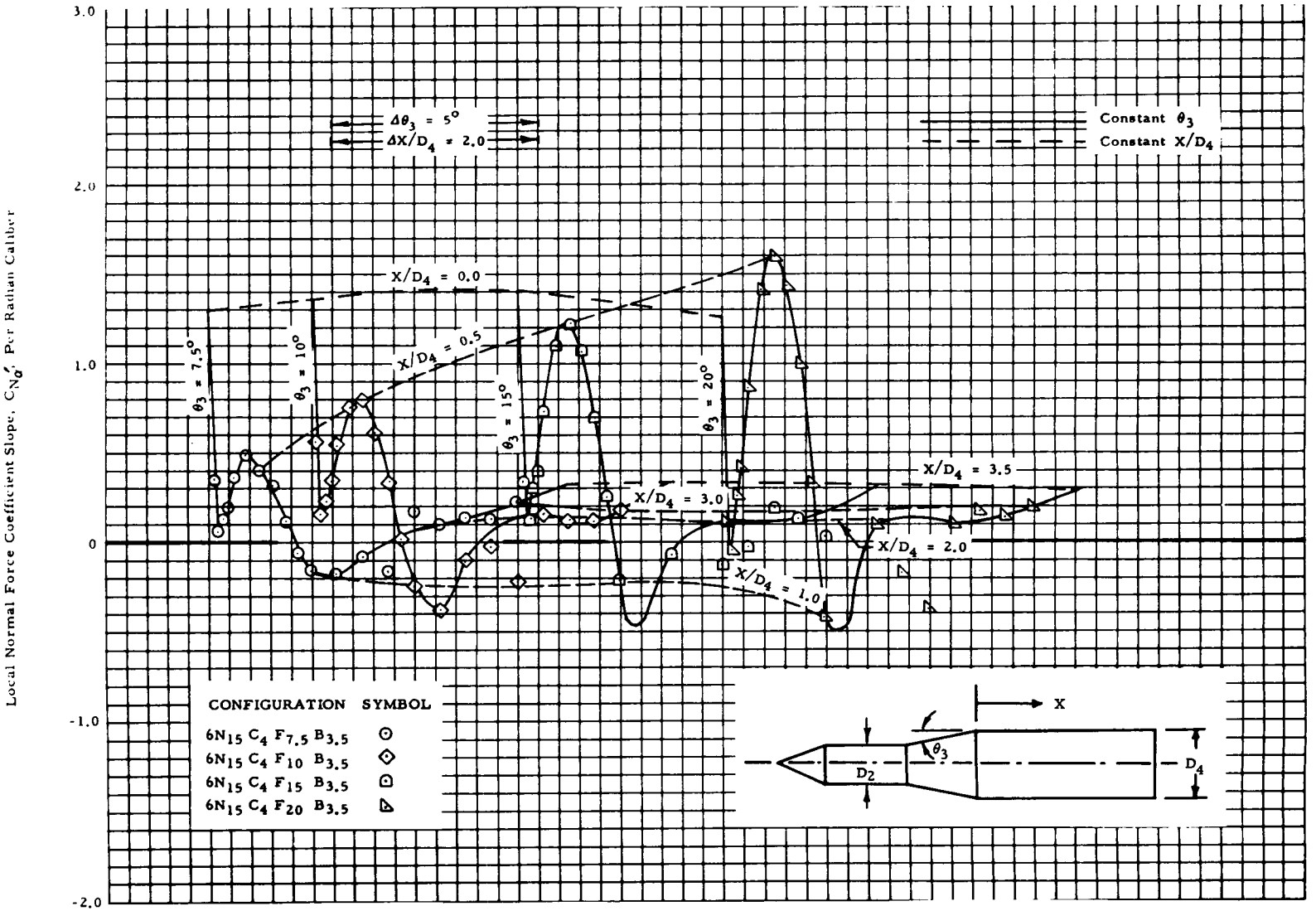

(5) M = 1.0

Figure 8b - The Effect of Flare Angle on Aft Cylinder Local Normal Force Slope Distributions for Cone-Cylinder-Flare-Cylinders, $D_2/D_4 = 0.6$ (Cont'd)

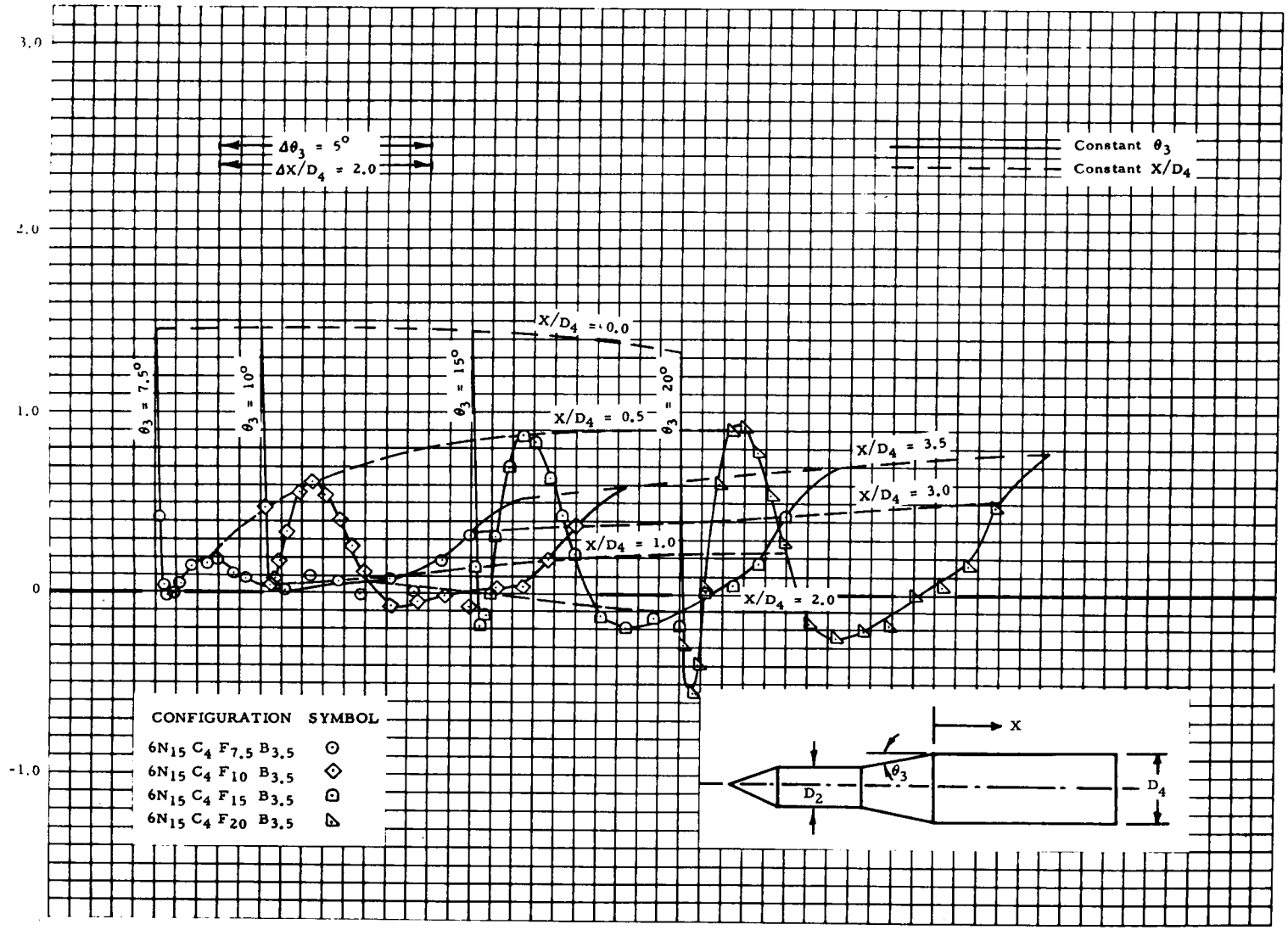

(6) M = 1.1

Figure 8b - The Effect of Flare Angle on Aft Cylinder Local Normal Force Slope Distributions for Cone-Cylinder-Flare-Cylinders, $D_2/D_4 = 0.6$ (Cont'd)

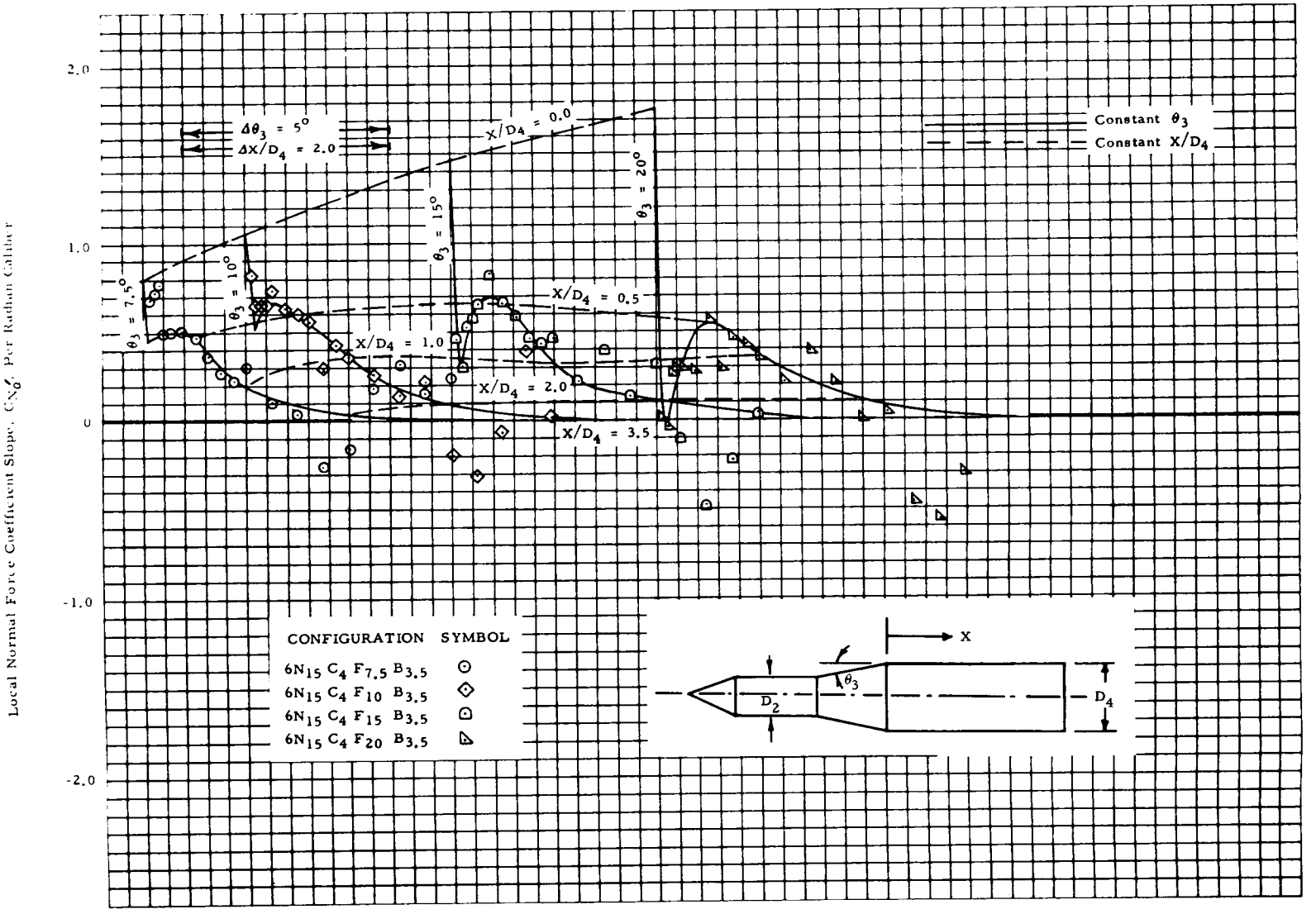

(7) M = 1.46

Figure 8b - The Effect of Flare Angle on Aft Cylinder Local Normal Force Slope Distributions for Cone-Cylinder-Flare-Cylinders, $D_2/D_4 = 0.6$ (Cont'd)

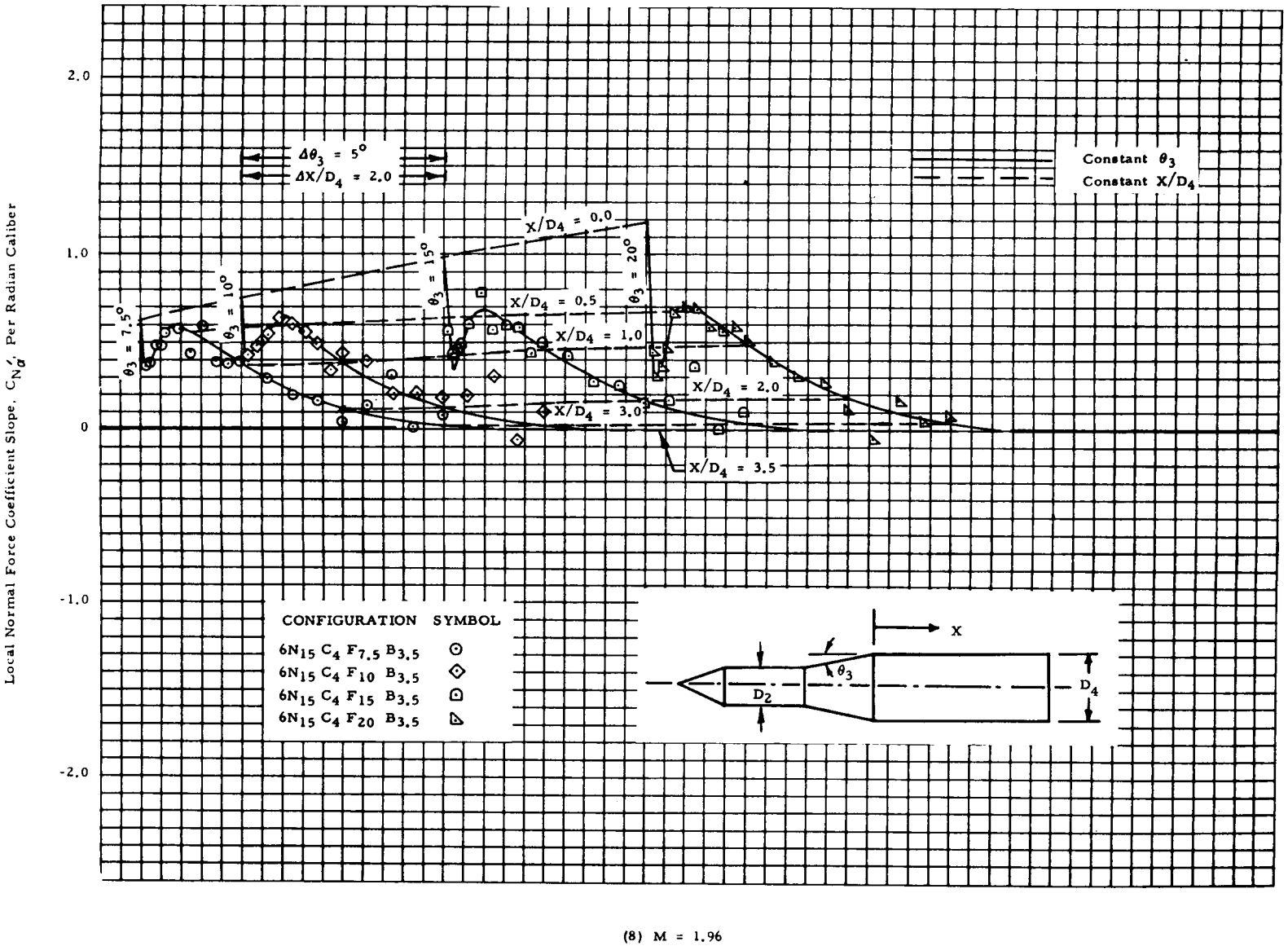

(8) M = 1.96

Figure 8b - The Effect of Flare Angle on Aft Cylinder Local Normal Force Slope Distributions for Cone-Cylinder-Flare-Cylinders, $D_2/D_4 = 0.6$ (Concluded)

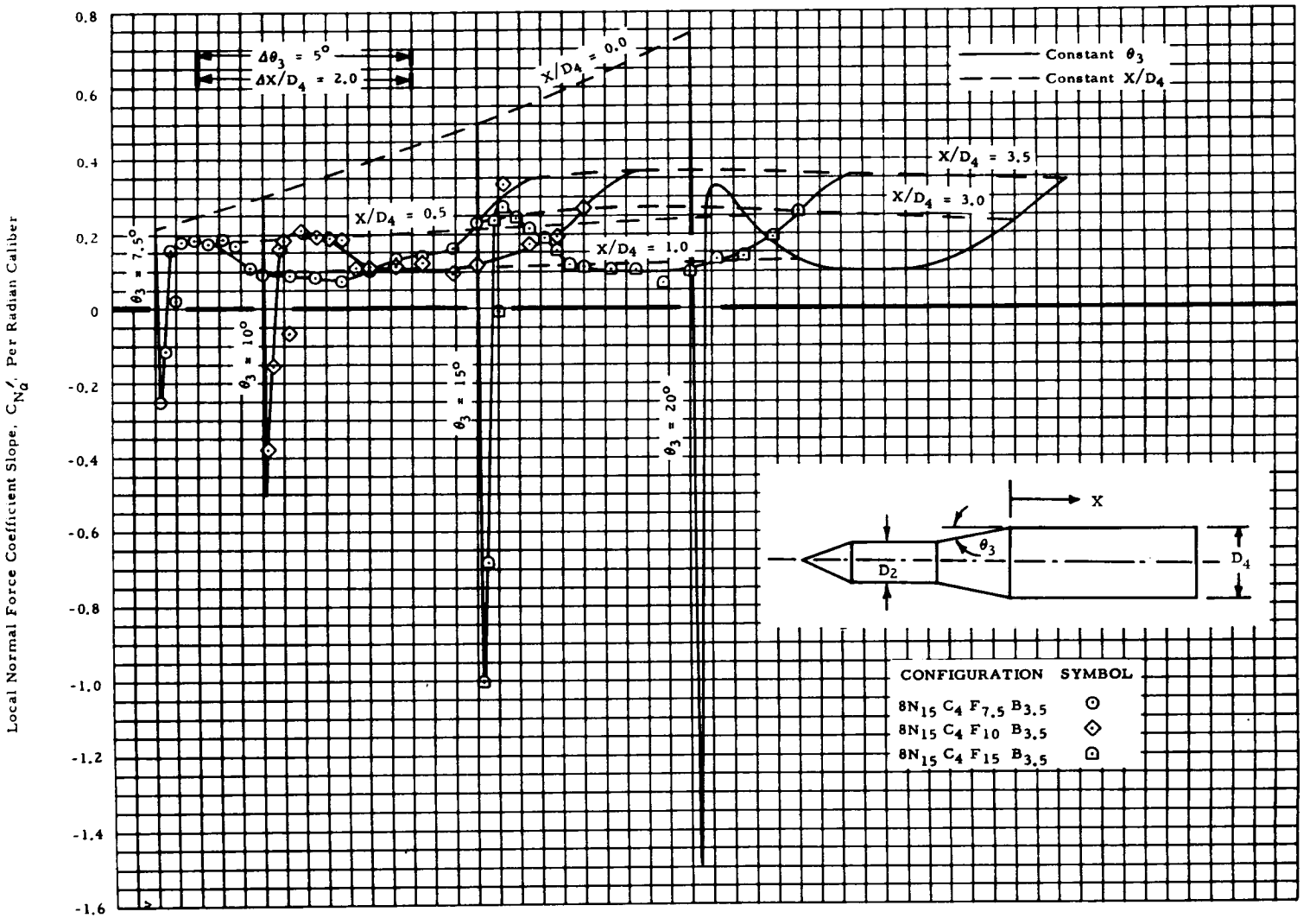

(1) M = 0.7

Figure 8c - The Effect of Flare Angle on Aft Cylinder Local Normal Force Slope Distributions for Cone-Cylinder-Flare-Cylinders, $D_2/D_4 = 0.8$

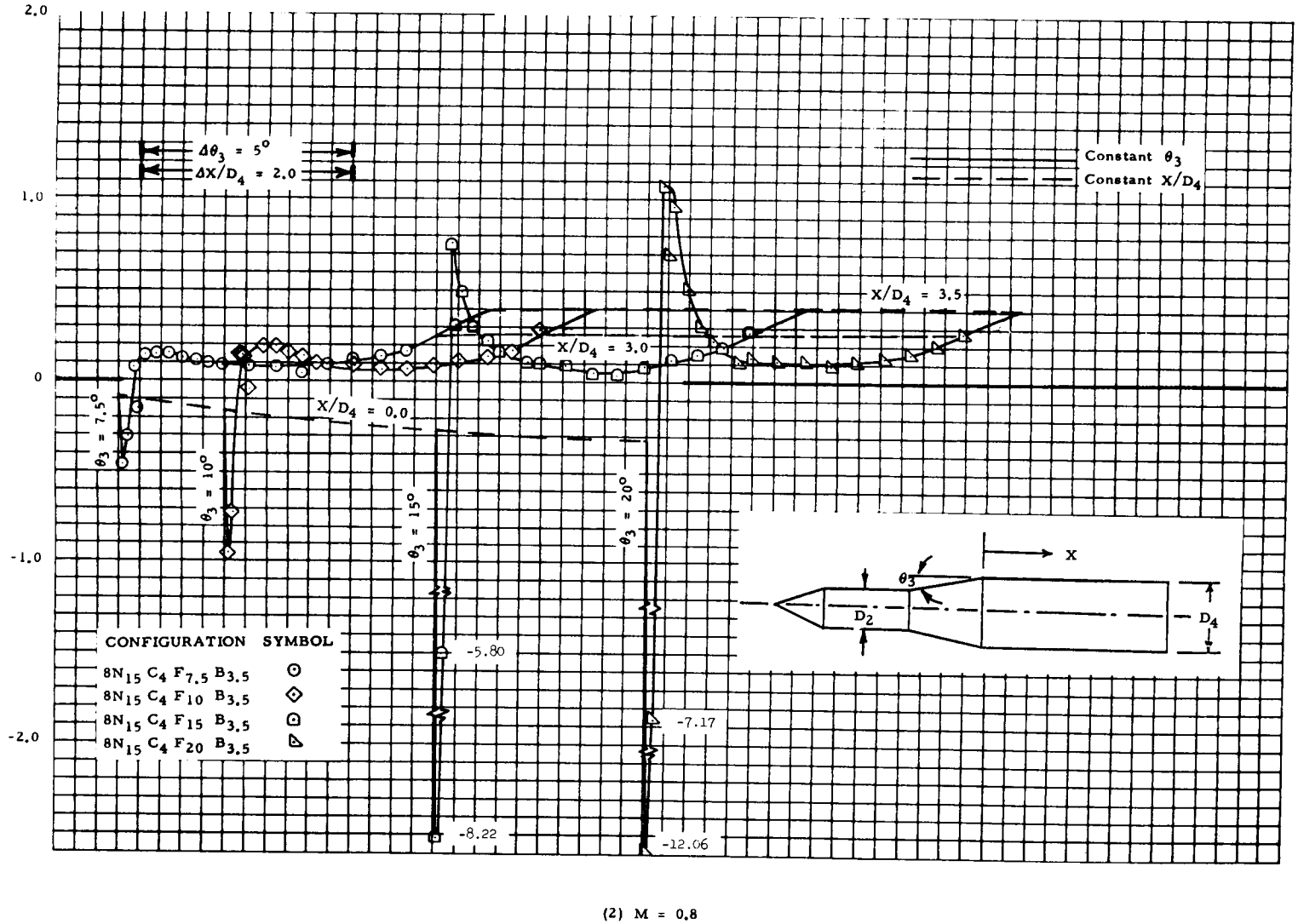

(2) M = 0.8

Figure 8c - The Effect of Flare Angle on Aft Cylinder Local Normal Force Slope Distributions for Cone-Cylinder-Flare-Cylinders, $D_2/D_4 = 0.8$ (Cont'd)

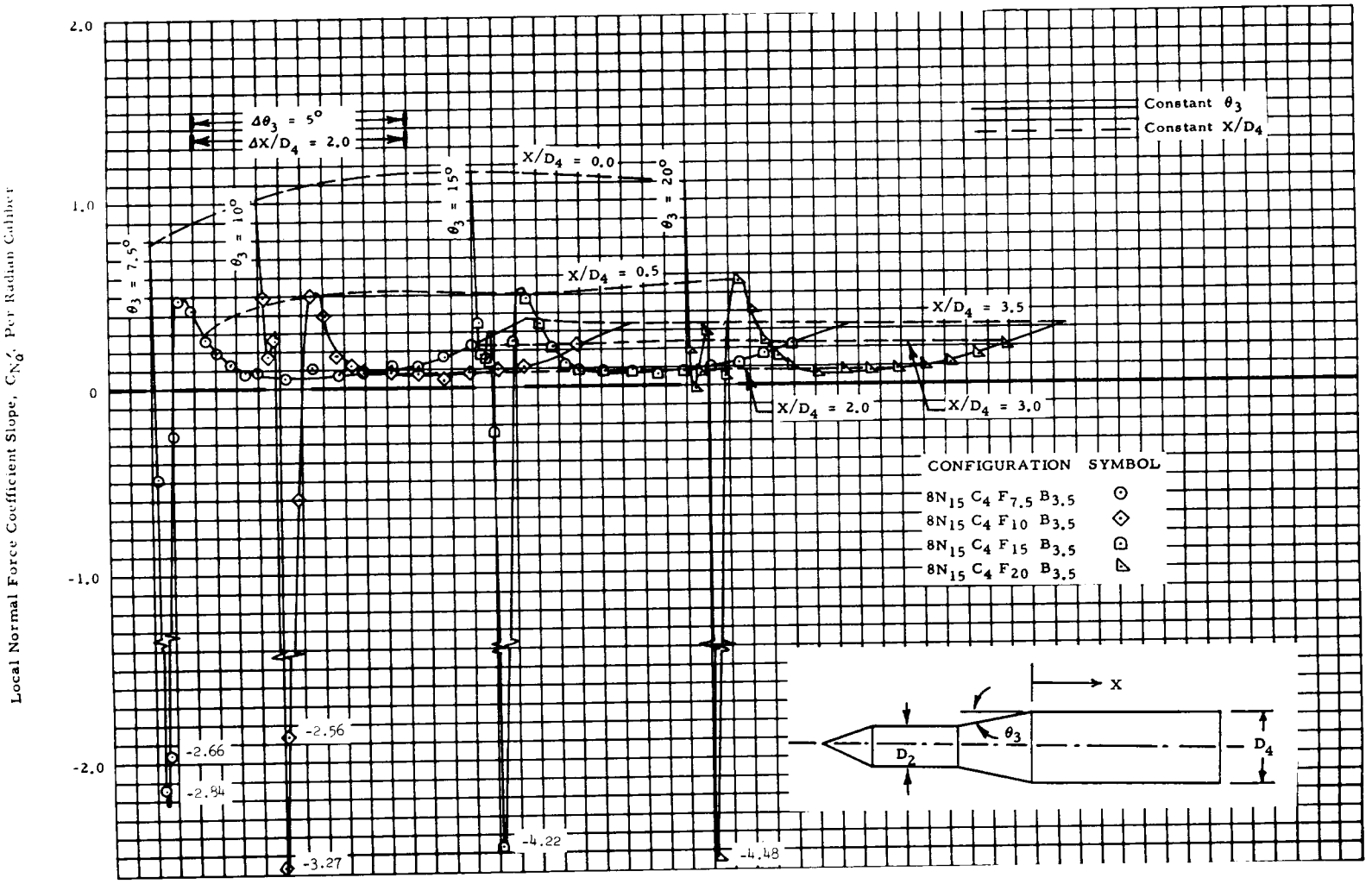

(3) M = 0.9

Figure 8c - The Effect of Flare Angle on Aft Cylinder Local Normal Force Slope Distributions for Cone-Cylinder-Flare-Cylinders, D_2/D_4 = 0.8 (Cont'd)

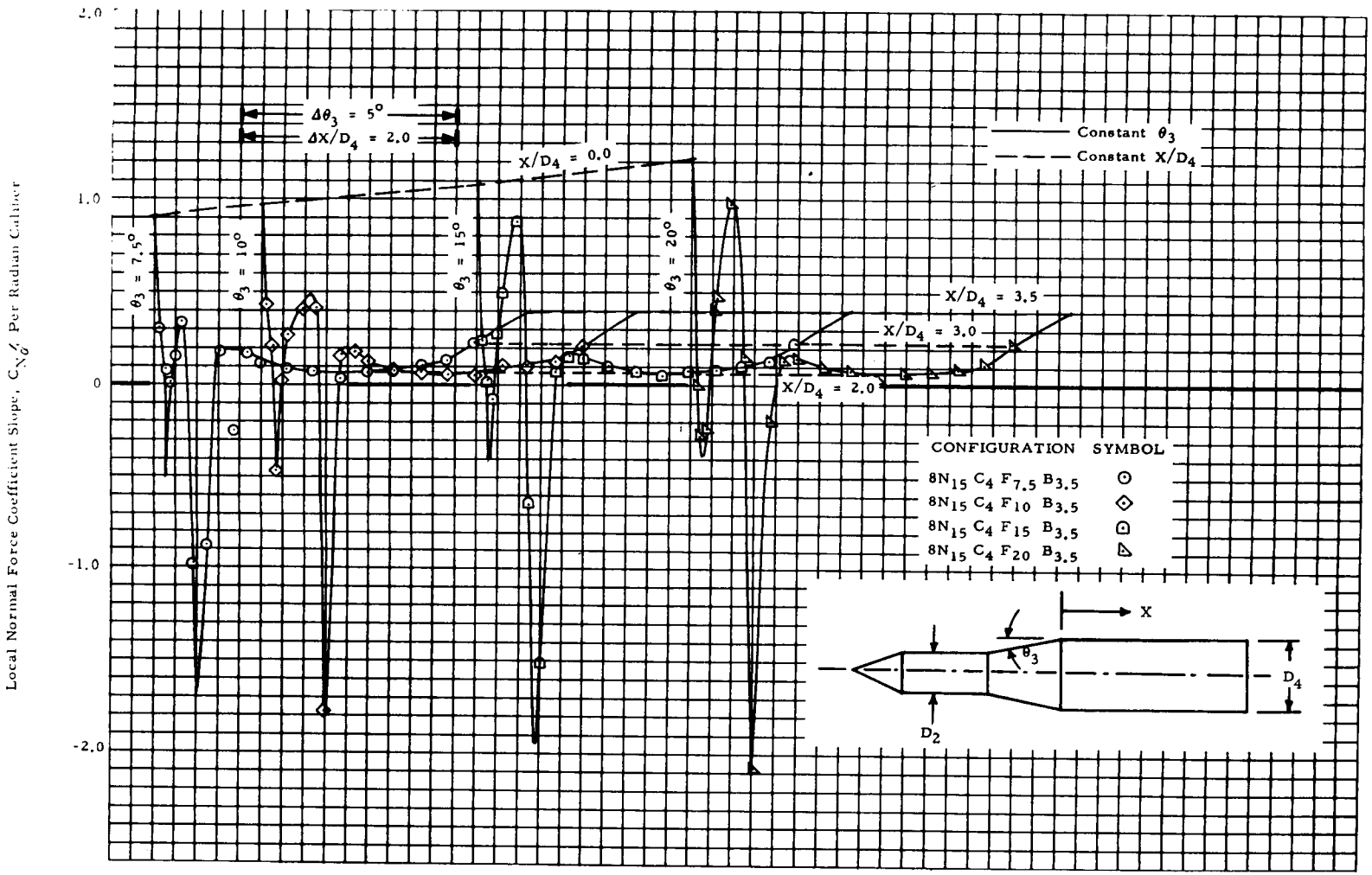

(4) M = 0.95

Figure 8c - The Effect of Flare Angle on Aft Cylinder Local Normal Force Slope Distributions for Cone-Cylinder-Flare-Cylinders, $D_2/D_4 = 0.8$ (Cont'd)

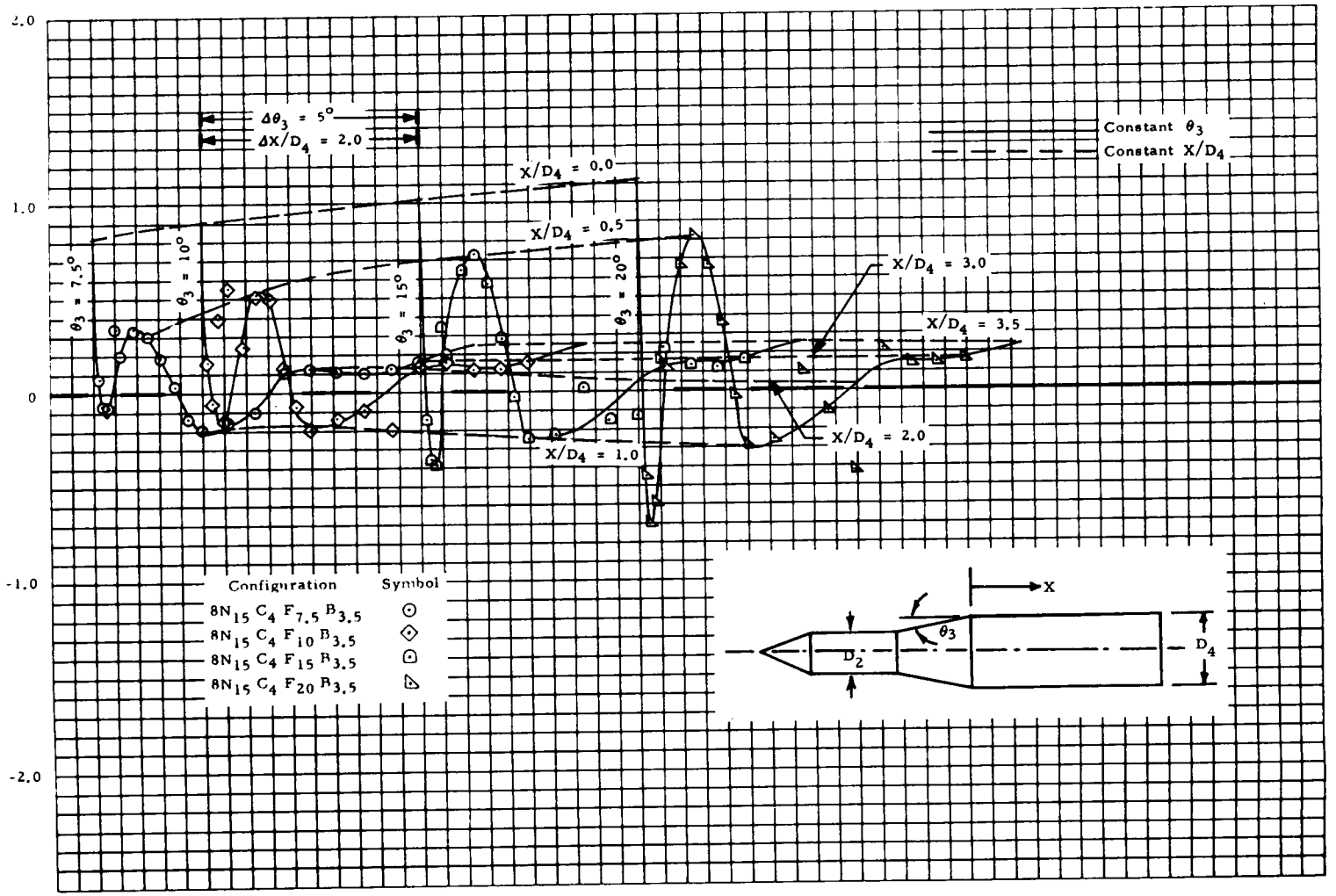

(5) M = 1.0

Figure 8c - The Effect of Flare Angle on Aft Cylinder Local Normal Force Slope Distributions for Cone-Cylinder-Flare-Cylinders, $D_2/D_4 = 0.8$ (Cont'd)

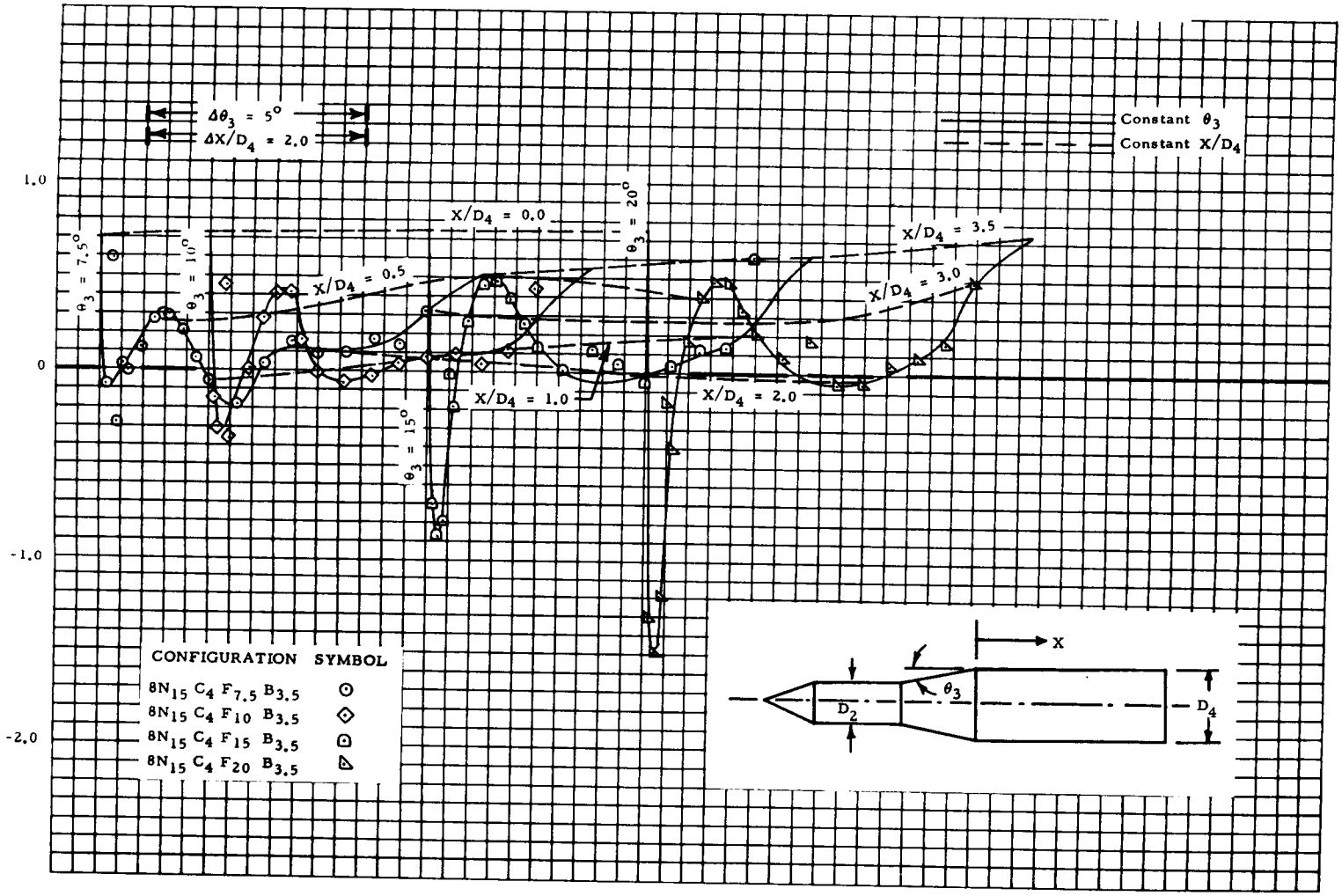

(6) M = 1.1

Figure 8c - The Effect of Flare Angle on Aft Cylinder Local Normal Force Slope Distributions for Cone-Cylinder-Flare-Cylinders, $D_2/D_4 = 0.8$ (Cont'd)

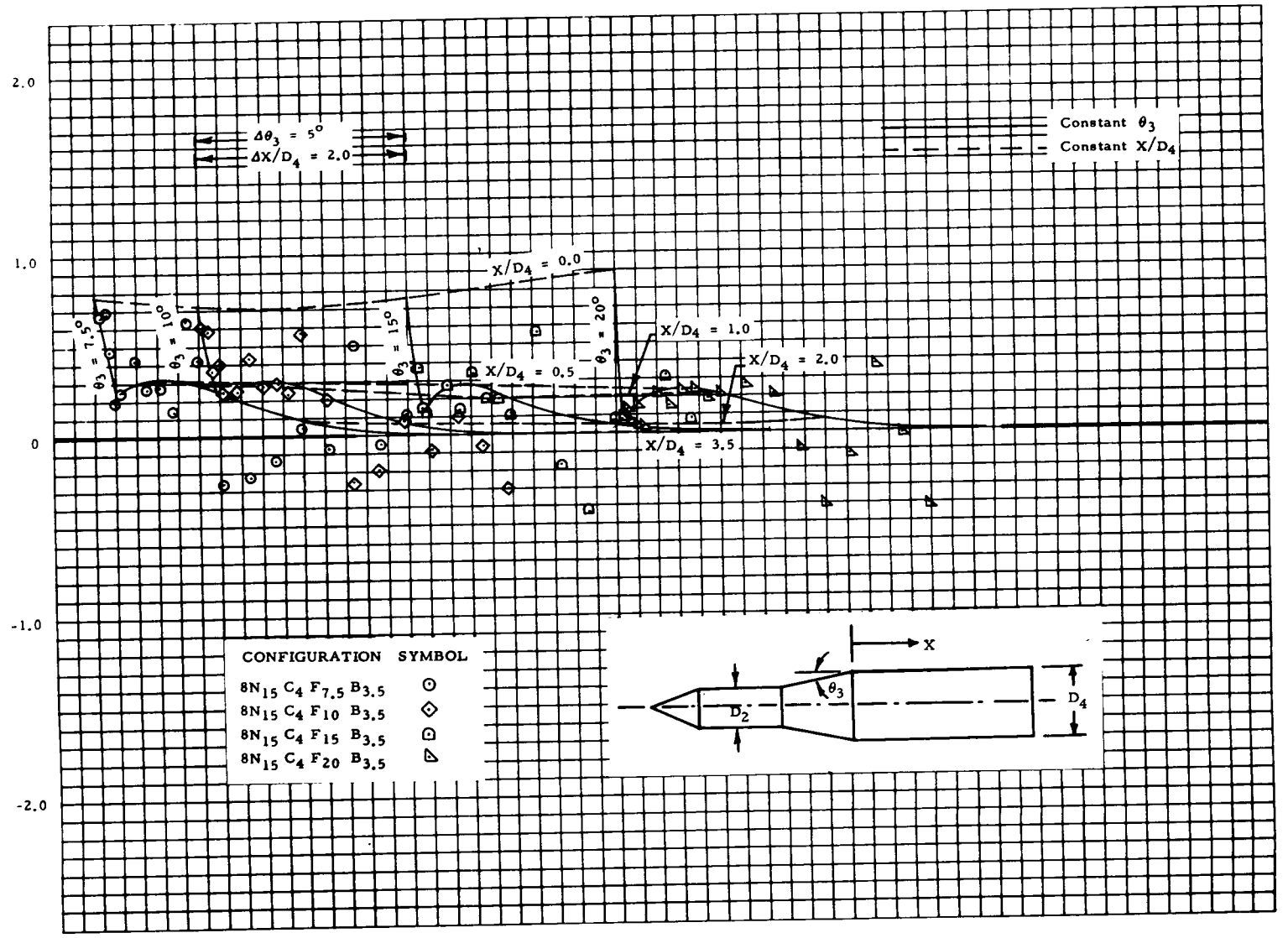

(7) M = 1.46

Figure 8c - The Effect of Flare Angle on Aft Cylinder Local Normal Force Slope Distributions for Cone-Cylinder-Flare-Cylinders, $D_2/D_4 = 0.8$ (Cont'd)

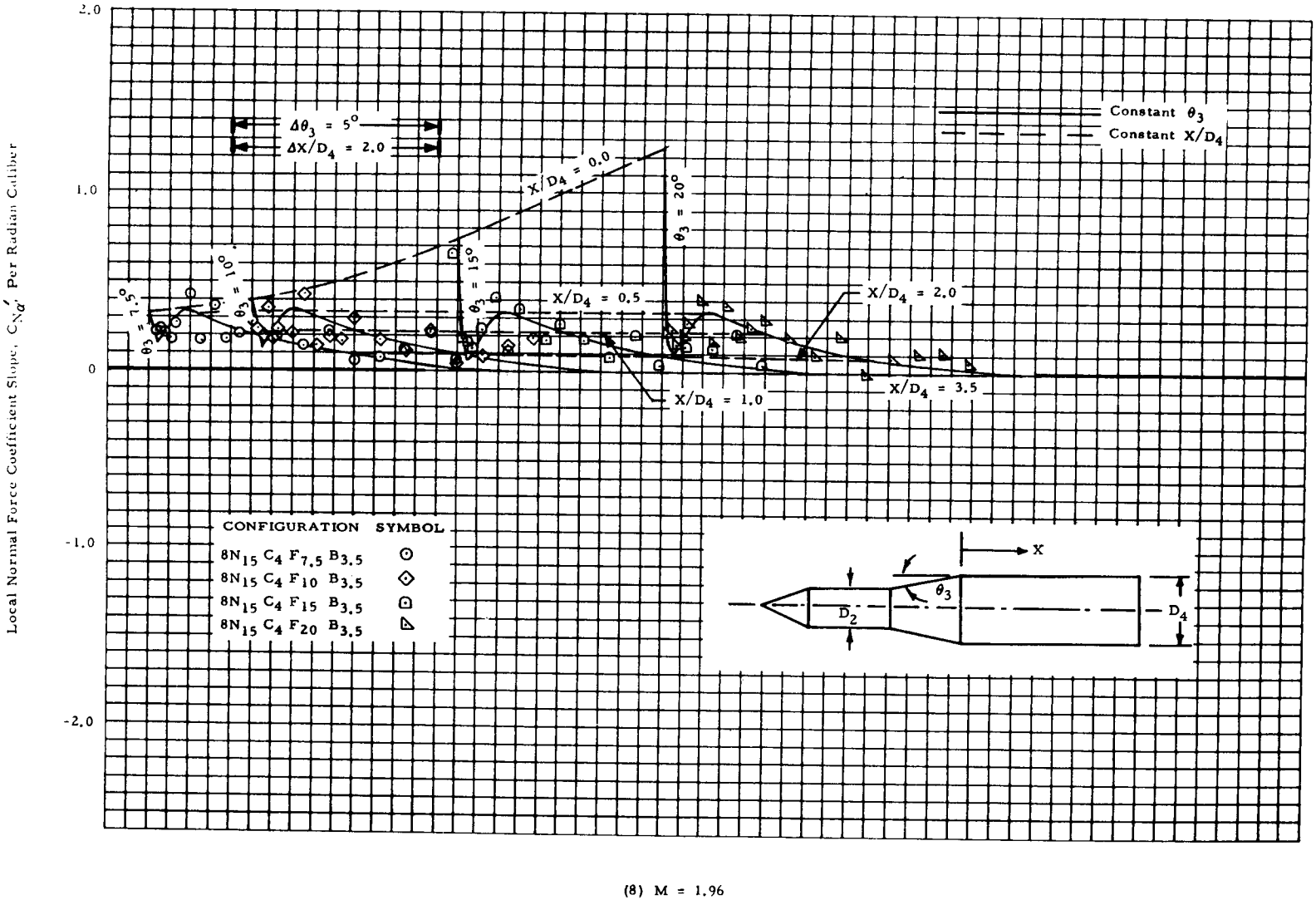

(8) M = 1.96

Figure 8c - The Effect of Flare Angle on Aft Cylinder Local Normal Force Distributions for Cone-Cylinder-Flare-Cylinders, $D_2/D_4 = 0.8$ (Concluded)

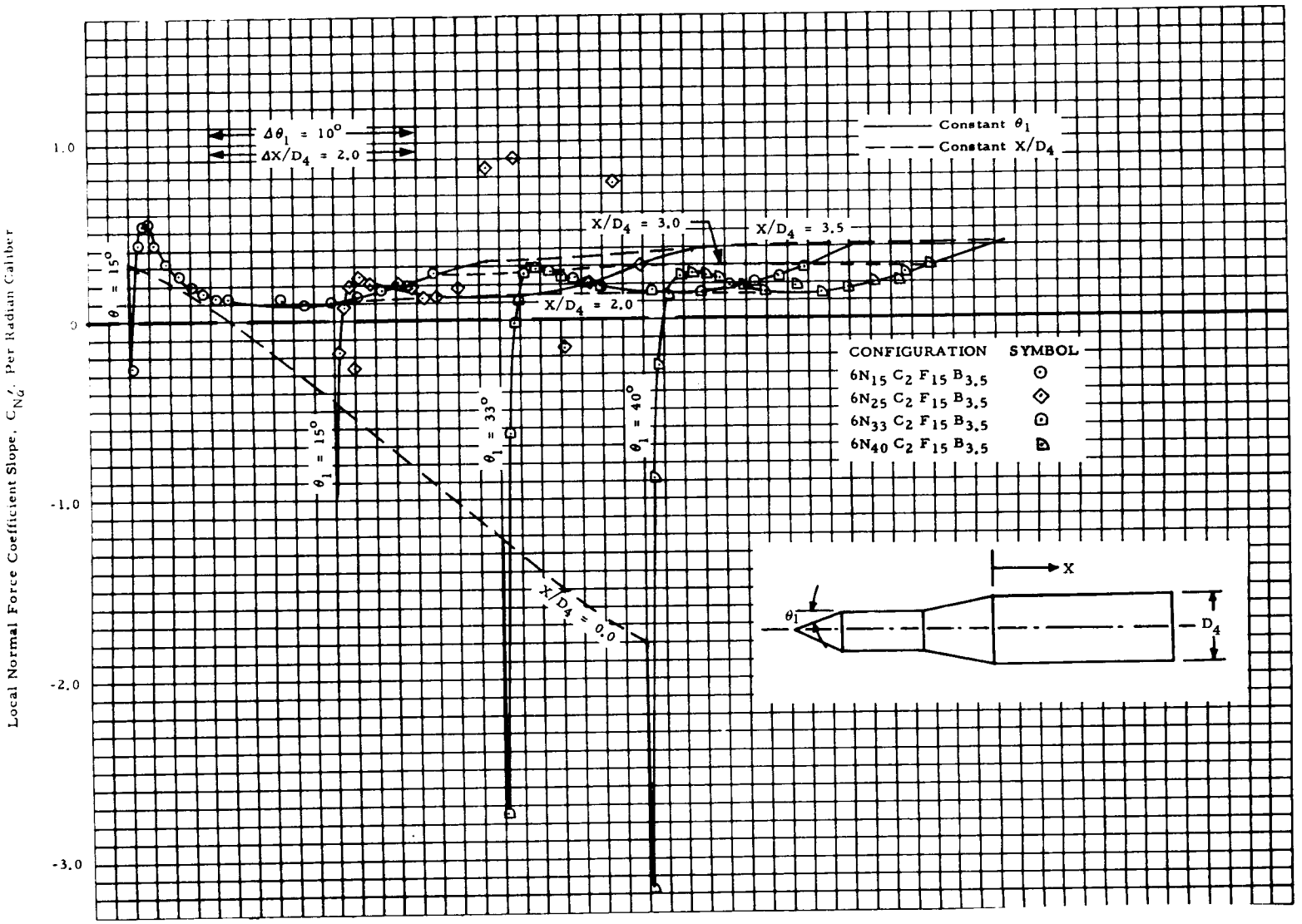

(a) M = 0.7

Figure 9 - The Effect of Cone Angle on Aft Cylinder Local Normal Force Slope Distributions for Cone-Cylinder-Flare-Cylinders

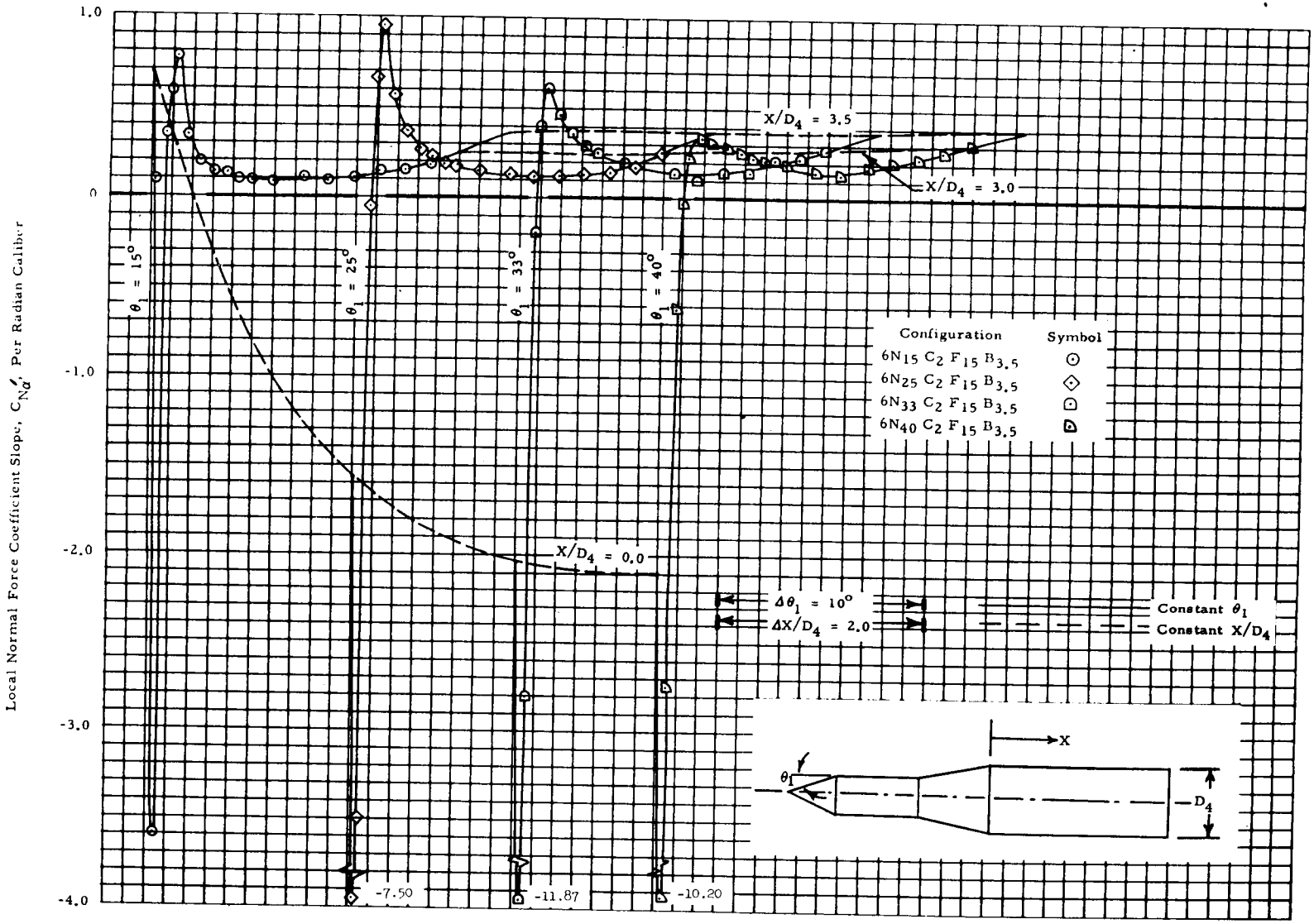

(b) M = 0.8

Figure 9 - The Effect of Cone Angle on Aft Cylinder Local Normal Force Slope Distributions for Cone-Cylinder-Flare-Cylinders (Cont'd)

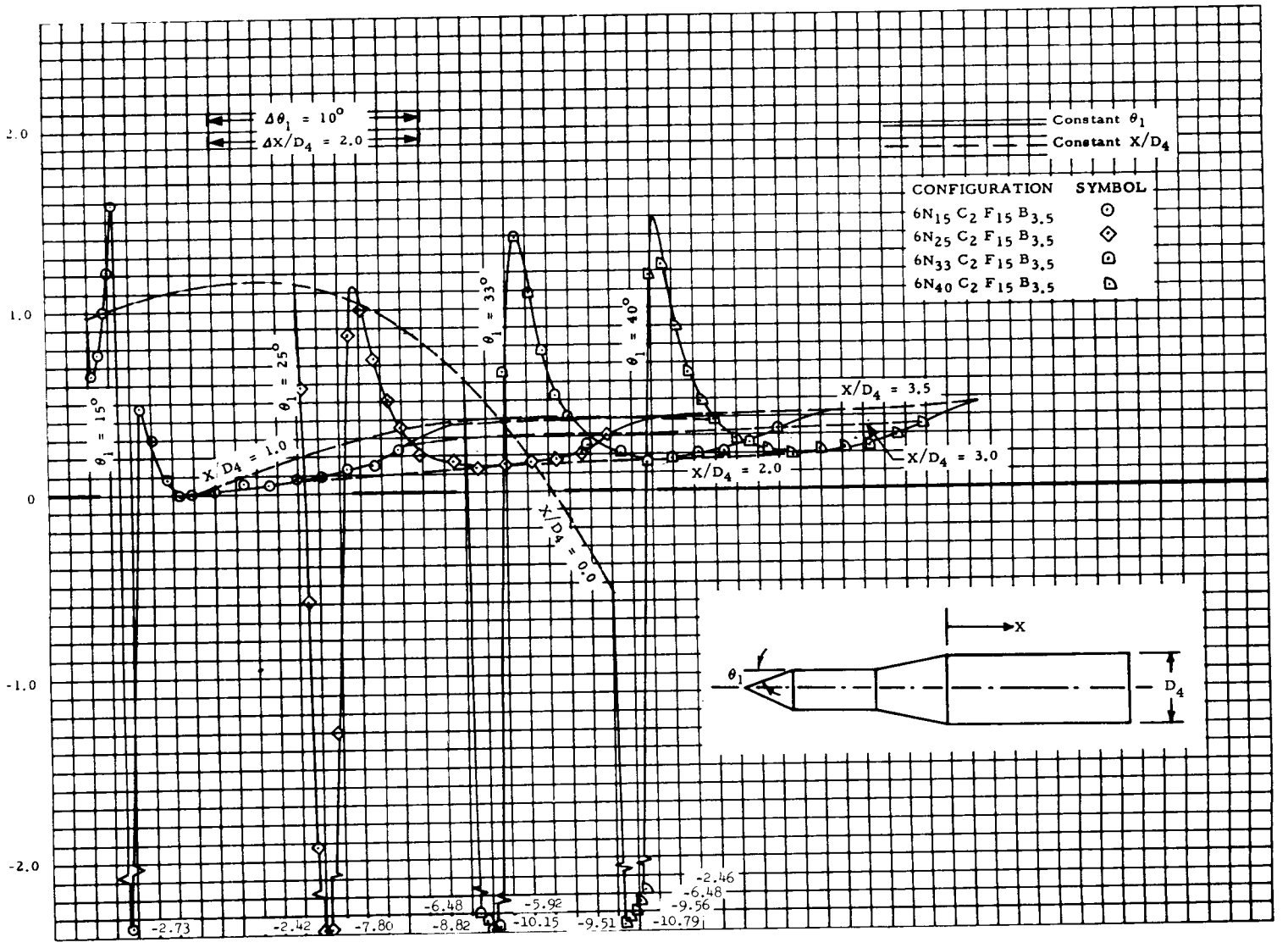

(c) M = 0.9

Figure 9 - The Effect of Cone Angle on Aft Cylinder Local Normal Force Slope Distributions for Cone-Cylinder-Flare-Cylinders (Cont'd)

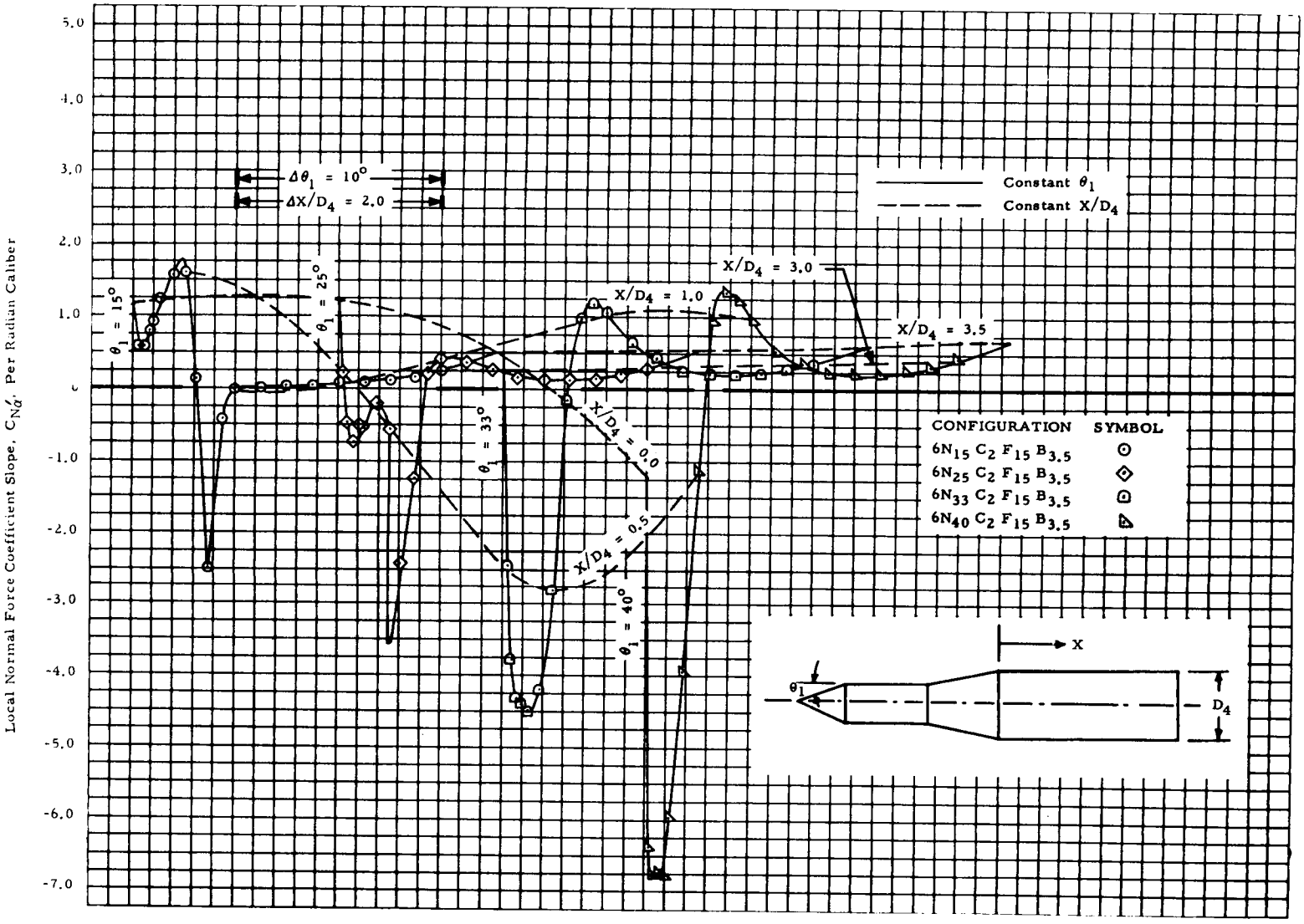

(d) M = 0.95

Figure 9 - The Effect of Cone Angle on Aft Cylinder Local Normal Force Slope Distributions for Cone-Cylinder-Flare-Cylinders. (Cont'd)

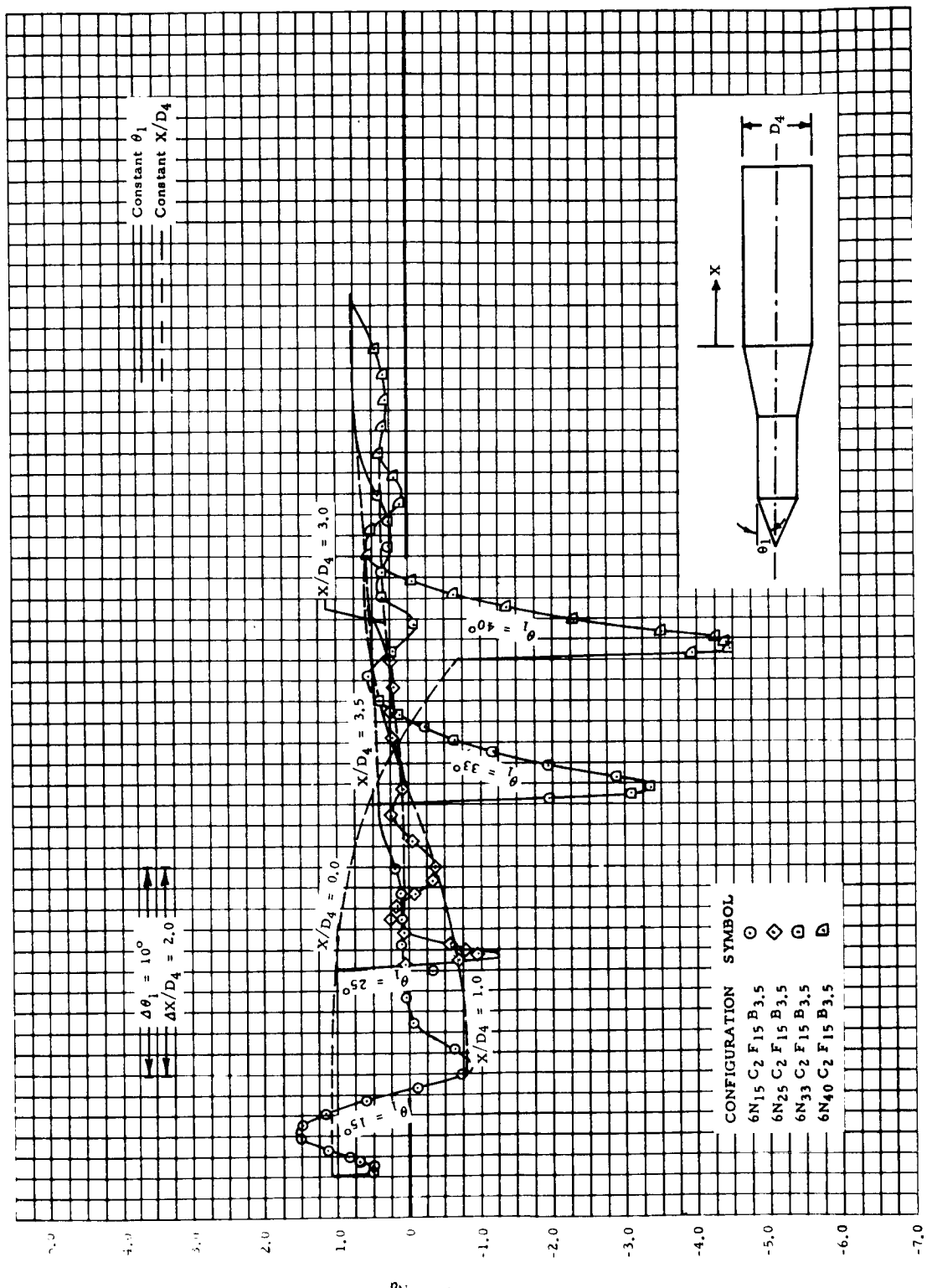

(e) M = 1.0

Figure 9 - The Effect of Cone Angle on Aft Cylinder Local Normal Force Slope Distributions for Cone-Cylinder-Flare-Cylinders (Cont'd)

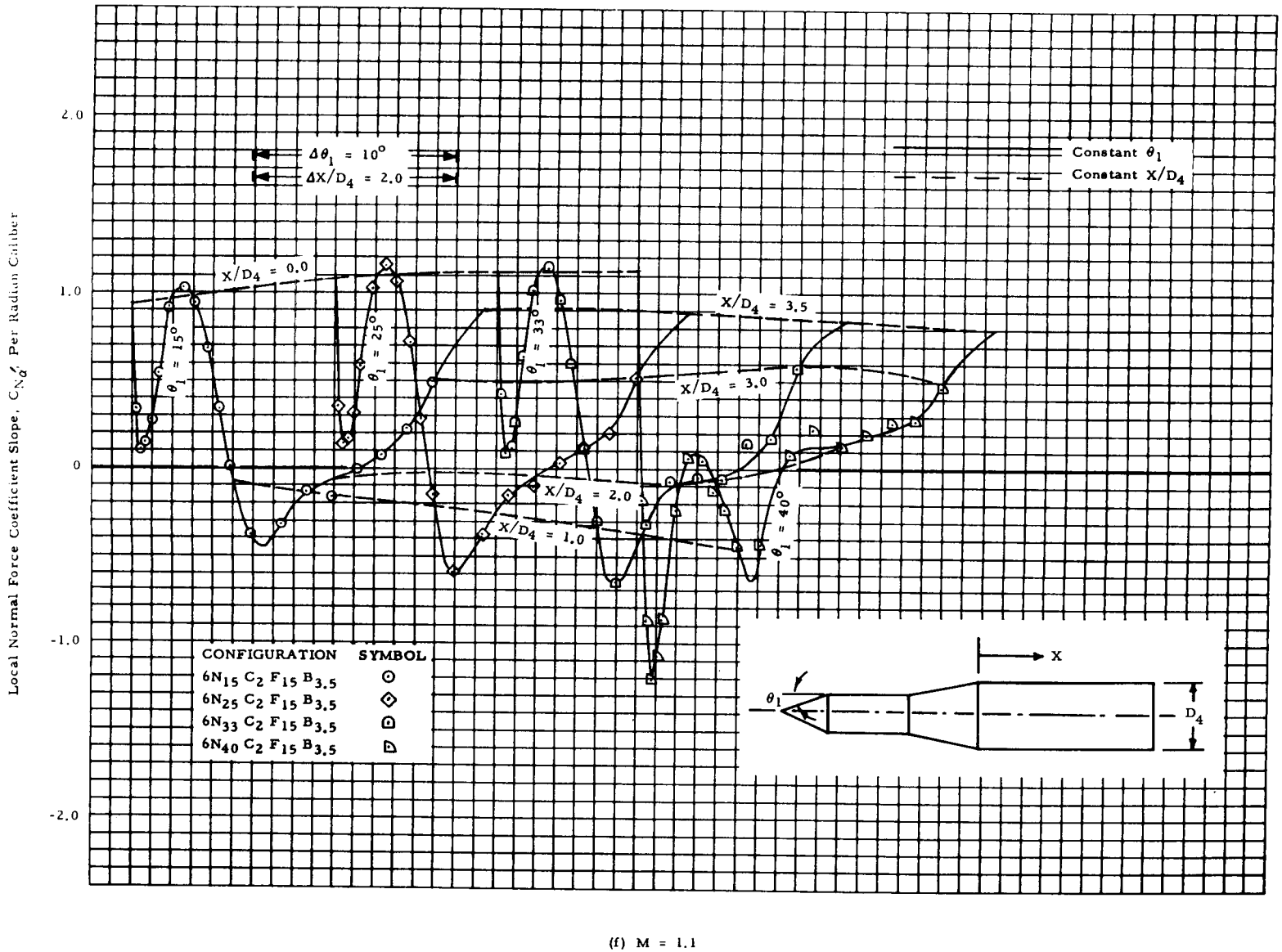

(f) M = 1.1

Figure 9 - The Effect of Cone Angle on Aft Cylinder Local Normal Force Slope Distributions for Cone-Cylinder-Flare-Cylinders (Cont'd)

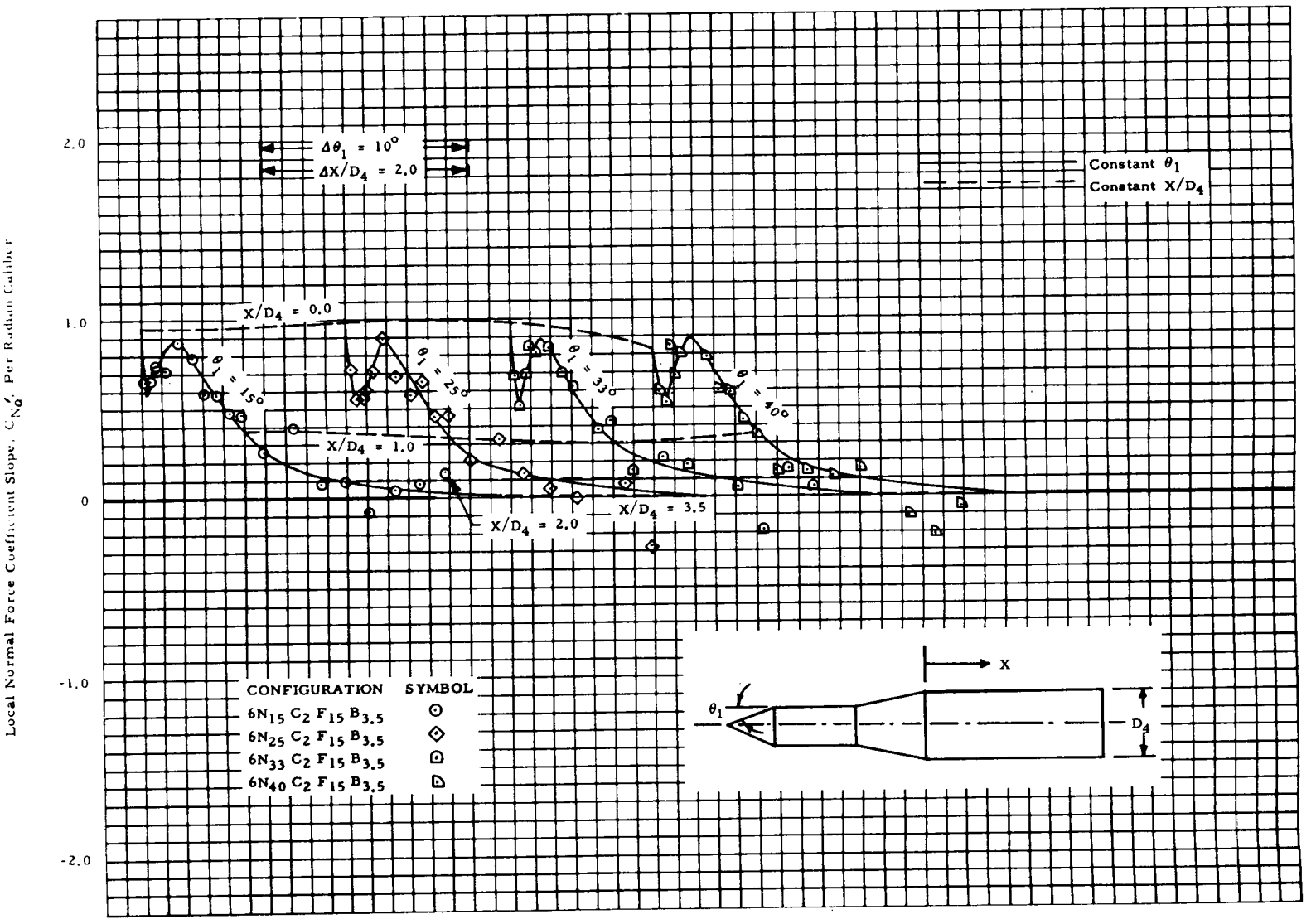

(g) M = 1.46

Figure 9 - The Effect of Cone Angle on Aft Cylinder Local Normal Force Slope Distributions for Cone-Cylinder-Flare-Cylinders (Cont'd)

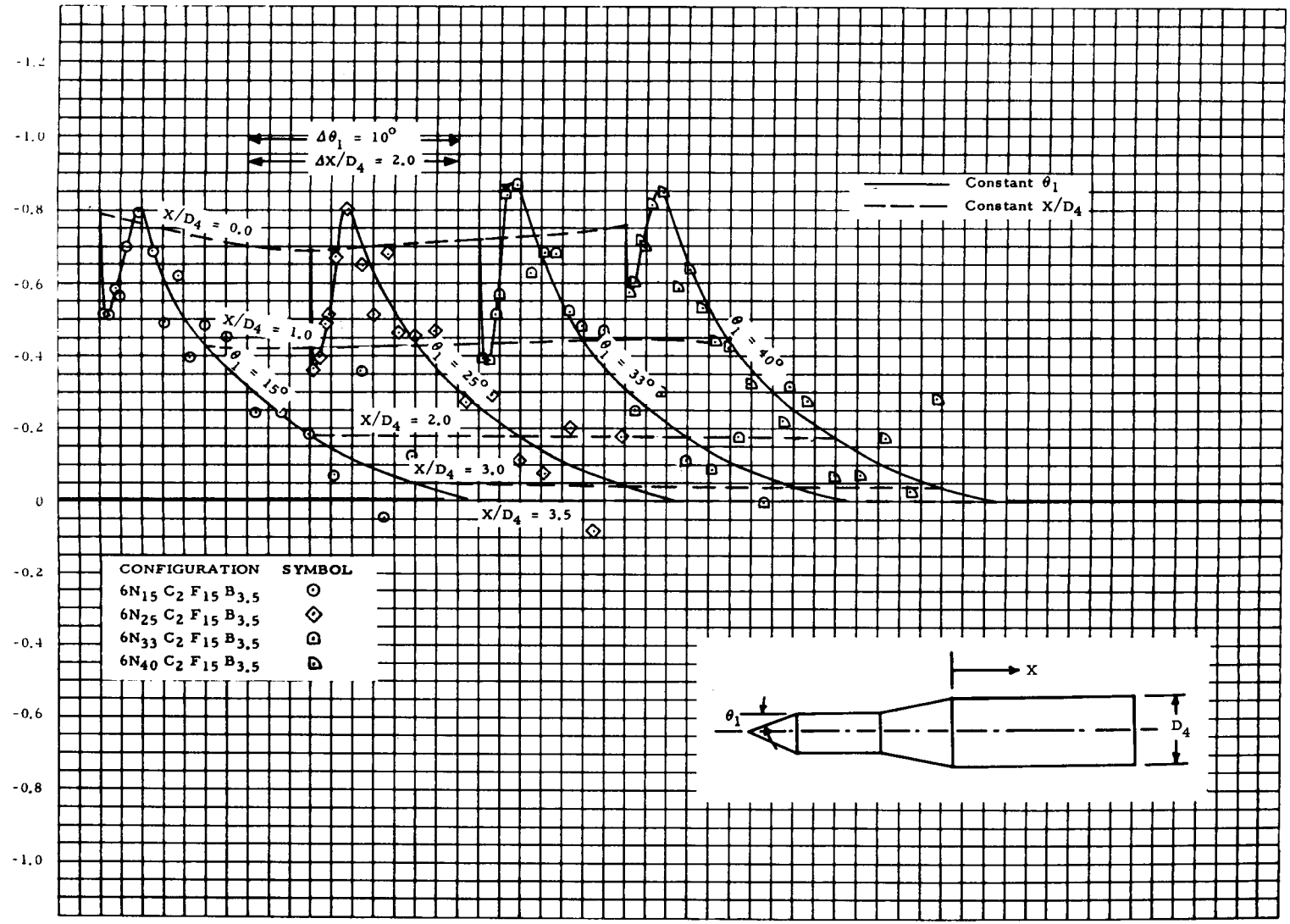

(h) M = 1.96

Figure 9 - The Effect of Cone Angle on Aft Cylinder Local Normal Force Slope Distributions for Cone-Cylinder-Flare-Cylinders (Concluded)

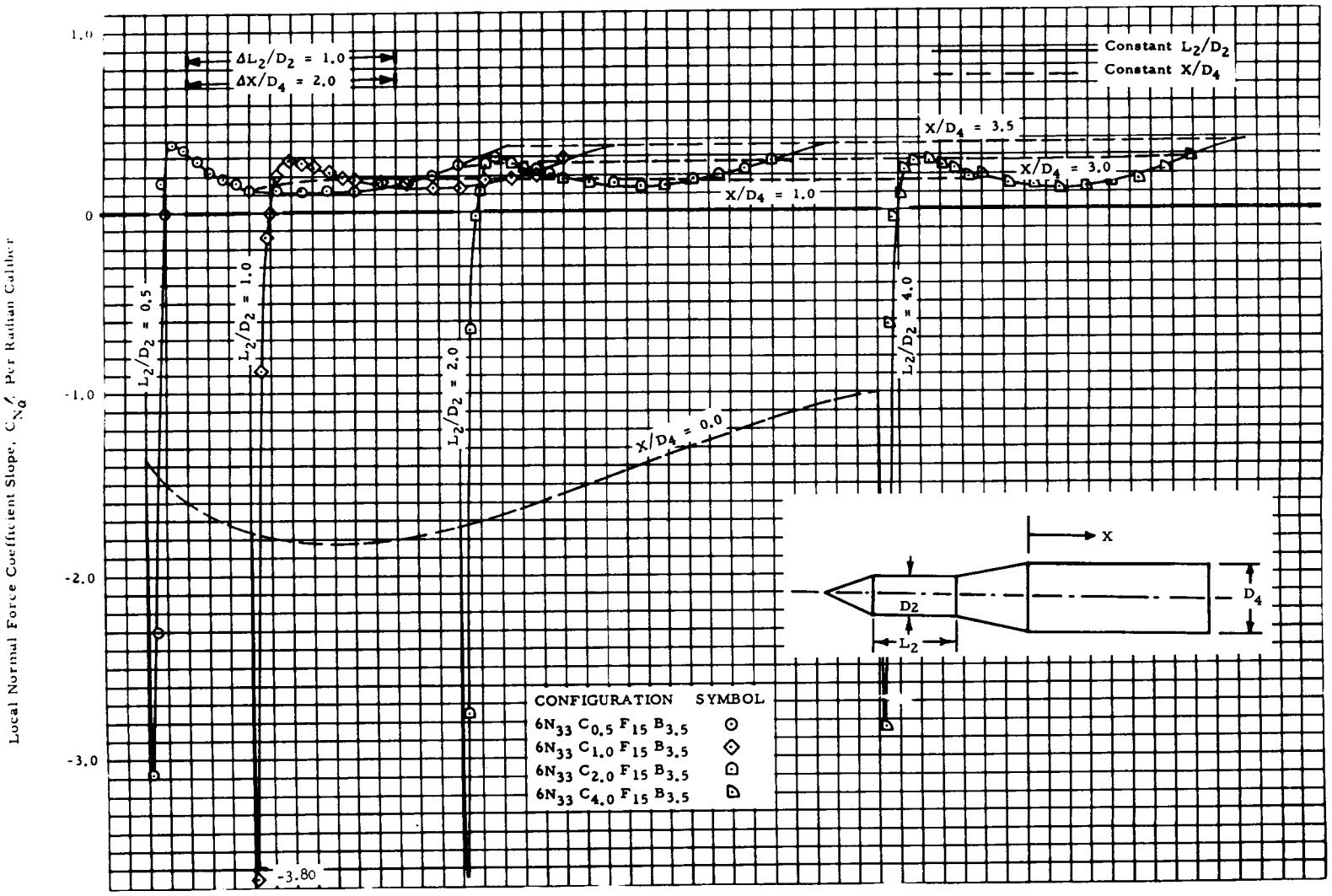

(a) M = 0.7

Figure 10 - The Effect of Forward Cylinder Length on Aft Cylinder Local Normal Force Distributions for Cone-Cylinder-Flare-Cylinders

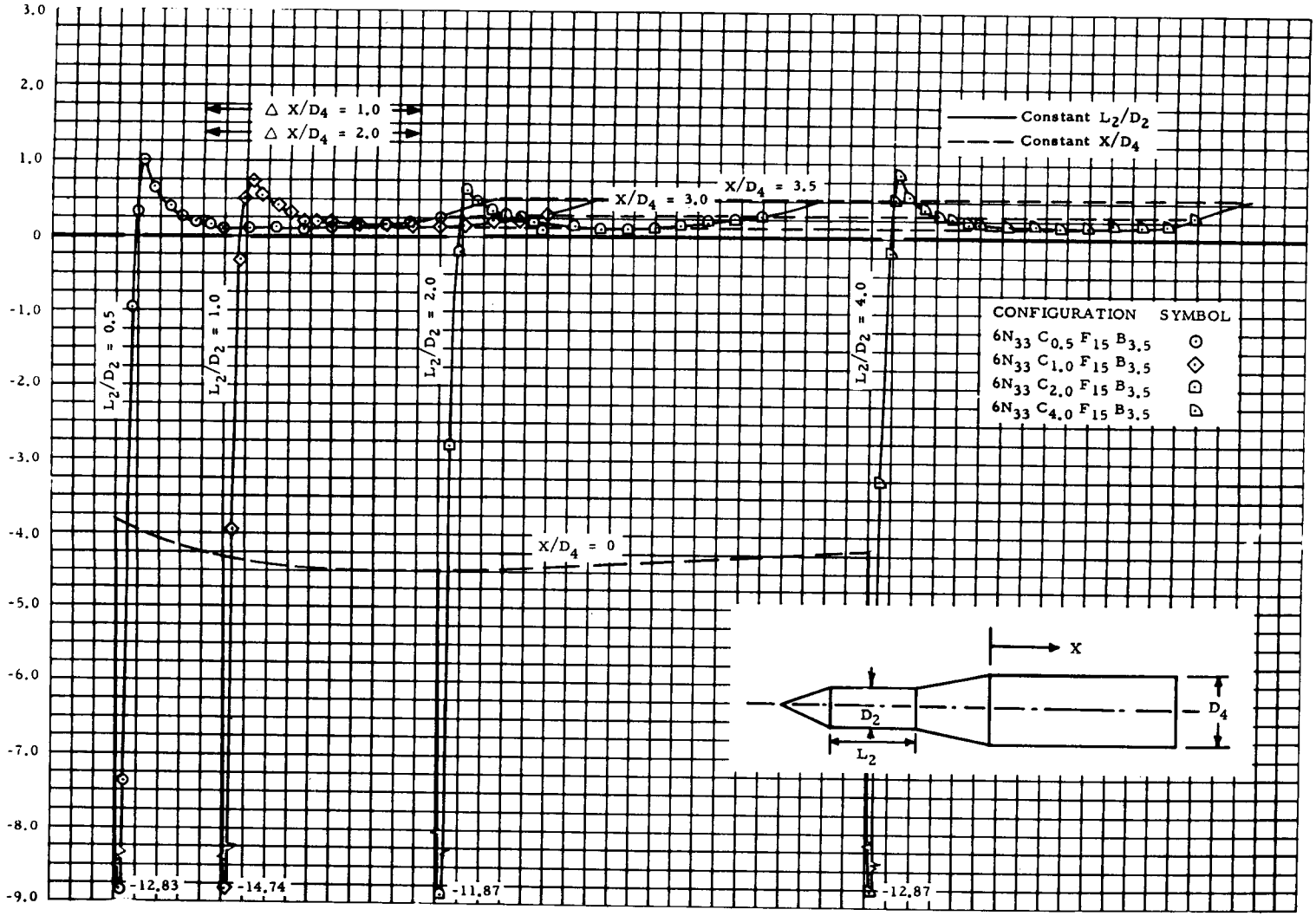

(b) M = 0.8

Figure 10 - The Effect of Forward Cylinder Length on Aft Cylinder Local Normal Force Distributions for Cone-Cylinder-Flare-Cylinders (Cont'd)

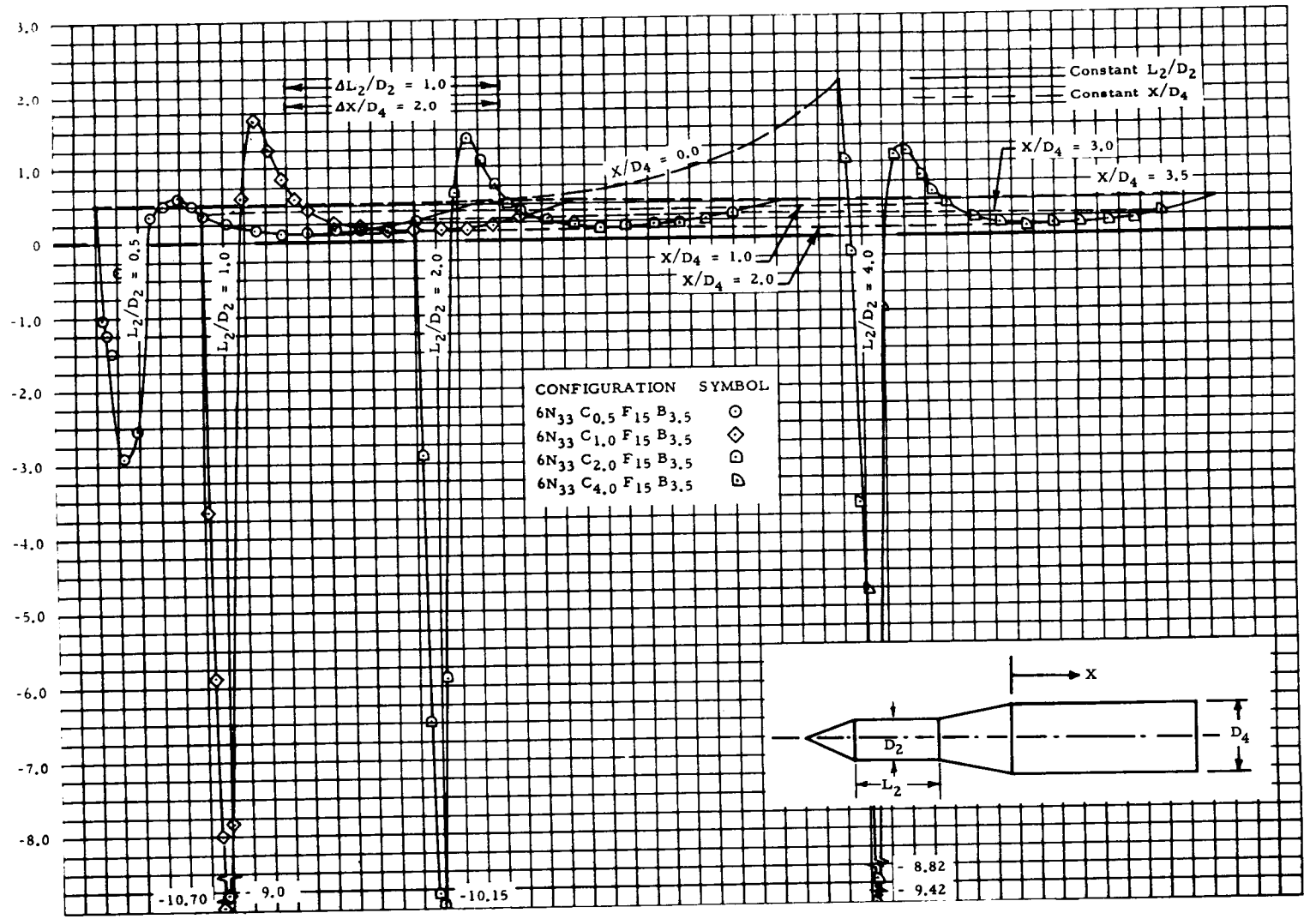

(c) M = 0.9

Figure 10 - The Effect of Forward Cylinder Length on Aft Cylinder Local Normal Force Distributions for Cone-Cylinder-Flare-Cylinders (Cont'd)

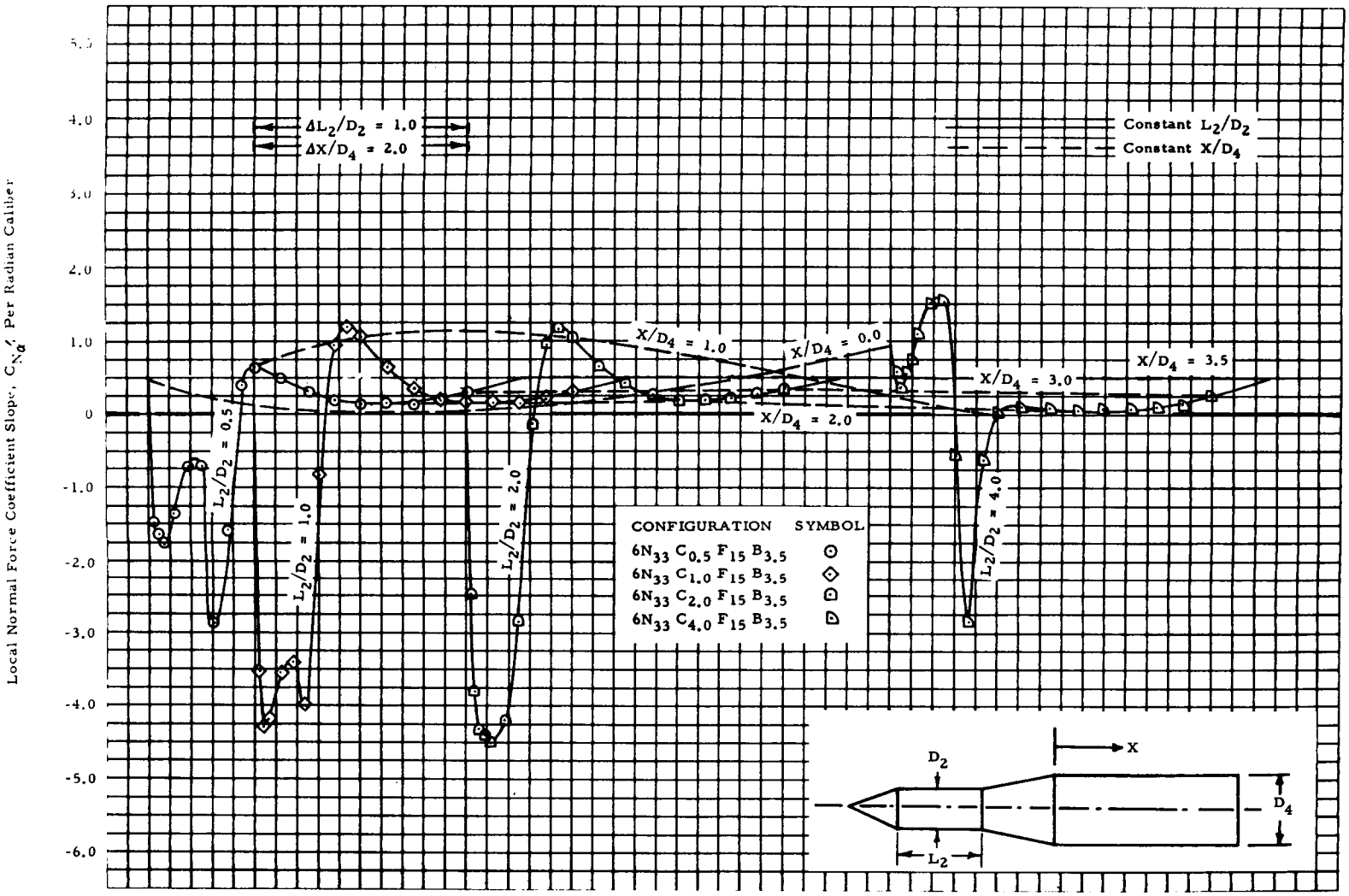

(d) M = 0.95

Figure 10 - The Effect of Forward Cylinder Length on Aft Cylinder Local Normal Force Distributions for Cone-Cylinder-Flare-Cylinders (Cont'd)

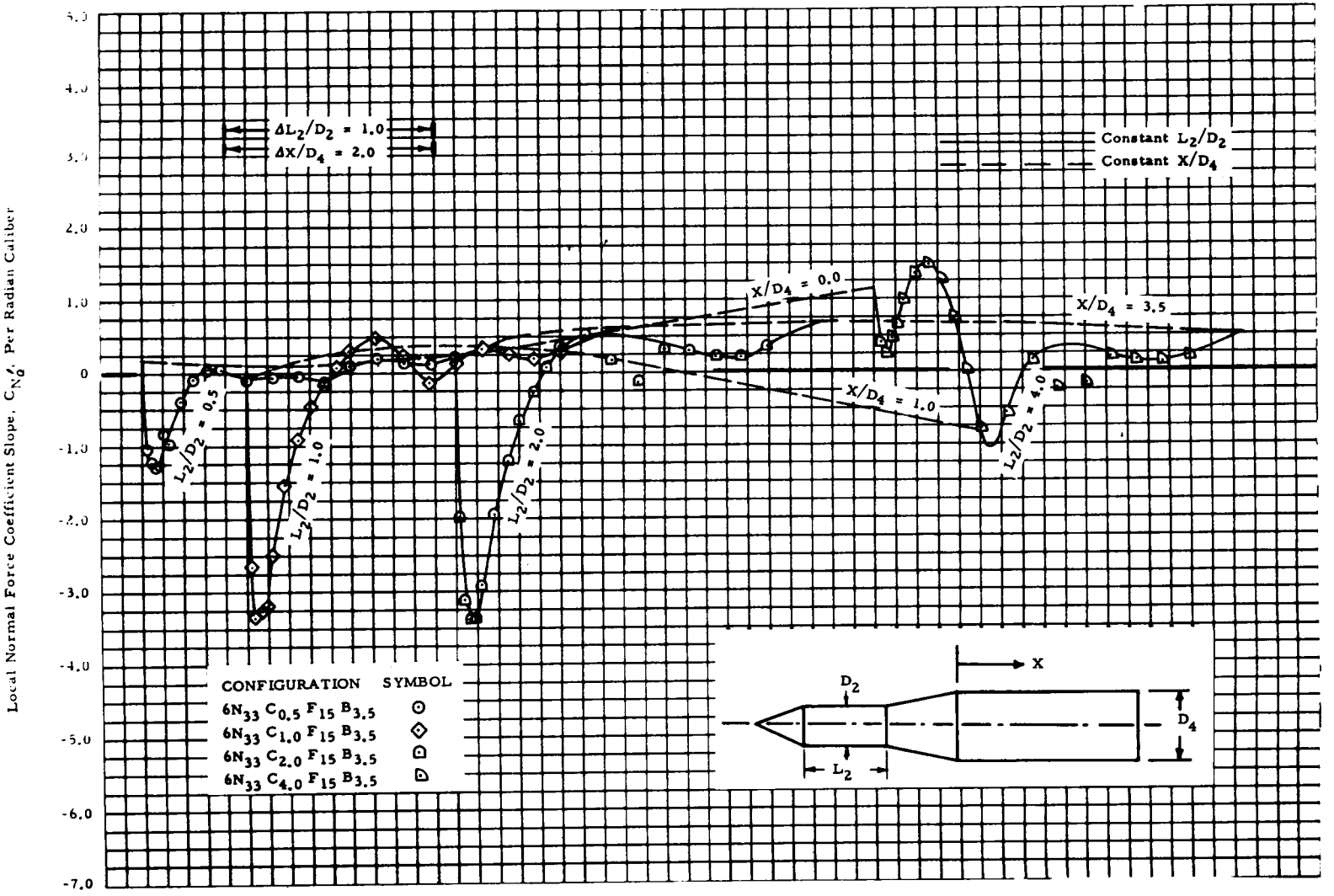

(e) M = 1.0

Figure 10 - The Effect of Forward Cylinder Length on Aft Cylinder Local Normal Force Distributions for Cone-Cylinder-Flare-Cylinders (Cont'd)

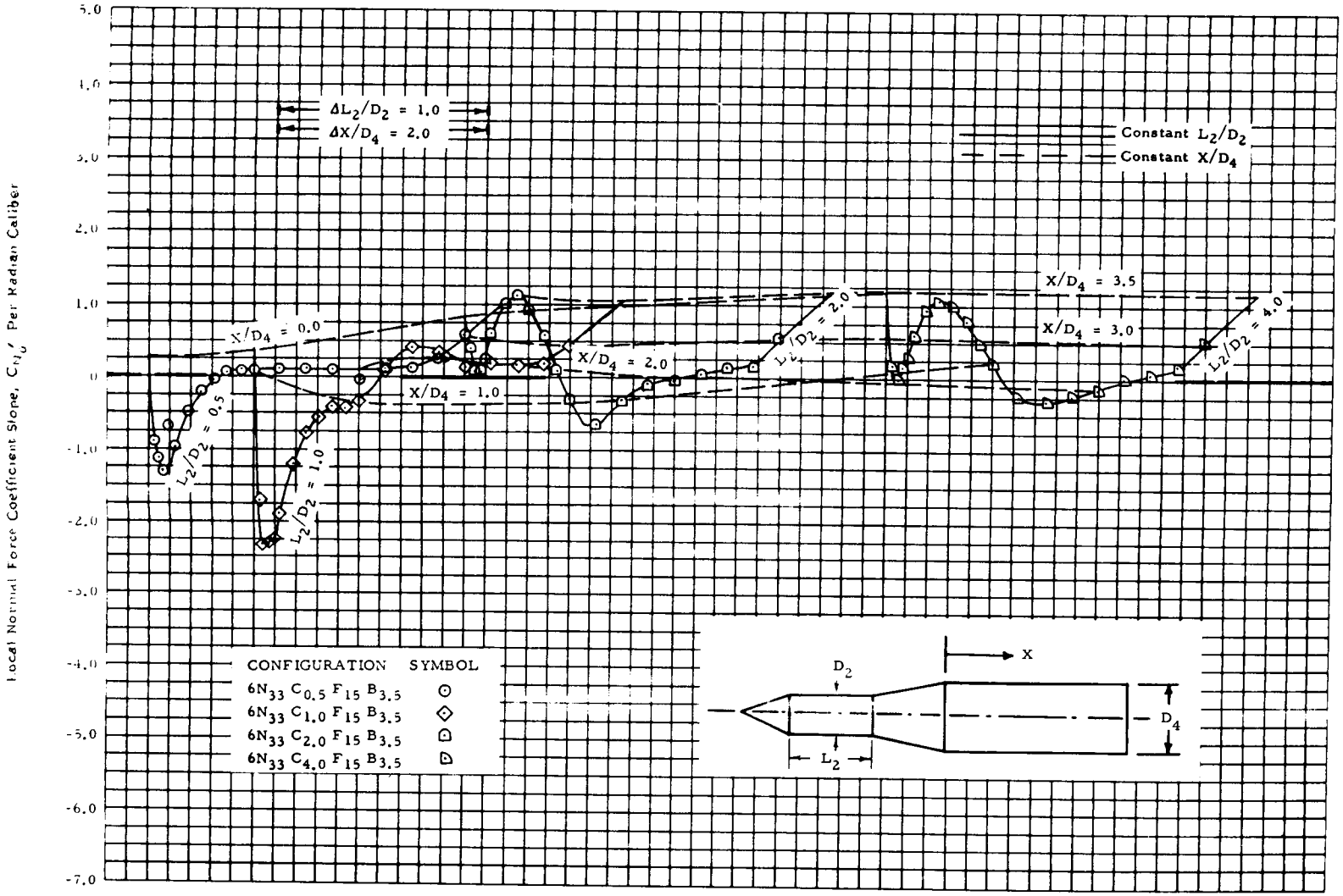

(f) M = 1.1

Figure 10 - The Effect of Forward Cylinder Length on Aft Cylinder Local Normal Force Distributions for Cone-Cylinder-Flare-Cylinders (Cont'd)

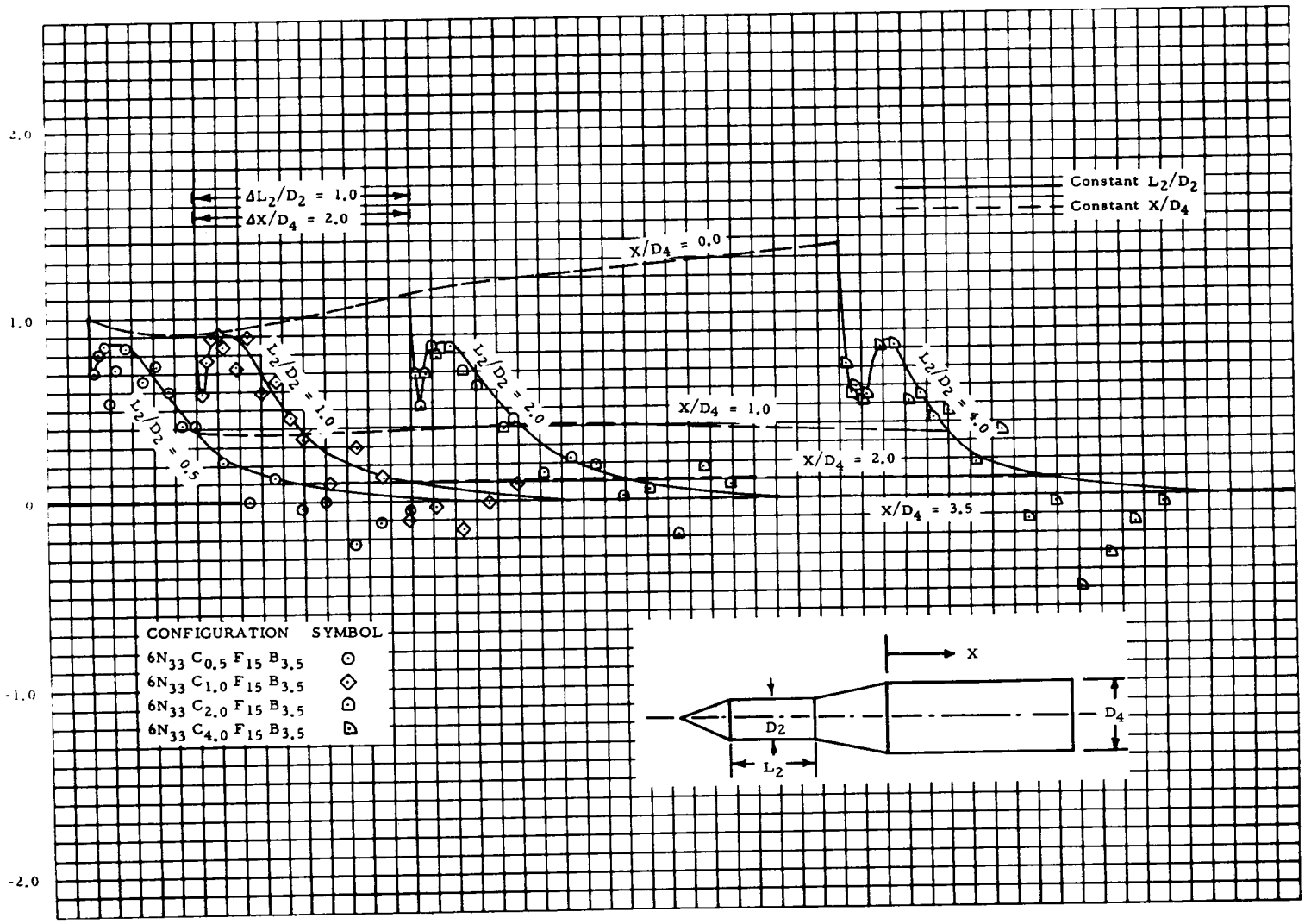

(g) M = 1.46

Figure 10 - The Effect of Forward Cylinder Length on Aft Cylinder Local Normal Force Distributions for Cone-Cylinder-Flare-Cylinders (Cont'd)

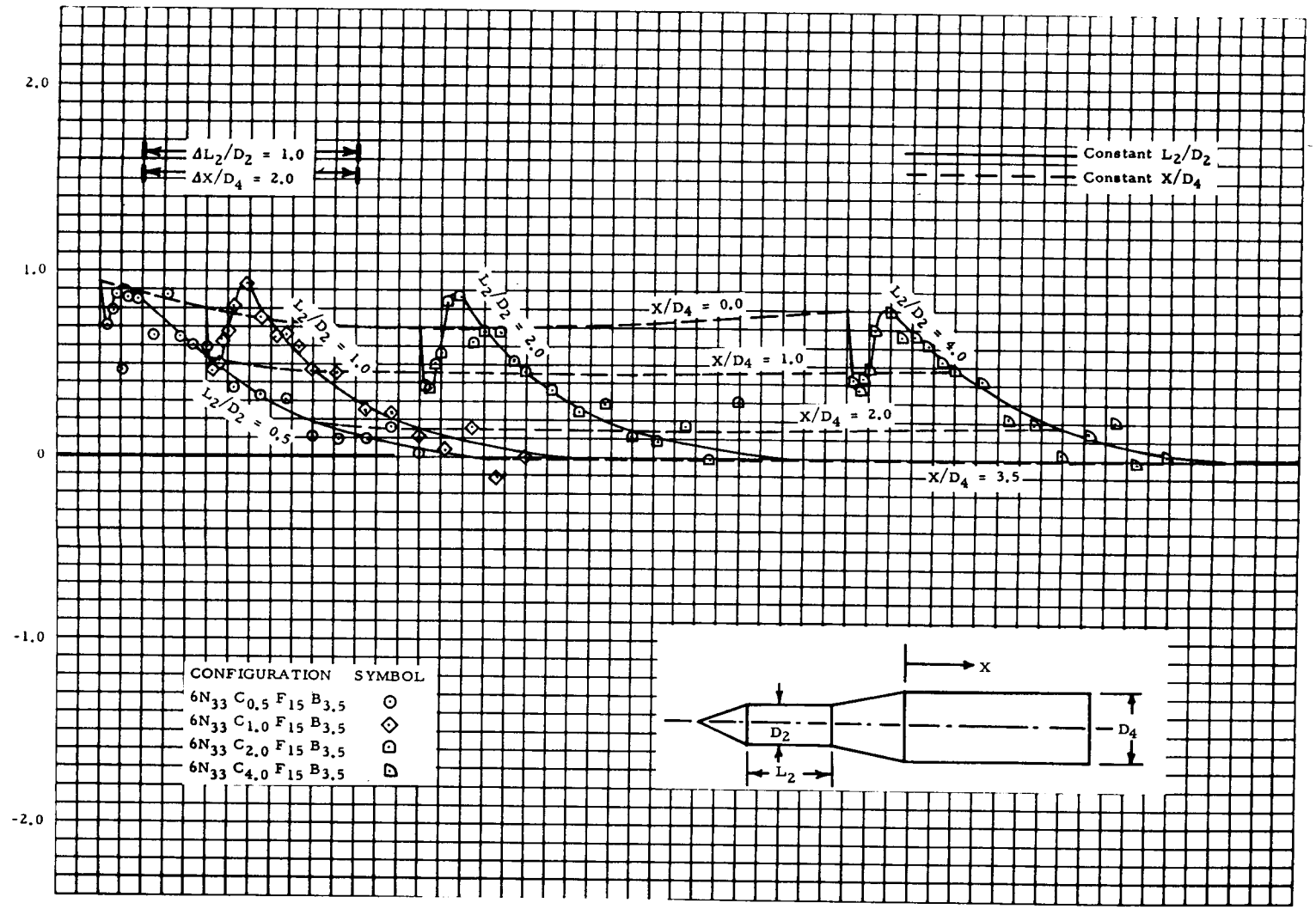

(h) M = 1.96

Figure 10 - The Effect of Forward Cylinder Length on Aft Cylinder Local Normal Force Distributions for Cone-Cylinder-Flare-Cylinder (Concluded)

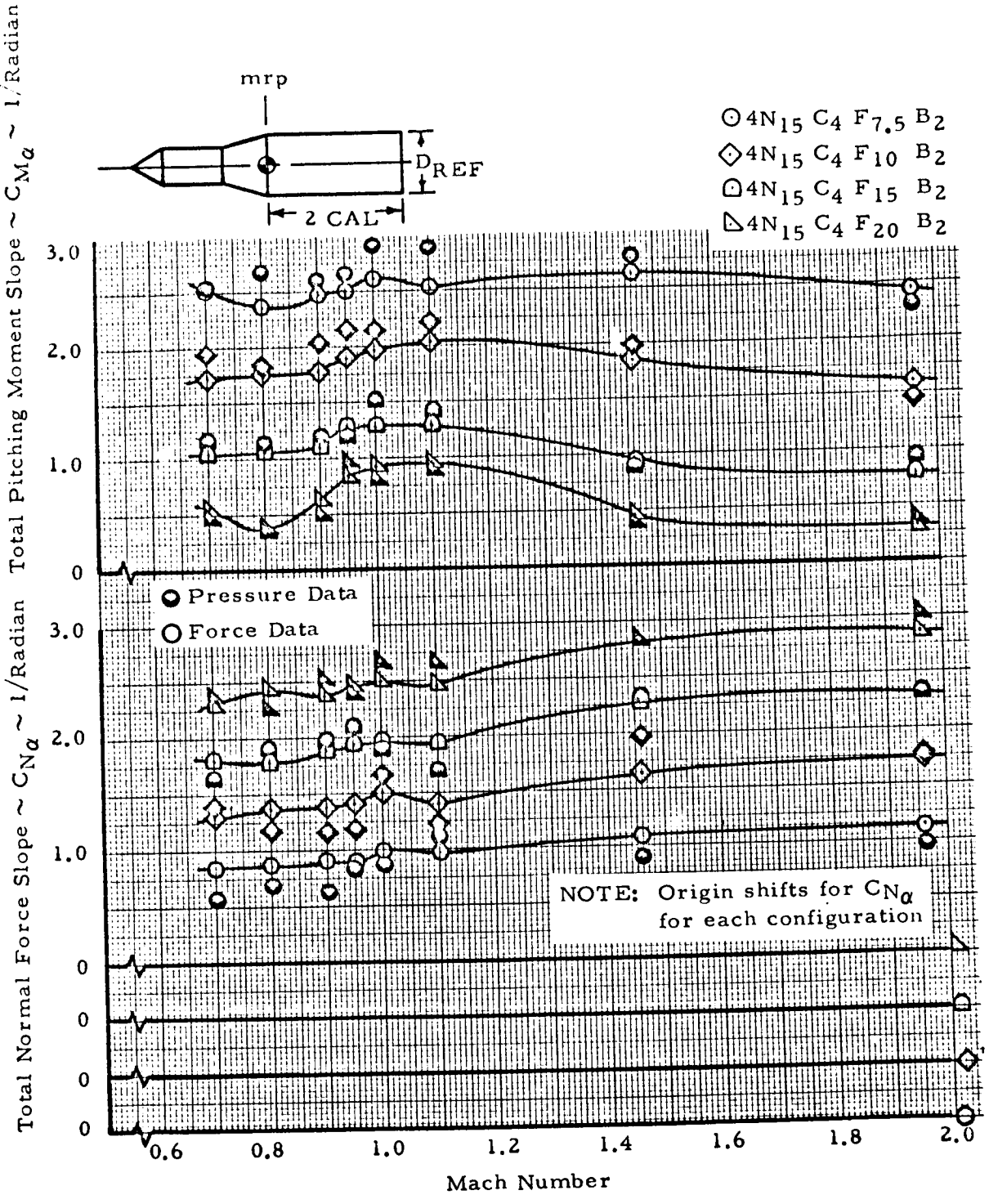

Figure 11a - Comparison of Total Normal Force and Pitching Moment from Force and Pressure Data

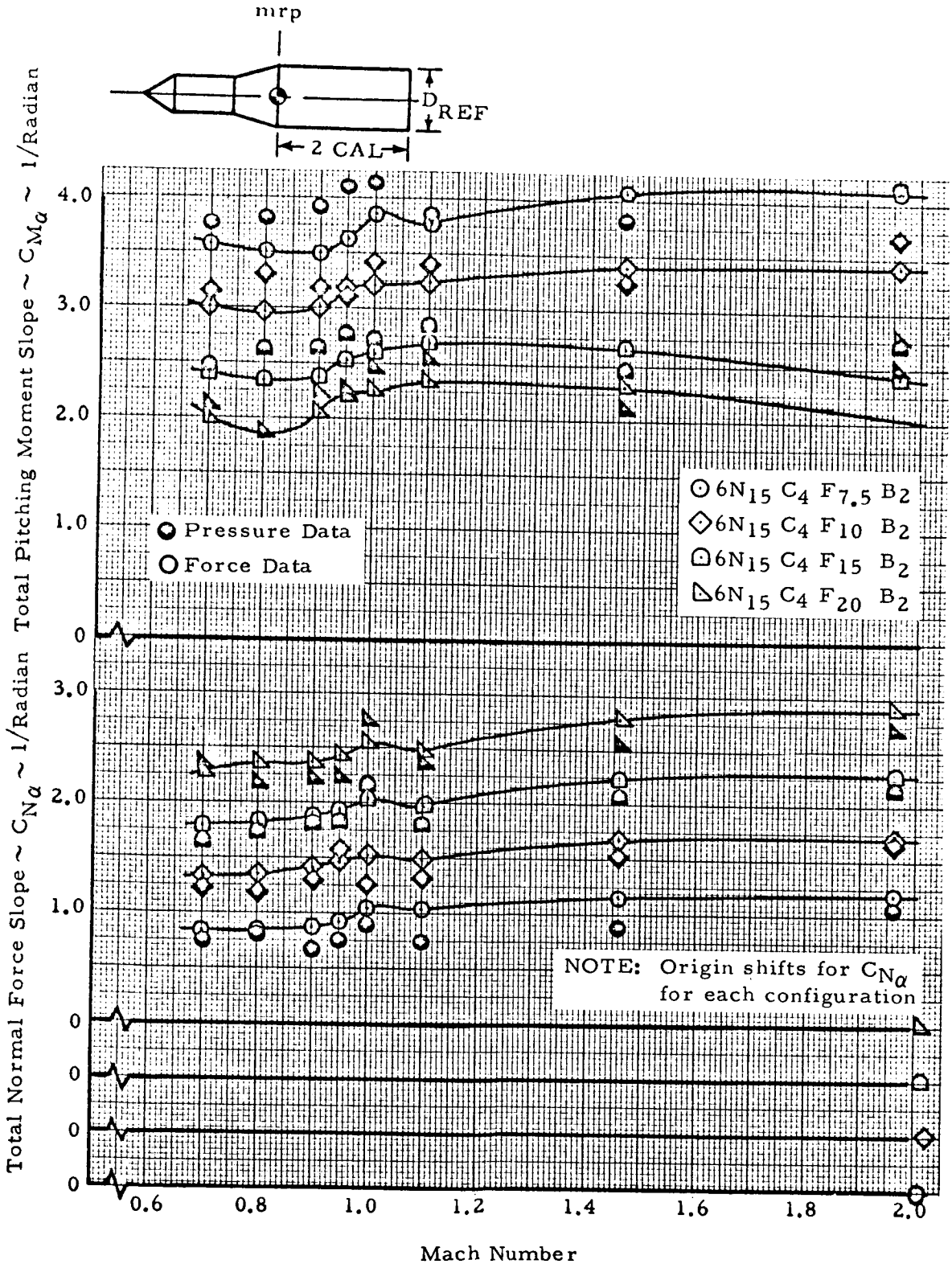

Figure 11b - Comparison of Total Normal Force and Pitching Moment from Force and Pressure Data

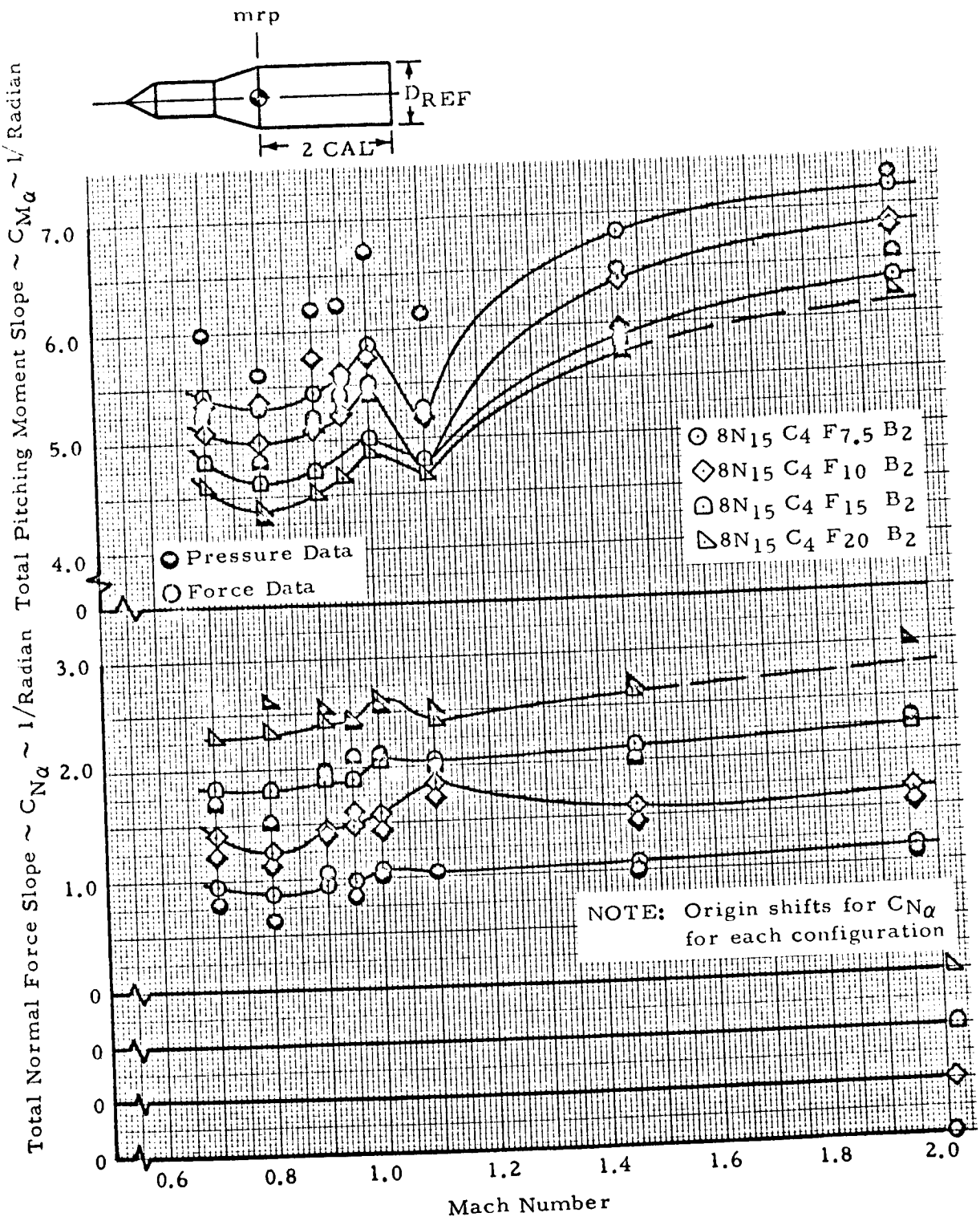

Figure 11c - Comparison of Total Normal Force and Pitching Moment from Force and Pressure Data

NASA-Langley, 1967 — 1 CR-737

10-5-67

"The aeronautical and space activities of the United States shall be conducted so as to contribute . . . to the expansion of human knowledge of phenomena in the atmosphere and space. The Administration shall provide for the widest practicable and appropriate dissemination of information concerning its activities and the results thereof."

—NATIONAL AERONAUTICS AND SPACE ACT OF 1958

NASA SCIENTIFIC AND TECHNICAL PUBLICATIONS

TECHNICAL REPORTS: Scientific and technical information considered important, complete, and a lasting contribution to existing knowledge.

TECHNICAL NOTES: Information less broad in scope but nevertheless of importance as a contribution to existing knowledge.

TECHNICAL MEMORANDUMS: Information receiving limited distribution because of preliminary data, security classification, or other reasons.

CONTRACTOR REPORTS: Scientific and technical information generated under a NASA contract or grant and considered an important contribution to existing knowledge.

TECHNICAL TRANSLATIONS: Information published in a foreign language considered to merit NASA distribution in English.

SPECIAL PUBLICATIONS: Information derived from or of value to NASA activities. Publications include conference proceedings, monographs, data compilations, handbooks, sourcebooks, and special bibliographies.

TECHNOLOGY UTILIZATION PUBLICATIONS: Information on technology used by NASA that may be of particular interest in commercial and other non-aerospace applications. Publications include Tech Briefs, Technology Utilization Reports and Notes, and Technology Surveys.

Details on the availability of these publications may be obtained from:

SCIENTIFIC AND TECHNICAL INFORMATION DIVISION

NATIONAL AERONAUTICS AND SPACE ADMINISTRATION

Washington, D.C. 20546